DNA-binding ruthenium complexes: cellular imaging and cytotoxicity

Martin Rhodri Gill

The University of Sheffield

Department of Chemistry

A thesis submitted for the degree of Doctor of Philosophy

September 2010

To my parents

"Everything is vague to a degree you do not realise until you have tried to make it precise." - Bertrand Russell

Abstract

The aim of this thesis was to investigate the cellular uptake, *in cellulo* DNA binding and cytotoxicity of Ru(II) complexes that reversibly bind to DNA *in vitro* with an accompanying increase in MLCT (metal-to-ligand charge-transfer) luminescence (the DNA light switch effect). Such complexes offer many advantages as luminescent probes of DNA structure but poor cellular uptake restricts their use in live cells. Using a combination of confocal laser scanning microscopy (CLSM) and transmission electron microscopy (TEM), Ru(II)tpphz (tpphz = tetrapyrido[3,2-a:2',3'-c:3'',2''-h:2''',3'''-j]phenazine) metallo-intercalators are shown to be internalised by MCF-7 human breast cancer cells where they successfully target nuclear DNA. Cell viability studies revealed a cytotoxic potency comparable to cisplatin, which is retained for cisplatin-resistant tumour cells. The dinuclear Ru(II)tpphz complex, $[\{Ru(phen)_2\}_2(tpphz)]^{4+}$ **[3.1]** (phen = 1,10-phenanthroline), was shown to function as a multifunctional biological imaging agent staining the DNA of eukaryotic and prokaryotic cells for both CLSM and TEM while confocal microscopy reveals multiple emission peaks that function as markers for cellular DNA structure. Cell viability studies revealed that **[3.1]** displays a high toxicity towards cancer cell lines over an extended incubation time, of particular interest as **[3.1]** binds quadruplex DNA with a high affinity. The synthesis of several derivatives of **[3.1]**, with bpy (2,2'-bipyridine), 5mp (5-methyl-phen) and dmp (2,9-dimethyl-phen) replacing phen as the ancillary ligand, has shown how the ancillary ligand can affect such properties as luminescence, DNA binding affinity, cellular uptake and cytotoxicity, which resulted in the derivation of the ancillary ligand "toxicity series" of dmp > phen > 5mp > bpy. Using inhibition studies, a common finding is the uptake mechanism of these Ru(II) complexes is a non-endocytic mode of active transport and nuclear uptake has been shown to be a concentration-dependent process. This work has established the rate of cellular uptake to be the most important factor that governs the cytotoxicity of such complexes and not *in vitro* DNA binding affinity.

List of publications

Directly originating from this thesis

M. R. Gill, J. Garcia-Lara, S. J. Foster, C. Smythe, G. Battaglia and J. A. Thomas, A ruthenium(II) polypyridyl complex for direct imaging of DNA structure in living cells, *Nat. Chem.*, **2009**, *1*, 662-667.

Other publications

P. Waywell, V. Gonzalez, M. R. Gill, H. Adams, A. J. H. Meijer, M. P. Williamson and J. A. Thomas, Structure of the Complex of $[Ru(tpm)(dppz)py]^{2+}$ with a B-DNA Oligonucleotide - A Single-Substituent Binding Switch for a Metallo-Intercalator, *Chem. Eur. J.*, **2010**, *16,* 2407-2417.

S. P. Foxon, T. Phillips, M. R. Gill, M. Towrie, A. W. Parker, M. Webb and J. A. Thomas, A Multifunctional Light Switch: DNA Binding and Cleavage Properties of a Heterobimetallic Ruthenium-Rhenium Dipyridophenazine Complex, *Ange. Chem. Int. Ed.*, **2007**, *46*, 3686-3688.

Acknowledgements

Firstly, I would like to thank the White Rose DTC for a PhD scholarship, enabling me to undertake a project that I have enjoyed. I thank my two supervisors, Jim and Beppe, for their constant enthusiasm, encouragement and patience, which contributed towards me actually doing some work and getting to visit two new countries. I would also like to thank Carl Smythe for his significant input and collaboration, which gave me a new impetus.

Thanks go to Irene, Nicola and Richard for their patient tuition of cell culture, Tom, Tim and Phil for their help with the chemistry, Chris Hill for TEM assistance, Liz Smythe for explaining endocytosis, Jorge and Prof. Foster for their bacterial work, Hanan and Adel for their synthetic contributions, Joe for our work together, the fountain of knowledge that is Wikipedia[*citation needed*], Mike, Ash, Marzia, Vanessa, Nick, Sukh, Dave, Fil, Ahmed, Ina and all other members, past and present, of the Thomas, Battaglia and Smythe groups for making each lab an interesting place in its own right to work in and I hope I contributed to that.

Out of the lab, and for making my time in Sheffield enjoyable, I would like to thank: Hayley, Ruth and Jenny, who deserve special mention for their attempts to keep me sane, Warren for our good-humoured arguments, Youseff and Iain for sports-related banter (SRB) and all of the E floor massive for general procrastination and friday drinks, tag-rugby folk, Kroto people and my fellow DTC-misfits.

Finally, I would like to acknowledge all the people back in South Wales: Ed, Chris, Mike, Pete, Ellie, Emma, the Sarah-Dai entity and Dan for their friendship and good times.

Declaration

Except where specific references have been made to other sources, the work within this thesis is the original work of the author. It has not been submitted, in whole or in part, for any other degree. Certain results have already been published in peer-reviewed journals.

Martin R. Gill

September 2010

Abbreviations

5mp	5-methyl-1,10-phenanthroline
A	adenine
A2780	cell line, origin: human ovarian carcinoma
A2780-CP70	cell line, origin: human ovarian carcinoma, cisplatin-resistant
ADP	adenosine diphosphate
ATP	adenosine triphosphate
a.u.	arbitrary units
bpy	2,2'-bipyridine
C	cytosine
carboplatin	c*is*-diammine(cyclobutane-1,1-dicarboxylate-*O,O'*)platinum(II)
CHO	cell line, origin: Chinese Hamster ovary
chrysi	chrysenequinone diimine
cisplatin	*cis*-diaminedichloroplatinum(II)
CLSM	confocal laser scanning microscopy
cpdppz	12-cyano-12,13-dihydro-11H-cyclopenta[b]dipyrido[3,2-a:2',3'-c]phenazine-12-carbonyl
CT-DNA	calf thymus DNA
dap	5,6-diamino-1,10-phenanthroline
DAPI	4',6-diamidino-2-phenylindole
DIP	4,7-diphenyl-1,10-phenanthroline
DMEM	cell media, Dulbecco's modified Eagle's medium
dmp	2,9-dimethyl-1,10-phenanthroline
DMSO	dimethyl sulphoxide
DNA	deoxyribonucleic acid
dppn	benzo[*i*]-dipyrido[3,2-a:2',3'-*c*]phenazine
dppz	dipyrido[3,2-a:2',3'-c]phenazine

dpq	1,10-phenanthroline-5,6-dione
en	ethylenediamine
ER	endoplasmic reticulum
FAB	fast-atom bombardment
FaDu	cell line, origin: human hypopharyngeal carcinoma
FCS	fetal calf serum
G	guanine
G_1, G_2, G_0	cell phases, gap
GS	ground state
HDF	primary cells, origin: human dermal fibroblast
HeLa	cell line, origin: human cervical carcinoma
HPLC	high performance liquid chromatography
HR	homologous recombination
hrs	hours
IC_{50}	half maximal inhibitory concentration
ISC	intersystem crossing
IT_{50}	half maximal inhibitory time
L5178Y-R	cell line, origin: mouse lymphoma
M	cell phase, mitosis
MCF-7	cell line, origin: human breast carcinoma
Me_2Trien	2,9-diamino-4,7-diazadecane
MLCT	metal-to-ligand charge-transfer
mins	minutes
MS	mass spectroscopy
MTT	3-(4,5-dimethylthiazol-2-yl)-2,5-diphenyltetrazoliumbromide
NDB	nucleic acid database
NMR	nuclear magnetic resonance
N^N	nitrogen-coordinating bidentate ancillary ligand

PBS	phosphate buffered saline
PDT	photodynamic therapy
phen	1,10-phenanthroline
Phi	9,10-phenanthrenequinone diimine
PI	propidium iodide
py	pyridine
RNA	ribonucleic acid
RNAi	RNA interference
RPMI	cell media, RPMI-1640 (Roswell Park Memorial Institute)
S	cell phase, synthesis
S. aureus	*Staphylococcus aureus*
Saos-2	cell line, origin: human osteosarcoma
T	thymine
taptp	4,5,9,18-tetraazaphenanthreno[9,10-b] triphenylene
TEM	transmission electron microscopy
tpm	tris-(1-pyrazolyl)methane
tpphz	tetrapyrido[3,2-a:2',3'-c:3'',2''-h:2''',3'''-j]phenazine
TRAP	telomere repair amplification protocol
Tris	tris(hydroxymethyl)aminomethane
UV-vis	ultraviolet-visible

Table of contents

Chapter 1

Introduction

1.1 DNA

In all eukaryotic and prokaryotic organisms the storage of genetic information is encoded almost entirely in the biopolymer deoxyribonucleic acid (DNA). The "genetic code" within DNA is contained in the cells of the organism and provides the blueprint for the formation of ribonucleic acid (RNA) and proteins, which are the functional components of cells. The flow of biological information, whereby a section of DNA is transcribed into RNA which in turn is responsible for the synthesis of specific proteins (translation), is set out in "the central dogma of molecular biology", as formalised by Crick (Figure 1.1).[1]

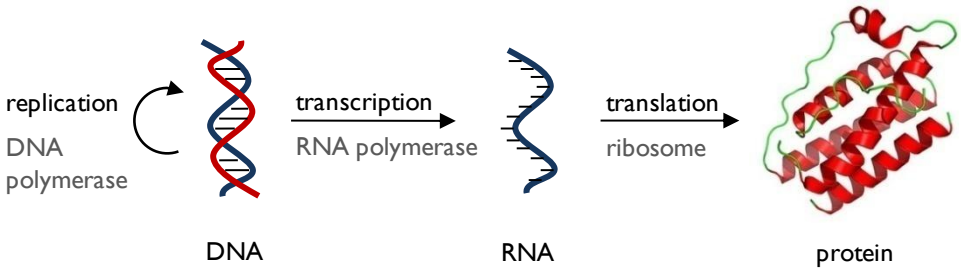

Figure 1.1 The central dogma of molecular biology.

The central dogma also describes the process of DNA replication which allows organisms to make copies of their genomes. Along with the ability of cells to replicate themselves, this enables each new generation of the cell (and therefore the organism) to undergo the exact same transfer of information encoded by the cell's DNA and this serves as the basis of biological inheritance and genetics.

1.1.1 DNA structure

DNA is a linear polymer composed of repeating nucleotide units, each comprised of a nitrogen heterocyclic base, a pentose sugar and a phosphate group (Figure 1.2). The four nitrogenous bases in DNA can be adenine (A), guanine (G), cytosine (C) or thymine (T) and it is through sequences of these bases that the genetic information of the organism is contained and then expressed *via* translation and transcription. Each nucleotide in the DNA molecule is linked by a phosphodiester bond between the 3' and 5' carbon atoms on adjacent sugar rings and sequences of DNA are written in the 5' → 3' direction.

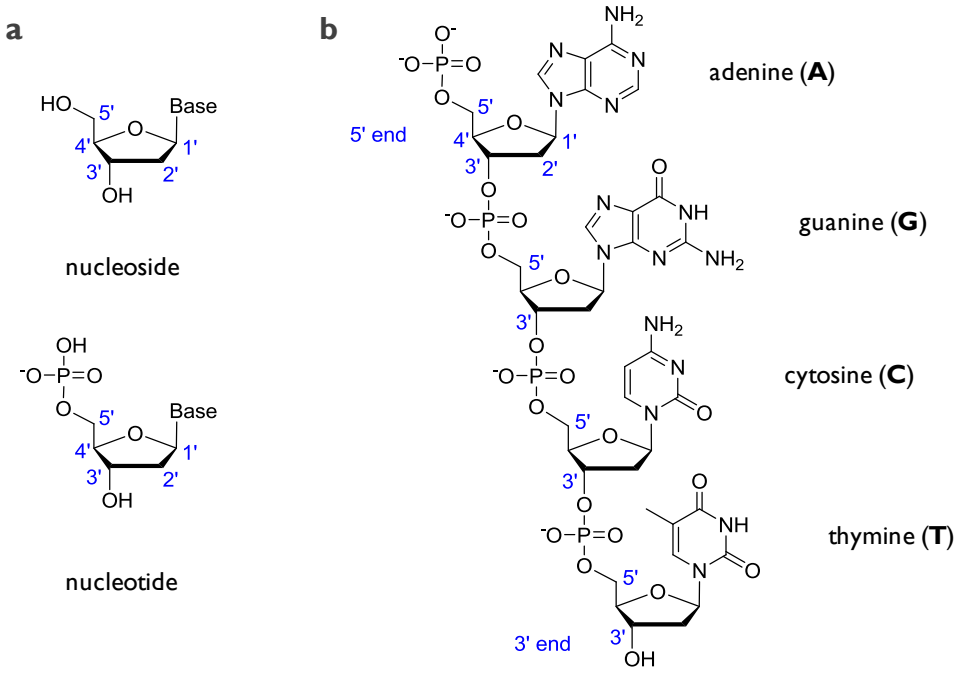

Figure 1.2 a, DNA nucleosides and nucleotides. **b,** Nucleotides of DNA lined by phosphodiester bonds and chemical structure of the nitrogenous bases.

The most energetically favourable form of DNA, and the form the molecule usually takes up in living organisms, is the right-handed double helix B-DNA, which was first described by Watson and Crick using Franklin's crystal structure.[2] The structure of B-DNA consists of two strands of DNA running in opposite directions held together by hydrogen bonding between pairs of

bases on opposing strands; adenine pairs with thymine and guanine pairs with cytosine (Figure 1.3a,b). The double helix of B-DNA possesses two grooves: the major groove (width = 12 Å) and minor groove (width = 6 Å) as shown in Figure 1.3c.

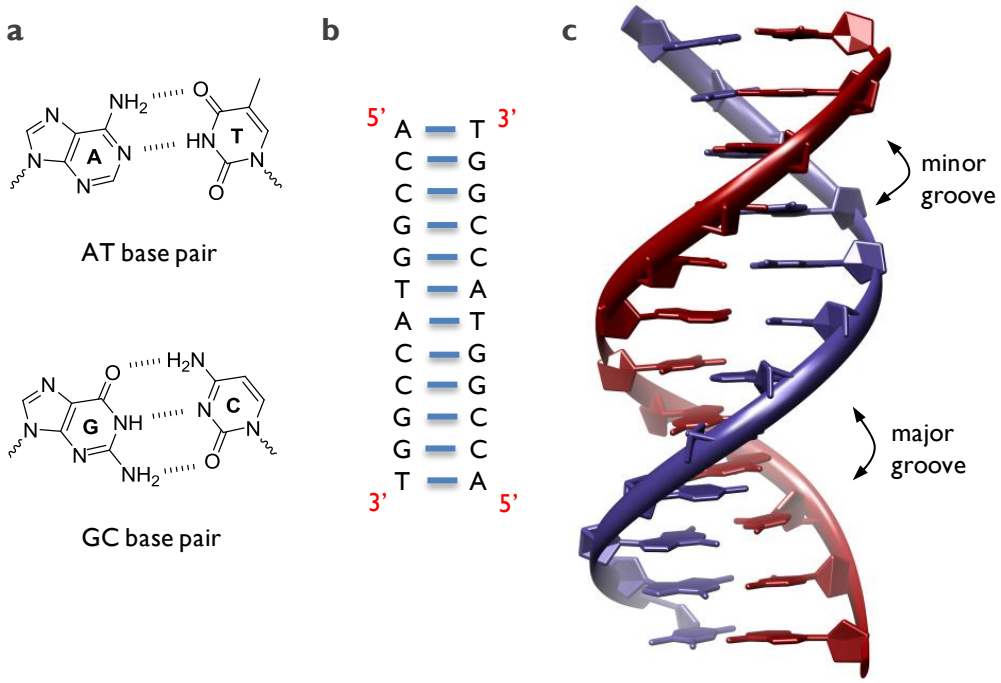

Figure 1.3 a, DNA base pairs. **b,** Two opposite strands of DNA are complimentary to each other. **c,** B-DNA double helix showing grooves (Nucleic acid Database (NDB) ID: BD0003).

1.1.2 Cellular DNA

In eukaryotic cells, the genomic DNA of the organism is organised into linear sets of chromosomes located within the cell nucleus (Figure 1.4a,b). The complete human genome contains over 3 x 10^9 base pairs which code for approximately 2 x 10^4 genes[3] and is stored on 23 chromosome pairs, one set originating from the mother and one from the father. To allow the large amount of DNA to fit into the relatively small cell nucleus, chromosomal DNA is folded with histone and scaffold proteins to form chromatin (Figure 1.4c). Chromatin is organised into two different forms: heterochromatin,

which contains tightly packed DNA, and euchromatin, which contains DNA in an extended form.[4] The compact chromatin structure is also dynamic, allowing protein access for vital processes such as gene transcription, DNA replication and DNA repair.[5]

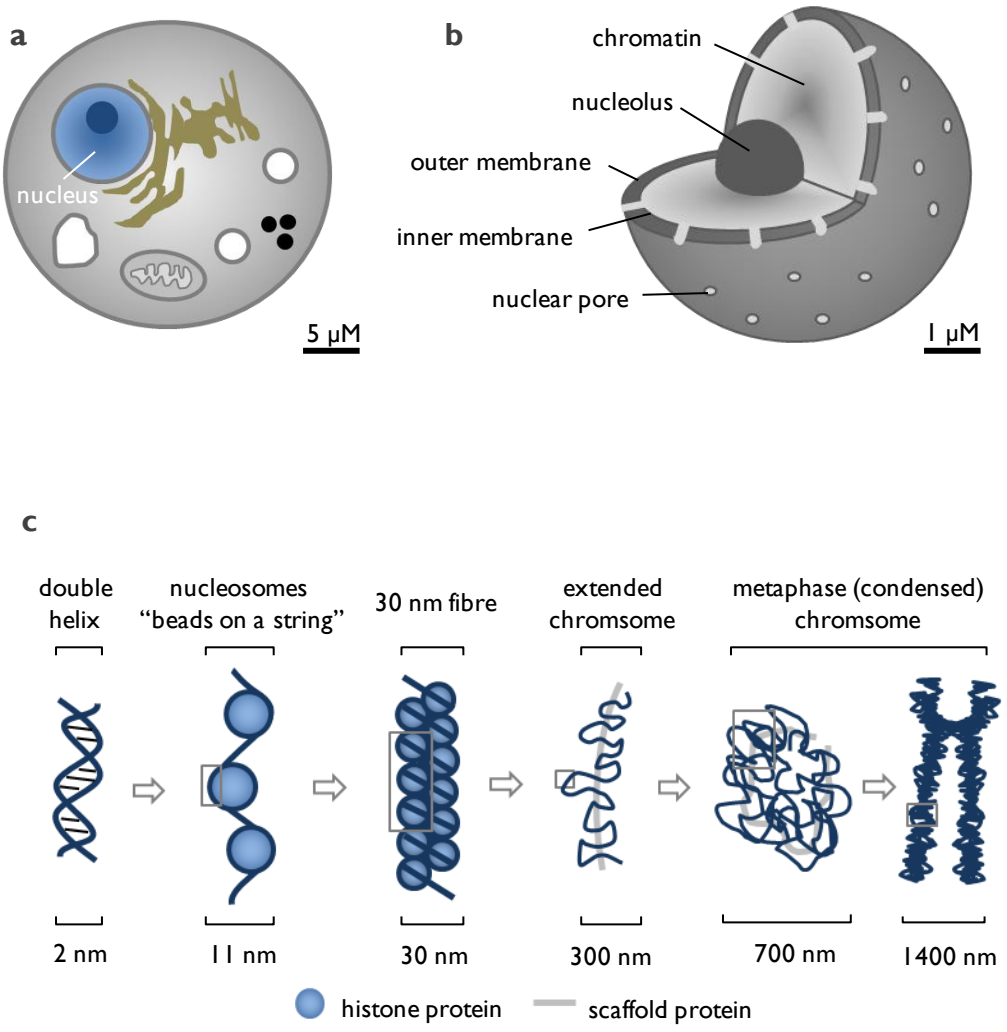

Figure 1.4 a, Eukaryotic cell showing location of nucleus. **b,** Cell nucleus structure. **c,** Chromatin structure showing DNA organisation.

1.1.2.1 Mitochondrial DNA

In addition to the nucleus, mitochondria of cells also contain DNA (Figure 1.5). Mitochondria are membrane-enclosed organelles 0.5 – 10 μm in diameter that generate chemical energy for the cell in the form of adenosine triphosphate (ATP), which is converted to adenosine diphosphate (ADP) in biochemical reactions. Mitochondrial DNA is a separate genome to that of the organism and takes the form of a circular DNA molecule containing approximately 17,000 base pairs.[4]

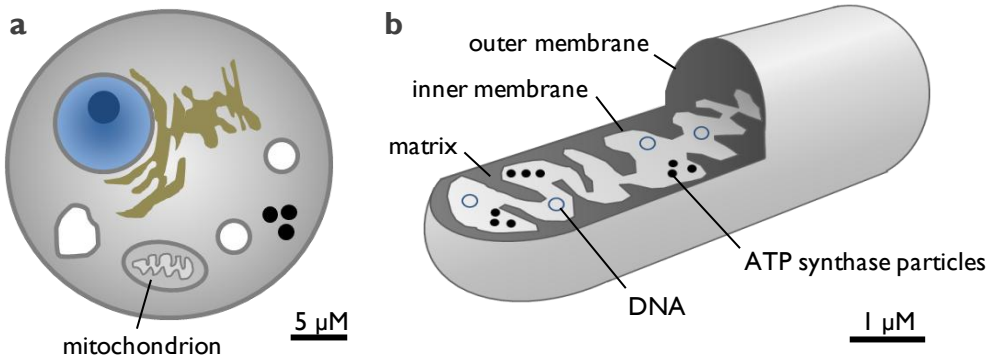

Figure 1.5 Mitochondrion location (**a**) and structure (**b**).

1.1.3 Cell division and the cell cycle

The ability for cells to divide and multiply is fundamentally important to the growth and maintenance of the organism. During eukaryotic cell division, chromosomes are first duplicated through DNA replication before pairs of chromosomes condense and then separate using a mitotic spindle into two identical sets located in opposite regions of the cell (mitosis). The parent cell then divides to form two daughter cells (cytokinesis), each of which contains one of these sets and thus an exact copy of the parental DNA (Figure 1.6a). The series of events that cells undergo leading up to cell division is described by the cell cycle. This consists of four distinct phases: G_1, S (DNA synthesis), G_2 and M (mitotic phase). G_1, S and G_2 phases are collectively known as interphase (Figure 1.6b). In addition to these there is

the resting phase G_0, where cells remain viable but do not proliferate. The cell cycle is strictly regulated by numerous proteins and monitored by checkpoints which operate within S-phase, between S and M phase, as well as at the G_1/S and G_2/M phase boundaries. In addition, a spindle checkpoint ensures that segregation of sister chromatids cannot occur unless all chromosome pairs are attached to the mitotic spindle, thus preventing aneuploidy (an abnormal number of chromosomes).[4]

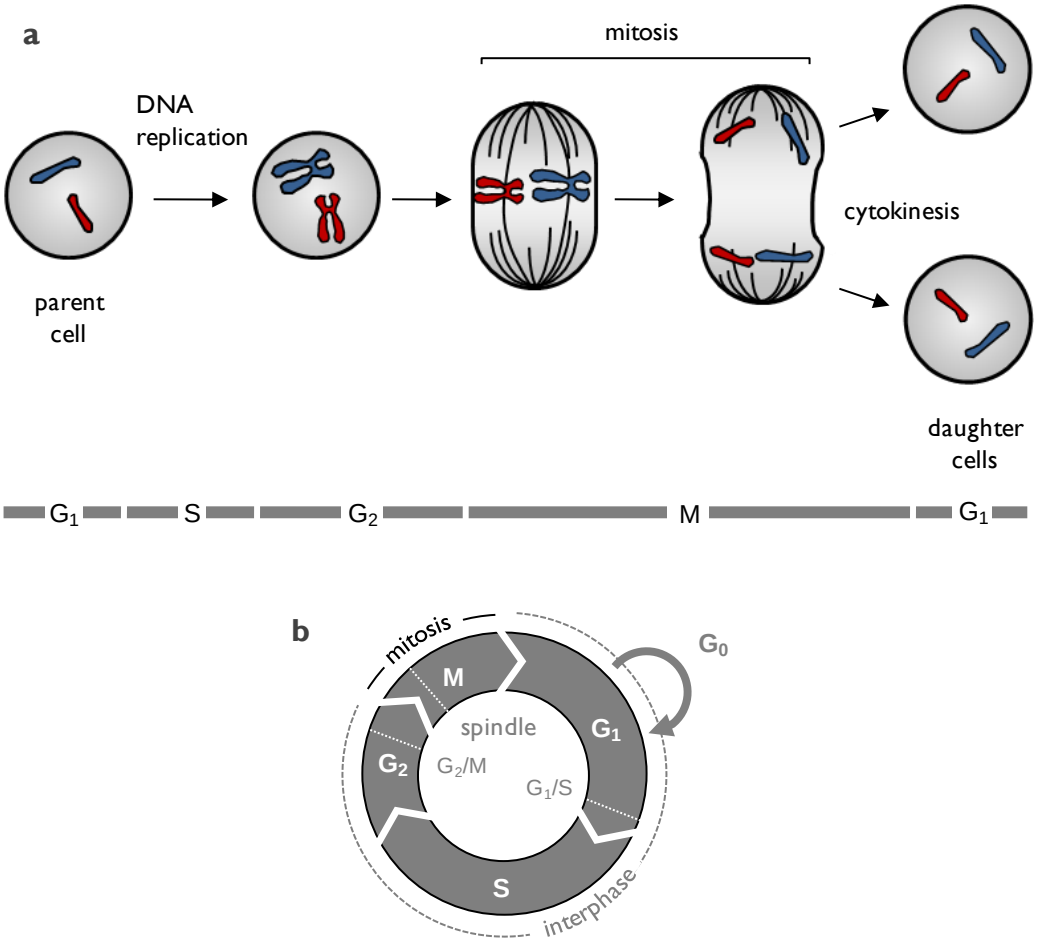

Figure 1.6 a, Mitotic cell division showing DNA content. Bar indicates cell cycle phase. **b,** The cell cycle with checkpoint locations indicated in dotted lines.

The condensed chromosome and mitotic spindle structures can be used to identify the different stages of mitosis whereas interphase chromosomes

exist in an extended form, compartmentalised into discrete territories in the nucleus (Figure 1.7).[6]

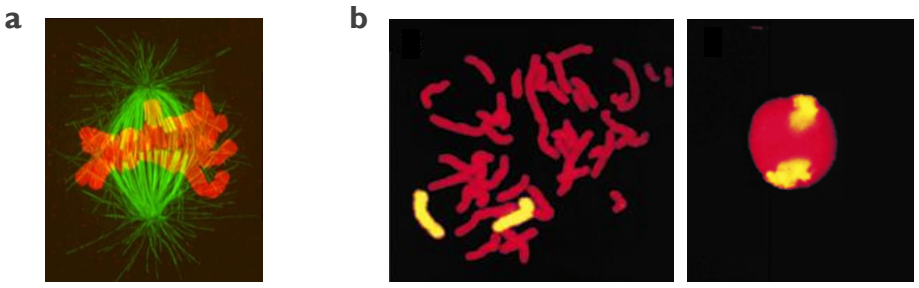

Figure 1.7 a, Mitotic chromosomes (stained red) and mitotic spindle (green). **b,** Individual chromosomes (yellow) from a metaphase spread (left) occupy distinct territories in the interphase nucleus (right).[6]

1.1.4 DNA replication

As previously discussed, the ability of the cells of an organism to replicate the DNA within them is essential for the growth and proliferation of that organism. For eukaryotes, this process initially involves the double helix of DNA being unwound by topoisomerase and helicases to form a replication fork before the synthesis of two new DNA strands by DNA polymerases (Figure 1.8a). A consequence of the specific Watson-Crick base pairing of DNA is that each strand is able to act as a template for the synthesis of the complementary strand, meaning that two identical copies of the DNA molecule are formed, essential for mitotic cell division. DNA polymerases are only able to synthesise DNA in the 5' to 3' direction and initially requires an 8-12 base segment of RNA to act as a primer. After this is completed, the RNA primer is removed and the remaining gaps are filled in by DNA polymerase. As a consequence, while synthesis of the leading strand is continuous, synthesis of the 3' to 5' strand (the lagging strand) occurs in short Okazaki fragments each requiring an RNA primer. The repair synthesis, which converts the RNA primer into DNA, has no binding site for the terminal 5' end and, as a result, the DNA cannot be fully synthesised,

resulting in a single stranded DNA overhang at the 3' end of the newly synthesised DNA molecule (Figure 1.8b).

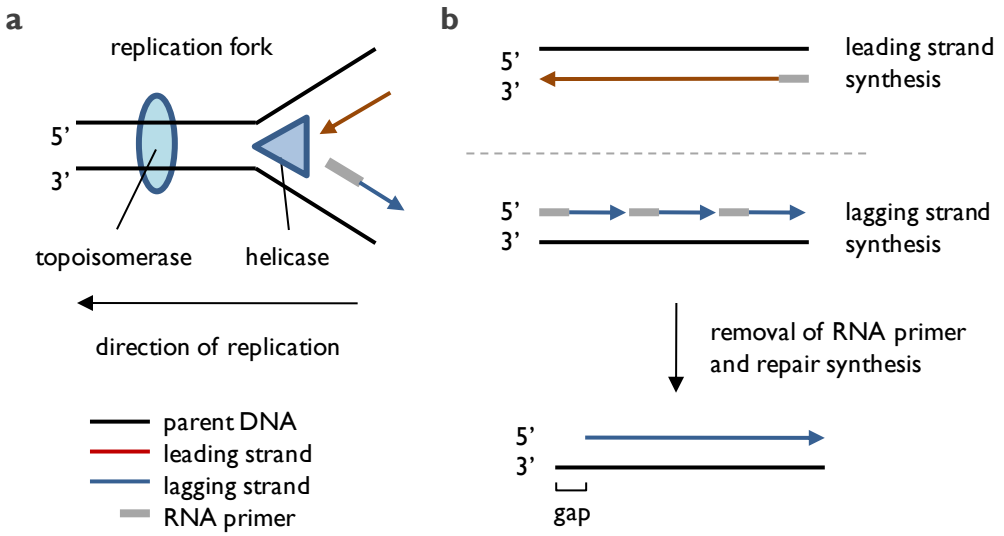

Figure 1.8 a, DNA replication fork. Topoisomerase and helicase unwind the DNA double helix and two new strands are synthesised. **b,** Synthesis of the leading strand and lagging strand. As synthesis occurs only in the 5' to 3' direction this leaves a single stranded overhang at the 3' end.

1.1.5 Telomeres

When a replication fork reaches the end of a linear chromosome there is no place to produce the RNA primer and so the DNA cannot be synthesised to the 3' end resulting in a gap.[4] For eukaryotic organisms that contain linear chromosomes (as opposed to the majority of prokaryotes, which possess circular chromosomes), this would result in the shortening of chromosomes and a loss in genetic information with each cell division. To overcome this "end replication problem", eukaryotes contain repetitive non-coding DNA sequences located at the end the end of their chromosomes called telomeres (Figure 1.9). The repeat sequence and length varies depending on the organism, although telomeric DNA that is rich in guanine is a common property.[7] The telomeric DNA overhang of cells is reduced each time the cell divides and it is thought this shortening serves as a control for the life cycle

of cells by placing a limit upon the number of divisions each cell is able to undergo.[8, 9]

Figure 1.9 a, Chromosome schematic showing telomeres. **b,** Fluorescence micrograph of HeLa metaphase chromosomes (red) showing labelled telomeres (green).[10]

1.1.6 Cancer

In the UK, one in three people will develop cancer during their lives[11] and cancer research represents one of the most active areas of modern science. So what defines and causes this disease? Cancer cells are cells that display uncontrolled growth along with the ability to invade neighbouring tissues. When this proliferation becomes uncontrollable, the cancer cells cluster together in a tumour, which can then spread to multiple areas of the body if not removed (metastases). Cancer is a result of multiple genetic changes which, in the majority of cases, has originated from DNA mutations within a single abnormal cell.[4] The targeting of these mutations for potential drug development is a common theme in anti-cancer research. For example, in half of all cancers the tumour suppressor p53 gene, which normally regulates the cell cycle once DNA damage or mutation has been detected, is either absent or damaged.[12] Attempts to restore the function of this gene to induce cell cycle arrest or apoptosis specifically in cancer cells (commonly at the G_1/S boundary) is a current anti-cancer therapeutic goal.[13] Another property of the majority of cancers is they possess short telomeres but the enzyme that controls the synthesis of telomeric DNA, telomerase, is very active.[14] This enables the cancer cells to escape telomere-dependent

mechanisms of cell death and proliferate, making the maintenance of telomeres crucial to the growth of cancers. For this reason, the inhibition of telomerase is viewed as an attractive target for cancer therapeutics.[15]

1.1.7 Quadruplex DNA

Quadruplex DNA is a non-duplex DNA structure and is formed from a unit of four guanine bases associated in a planar Hoogsteen base-pair arrangement called a G-tetrad. Quadruplexes comprise of stacked G-tetrads held together by π-π stacking interactions and are stabilised by monovalent cations such as Na^+ and K^+ (Figure 1.10a,b). Figure 1.10c,d shows the crystal structure of a four-stranded "propeller type" G3 quadruplex (G*n* = *n* tetrats) solved by Neidle and co-workers.[16] A wide variety of quadruplex topologies have been observed, with variation in strand direction, loop size and base sequence.[17] G-rich DNA sequences readily form quadruplexes in the presence of such ions *in vitro* but the existence and exact role of quadruplexes *in vivo* remains under debate.

1.1.7.1 Biological significance

As human telomeric DNA is composed of G-rich TTAGGG repeats (telomere length ~2 x 10^3 and a single stranded 3' overhang of ~200 bases),[18] these regions are therefore prime candidates for the formation of quadruplexes *in vivo*. As telomerase is a reverse transcriptase that requires single stranded DNA as a template for the synthesis of new telomeric DNA, the formation of quadruplexes at the single stranded overhang of chromosomes would be predicted to interfere with telomere maintenance. Thus, targeting the telomerase/telomere relationship is a current anti-cancer strategy and, as part of this approach, it is thought that the induction/stabilisation of quadruplex DNA using small molecules may potentially halt tumour growth while displaying minimal cytotoxicity towards normal cells.[19, 20] G-rich sequences exist elsewhere in the genome and it has been proposed that

quadruplexes may be directly involved in such applications as gene regulation and transcription.[21]

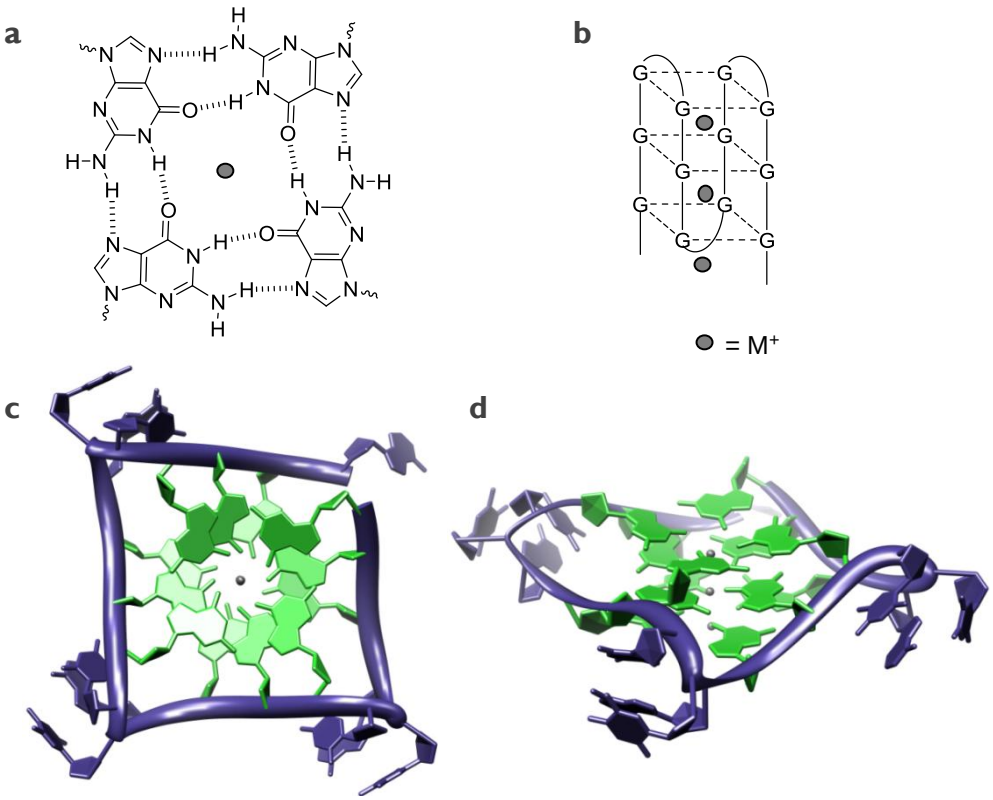

Figure 1.10 a, G-tetrad. **b,** Quadruplex formed by stacking of G-tetrads. M^+ = Na^+ or K^+. **c, d,** Crystal structure of quadruplex DNA (NDB ID: UD0017).

1.2 Small molecule binding to DNA

The processes described by the central dogma are initiated, regulated and terminated by molecules and/or proteins that bind to nucleic acids in site-specific ways. Consequently, synthetic molecules that are able to interact with nucleic acids are able to interfere with these steps (positively or negatively) and so find a variety of uses as biophysical and therapeutic agents. The structure of DNA allows several different mechanisms by which small molecules can bind to DNA, which will be described in this section.

1.2.1 Irreversible binding

Molecules can form covalent bonds to the phosphodiester backbone, sugar residues or bases of the DNA molecule. The induction of DNA damage by a drug molecule forms the basis of "classical chemotherapy", where, as a result of genetic instability, cancer cells are unable to affect the correct cell cycle checkpoint response to the induced damage and consequently undergo cell cycle arrest (typically at the G_1/S and G_2/M checkpoints), which ultimately leads to cell death. Rapidly dividing cells, such as cancer cells, are preferentially targeted by this approach.[22]

1.2.2 Reversible binding

As well as irreversibly forming covalent bonds, small molecules are also able to bind reversibly to DNA. This can occur by three main mechanisms: electrostatic interactions, groove binding and intercalation.

1.2.2.1 Electrostatic interactions

The negative charge of DNA means that cationic molecules are able to associate with the biopolymer. These can range from simple cations such as Na^+ and Mg^{2+} to cationic polyamines such as spermidine and spermine (Figure 1.11), which have been suggested to be able to modulate DNA-protein interactions *via* DNA binding and disrupt cellular function, particularly cell proliferation, as a result.[23]

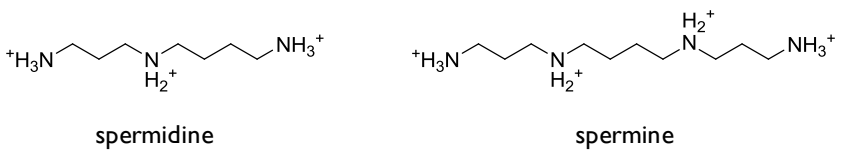

spermidine spermine

Figure 1.11 Cationic polyamines spermidine and spermine.

1.2.2.2 Groove binding

The major and minor groove in B-DNA provide suitable binding sites through reversible van der Waals, hydrophobic and hydrogen bonding interactions. An example of a minor-groove binding molecule is Hoechst 33258, which is a commonly used fluorescent DNA stain. Figure 1.12 shows the crystal structure of Hoechst 33258 located in the minor groove and the nuclear DNA of HeLa cervical cancer cells fluorescently labelled by the molecule.

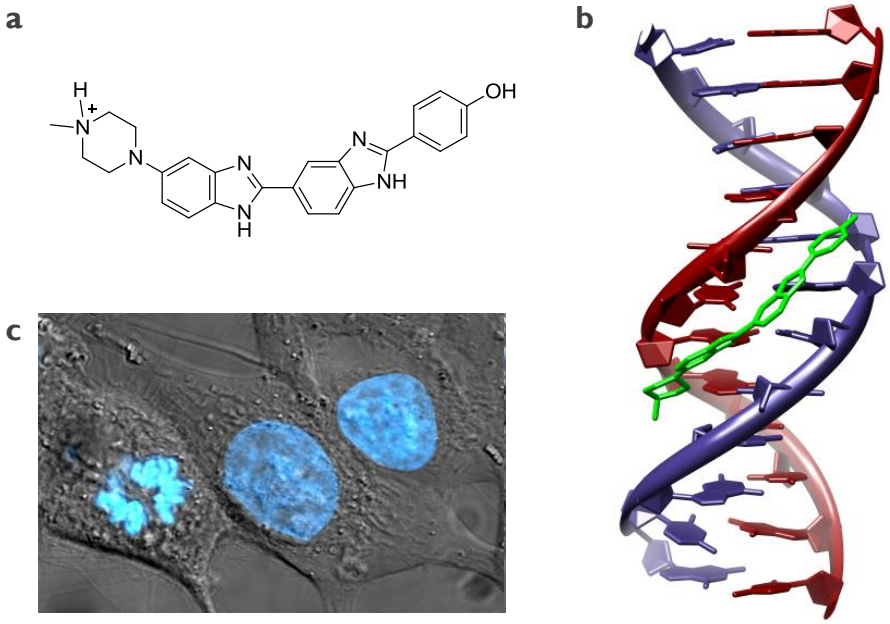

Figure 1.12 a, Chemical structure of the groove-binder Hoechst 33258. **b,** X-ray crystal structure of Hoechst 33258 located in the minor groove of B-DNA (NDB ID: GDL022). **c,** Fluorescence microscopy image showing the DNA of HeLa cells stained by Hoechst 33258.[24]

1.2.2.3 Intercalation

First described by Lerman in 1961,[25] this mode of reversible DNA-binding interaction involves planar aromatic compounds being inserted between adjacent base pairs in the DNA double helix. Intercalation involves significant π system overlap between DNA bases and the intercalated

molecule, as well as van der Waals and electrostatic interactions, which has the effect of unwinding and lengthening the DNA double helix.[26] An example of an intercalating molecule is ethidium bromide, which is used as a nucleic acid stain in applications such as gel electrophoresis as it shows an increase of fluorescence upon intercalation (Figure 1.13). Ethidium bromide displays a high affinity for DNA and is a potent mutagen and carcinogen as a result.[27]

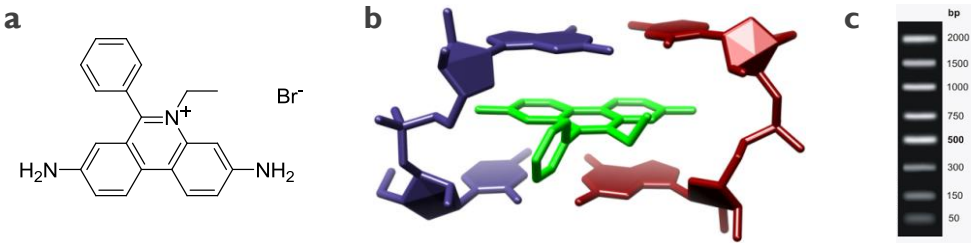

Figure 1.13 a, Chemical structure of the ethidium bromide. **b,** Crystal structure of ethidium bromide intercalating between DNA base pairs (NDB ID: DRB006). **c,** Ethidium bromide as a DNA stain in gel electrophoresis.[28]

1.2.3 Small molecule binding to quadruplex DNA

As well as irreversibly binding to quadruplex DNA, a molecule may reversibly bind with the loops, grooves, end-stack or intercalate between successive G-tetrads. There have been numerous compounds reported to stabilise quadruplex DNA and such complexes tend to have a large planar aromatic surface area with many possessing a positive charge. Examples of quadruplex-stabilising small molecules include the cationic porphyrin TMPyP4[29] and the trisubstituted acridine-based compound BRACO-19[30] (Figure 1.14), both of which are potent inhibitors of telomerase. Furthermore, BRACO-19 has been shown to inhibit tumour growth *in vivo*; consistent with the notion that quadruplex binding molecules may be effective therapeutics by interfering with mechanisms of telomere length maintenance.[30]

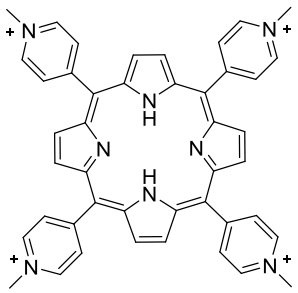

TMPyP4

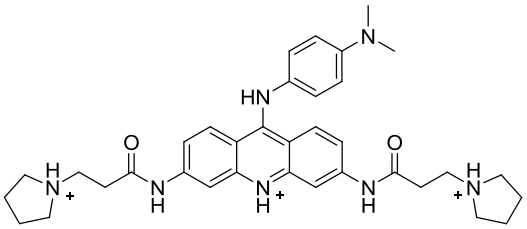

BRACO-19

Figure 1.14 Quadruplex DNA-stabilising molecules TMPyP4 and BRACO-19.

1.3 Cellular uptake of small molecules

To interact with DNA in living cells, molecules must be able to enter the interior of cells. Eukaryotic cells are surrounded by a cell membrane composed of a phospholipid bilayer. This bilayer contains phospholipids, composed of a hydrophilic head group attached to hydrophobic hydrocarbon chains, and a variety of proteins and lipids to regulate the cellular uptake of extracellular particles. The hydrophobic interior of the bilayer means that membrane diffusion is determined by the polarity and size of the molecule; the more polar or larger the molecule, the more difficult it is to permeate the membrane. Generally if a molecule is more polar than water or larger than 500 Da it will require a transport mechanism to facilitate cellular uptake.[4]

1.3.1 Passive and active transport

Vital molecules such as amino acids, sugars and ions pass across the cell membrane through the action of membrane pumps, channels or carrier proteins. This may be energy-independent (passive transport), driven by an electrochemical gradient, or energy-dependent (active transport), usually driven by the conversion of ATP to ADP (Figure 1.15). These mechanisms

are highly selective and rely upon protein-specific binding to a target molecule or ion.[4]

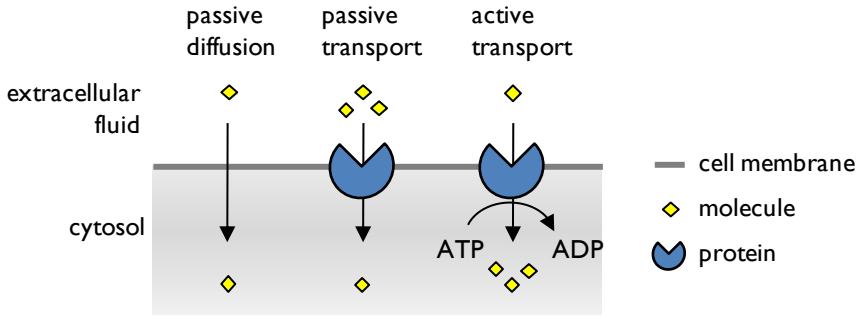

Figure 1.15 Passive and active transport across the cell membrane.

1.3.2 Endocytosis

Typically used to internalise large, polar molecules, endocytosis involves the invagination and pinching off of the cell membrane to form endocytic vesicles which carry their contents to the target organelle within the cell. This is frequently triggered by a specific protein-binding event at the cell surface to a receptor. Endocytic pathways usually involve the delivery of internalised molecules to early endosomes for sorting. The contents can then be released, delivered to a target organelle, processed in late endosomes, digested in lysosomes or released into the extracellular fluid *via* exocytosis, as required, with the exact fate depending upon the uptake pathway. All endocytic pathways are energy-dependent and are divided into phagocytosis (uptake of solids) and pinocytosis (uptake of liquids).[31]

1.3.2.1 Mechanisms of endocytosis

Phagocytosis is the cellular engulfing of large molecular aggregates, solid particles, such as cell debris and bacteria, and is distinct from the processes required to internalised liquids. Macropinocytosis involves cell surface ruffling and the formation of macropinosomes (diameter >1 μm). The ruffling is controlled by the cell and can vary with cell type and external

signalling. This process provides an efficient route for non-selective endocytosis of soluble macromolecules.[32] Clathrin-mediated endocytosis is the main route of endocytosis used by most cells and involves the molecule binding to specific receptors on the surface of the cell membrane and the formation of clathrin-coated pits (diameter 100-150 nm), which are then internalised to generate clathrin-coated vesicles. Clathrin then disassociates and the uncoated vesicles fuse together, forming early endosomes. The progressive acidification of early endosomes promotes the dissociation of internalised molecules from their receptors which are subsequently recycled to the membrane surface.[33] Other mechanisms of internalisation include the formation of caveolae, small pits in the cell membrane (diameter 50-100 nm), which provide a non-acidic mechanism of internalisation and are used to transport molecules such as cholesterol. In addition to this, numerous clathrin- and caveolae-independent endocytosis mechanisms have also been described.[34] The different mechanisms of endocytosis are shown in Figure 1.16.

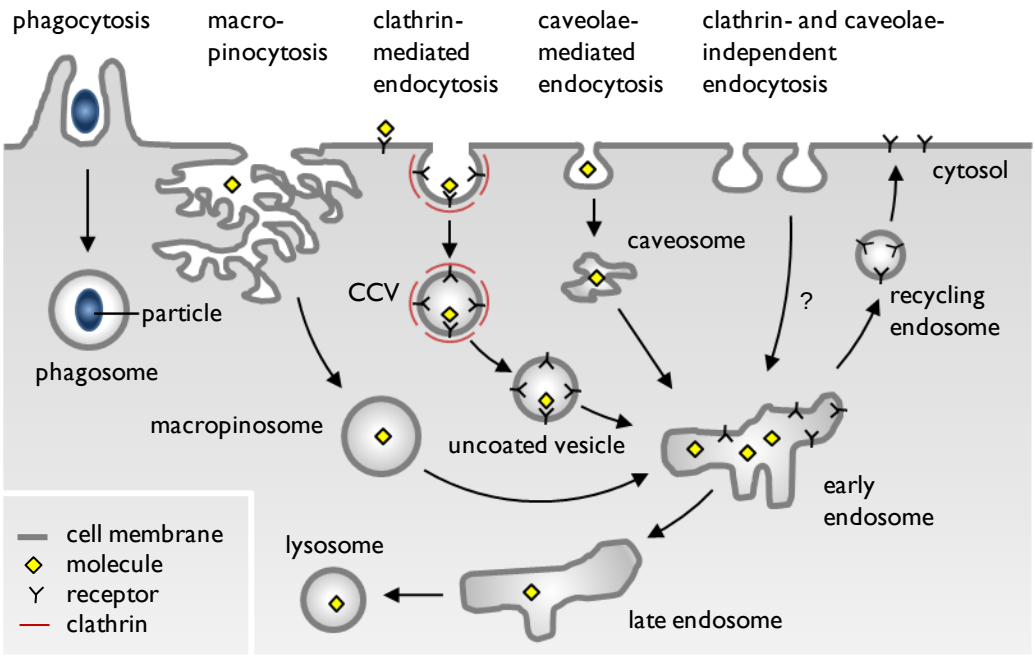

Figure 1.16 Mechanisms of endocytosis.

1.4 Binding of metal complexes to DNA

Metal complexes, because of their cationic nature, three-dimensional structures and chemical activity, possess a natural ability to bind to DNA. This can occur either by irreversible binding or reversible-binding *via* the mechanisms described in Section 1.2. Coordination complexes are ideal for designing DNA-interactive molecules due to attributes such as: available coordination sites for DNA binding, the ability to perform redox reactions with DNA or generate reactive oxygen containing species (an attribute particularly relevant to photodynamic therapy (PDT)). The specific ability to bind to and then cleave DNA means that there is the potential to develop these systems as therapeutics *via* interfering wizth the essential cellular processes of transcription and translation. The photophysical properties of numerous complexes also mean that metal complexes are being examined as diagnostic probes of DNA.

1.4.1 Irreversible binding

Irreversible binding of metal complexes to DNA occurs by the formation of coordination bonds from the Lewis acid metal centre of the complex to the lone pairs of nitrogen or oxygen atoms of the DNA molecule, which function as the Lewis base.

1.4.1.1 Platinum-based anti-cancer drugs

One of the most famous examples of a metal complex that binds to DNA irreversibly is the chemotherapy agent cisplatin (*cis*-diaminedichloroplatinum(II)) – Figure 1.17a. Originally developed by Rosenberg and co-workers,[35] cisplatin and its derivatives are still some of the most widely used anti-cancer drugs.[36] The proposed mechanism of cytotoxicity is derived from the displacement of the labile Cl- ligands

followed by the formation of covalent bonds between the Pt(II) centre and available nitrogen atoms on the nucleotide bases of DNA, commonly N7 atoms on the two purine bases (Figure 1.17b). The generation of a covalent intrastrand cross-link *in vitro* has the effect of kinking the structure of the DNA molecule, as demonstrated by crystal structure[37] and NMR solution structure[38] (Figure 1.17c). This has been suggested to inhibit DNA replication and transcription *in vivo*, ultimately leading to apoptosis (programmed cell death) or cell cycle arrest.[39]

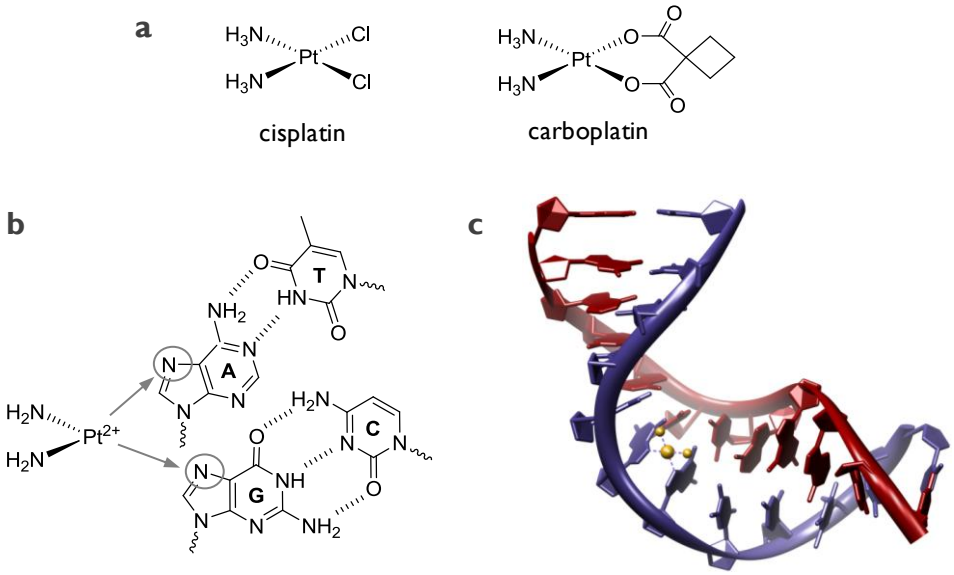

Figure 1.17 a, Platinum anti-cancer drugs cisplatin and carboplatin. **b,** Irreversible binding of cisplatin derivatives to DNA. **c,** NMR solution structure of cisplatin bound to B-DNA (NDB ID: 1A84).

The high toxicity of cisplatin and severe side-effects led researchers to develop cisplatin derivatives such as carboplatin, which has a bidentate dicarboxylate leaving group instead two Cl^- ligands (Figure 1.17a). The presence of a more stable leaving group was designed to lower toxicity without affecting the antitumour efficiency and, as a result, carboplatin exhibits slower DNA binding kinetics but also displays reduced side-effects.[36]

A major limitation of cisplatin-based chemotherapy arises from drug resistance, which may occur by: a reduction in cisplatin uptake, an increase in platinum-DNA adduct repair and/or increased drug inactivation.[40] To combat the issue of acquired cisplatin-resistance in tumours, recent years have seen the development of new platinum-based agents, such as satraplatin and picoplatin, which exhibit a broader spectrum of antitumour activity.[36]

1.4.1.2 Non-platinum-based anti-cancer drugs

Due to the limitations of cisplatin and derivatives, metallo-pharmaceuticals based on non-platinum metal centres have been explored in the ongoing search for new therapeutics. Advantages over platinum-based drugs are: additional coordination sites, aptitude for redox activation, lower toxicity and reduced side effects.[41] Specifically in this area, ruthenium (Ru(II) and Ru(III)) complexes have shown promise and a number of organometallic and coordination systems containing labile leaving groups have been investigated for anti-cancer activity.[42-44] This "targeted chemotherapy" approach has seen drugs such as NAMI-A (Figure 1.18a) enter clinical trials.

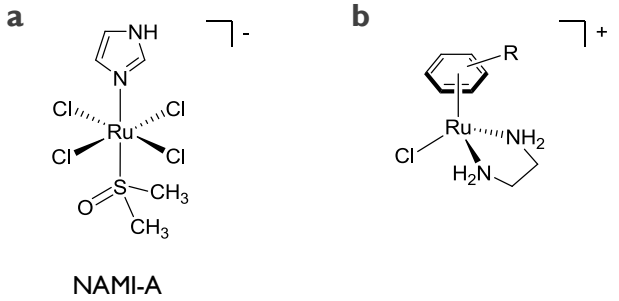

Figure 1.18 Ruthenium anti-cancer drugs. **a,** Ru(III) complex NAMI-A. **b,** Ru(II) arene complexes $[Ru(\eta^6\text{-arene})(en)Cl]^+$ (en = ethylenediamine, R = arene).

Although less toxic than cisplatin, NAMI-A has the advantage that it can be orally administered, is active against a range of tumours and exhibits antimetastatic activity.[45] In other work, the Sadler group have developed Ru(II) arene complexes as potential anti-cancer agents (Figure 1.18b). Displaying a similar toxicity to cisplatin, these complexes specifically target guanine bases in DNA where they form strong monofunctional adducts.[46, 47] It is thought they display a different mechanism of toxicity than Pt(II)- or Ru(III)-based anti-cancer drugs and work is now moving towards clinical trials.[47]

1.4.2 Reversible binding

In addition to complexes able to form irreversible coordination (covalent) bonds with DNA, metal coordination complexes are of interest for their ability to reversibly bind to DNA. Such systems possess a metal centre coordinated to a rigid, three-dimensional arrangement of ligands. These ligands can be easily interchanged and modified to control the DNA-binding, DNA-recognition, hydrophobic, cellular uptake and photophysical properties of the molecule as a whole, something not offered by conventional organic molecular recognition agents. The specific selectivity in the DNA-binding of these molecules means that such complexes may find future potential applications as probes of DNA structure and function in roles ranging from molecular biology to medicine. This area of research has been dominated by octahedral d^6 metal polypyridine complexes (most commonly Ru(II), Rh(III) and Re(I) metal centres) due to their kinetic inertness, well-developed substitution chemistry and useful photophysical properties.

1.4.2.1 Early work

Early work on the reversible DNA binding of metal complexes focussed on octahedral Ru(II) tris(phenanthroline) complexes and derivatives. Ru(II)

complexes were chosen because of their chemical stability, high luminescence and intense metal-to-ligand charge-transfer (MLCT) band in the visible spectrum.[48] The polypyridine ligands initially used were the bidentate ligands 2,2'-bipyridine (bpy), 1,10-phenanthroline (phen) and 4,7-diphenyl-1,10-phenanthroline (DIP) (Figure 1.19).[49] By examining the variation in photophysical properties in the presence of DNA it was shown that $[Ru(bpy)_3]^{2+}$ showed little or no binding, while results for $[Ru(phen)_3]^{2+}$ and $[Ru(DIP)_3]^{2+}$ suggested two binding modes to duplex DNA, comprising of an electrostatic and intercalative interaction. As the complexes are chiral, the syntheses produce a mixture of the Λ and Δ enantiomers. This chiral mixture was resolved and the DNA-binding of each enantiomer studied. Significant enantiomeric selectivity observed for the complex containing the most extended ligand, $[Ru(DIP)_3]^{2+}$, where the Δ isomer was able to intercalate while the Λ isomer could only bind electrostatically to DNA. The binding affinity of these complexes was low (equilibrium binding constant $K_b \sim 10^3\ M^{-1}$) and Barton and co-workers realised that to enhance the binding affinity for DNA a further increase in ligand surface area was required.

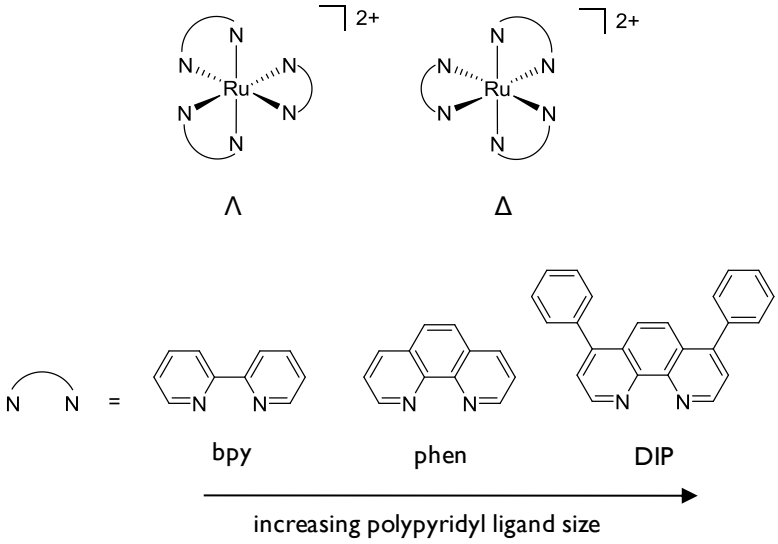

Figure 1.19 Octahedral Ru(II) tris(phenanthroline) complexes and derivatives.

1.4.2.2 The DNA light switch effect

Research then focussed on using the dipyrido[3,2-a:2',3'-c]phenazine (dppz) ligand, which possesses a large aromatic surface area for intercalation. The DNA binding studies on $[Ru(bpy)_2(dppz)]^{2+}$ and $[Ru(phen)_2(dppz)]^{2+}$ then resulted in breakthrough work in this field, with the Barton group reporting that the dppz-based complexes bind to DNA with a high affinity ($K_b \sim 10^6\ M^{-1}$) and, importantly, display intense MLCT luminescence on the addition of DNA as a direct result of intercalation whereas luminescence of the unbound complex is quenched (Figure 1.20).[50, 51] This was termed the DNA "light switch" effect and has been used extensively to study the interaction of a wide variety of metal complexes with DNA as the binding process can be measured using UV-visible and fluorescence spectroscopy.[52]

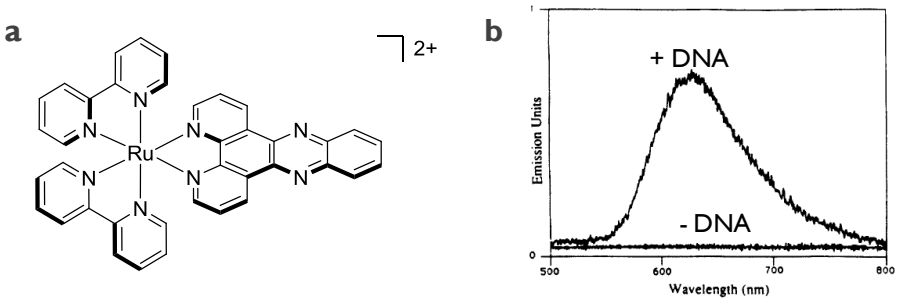

Figure 1.20 a, Metallo-intercalator $[Ru(bpy)_2(dppz)]^{2+}$. **b,** The light switch effect of $[Ru(bpy)_2(dppz)]^{2+}$ upon the addition of DNA.[50]

The MLCT luminescence was characterised by Sauvage *et al*. and they deduced that the light-induced charge transfer is directed from the Ruthenium atom to a π^* orbital primarily located on the dppz ligand.[53] This ^{1}MLCT excited state then decays rapidly *via* intersystem crossing to a ^{3}MLCT excited state primarily localised on the phenazine nitrogen atoms. In aqueous conditions water quenches this excited state by hydrogen bonding with the phenazine nitrogen atoms[54] but when the dppz is shielded from water (as during intercalation) the luminescence is activated and the complex effectively acts as though it is in organic solvent (Figure 1.21). As

the mechanism of the light switch effect specifically involves the dppz ligand, it follows that in many cases the ancillary ligands may be substituted and the light switch effect will still be preserved.[55]

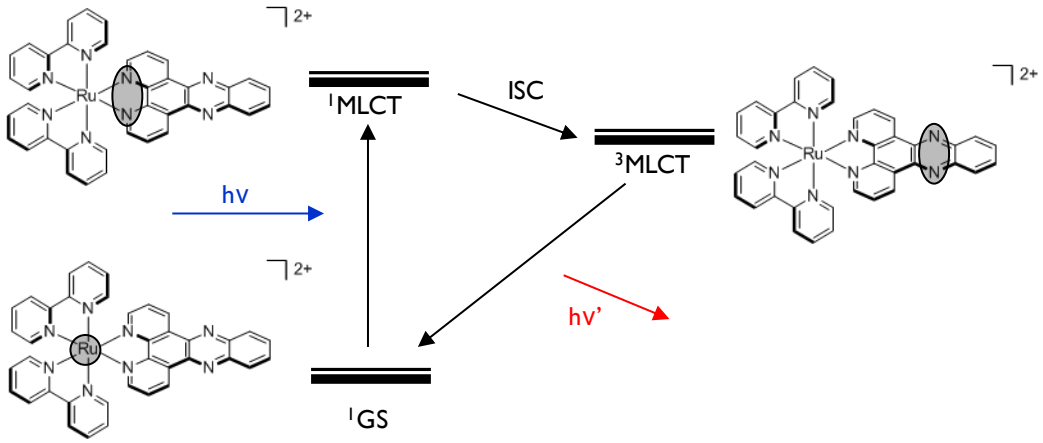

Figure 1.21 Jablonski diagram showing excited states involved in the DNA light switch effect and the primary location of the relative electron orbital. GS = ground state, MLCT = metal-to-ligand charge-transfer. ISC = intersystem crossing. hv = excitation energy, hv' = emission energy.

Norden and Lincoln examined the photophysical properties of the resolved Δ and Λ isomers of $[Ru(phen)_2(dppz)]^{2+}$.[56] They confirmed that intercalation is the binding mode for both Δ and Λ isomers and found that the relative quantum yield of the Δ isomer bound to DNA is 6-10 times higher than that of the Λ isomer, meaning the Δ isomer contributed 85% of the light switch emission observed for the racemic $[Ru(phen)_2(dppz)]^{2+}$. This work also confirmed the presence of two emitting species, one with a significantly longer lifetime than the other. Possible interpretations of such a finding include the existence of two different intercalative geometries, one of which sees the ligand buried more deeply within the double helix. Studies into the exact binding geometry of Δ-$[Ru(phen)_2(dppz)]^{2+}$ have been inconclusive in determining whether the complex binds *via* the minor or major groove,[57, 58] suggesting that this may be dependent upon the DNA sequence or an artefact of the techniques employed to measure the binding.

1.4.2.3 Site-specific recognition agents

As metallo-intercalators have a rigid three dimensional structure with well-defined symmetry and easily interchangeable ancillary ligands, this makes them candidates for the selective recognition of specific DNA sequences – a suggested part in the potential use of DNA-intercalators as antitumoral drugs.[59] Extensive research by the Barton group on a large number of metallo-intercalators, commonly using Ru(II), Re(I) and Rh(III) systems, has revealed that both stereochemistry and van der Waals interactions between ancillary ligands and bases are key factors in developing site-specific recognition agents for a variety of different DNA sequences.[60, 61] Figure 1.22 shows the crystal structure of the sequence-specific photo-oxidant $[Rh(Me_2Trien)(Phi)]^{3+}$ (Me_2Trien = 2,9-Diamino-4,7-diazadecane, Phi = 9,10-phenanthrenequinone diimine) intercalating system bound to its target sequence.[62] This complex is able to cause DNA strand cleavage and promote electron transfer through the double helix, which can damage DNA bases and may be able to influence cellular function.

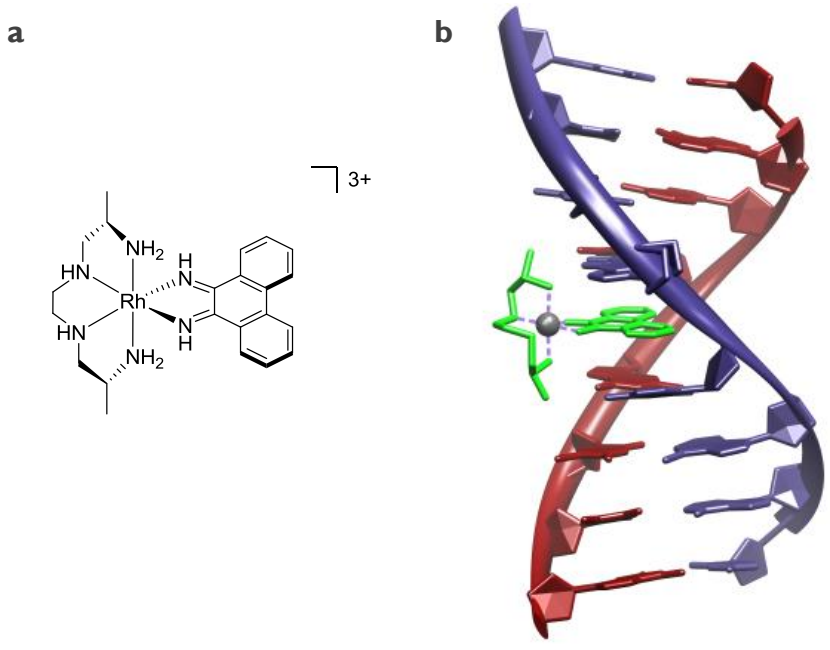

Figure 1.22 a, Site-specific $[Rh(Me_2Trien)(Phi)]^{3+}$ intercalating complex. **b,** Crystal structure of the Rh(III) complex bound to its target TGCA DNA sequence (NDB ID: UD0005).

Work in the Thomas group has seen the development of numerous d^6 transition metal complexes able to reversibly bind to DNA with sequence- and structure-specificity.[52] These include: achiral dppz intercalating systems that demonstrate sequence-specificity in their DNA binding[63, 64] and a Ru(II)-Re(I) hetero-bimetallic dppz metallo-intercalator that displays both DNA light switch and DNA-cleaving properties (Figure 1.23).[65]

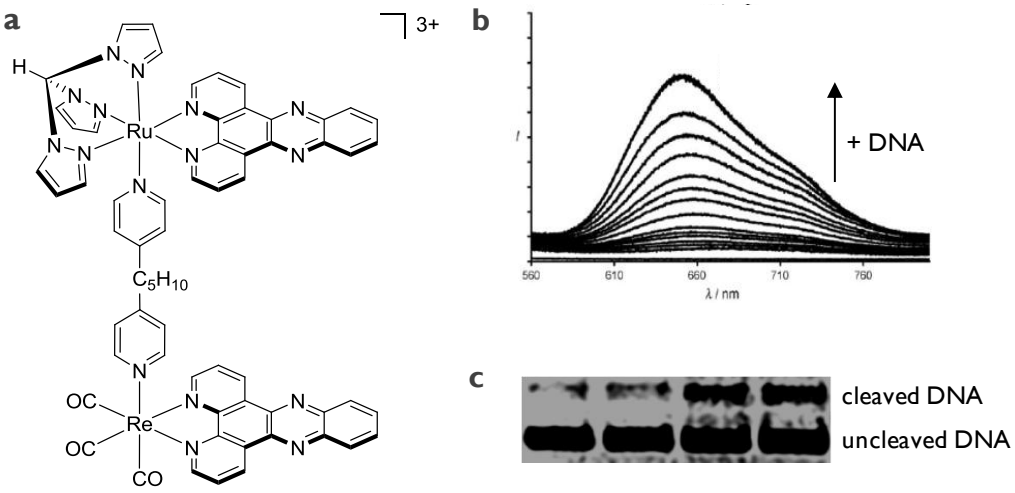

Figure 1.23 a, Hetero-bimetallic Ru(II)-Re(I) dppz metallo-intercalator. **b,** Luminescence increase upon the addition of DNA to the complex. **c,** Photocleavage of DNA by Ru(II)-Re(I) complex: Lane 1 is untreated plasmid, lanes 2 – 4 show increasing cleavage over time (30, 60, 90 mins). DNA stained with ethidium bromide.[65]

1.4.2.4 Mismatch recognition

Mismatched DNA can occur as a result of errors during DNA replication and, if left uncorrected, these mismatches can lead to potentially harmful genetic mutations, including the formation of cancerous tumours.[4] Work by the Barton group has included the development of several Ru(II) and Rh(III) imine complexes for high-affinity DNA base-pair mismatch recognition.[61, 66-68] The steric bulk of the intercalating imine ligand promotes localisation at CC (for the Ru(II) complexes) and CA or CT (for the Rh(III) complexes)

mismatch base-pairs, with the complexes then able to act as luminescent probes for the mismatch sites. The most notable of these complexes is $[Rh(bpy)_2(chrysi)]^{3+}$ (chrysi = chrysenequinone diimine) (Figure 1.24a), which selectively binds to CA base pair mismatch sites in the double helix and is also able to cleave the DNA backbone upon photoactivation.[66]

1.4.2.5 Metallo-insertion

Insertion refers to the circumstance wherein a planar aromatic ligand extends into the stack of base pairs in the DNA double helix upon binding, similar to an intercalator, but instead of unwinding the DNA, displaces and ejects a single base pair.[25] The planar aromatic ligand acts as a direct π stacking replacement for the ejected base pair. X-ray crystallographic structural studies into the mechanism of binding to duplex DNA of the mismatch-detecting complex $[Rh(bpy)_2(chrysi)]^{3+}$ revealed that this mismatch targeting occurs by insertion, rather than intercalation (Figure 1.24b).[69, 70] These results are the first time metallo-insertion as a mode of binding has been observed.

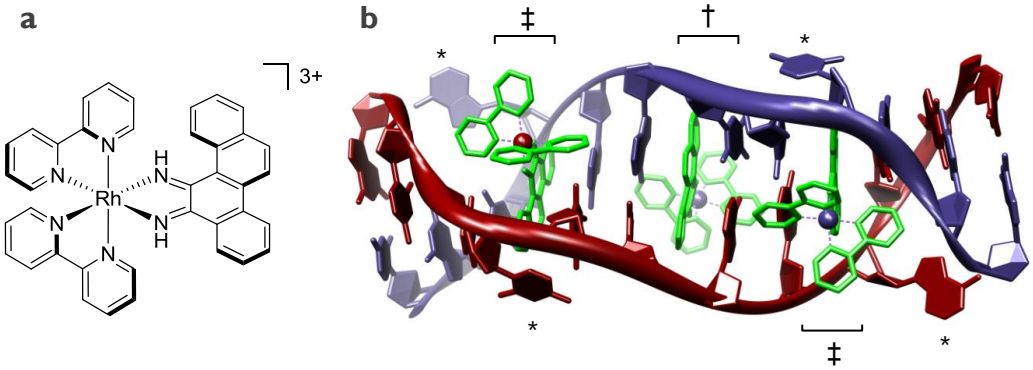

Figure 1.24 a, Mismatch recognition complex $[Rh(bpy)_2(chrsi)]^{3+}$. **b,** Crystal structure of $[Rh(bpy)_2(chrsi)]^{3+}$ bound to DNA (NDB ID: DD0088). The molecule displays two modes of binding: metallo-intercalation (†) and metallo-insertion (‡), * designates each ejected base.

1.4.3 Metal complexes and quadruplex DNA

Numerous groups have developed metal complexes as quadruplex DNA-binding agents. Metal complexes are ideal in such a role as they possess well defined (and modifiable) geometries, ligands containing delocalised π systems that can stack on the face of the quadruplex, a positively charged metal centre that can associate in the centre of the G-tetrad and also charged terminal groups that can bind favourably with the grooves and loops of the quadruplex.[71] Numerous such complexes have been developed and recent research in this area has included nickel and platinum complexes that selectively stabilise quadruplex structures over duplex DNA[72, 73] and work by the Thomas group has produced ruthenium complexes that are capable of spectroscopically differentiating between duplex and quadruplex structures[74, 75] (Figure 1.25).

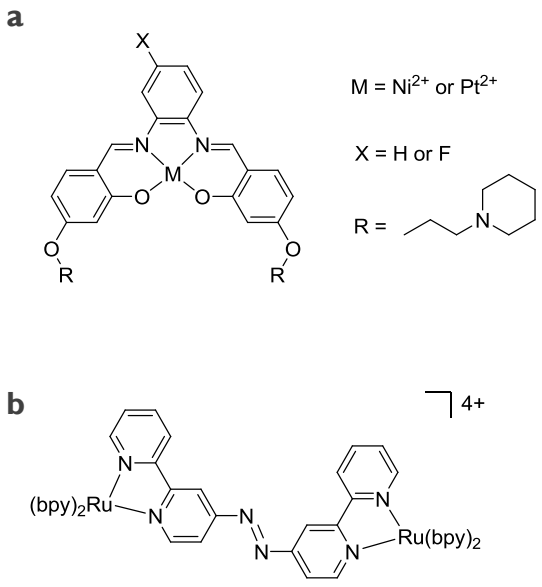

Figure 1.25 Quadruplex DNA-binding metal complexes. **a,** Metal salphen complex with cyclic amine side arms. **b,** Dimetallic $[\{Ru(bpy)_2\}_2(4\text{-azo})]^{4+}$ complex (4-azo = 4,4''-azobis(2,2'-bipyridine)).

1.5 Metal complexes in cellular imaging applications

As previously discussed, there has been a large amount of research into metal complexes that reversibly bind to DNA *in vitro* and attention to their application in biological systems is growing. DNA represents a particularly attractive target molecule due its biological significance and role in processes such as transcription and replication. In this context, the use of luminescent, kinetically inert metal complexes that possess spectroscopically active metal centres are attractive potential probes of DNA structure and function. Advantages of such systems are their high DNA binding affinities, sequence- and structure- specificity, interesting photophysical properties and flexible chemistry, which allows both ancillary and DNA-binding ligands to be interchanged or functionalised. Specifically for cellular imaging, metal complexes offer a very attractive set of optical imaging properties which include: photostability, low MLCT excitation energies in the visible region of the spectrum and high Stokes shifts (the difference between excitation and emission energies), which helps eliminate the problem of autofluorescence due to endogenous (organic) fluorophores.

With this in mind, the study of the cellular uptake properties and *in cellulo* DNA binding of metal complexes is of key importance in their development towards biological applications. Specifically, the ability of many complexes to act as luminescent light switches when bound to DNA presents a method by which to assess cellular uptake and DNA binding using fluorescence-based techniques such as confocal laser scanning microscopy (CLSM) and flow cytometry. There has been much research into the mechanism of uptake of anticancer drugs such as cisplatin, as internalisation routes can affect uptake kinetics and intracellular location, thereby determining the fate, and resultant biological activity, of the molecule. Consequently there have been numerous recent studies into the cellular internalisation of this class of metal complexes and the progress in this area will now be reviewed.

1.5.1 MLCT light switch complexes

In one of the earliest reported studies, the intercalator $[Ru(bpy)_2(taptp)]^{2+}$ (taptp = 4,5,9,18-tetraazaphenanthreno[9,10-b] triphenylene) was observed to act as an indicator of cell viability for both flow cytometry and confocal microscopy.[76] This non-membrane-permeable complex was found to exclusively stain the nuclei of dead cells in a manner analogous to the dead cell stain propidium iodide (PI). A key early study in this area was conducted by Norden, Lincoln *et al.* where the potential of the liposome-permeable, high DNA-affinity bisintercalating complex Δ-Δ $[\mu$-C4(cpdppz)$_2$-(phen)$_4$Ru$_2]^{4+}$ (K_b ~10^8 M^{-1}) (cpdppz = 12-cyano-12,13-dihydro-11H-cyclopenta[b]dipyrido[3,2-a:2',3'-c]phenazine-12-carbonyl)[77] to interfere with DNA metabolism was investigated by examining the uptake in V79 Chinese hamster cells.[78] The potential use of the complex as a nuclear DNA stain was clearly illustrated by the complex staining the chromosomes in fixed cells and using electroporation to facilitate membrane-diffusion in live cells (Figure 1.26). A low cytotoxicity over a 24 hour incubation time was observed, although at a higher concentration (100 μM) cell viability dropped to 55%. They suggested that a pinocytic mechanism of uptake was occurring due to small areas of low emission in the cytoplasm.

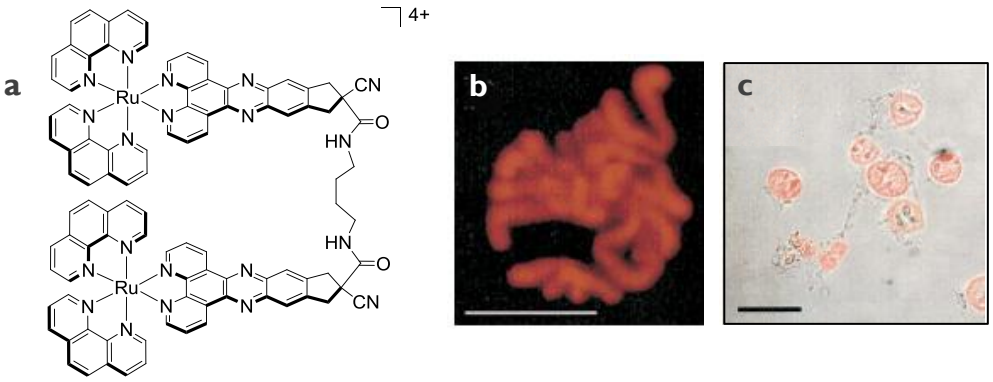

Figure 1.26 a, Norden and Lincoln's Ru(II) dimer. **b,** Image of chromosomes in fixed V79 Chinese hamster cell. Scale bar = 10 μm. **c,** Nuclear DNA stained in electroporated V79 cells. Scale bar = 20 μm.[78]

Having pioneered research into reversibly-binding metal polypyridine complexes, the Barton group turned their attention towards examining the cellular uptake properties of their well-characterised dppz DNA-binding systems using the MLCT light switch emission of the complexes to assess cellular uptake and localisation.[79] Using flow cytometry and confocal microscopy, a series of Ru(II)dppz complexes were found to be internalised by the HeLa human cervical cancer cell line. They found that uptake efficiency was dependent on the nature of the ancillary ligands, with more hydrophobic ancillary ligands such as DIP (Figure 1.27a) promoting increased cellular uptake, consistent with a mechanism of passive diffusion into the cytosol (Figure 1.27b,c).[80] A surprising result of this work was the absence of MLCT emission from the nuclei of cells (Figure 1.27d). A later study showed a fluorescein-tagged related complex to be "redirected" to the nucleus in comparison to the untagged complex. The fluorescein emission clearly demonstrated nuclear localisation of the complex but again no nuclear MLCT luminescence was observed.[81]

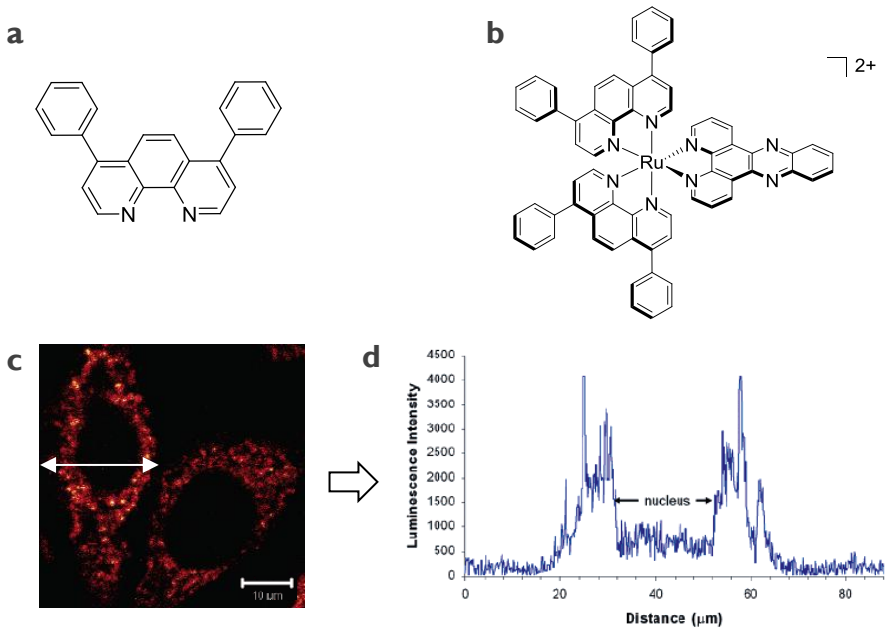

Figure 1.27 a, Hydrophobic DIP ligand. **b,** $[Ru(DIP)_2(dppz)]^{2+}$. **c,** CLSM image showing cellular uptake of $[Ru(DIP)_2(dppz)]^{2+}$ in HeLa cells and emission intensity profile (**d**).[79]

These results illustrated the main factor inhibiting the use of these complexes *in cellulo*; that of limited membrane-permeability. This is not surprising when we consider that such molecules are usually large, positively charged, hydrophilic and polar. In the attempt to produce membrane-permeable DNA-binding metal systems, research has seen the employment of hydrophobic ancillary ligands such as DIP, conjugation to biological molecules such as peptides or steroids, or a combination of both approaches. For example, Amoroso *et al.* used a rhenium *fac*-tricarbonyl bisimine system specifically designed for high hydrophobicity and their preliminary studies revealed high cytotoxicity but some *in cellulo* non-specific MLCT fluorescence.[82] Their subsequent work then showed a monocationic, small Re(I) *fac*-tricarbonyl bipyridine complex with a long luminescence lifetime and large Stokes shift to accumulate in mitochondria of MCF-7 cells, as demonstrated by colocalisation studies. The specific localisation within mitochondria upon internalisation was achieved using the addition of a chloromethyl group for thiol-reactivity (Figure 1.28).[83] This illustrates how metal coordination complexes may be designed for specific intracellular targeting *via* ligand reactivity.

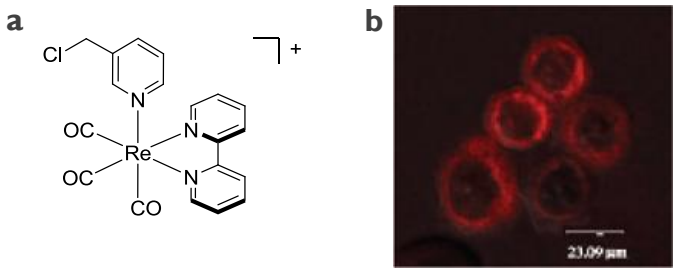

Figure 1.28 a, Re(I) fac-tricarbonyl bipyridine complex functionalised with chloromethane group. **b,** Mitochondrial staining observable by CLSM and MLCT luminescence.[83]

The Barton group used a cell-penetrating peptide to facilitate diffusion and nuclear uptake of a mismatch-specific rhodium intercalator although the

specificity of the DNA binding was lost upon conjugation to the peptide.[84] K. Lo *et al.* have designed luminescent probes based on polypyridine ruthenium complexes chemically attached to estradiol units, with the aim of functioning as biological probes for estrogen-receptors. The DIP ligand was employed in an ancillary role to increase hydrophobicity of the molecule and facilitate passive diffusion, with the results showing drug accumulation in the cytoplasm of HeLa cells as imaged by MLCT-luminescence (Figure 1.29).[85] Neugebauer *et al.* presented two polyarganine labelled ruthenium polypyridine complexes which display long lived, intense and oxygen-sensitive luminescence, finding one of these complexes to be transported across the cell membrane by passive diffusion.[86]

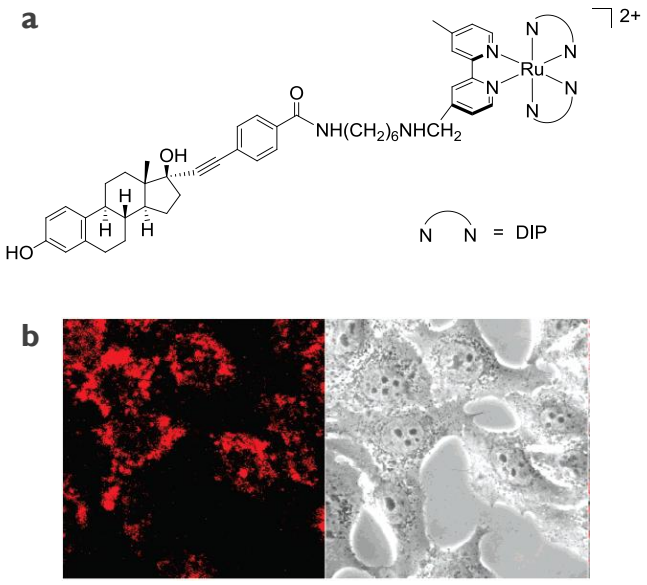

Figure 1.29 a, Steroid-conjugated Ru(II) complex. **b,** Uptake of steroid-conjugated complex shows non-nuclear localisation.[85]

In other work, Yu *et al.* showed two Ir(III) organometallic complexes to be phosphorescent dyes for live cell imaging. These two membrane-permeable molecules were internalised by cells rapidly (20 μM, 10 mins) where they located in the cytoplasm (Figure 1.30).[87] Advantages of these systems are their large emission lifetimes and reduced photobleaching. Both complexes

display a large Stokes shift, with the complex containing the extended polypyridyl ligand (Figure 1.30c) possessing the greater Stokes shift (> 200 nm); an example of how the emission properties can be tuned by subtle ligand modification.

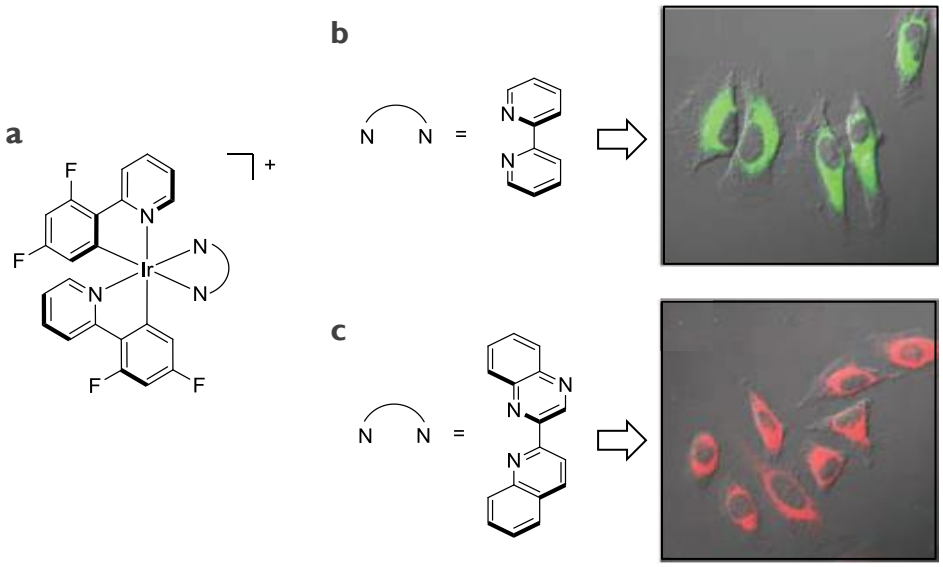

Figure 1.30 a, General structure of phosphorescent Ir(III) complexes. **b, c,** CLSM images of HeLa cells incubated with each Ir(III) complex.[87]

1.5.2 Non-MLCT luminescent metal complexes

Musatkina *et al.* presented a membrane-permeable Ru(II) complex (Figure 1.31a) that acts as an effective DNA dye for living cells, with the complex remaining inside the cell for multiple days.[88]

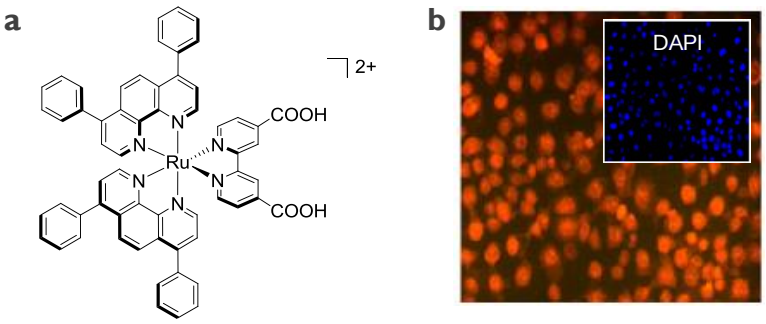

Figure 1.31 a, Dicarboxylic polypyridyl Ru(II) complex. **b,** Cellular DNA staining by the complex (outset) as confirmed by DAPI co-staining (inset).[88]

Using the DIP ligand to achieve cellular uptake, the mode of binding of the complex to DNA is electrostatic and *via* π–π stacking, with the carboxylated pyridine involved in the binding site. In this study, the monomers tested were not light switch complexes (i.e. they are luminescent before going into cells) so the signal to background noise ratio was inadequate for good contrast, but co-staining experiments using the commonly used DNA dye DAPI (4',6-diamidino-2-phenylindole) did prove the nucleus was being targeted (Figure 1.31b). The molecule has the advantage of low cytotoxicity, excitation in the visible area (λ_{ex} = 450 - 490 nm) of the spectrum and a Stokes shift of 170 nm.

Pascu *et al.* investigated the potential of Zn(II) and Cu(II) bis(thiosemicarbazonato) complexes as *in cellulo* probes (Figure 1.32).[89] They found that the intrinsically fluorescent Zn(II) complex is soluble in biocompatible media and is taken up by HeLa cells, where it is then observable throughout the cell by epifluorescence microscopy (λ_{ex} = 330-380 nm, λ_{em} = 523-643 nm) and CLSM (λ_{ex} = 488 nm, λ_{em} >515 nm). A later study showed such complexes demonstrate a toxicity of the same magnitude as cisplatin, apparently *via* mitochondria disruption.[90]

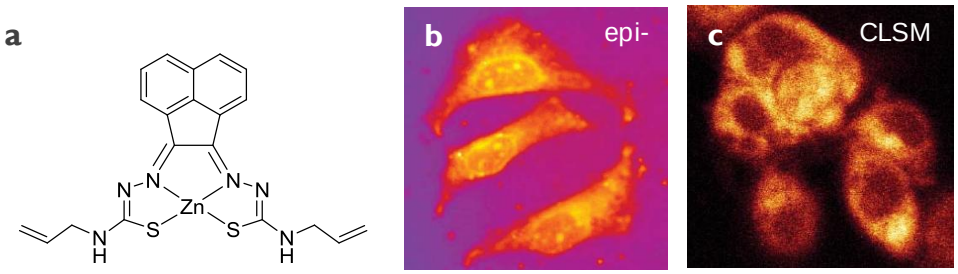

Figure 1.32 a, Zn(II) bis(thiosemicarbazonato) complex. **b, c,** Epi- and CLSM fluorescence microscopy images of Zn(II) complex in HeLa (**b**) and MCF-7 human breast cancer cells (**c**).[89]

Williams and co-workers have successfully developed charge-neutral platinum(II) complexes of the general formula [PtLCl] (where HL = 1,3-di(2-pyridyl)benzene and derivatives) that display low cytotoxicity, microsecond lifetimes and high emission quantum yields, which have been examined for their cellular imaging potential.[91, 92] They showed that [PtL^{R}Cl] (R = H, Figure 1.33a) is rapidly accumulated by a range of live cell types and preferentially localises in intracellular nucleic acid structures, in particular nucleoli (Figure 1.33b,c). The long lifetime of these platinum complexes makes them candidates for use in time-resolved emission imaging microscopy, a technique designed to eliminate the short emission lifetime autofluorescence.

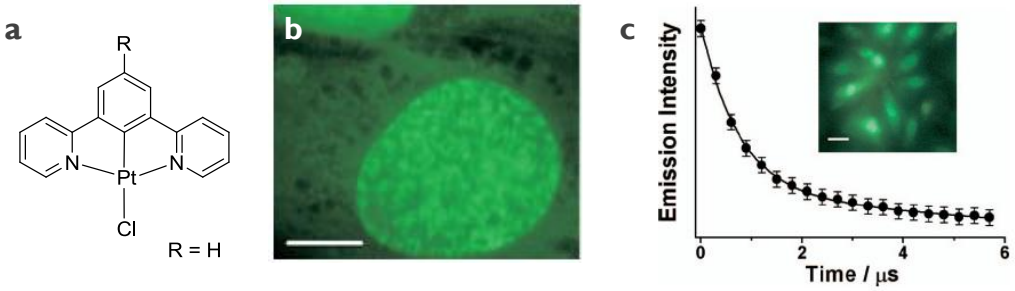

Figure 1.33 a, Pt(II) based imaging agent that displays nuclear staining in CHO Chinese hamster cells (**b**) with a microsecond lifetime emission (**c**).[91]

1.5.3 Lanthanide complexes

Cellular imaging using metal complexes is not limited to transition metal chemistry and lanthanide complexes have also been proposed as potential cellular imaging and biomolecular probes. The Parker group has conducted extensive research into the development of numerous lanthanide complexes towards cellular imaging agents. Their work has included the incorporation of a lanthanide metal centre (typically Eu(III) or Tb(III)) into a seven- or nine-coordinate ligand which acts as the sensitising chromophore.[93-102] Fast energy transfer between the two then results in the luminescence emission

of the lanthanide.[94] They have used this methodology to develop a wide range of emissive complexes that localise within various intracellular regions, including mitochondria[99, 100] and nucleoli (Figure 1.34a-c).[95-97] Specifically for DNA-targeting, they showed that complexes containing 2-tetraazatriphenylene, a ligand structurally similar to dppz, are taken up by N1H 3T3 cells and tend to localise inside the cell nucleus when a sufficient external concentration gradient is present (Figure 1.34d,e).[93] For these cationic lanthanide systems, a common result was cellular uptake takes place *via* macropinocytosis[101] although certain complexes were shown to be membrane-permeable.[95]

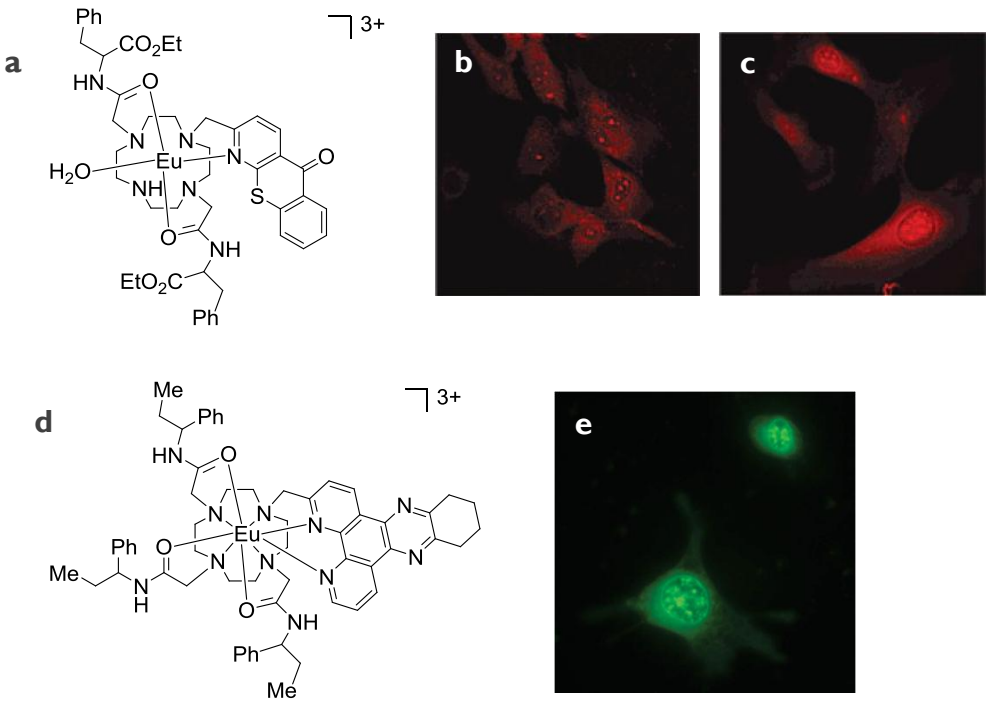

Figure 1.34 a, Eu(III) complex that displays nucleolar luminescence in live (**b**) and fixed (**c**) N1H 3T3 cells.[95] **d,** Eu(III) complex that stains the DNA of NIH 3T3 cells (**e**).[93]

In other work on lanthanide-based systems, the Bunzli group have been developing highly luminescent lanthanide bimetallic helicates that consist of

the three ligand strands self-assembled around two metallic centres as potential cellular imaging probes.[103-106] These systems offer tunable chemical and photophysical properties, intense luminescence and low cytotoxicity. The helicates are stable chemical species which remain intact within the cell medium and cytosolic uptake and staining is observed. Using co-staining experiments, they suggested that the helicates enter the cells by endocytosis and are then are transported to the endoplasmic reticulum *via* lysosomes.[106]

1.6 Summary

Due to the biological significance of DNA, small molecules that bind to DNA find a variety of applications ranging from biomolecular imaging agents to anti-cancer therapeutics. Metal complexes, particularly d^6 octahedral polypyridyl complexes that reversibly bind to DNA, offer an attractive scaffold for the design of specific probes of DNA structure and function. Their high binding affinities, structure- and sequence- specificities along with distinctive photophysical properties - such as acting as luminescent light switches for DNA - make such complexes ideal candidates for the development of highly sensitive and structure-specific DNA probes. As a result, there is now growing attention being drawn to their biological function(s), in particular developing these complexes as biomolecular probes for cellular applications. The luminescent properties of the complexes means that their cellular internalisation and *in cellulo* DNA binding can be directly measured using techniques such as confocal laser scanning microscopy and flow cytometry.

1.7 Aim of studies

The aim of this thesis was to investigate the cellular internalisation and DNA targeting of luminescent Ru(II) systems developed by the Thomas group that bind reversibly to DNA *in vitro*. The ability of such complexes to act as molecular light switches for DNA means that *in cellulo* DNA binding and cellular uptake may be examined in high resolution by confocal laser scanning microscopy. The luminescent properties of these complexes mean that there exists the potential they may be used DNA imaging agents in cells and so the application of such complexes in cellular imaging for both live and fixed cell microscopy was explored. As such complexes have been designed to bind to DNA with a high affinity, they have potential to interfere with cellular process such as DNA replication and transcription, and so the cytotoxicity towards selected cancer cell lines was assessed.

1.8 References

1. F. H. C. Crick, Central Dogma of Molecular Biology, *Nature*, 1970, **227**, 561-563.
2. J. D. Watson and F. H. C. Crick, Molecular structure of nucleic acids; a structure for deoxyribose nucleic acid, *Nature*, 1953, **171**, 737-738.
3. S. Levy, et al., The Diploid Genome Sequence of an Individual Human, *PLoS Biol.*, 2007, **5**, e254.
4. B. Alberts, A. Johnson, J. Lewis, M. Raff, K. Roberts and P. Walter, *Molecular Biology of the Cell*, 5th edn., Garland Science, New York, 2007.
5. K. J. Polach and J. Widom, Mechanism of Protein Access to Specific DNA Sequences in Chromatin: A Dynamic Equilibrium Model for Gene Regulation, *J. Mol. Biol.*, 1995, **254**, 130-149.
6. T. Cremer and C. Cremer, Chromosome territories, nuclear architecture and gene regulation in mammalian cells, *Nat. Rev. Genet.*, 2001, **2**, 292-301.

7. E. H. Blackburn, Structure and function of telomeres, *Nature*, 1991, **350**, 569-573.
8. C. B. Harley, A. B. Futcher and C. W. Greider, Telomeres shorten during ageing of human fibroblasts, *Nature*, 1990, **345**, 458-460.
9. R. C. Allsopp, H. Vaziri, C. Patterson, S. Goldstein, E. V. Younglai, A. B. Futcher, C. W. Greider and C. B. Harley, Telomere length predicts replicative capacity of human fibroblasts, *Proc. Natl. Acad. Sci. U. S. A.*, 1992, **89**, 10114-10118.
10. C. M. Azzalin, P. Reichenbach, L. Khoriauli, E. Giulotto and J. Lingner, Telomeric Repeat Containing RNA and RNA Surveillance Factors at Mammalian Chromosome Ends, *Science*, 2007, **318**, 798-801.
11. www.statistics.gov.uk
12. M. Hollstein, D. Sidransky, B. Vogelstein and C. C. Harris, p53 mutations in human cancers, *Science*, 1991, **253**, 49-53.
13. A. Vazquez, E. E. Bond, A. J. Levine and G. L. Bond, The genetics of the p53 pathway, apoptosis and cancer therapy, *Nat. Rev. Drug Discovery*, 2008, **7**, 979-987.
14. C. B. Harley, Telomerase and cancer therapeutics, *Nat. Rev. Cancer*, 2008, **8**, 167-179.
15. S. Zimmermann and U. M. Martens, Telomeres and telomerase as targets for cancer therapy, *Cell. Mol. Life Sci.*, 2007, **64**, 906-921.
16. G. N. Parkinson, M. P. H. Lee and S. Neidle, Crystal structure of parallel quadruplexes from human telomeric DNA, *Nature*, 2002, **417**, 876-880.
17. S. Burge, G. N. Parkinson, P. Hazel, A. K. Todd and S. Neidle, Quadruplex DNA: sequence, topology and structure, *Nucl. Acids Res.*, 2006, **34**, 5402-5415.
18. W. E. Wright, V. M. Tesmer, K. E. Huffman, S. D. Levene and J. W. Shay, Normal human chromosomes have long G-rich telomeric overhangs at one end, *Genes Dev.*, 1997, **11**, 2801-2809.
19. H. Han and L. H. Hurley, G-quadruplex DNA: a potential target for anti-cancer drug design, *Trends in Pharmacological Sciences*, 2000, **21**, 136-142.
20. S. Neidle and G. N. Parkinson, Telomere maintenance as a target for anticancer drug discovery, *Nat. Rev. Drug Discovery*, 2002, **1**, 383-393.
21. J. L. Huppert and S. Balasubramanian, G-quadruplexes in promoters throughout the human genome, *Nucl. Acids Res.*, 2007, **35**, 406-413.
22. M. B. Kastan and J. Bartek, Cell-cycle checkpoints and cancer, *Nature*, 2004, **432**, 316-323.

23. T. Thomas and T. J. Thomas, Polyamines in cell growth and cell death: molecular mechanisms and therapeutic applications, *Cell. Mol. Life Sci.*, 2001, **58**, 244-258.
24. en.Wikipedia.org
25. L. S. Lerman, Structural considerations in the interaction of DNA and acridines, *J. Mol. Biol.*, 1961, **3**, 18-30.
26. E. C. Long and J. K. Barton, On demonstrating DNA intercalation, *Acc. Chem. Res.*, 1990, **23**, 271-273.
27. P. S. Pearlman and H. R. Mahler, Molecular Consequnces of Ethidium Bromide Mutagenesis, *Nat. New Biol.*, 1971, **231**, 12-16.
28. www.NorgenBiotek.com
29. R. T. Wheelhouse, D. Sun, H. Han, F. X. Han and L. H. Hurley, Cationic Porphyrins as Telomerase Inhibitors: the Interaction of Tetra-(N-methyl-4-pyridyl)porphine with Quadruplex DNA, *J. Am. Chem. Soc.*, 1998, **120**, 3261-3262.
30. A. M. Burger, F. Dai, C. M. Schultes, A. P. Reszka, M. J. Moore, J. A. Double and S. Neidle, The G-Quadruplex-Interactive Molecule BRACO-19 Inhibits Tumor Growth, Consistent with Telomere Targeting and Interference with Telomerase Function, *Cancer Res.*, 2005, **65**, 1489-1496.
31. G. J. Doherty and H. T. McMahon, Mechanisms of Endocytosis, *Annu. Rev. Biochem.*, 2009, **78**, 857-902.
32. J. A. Swanson and C. Watts, Macropinocytosis, *Trends in Cell Biology*, 1995, **5**, 424-428.
33. S. D. Conner and S. L. Schmid, Regulated portals of entry into the cell, *Nature*, 2003, **422**, 37-44.
34. S. Kumari, S. Mg and S. Mayor, Endocytosis unplugged: multiple ways to enter the cell, *Cell Res.*, 2010, **20**, 256-275.
35. V. H. Mansour, B. Rosenberg, L. Vancamp and J. E. Trosko, Platinum compounds: a new class of potent antitumor agents, *Nature*, 1969, **222**, 385-386.
36. L. R. Kelland, The resurgence of platinum-based cancer chemotherapy, *Nat. Rev. Cancer*, 2007, **7**, 573-584.
37. P. M. Takahara, A. C. Rosenzweig, C. A. Frederick and S. J. Lippard, Crystal structure of double-stranded DNA containing the major adduct of the anticancer drug cisplatin, *Nature*, 1995, **377**, 649-652.

38. A. Gelasco and S. J. Lippard, NMR Solution Structure of a DNA Dodecamer Duplex Containing a cis-Diammineplatinum(II) d(GpG) Intrastrand Cross-Link, the Major Adduct of the Anticancer Drug Cisplatin, *Biochemistry*, 1998, **37**, 9230-9239.

39. D. Wang and S. J. Lippard, Cellular processing of platinum anticancer drugs, *Nat. Rev. Drug Discovery*, 2005, **4**, 307-320.

40. Z. H. Siddik, Cisplatin: mode of cytotoxic action and molecular basis of resistance, *Oncogene*, 2003, **22**, 7265-7279.

41. M. J. Clarke, F. Zhu and D. R. Frasca, Non-Platinum Chemotherapeutic Metallopharmaceuticals, *Chem. Rev.*, 1999, **99**, 2511-2534.

42. M. J. Clarke, Ruthenium metallopharmaceuticals, *Coord. Chem. Rev.*, 2003, **236**, 209-233.

43. W. H. Ang and P. J. Dyson, Classical and Non-Classical Ruthenium-Based Anticancer Drugs: Towards Targeted Chemotherapy, *Eur. J. Inorg. Chem.*, 2006, 4003-4018.

44. P. C. A. Bruijnincx and P. J. Sadler, New trends for metal complexes with anticancer activity, *Curr. Opin. Chem. Biol.*, 2008, **12**, 197-206.

45. E. Alessio, G. Mestroni, A. Bergamo and G. Sava, Ruthenium Antimetastatic Agents, *Curr. Top. Med. Chem.*, 2004, **15**, 1525-1535.

46. R. E. Morris, et al., Inhibition of Cancer Cell Growth by Ruthenium(II) Arene Complexes, *J. Med. Chem.*, 2001, **44**, 3616-3621.

47. Y. K. Yan, M. Melchart, A. Habtemariam and P. J. Sadler, Organometallic Chemistry, Biology and Medicine: Ruthenium Arene Anticancer Complexes, *Chem. Commun.*, 2005, 4764-4776.

48. J. K. Barton, A. Danishefsky and J. Goldberg, Tris(phenanthroline)ruthenium(II): stereoselectivity in binding to DNA, *J. Am. Chem. Soc.*, 1984, **106**, 2172-2176.

49. C. V. Kumar, J. K. Barton and N. J. Turro, Photophysics of ruthenium complexes bound to double helical DNA, *J. Am. Chem. Soc.*, 1985, **107**, 5518-5523.

50. A. E. Friedman, J. C. Chambron, J. P. Sauvage, N. J. Turro and J. K. Barton, A molecular light switch for DNA: $Ru(bpy)_2(dppz)^{2+}$, *J. Am. Chem. Soc.*, 1990, **112**, 4960-4962.

51. R. M. Hartshorn and J. K. Barton, Novel dipyridophenazine complexes of ruthenium(II): exploring luminescent reporters of DNA, *J. Am. Chem. Soc.*, 1992, **114**, 5919-5925.

52. C. Metcalfe and J. A. Thomas, Kinetically inert transition metal complexes that reversibly bind to DNA, *Chem. Soc. Rev.*, 2003, **32**, 215-224.

53. E. Amouyal, A. Homsi, J. C. Chambron and J.-P. Sauvage, Synthesis and study of a mixed-ligand ruthenium(II) complex in its ground and excited states : bis(2,2'-bipyridine)(dipyrido[3,2-a :2',3'-c]phenazine-N4N5)ruthenium(II), *Dalton Trans.*, 1990, 1841-1845.

54. C. Turro, S. H. Bossmann, Y. Jenkins, J. K. Barton and N. J. Turro, Proton Transfer Quenching of the MLCT Excited State of $Ru(phen)_2dppz^{2+}$ in Homogeneous Solution and Bound to DNA, *J. Am. Chem. Soc.*, 1995, **117**, 9026-9032.

55. Y. Jenkins, A. E. Friedman, N. J. Turro and J. K. Barton, Characterization of dipyridophenazine complexes of ruthenium(II): The light switch effect as a function of nucleic acid sequence and conformation, *Biochemistry*, 1992, **31**, 10809-10816.

56. C. Hiort, P. Lincoln and B. Norden, DNA binding of Δ-and Λ-$[Ru(phen)_2dppz]^{2+}$, *J. Am. Chem. Soc.*, 1993, **115**, 3448-3454.

57. E. Tuite, P. Lincoln and B. Norden, Photophysical Evidence That Δ-and Λ-$[Ru(phen)_2(dppz)]^{2+}$ Intercalate DNA from the Minor Groove, *J. Am. Chem. Soc.*, 1997, **119**, 239-240.

58. R. E. Holmlin, E. D. A. Stemp and J. K. Barton, $Ru(phen)_2dppz^{2+}$ Luminescence: Dependence on DNA Sequences and Groove-Binding Agents, *Inorg. Chem.*, 1998, **37**, 29-34.

59. R. Martínez and L. Chacón-García, The Search of DNA-Intercalators as Antitumoral Drugs: What it Worked and What did not Work, *Curr. Med. Chem.*, 2005, **12**, 127-151.

60. K. E. Erkkila, D. T. Odom and J. K. Barton, Recognition and Reaction of Metallointercalators with DNA, *Chem. Rev.*, 1999, **99**, 2777-2796.

61. B. M. Zeglis, V. C. Pierre and J. K. Barton, Metallo-intercalators and metallo-insertors, *Chem. Commun.*, 2007, 4565-4579.

62. C. L. Kielkopf, K. E. Erkkila, B. P. Hudson, J. K. Barton and D. C. Rees, Structure of a photoactive rhodium intercalated into DNA, *Nat. Struct. Mol. Biol.*, 2000, **7**, 117-121.

63. C. Metcalfe, H. Adams, I. Haq and J. A. Thomas, A ruthenium dipyridophenazine complex that binds preferentially to GC sequences, *Chem. Commun.*, 2003, 1152-1153.

64. S. P. Foxon, C. Metcalfe, H. Adams, M. Webb and J. A. Thomas, Electrochemical and Photophysical Properties of DNA Metallo-intercalators Containing the Ruthenium(II) Tris(1-pyrazolyl)methane Unit, *Inorg. Chem.*, 2007, **46**, 409-416.

65. S. P. Foxon, T. Phillips, M. R. Gill, M. Towrie, A. W. Parker, M. Webb and J. A. Thomas, A Multifunctional Light Switch: DNA Binding and Cleavage Properties of a Heterobimetallic Ruthenium-Rhenium Dipyridophenazine Complex, *Ange. Chem. Int. Ed.*, 2007, **46**, 3686-3688.

66. B. A. Jackson and J. K. Barton, Recognition of Base Mismatches in DNA by 5,6-Chrysenequinone Diimine Complexes of Rhodium(III): A Proposed Mechanism for Preferential Binding in Destabilized Regions of the Double Helix, *Biochemistry*, 2000, **39**, 6176-6182.

67. H. Junicke, J. R. Hart, J. Kisko, O. Glebov, I. R. Kirsch and J. K. Barton, A rhodium(III) complex for high-affinity DNA base-pair mismatch recognition, *Proc. Natl. Acad. Sci. U. S. A.*, 2003, **100**, 3737-3742.

68. E. Ruba, J. R. Hart and J. K. Barton, $[Ru(bpy)_2(L)]Cl_2$: Luminescent Metal Complexes That Bind DNA Base Mismatches, *Inorg. Chem.*, 2004, **43**, 4570-4578.

69. V. r. C. Pierre, J. T. Kaiser and J. K. Barton, Insights into finding a mismatch through the structure of a mispaired DNA bound by a rhodium intercalator, *Proc. Natl. Acad. Sci. U. S. A.*, 2007, **104**, 429-434.

70. B. M. Zeglis, V. r. C. Pierre, J. T. Kaiser and J. K. Barton, A Bulky Rhodium Complex Bound to an Adenosine-Adenosine DNA Mismatch: General Architecture of the Metalloinsertion Binding Mode, *Biochemistry*, 2009, **48**, 4247-4253.

71. S. Georgiades, N. Abd Karim, K. Suntharalingam and R. Vilar, Interaction of Metal Complexes with G-Quadruplex DNA, *Ange. Chem. Int. Ed.*, 2010, **49**, 4020-4034.

72. J. E. Reed, A. A. Arnal, S. Neidle and R. n. Vilar, Stabilization of G-Quadruplex DNA and Inhibition of Telomerase Activity by Square-Planar Nickel(II) Complexes, *J. Am. Chem. Soc.*, 2006, **128**, 5992-5993.

73. K. Roxanne, F. Johans, M. Nicolas and F. S. Hanadi, Platinum Phenanthroimidazole Complexes as G-Quadruplex DNA Selective Binders, *Chem. Eur. J.*, 2008, **14**, 1145-1154.

74. C. Rajput, R. Rutkaite, L. Swanson, I. Haq and J. A. Thomas, Dinuclear Monointercalating Ru(II) Complexes That Display High Affinity Binding to Duplex and Quadruplex DNA, *Chem. Eur. J.*, 2006, **12**, 4611-4619.

75. V. Gonzalez, T. Wilson, I. Kurihara, A. Imai, J. A. Thomas and J. Otsuki, A dinuclear ruthenium(ii) complex that functions as a label-free colorimetric sensor for DNA, *Chem. Commun.*, 2008, 1868-1870.

76. M. E. Jiménez-Hernández, G. Orellana, F. Montero and M. T. Portolés, A Ruthenium Probe for Cell Viability Measurement Using Flow Cytometry, Confocal Microscopy and Time-resolved Luminescence, *Photochem. Photobiol.*, 2000, **72**, 28-34.

77. B. Onfelt, P. Lincoln and B. Norden, A Molecular Staple for DNA: Threading Bis-intercalating $[Ru(phen)_2dppz]^{2+}$ Dimer, *J. Am. Chem. Soc.*, 1999, **121**, 10846-10847.

78. B. Onfelt, L. Gostring, P. Lincoln, B. Norden and A. Onfelt, Cell Studies of the Bisintercalator $[u\text{-}C_4(cpdppz)_2\text{-}(phen)_4Ru_2]^{4+}$: toxic effects and properties as a light emitting DNA probe in V79 Chinese hampster cells, *Mutagenesis*, 2002, **17**, 317-320.

79. C. A. Puckett and J. K. Barton, Methods to Explore Cellular Uptake of Ruthenium Complexes, *J. Am. Chem. Soc.*, 2007, **129**, 46-47.

80. C. A. Puckett and J. K. Barton, Mechanism of Cellular Uptake of a Ruthenium Polypyridyl Complex, *Biochemistry*, 2008, **47**, 11711-11716.

81. C. A. Puckett and J. K. Barton, Fluorescein Redirects a Ruthenium-Octaarginine Conjugate to the Nucleus, *J. Am. Chem. Soc.*, 2009, **131**, 8738-8739.

82. A. J. Amoroso, et al., Rhenium fac tricarbonyl bisimine complexes: biologically useful fluorochromes for cell imaging applications, *Chem. Commun.*, 2007, 3066-3068.

83. A. J. Amoroso, R. J. Arthur, M. P. Coogan, J. B. Court, V. Fernandez-Moreira, A. J. Hayes, D. Lloyd, C. Millet and S. J. A. Pope, 3-Chloromethylpyridyl bipyridine fac-tricarbonyl rhenium: a thiol-reactive luminophore for fluorescence microscopy accumulates in mitochondria, *New J. Chem.*, 2008, **32**, 1097-1102.

84. J. Brunner and J. K. Barton, Targeting DNA Mismatches with Rhodium Intercalators Functionalized with a Cell-Penetrating Peptide, *Biochemistry*, 2006, **45**, 12295-12302.

85. K. K.-W. Lo, T. K. M. Lee, J. S. Y. Lau, W. L. Poon and S. H. Cheng, Luminescent Biological Probes Derived from Ruthenium(II) Estradiol Polypyridine Complexes, *Inorg. Chem.*, 2008, **47**, 200-208.

86. U. Neugebauer, Y. Pellegrin, M. Devocelle, R. J. Forster, W. Signac, N. Moran and T. E. Keyes, Ruthenium polypyridyl peptide conjugates: membrane permeable probes for cellular imaging, *Chem. Commun.*, 2008, 5307-5309.

87. M. Yu, Q. Zhao, L. Shi, F. Li, Z. Zhou, H. Yang, T. Yi and C. Huang, Cationic iridium(III) complexes for phosphorescence staining in the cytoplasm of living cells, *Chem. Commun.*, 2008, 2115-2117.

88. E. Musatkina, H. Amouri, M. Lamoureux, T. Chepurnykh and C. Cordier, Mono- and dicarboxylic polypyridyl-Ru complexes as potential cell DNA dyes and transfection agents, *J. Inorg. Biochem.*, 2007, **101**, 1086-1089.

89. S. I. Pascu, et al., Designing Zn(II) and Cu(II) derivatives as probes for in vitro fluorescence imaging, *Dalton Trans.*, 2007, 4988-4997.

90. S. I. Pascu, et al., Cellular confocal fluorescence studies and cytotoxic activity of new Zn(II) bis(thiosemicarbazonato) complexes, *Dalton Trans.*, 2008, 2107-2110.

91. S. W. Botchway, M. Charnley, J. W. Haycock, A. W. Parker, D. L. Rochester, J. A. Weinstein and J. A. G. Williams, Time-resolved and two-photon emission imaging microscopy of live cells with inert platinum complexes, *Proc. Natl. Acad. Sci. U. S. A.*, 2008, **105**, 16071-16076.

92. C.-K. Koo, et al., A Bioaccumulative Cyclometalated Platinum(II) Complex with Two-Photon-Induced Emission for Live Cell Imaging, *Inorg. Chem.*, 2009, **48**, 872-878.

93. R. A. Poole, G. Bobba, M. J. Cann, J.-C. Frias, D. Parker and R. D. Peacock, Synthesis and characterisation of highly emissive and kinetically stable lanthanide complexes suitable for usage 'in cellulo', *Org. Biomol. Chem.*, 2005, **3**, 1013-1024.

94. S. Pandya, J. Yu and D. Parker, Engineering emissive europium and terbium complexes for molecular imaging and sensing, *Dalton Trans.*, 2006, 2757-2766.

95. J. Yu, D. Parker, R. Pal, R. A. Poole and M. J. Cann, A Europium Complex That Selectively Stains Nucleoli of Cells, *J. Am. Chem. Soc.*, 2006, **128**, 2294-2299.

96. R. Pal and D. Parker, A single component ratiometric pH probe with long wavelength excitation of europium emission, *Chem. Commun.*, 2007, 474-476.

97. R. Pal and D. Parker, A ratiometric optical imaging probe for intracellular pH based on modulation of europium emission, *Org. Biomol. Chem.*, 2008, **6**, 1020-1033.

98. R. A. Poole, C. P. Montgomery, E. J. New, A. Congreve, D. Parker and M. Botta, Identification of emissive lanthanide complexes suitable for cellular imaging that resist quenching by endogenous anti-oxidants, *Org. Biomol. Chem.*, 2007, **5**, 2055-2062.

99. F. Kielar, A. Congreve, G.-l. Law, E. J. New, D. Parker, K.-L. Wong, P. Castreno and J. d. Mendoza, Two-photon microscopy study of the intracellular compartmentalisation of emissive terbium complexes and their oligo-arginine and oligo-guanidinium conjugates, *Chem. Commun.*, 2008, 2435-2437.

100. B. S. Murray, E. J. New, R. Pal and D. Parker, Critical evaluation of five emissive europium(III) complexes as optical probes: correlation of cytotoxicity, anion and protein affinity with complex structure, stability and intracellular localisation profile, *Org. Biomol. Chem.*, 2008, **6**, 2085-2094.

101. E. J. New and D. Parker, The mechanism of cell uptake for luminescent lanthanide optical probes: the role of macropinocytosis and the effect of enhanced membrane permeability on compartmentalisation, *Org. Biomol. Chem.*, 2009, **7**, 851-855.

102. E. J. New, D. Parker and R. D. Peacock, Comparative study of the constitution and chiroptical properties of emissive terbium and europium complexes with a common tetraazatriphenylene sensitiser; the nature of the sensitiser determines quenching sensitivity and cellular uptake, *Dalton Trans.*, 2009, 672-679.

103. A.-S. Chauvin, S. Comby, S. Bo, C. D. B. Vandevyver, F. Thomas and J.-C. G. Bunzli, A Polyoxyethylene-Substituted Bimetallic Europium Helicate for Luminescent Staining of Living Cells, *Chem. Eur. J.*, 2007, **13**, 9515-9526.

104. C. D. B. Vandevyver, A.-S. Chauvin, S. Comby and J.-C. G. Bunzli, Luminescent lanthanide bimetallic triple-stranded helicates as potential cellular imaging probes, *Chem. Commun.*, 2007, 1716-1718.

105. A.-S. Chauvin, S. Comby, B. Song, C. D. B. Vandevyver and J.-C. G. Bunzli, A Versatile Ditopic Ligand System for Sensitizing the Luminescence of Bimetallic Lanthanide Bio-Imaging Probes, *Chem. Eur. J.*, 2008, **14**, 1726-1739.

106. E. Deiters, B. Song, A.-S. Chauvin, C. D. B. Vandevyver, F. Gumy and J.-C. G. Bünzli, Luminescent Bimetallic Lanthanide Bioprobes for Cellular Imaging with Excitation in the Visible-Light Range, *Chem. Eur. J.*, 2009, **15**, 885-900.

Chapter 2

Ru(II) metallo-intercalators

2.1 Introduction

Ever since the discovery that $[Ru(bpy)_2(dppz)]^{2+}$ and $[Ru(phen)_2(dppz)]^{2+}$ (bpy = 2,2'-bipyridine, dppz = dipyrido[3,2-a:2',3'-c]phenazine, phen = 1,10-phenanthroline) can intercalate into DNA with the characteristic activation of MLCT luminescence,[1, 2] there has been a large amount of research into the *in vitro* DNA-binding properties of metallo-intercalators, especially those which contain dppz as the intercalating ligand and ruthenium(II) as the metal centre (Figure 2.1). This chapter is concerned with the *in cellulo* DNA binding properties and cytotoxicity of Ru(II) metallo-intercalators, including dppz-based systems. It describes work exploring their potential as luminescent DNA imaging agents in live and fixed cells and also as therapeutic agents.

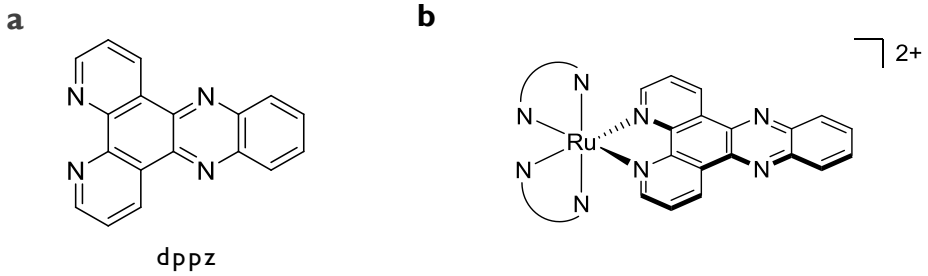

Figure 2.1 a, dppz intercalating ligand. **b,** Ru(II)dppz metallo-intercalator $[Ru(N^N)_2(dppz)]^{2+}$ containing two bidentate ancillary N^N ligands.

2.1.1 Ru(II)dppz complexes

Work by the Thomas group has developed a series of achiral ruthenium-dppz "light switch" systems that bind to DNA with a high affinity and sequence-specificity.[3] Employing the tridentate tpm (tpm = tris-(1-pyrazolyl)methane) "scorpionate" ligand to cap one face of the octahedral geometry, these complexes offer synthetic advantages over $[Ru(N\hat{}N)_2(dppz)]^{2+}$ systems, in particular a vacant coordination site which can be easily modified by substitution to modulate the DNA binding properties of the molecule as a whole (Figure 2.2). Indeed, 2D NMR binding studies on a series of related $[Ru(tpm)(L)(dppz)]^{2+}$ complexes containing pyridine derivatives as the axial ligand, L, have revealed how the nature of this ligand has a profound effect on the DNA binding mode and affinity, even to the extent of preventing intercalation.[4]

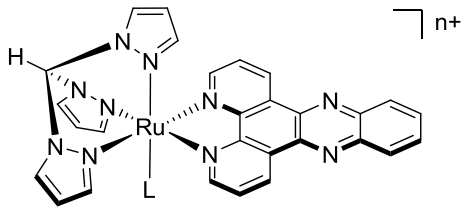

Figure 2.2 $[Ru(tpm)(L)(dppz)]^{n+}$ metallo-intercalator.

To examine the cellular internalisation and potential of these complexes in cellular DNA imaging applications, two such complexes were synthesised: $[Ru(tpm)(NCMe)(dppz)]^{2+}$ **[2.1]** and $[Ru(tpm)(py)(dppz)]^{2+}$ **[2.2]**, containing acetonitrile (NCMe) and pyridine (py) in the available coordination site respectively (Figure 2.3a). Both complexes have previously been demonstrated to bind to DNA with a high affinity (K_b = 2.9×10^6 and 4.7×10^6 M^{-1} for **[2.1]** and **[2.2]** respectively) and to display the light switch effect upon intercalation (Figure 2.3b,c).[3, 4] Each complex therefore represents a useful model for the investigation of the cellular DNA binding of this class of complexes.

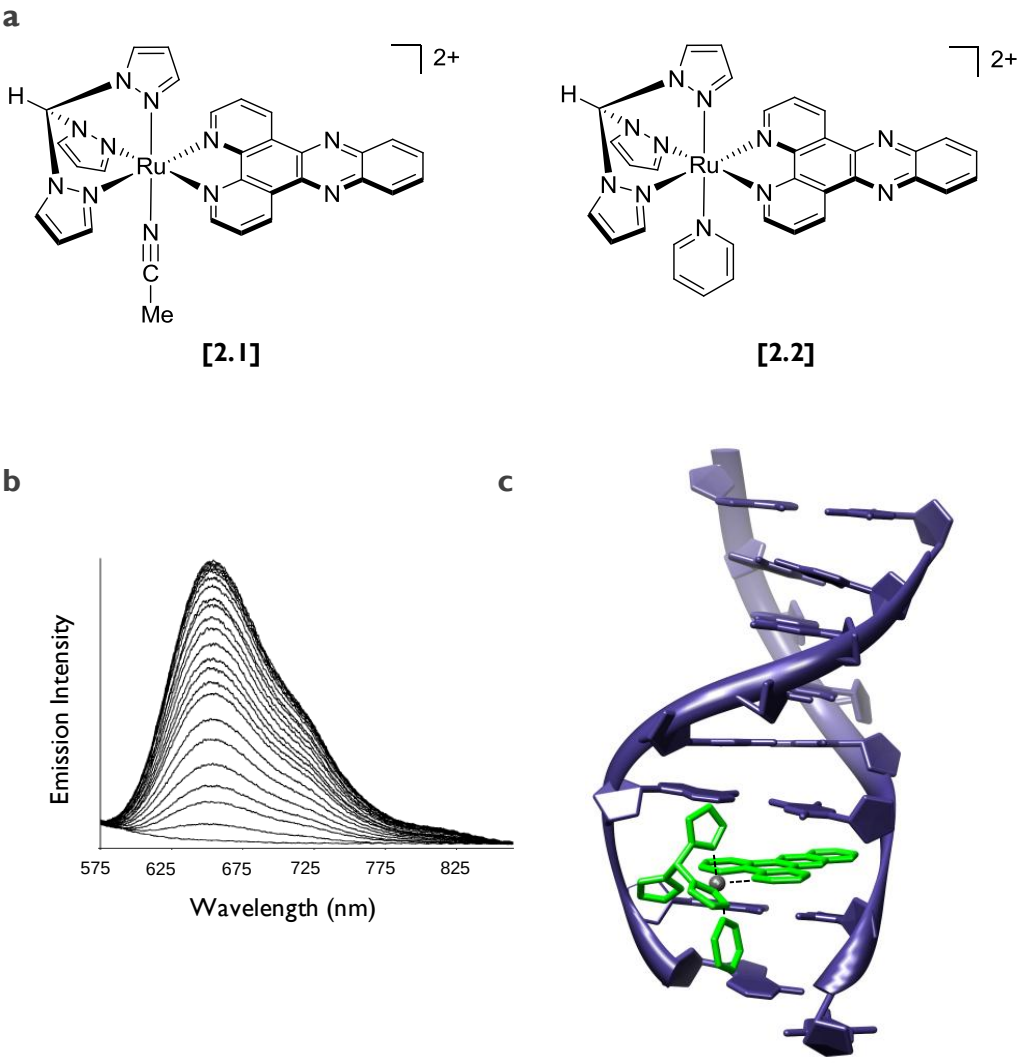

Figure 2.3 a, [Ru(tpm)(L)(dppz)]$^{2+}$ complexes relevant to this study where L = NCMe **[2.1]** or py **[2.2]**. **b,** Light switch effect of **[2.2]** upon addition of DNA.[3] **c,** Structure of **[2.2]** intercalated with DNA *via* the minor groove (PDB file courtesy of Dr P. Waywell).

2.1.2 Ru(II)tpphz complexes

Not limiting this study to Ru(II) complexes containing the dppz intercalating ligand, the two metallo-intercalators $[Ru(phen)_2(tpphz)]^{2+}$ **[2.3]** and $[Ru(bpy)_2(tpphz)]^{2+}$ **[2.4]**, both of which contain the tpphz (tetrapyrido[3,2-a:2',3'-c:3'',2''-h:2''',3'''-j]phenazine) intercalating ligand (Figure 2.4), were also investigated. In two almost identical studies, **[2.4]** was reported to show a high affinity for DNA (K_b = 8.8 × 10^6 M^{-1}),[5,6] a higher affinity than that reported for the analogous dppz complex. The binding parameter estimates for **[2.3]** (K_b = 3.0 × 10^5 M^{-1})[7] are comparable to those previously reported for **[2.4]**, with **[2.4]** displaying the greater affinity for DNA.

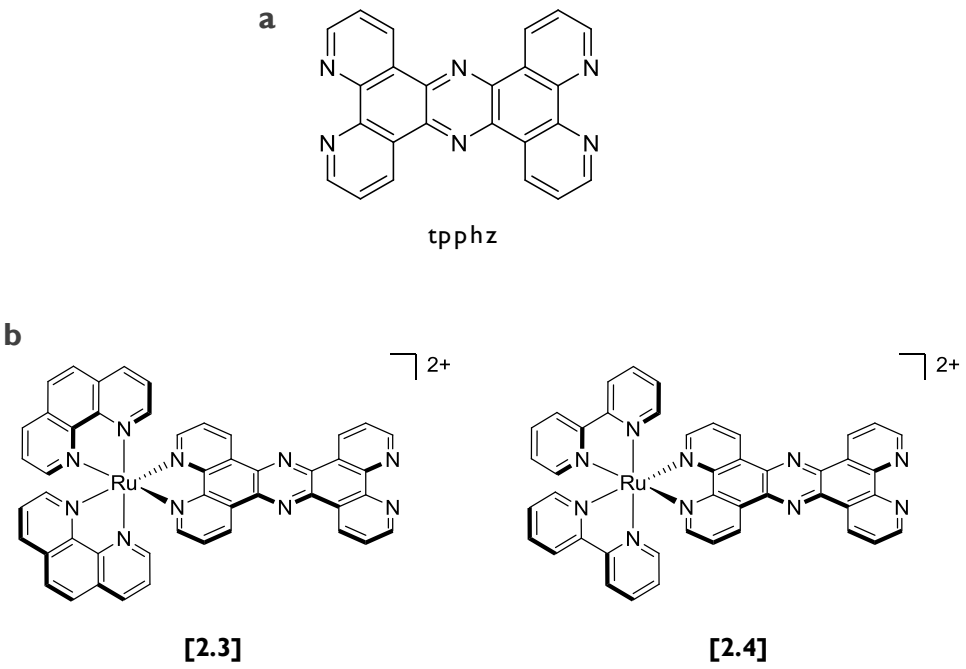

Figure 2.4 a, tpphz intercalating ligand. **b,** Ru(II)tpphz metallo-intercalators with either 1,10-phenanthroline **[2.3]** or bipyridine **[2.4]** as the ancillary ligands.

2.2 Synthesis

2.2.1 Ru(II)dppz complexes

The ligands tpm and dppz, through the intermediate dpq (1,10-phenanthroline-5,6-dione), were synthesised by published procedures (Scheme 2.1).[8, 9]

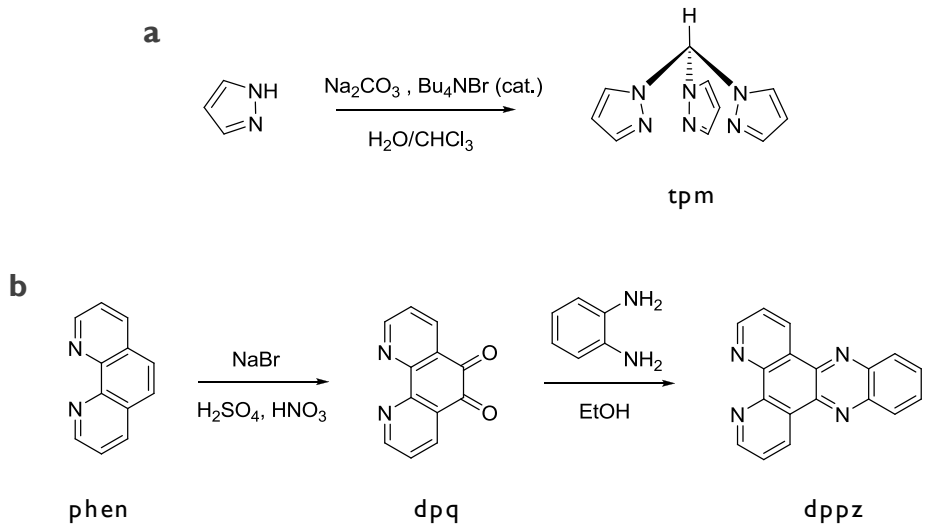

Scheme 2.1 a, Synthesis of tpm (yield = 33 %). **b,** Synthesis of dppz (overall yield = 30 %).

The synthesis of $Ru(tpm)Cl_3$ and $[Ru(tpm)(Cl)(dppz)]^+$ were accomplished by adapted literature procedures (Scheme 2.2a).[3, 10] Using $[Ru(tpm)(Cl)(dppz)]^+$ as a precursor complex, the derivatives $[Ru(tpm)(NCMe)(dppz)]^{2+}$ **[2.1]** and $[Ru(tpm)(py)(dppz)]^{2+}$ **[2.2]** were synthesised by substitution of the chloride ligand with acetonitrile and pyridine respectively (Scheme 2.2b).[3]

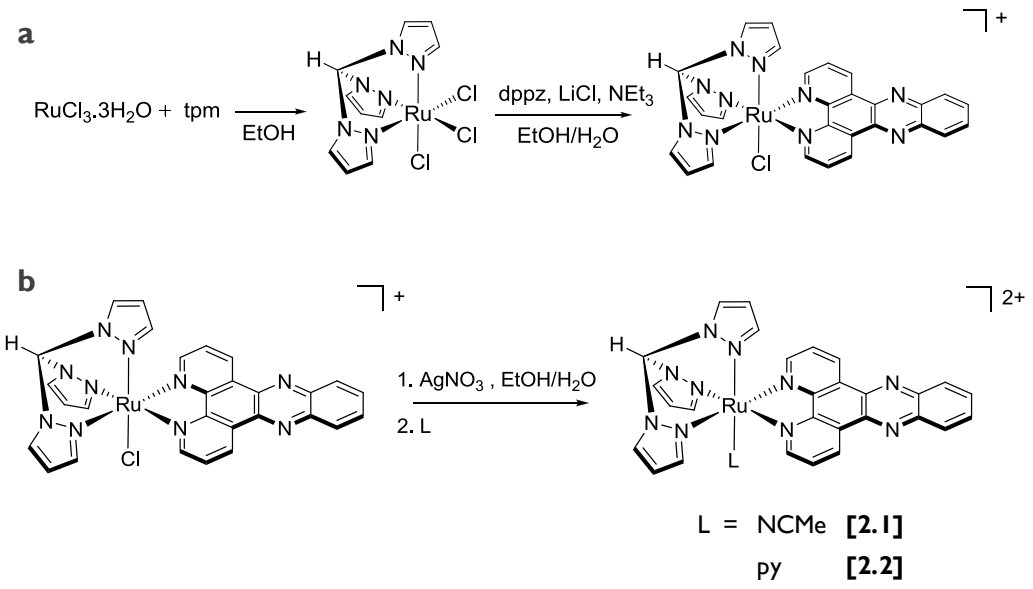

Scheme 2.2 a, Synthesis of $[Ru(tpm)(Cl)(dppz)]^{2+}$ precursor (overall yield = 17 %). **b,** Synthesis of **[2.1]** and **[2.2]** (yields ranged from 45-77 %).

Each complex was synthesised as their hexafluorophosphate salt and characterised by NMR and mass spectroscopy. They were converted into their water-soluble chloride salts by counter-ion metathesis.

2.2.2 Ru(II)tpphz complexes

$[Ru(phen)_2(tpphz)]^{2+}$ **[2.3]** and $[Ru(bpy)_2(tpphz)]^{2+}$ **[2.4]** and were synthesised according to published procedures and characterised by H. Derrat.[7, 11] Both complexes were used as their chloride salts.

2.3 Partition coefficients

To traverse the cell membrane, a molecule needs to be hydrophobic enough to pass through the lipid bilayer but not so hydrophobic that it remains within the membrane. Generally, if a molecule is more polar than water it will be membrane-impermeable. The octanol/water partition coefficient, log P (Equation 2.1), is a ratio of the solubility of a molecule in the two solvents and thus provides a measure of the hydrophobicity/hydrophilicity of the molecule. Molecules with a negative log P are more soluble in the water phase and therefore are hydrophilic whereas a positive log P value indicates the molecule is more soluble in the octanol phase and therefore is hydrophobic. This in turn gives an indication of lipophilicity; lipophilic molecules will posses large octanol/water partition coefficients, although it should be noted a hydrophobic molecule is not automatically lipophilic. Log P is frequently used in addition with factors such as molecular weight to evaluate the drug-likeness of a compound in medicinal chemistry and pharmacology.[12] Work by Puckett and Barton showed the cellular uptake of a series of Ru(II)dppz systems to be "lipophilicity"-based; by varying the ancillary ligand, complexes with a greater hydrophobicity were shown to display the greater uptake in cells.[13]

$$\log \mathrm{P}_{octanol/\,water} = \log\left(\frac{[complex]_{octanol}}{[complex]_{water}}\right)$$

Equation 2.1 Calculation of octanol/water partition coefficient log P.

The octanol/water partition coefficients of **[2.1]** - **[2.4]** were measured using the "shake flask" method and the results are displayed in Table 2.1 along with the mass of each complex, excluding the counter-ion, to provide a measure of the relative size of each complex.

Complex		Mass / Da	log P
$[Ru(tpm)(NCMe)(dppz)]^{2+}$	**[2.1]**	639	-1.19 ± 0.10
$[Ru(tpm)(py)(dppz)]^{2+}$	**[2.2]**	677	-0.74 ± 0.08
$[Ru(phen)_2(tpphz)]^{2+}$	**[2.3]**	846	-1.24 ± 0.12
$[Ru(bpy)_2(tpphz)]^{2+}$	**[2.4]**	798	-2.08 ± 0.15
$[Ru(phen)_2(dppz)]^{2+}$		744	-1.48*
$[Ru(bpy)_2(dppz)]^{2+}$		696	-2.50*

Table 2.1 Measured octanol/water partition coefficients for **[2.1]** - **[2.4]** along with complex mass. *$[Ru(bpy)_2(dppz)]^{2+}$ and $[Ru(phen)_2(dppz)]^{2+}$ are included for comparison.[13]

As can be seen from Table 2.1, both **[2.1]** and **[2.2]** possess a negative log P value, indicating that they are more soluble in water than octanol and therefore hydrophilic, with the larger complex **[2.2]**, which contains pyridine as the axial ligand, being the more hydrophobic. The log P values measured correlated well with data obtained *via* the molinspiration chemical properties calculation software.[14] This log P calculation software was developed by fitting calculated with experimental log P values for more than twelve thousand drug-like molecules, to obtain hydrophobicity values for multiple fragments and group contributions. Although not able to calculate log P for coordination complexes, ligands may be directly compared if they have an equal denticity. As shown in Table 2.2, pyridine is more hydrophobic than acetonitrile (calculated log P values of 0.70 and 0.47 respectively) and accordingly **[2.2]** is more hydrophobic than **[2.1]** by a similar order of magnitude.

The two Ru(II)tpphz systems display a greater hydrophilicity (log P = -1.24 and -2.08 for **[2.3]** and **[2.4]** respectively) than the Ru(II)dppz complexes (Table 2.1). Although still strongly hydrophilic, each complex is more hydrophobic than its respective dppz analogue, as shown by the literature values for $[Ru(phen)_2(dppz)]^{2+}$ and $[Ru(bpy)_2(dppz)]^{2+}$ (-1.48 and -2.50 respectively).[13] This is in agreement with the calculated log P values for each intercalating ligand from Table 2.2, with tpphz displaying a greater hydrophobicity than dppz (log P = 4.18 and 3.70 for tpphz and dppz respectively). Accordingly, the difference in log P values between the relevant Ru(II)dppz and Ru(II)tpphz complex is a similar order of magnitude as the difference between the two intercalating ligands.

Ligand	Mass / Da	Volume / Å^3	log P
NCMe	41	46	0.47
py	79	80	0.70
bpy	156	147	1.44
phen	180	163	1.90
dppz	282	243	3.71
tpphz	384	323	4.18

Table 2.2 Calculated ligand octanol/water partition coefficients, masses and molecular volumes. Log P and molecular volume values calculated using molinspiration property calculation software.[14]

From these values, it would not be predicted that any of these complexes could diffuse across the cell membrane as they are large, polar, hydrophilic molecules; although for accurate quantification diffusion studies across an artificial membrane would be required.

2.4 Live cell uptake and imaging

Since all complexes bind to duplex DNA with high affinity and display light switching effects their cellular uptake can, potentially, be measured by luminescent microscopy. Using this approach, each complex would be predicted to behave as a luminescent probe of cellular DNA if they are internalised and therefore the cellular uptake properties of each complex can be examined. To examine the potential of **[2.1]** - **[2.4]** for such a role, MCF-7 human breast cancer cells were incubated with solutions of each complex and the cellular uptake and *in cellulo* DNA binding was examined using CLSM (confocal laser scanning microscopy). CLSM is a high-resolution fluorescence imaging technique and offers numerous advantages over conventional fluorescence microscopy, in particular the ability to eliminate out-of-focus emission. For biological imaging, cells are usually labelled with organelle- or macromolecule-specific fluorescent dyes, although unlabelled samples may be viewed directly using phase contrast bright field imaging.

In each individual case, the Ru(II) complex was excited at 458 nm using a He-Ne laser and the luminescence emission at 640-700 nm (for **[2.1]** and **[2.2]**) or 600-640 (for **[2.3]** and **[2.4]**) recorded. These wavelengths correspond to ^{1}MLCT excitation and the resultant ^{3}MLCT emission observed from the corresponding *in vitro* DNA binding study.[3, 6] These luminescent properties mean that each Ru(II) complex has a Stokes shift value of >150 nm; a considerable advantage in an imaging context, as discussed in Section 1.5. To determine the health of the cells after incubation, a standard live/dead staining procedure using the two commercially available dyes SYTO 9 (®) and propidium iodide (PI) was performed. SYTO 9 is a green-emitting nucleic acid dye which stains the DNA and RNA of live cells, while the purple-emitting PI stains the DNA of non-viable cells upon intercalation. The live/dead staining properties of each molecule can essentially be explained in terms of membrane-permeability: SYTO 9 (log P = 0.93)[15] is a

membrane-permeable molecule whereas PI (log P = -3.73)[14] is membrane-impermeable. These properties are implied by the respective hydrophobicity or hydrophilicity of each molecule. As the membrane of a dead cell is usually perforated, PI is able to enter and bind to nuclear DNA; therefore PI staining provides an indication of cell viability. In addition to nuclear staining, SYTO 9 generally shows mitochondrial staining as the molecule is able to diffuse into these organelles and bind to mitochondrial DNA.

2.4.1 Ru(II)dppz complexes

As shown by Figure 2.5, incubation of MCF-7 cells with **[2.1]** or **[2.2]** (200 μM, 24 hrs) displays no *in cellulo* luminescence in either live or dead cells.

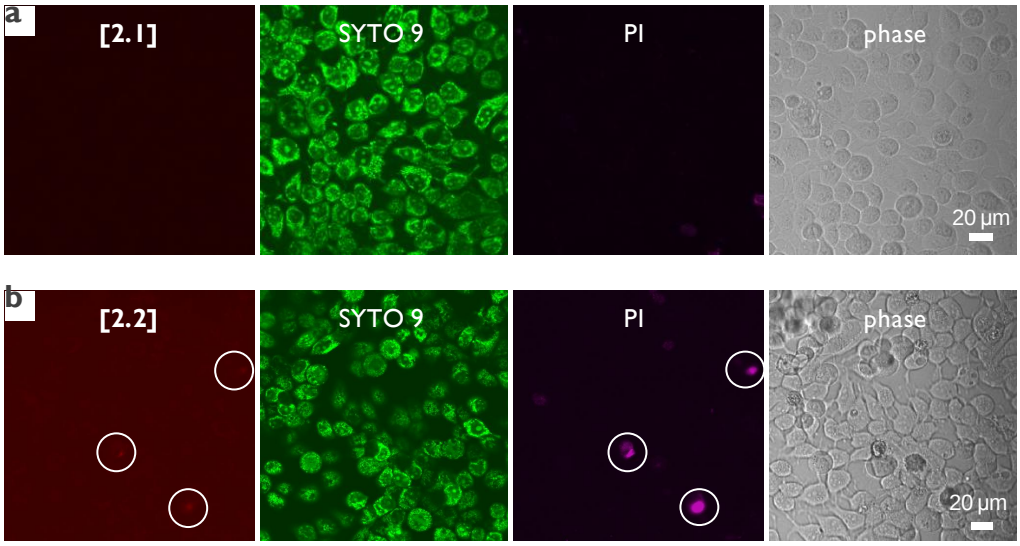

Figure 2.5 CLSM of MCF-7 cells incubated with **[2.1]** (**a**) and **[2.2]** (**b**) (100 μM, 24 hrs). From left to right: luminescence emission of **[2.1]** or **[2.2]** (red), live cell stain SYTO 9 (green), dead cell stain propidium iodide (PI) (purple) and phase contrast image.

The absence of luminescence from live cells would be explained by a poor rate of cellular uptake and is not a surprising result; both molecules are

hydrophilic, relatively large and polar and so would not be predicted to be membrane permeable. However, the absence of luminescence in dead cells was unexpected; a non-membrane-permeable nucleic acid dye should behave in a manner analogous to PI, but the Ru(II)dppz complex is clearly not demonstrating this behaviour. This effect is highlighted in Figure 2.5b, where cells stained by PI show no emission due to **[2.3]**. The live/dead staining also shows that neither complex demonstrates significant toxicity, where the majority of cells remain viable under these incubation conditions.

2.4.2 Ru(II)tpphz complexes

In contrast to the achiral Ru(II)dppz systems, incubation of MCF-7 cells with Ru(II)tpphz complexes **[2.3]** and **[2.4]** does result in CLSM-observable *in cellulo* luminescence (Figure 2.6). Examining the cellular location of the emission in more detail, Figure 2.7 shows that *in cellulo* luminescence appears to be from non-nuclear locations, although the low emission signals makes further deductions difficult.

Considering the lack of luminescence observed for each Ru(II)dppz complex, these results were especially encouraging. The DNA binding properties of metallo-intercalators is a much-researched area and developing molecules that bind with a high affinity and specificity to DNA is a key goal in this research. Such complexes can function as DNA imaging agents due to their favourable photophysical properties, which include: novel excitation/emission wavelengths, photostability, water solubility and chemical stability. Additionally, nuclear accumulation of such complexes would indicate that they could have potential as therapeutics by interfering with various cellular processes such as transcription and translation.

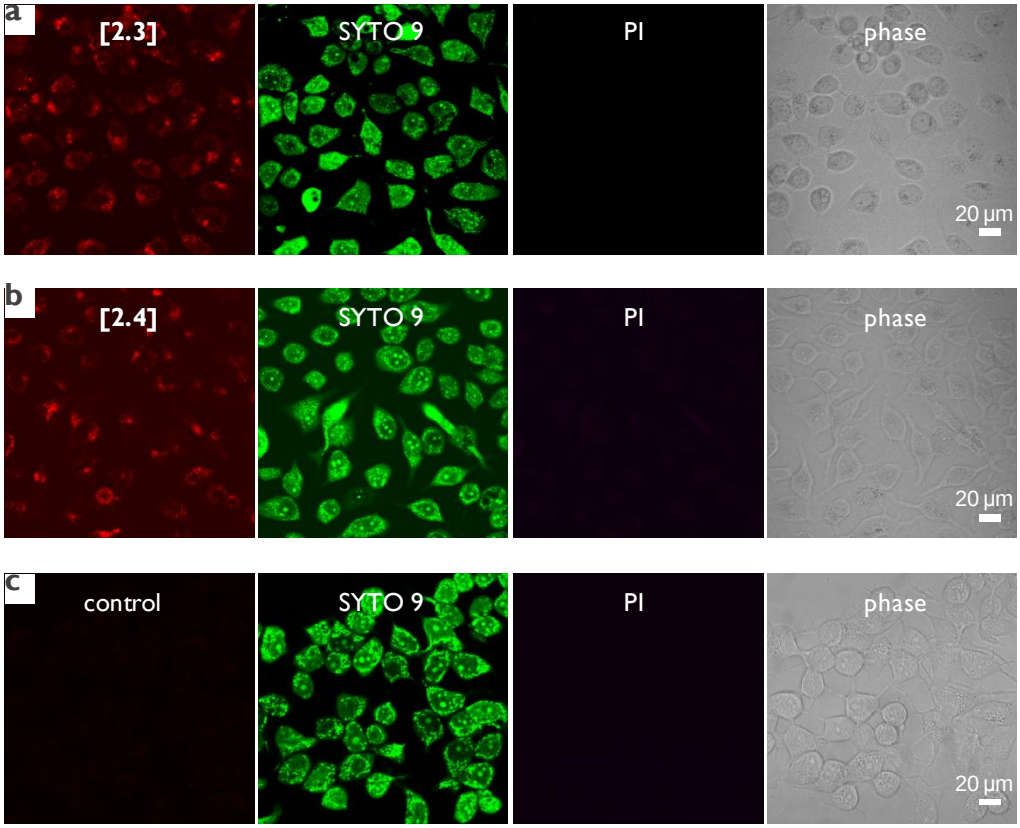

Figure 2.6 a, b, CLSM imaging of MCF-7 cells incubated with Ru(II)tpphz complexes **[2.3]** (**a**) or **[2.4]** (**b**) (100 µM, 24 hrs). **c,** Negative control. From left to right: luminescence emission of Ru(II)tpphz complex (red), SYTO 9 (green), PI (purple) and phase contrast image.

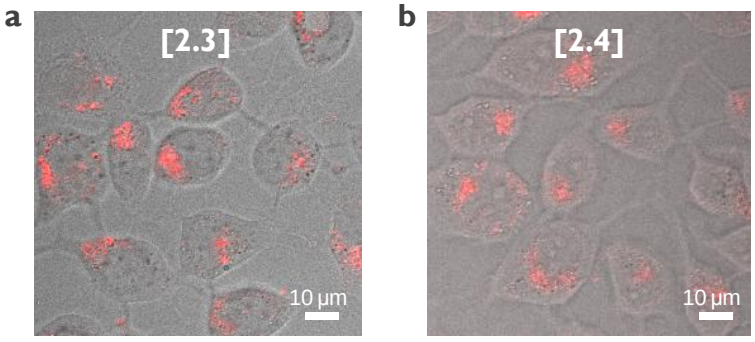

Figure 2.7 Location of MLCT luminescence. Images of MCF-7 cells incubated with Ru(II)tpphz complexes **[2.3]** (**a**) or **[2.4]** (**b**) (100 µM, 24 hrs). The Ru(II) signal and phase contrast images are overlaid.

2.4.3 $[Ru(phen)_2(tpphz)]^{2+}$

With the observation of *in cellulo* luminescence of **[2.3]**, and in an attempt to improve the uptake and nuclear staining properties of the complex, staining experiments were repeated in serum-free conditions and the effects of concentration were also investigated. Co-staining experiments with currently used DNA stains were also carried out to investigate whether the molecule is imaging cellular DNA.

2.4.3.1 Effects of serum and concentration

Many currently used protocols in biology require serum-free conditions as serum proteins can bind to active molecules and so impede cellular uptake. It was found that serum-free media clearly improved the cellular uptake of **[2.3]** resulting in evidence of nuclear staining by the complex (Figure 2.8).

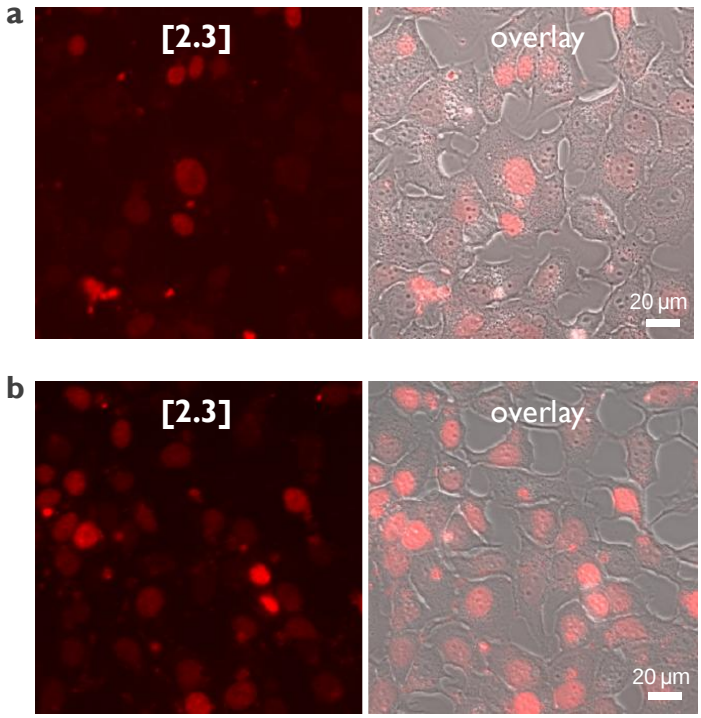

Figure 2.8 CLSM of MCF-7 cells incubated with 100 µM **[2.3]** in serum-free media for 1 hr (**a**) or 3 hrs (**b**). Left: Ru(II)tpphz emission (red). Right: Overlay image of Ru(II)tpphz emission and phase contrast.

In an attempt to further increase nuclear staining, the concentration of the complex was increased to 200 μM and, as Figure 2.9a shows, this resulted in clearer apparent nuclear staining. Using this higher concentration, the nuclei of cells appear stained in both serum and serum-free conditions – with a greater uptake being observed in serum-free conditions (Figure 2.9b and Table 2.3). As no nuclear staining was observed at 100 μM for 24 hrs compared to multiple cell nuclei stained using 200 μM in a short space of time, this apparent non-linear behaviour of concentration v. time indicates the complexity of the cellular internalisation process of this complex.

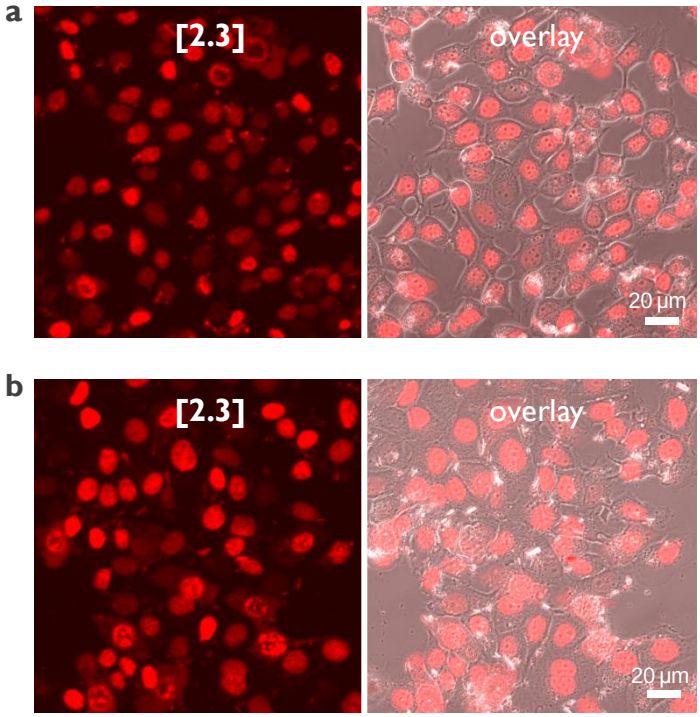

Figure 2.9 CLSM of MCF-7 cells incubated with 200 μM **[2.3]** in either serum-containing media (**a**) or serum-free media (**b**) for 1 hr. Left: **[2.3]** emission (red). Right: Overlay image of **[2.3]** emission and phase contrast.

Conditions	Nuclei stained / %	Rel. emission intensity / %
- serum	96 ± 3	100
+ serum	93 ± 2	65

Table 2.3 Extent of nuclear staining of MCF-7 cells by **[2.3]** (200 μM, 1 hr) in serum-free and serum-containing conditions. For relative emission intensity / cell, incubation in serum-free conditions used as 100 %.

This demonstrates that factors such as: concentration, incubation time and the presence of media serum can determine the rate of cellular uptake and extent of nuclear staining (with the associated toxicity properties) of the complex. Clearly this is of relevance in the development of such systems for *in cellulo* applications. Indeed, in a recent study by Puckett and Barton the use of serum-free conditions was also found to optimise the uptake of luminescence ruthenium peptide conjugates.[16]

2.4.3.2 Co-staining with nucleic acid stains

Co-staining with the commonly used nuclear DNA marker stain DAPI (Figure 2.10) shows a strong overlap of the two emission signals (indicated by the white signal in Figure 2.10c), confirming that **[2.3]** is indeed targeting the nuclei and strongly suggesting that it is DNA being imaged. In contrast, co-staining with SYTO 9, which binds to RNA and mitochondrial DNA in addition to nuclear DNA, shows a much lower overlap of emission signals with **[2.3]** (Figure 2.11). As **[2.3]** requires intercalation to activate the light switch, binding to single stranded RNA would not be predicted to result in luminescence and so should not be observed in these experiments. These experiments also show staining by **[2.3]** is nuclear specific; for example, there is no apparent mitochondrial DNA staining.

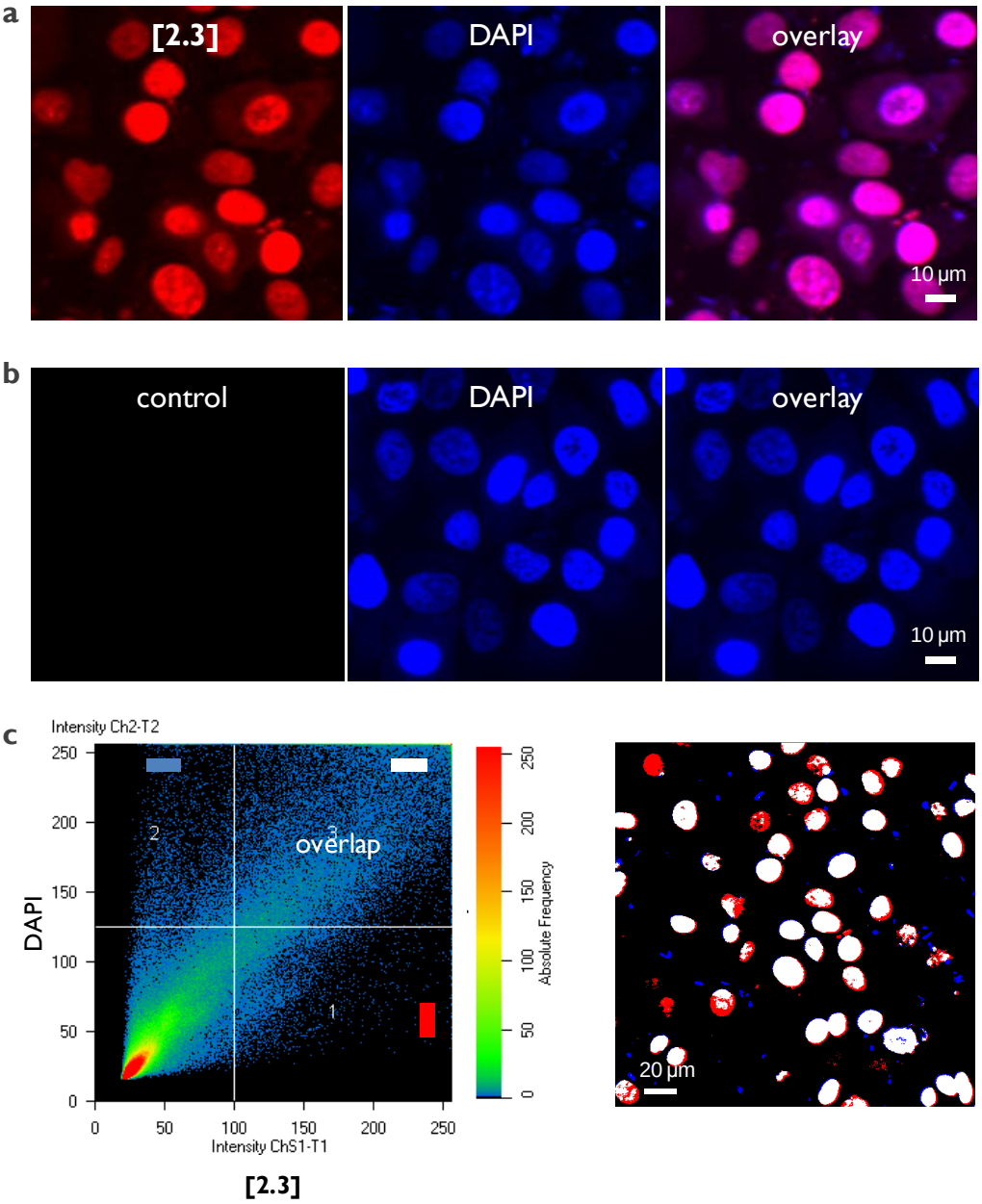

Figure 2.10 a, Co-staining of **[2.3]** (red) with DAPI (blue). **b,** Negative control experiment. **c,** Co-localisation of **[2.3]** and DAPI emission signals (blue = region 2, DAPI, red = region 1, **[2.3]**, white = region 3, overlap).

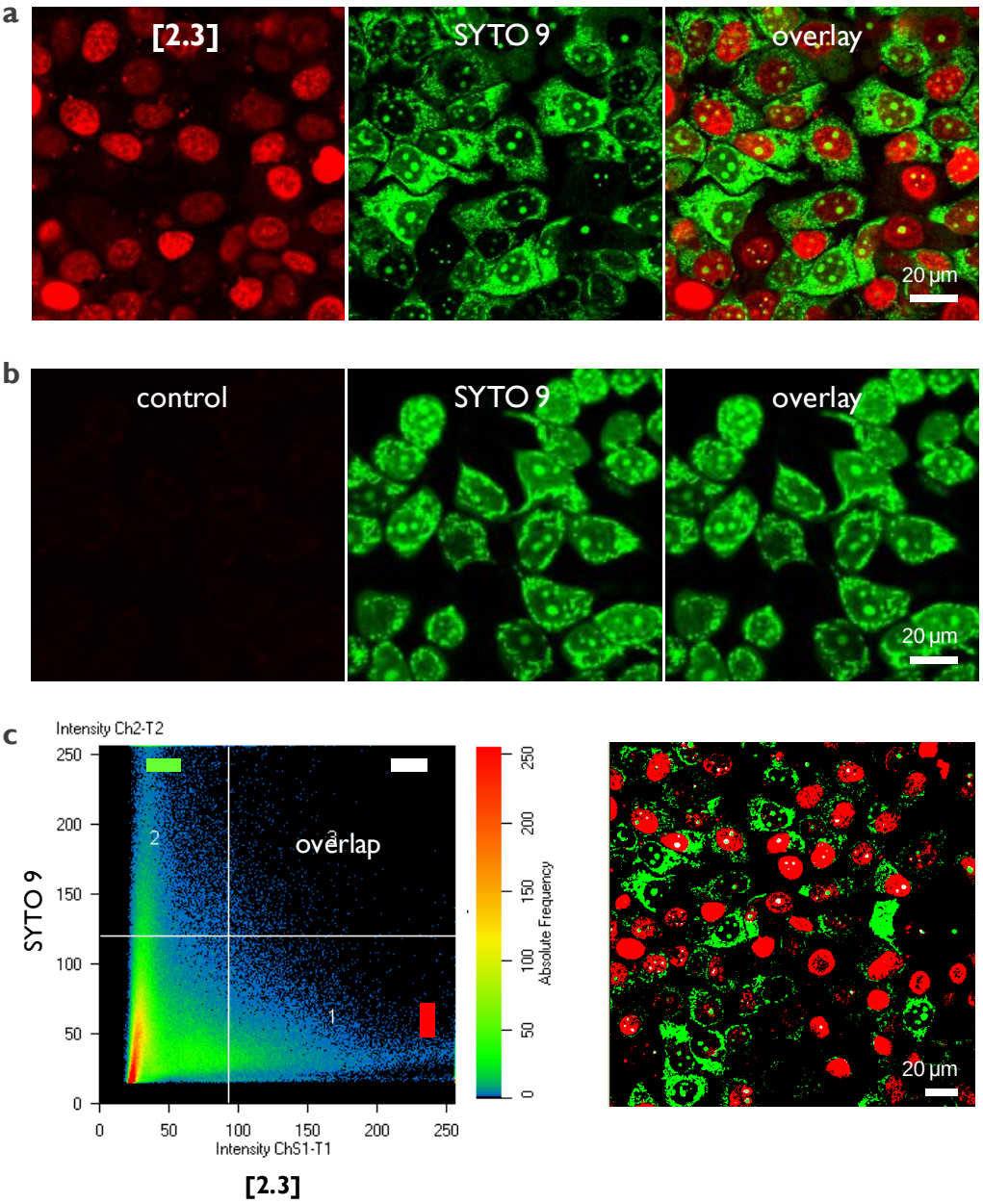

Figure 2.11 a, Co-staining of **[2.3]** (red) with SYTO 9 (green). **b,** Negative control experiment. **c,** Co-localisation of **[2.3]** and SYTO 9 emission signals (green = region 2, SYTO 9, red = region 1, **[2.3]**, white = region 3, overlap).

2.4.3.3 Emission profile

To characterise the emission profile in more detail, a lambda stack experiment, which collects the emission intensity across a range of wavelengths, was conducted. A representative example shows the emission profile of **[2.3]** in the nuclei of cells to be relatively broad, with the maximum emission located at 620-630 nm (Figure 2.12). This is in good agreement with *in vitro* DNA binding luminescence titration data, where intercalation is accompanied by such emission,[7] and offers further evidence that **[2.3]** is targeting cellular DNA in live cells.

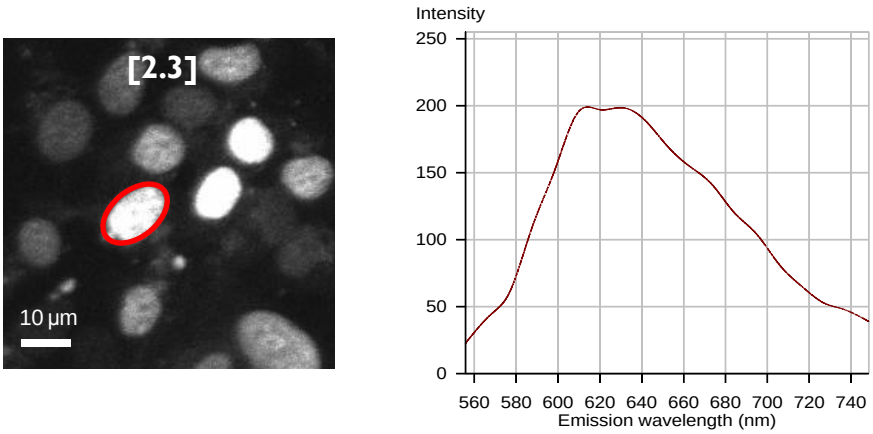

Figure 2.12 Emission profile of **[2.3]** *in cellulo* luminescence (right) from stained cell (left, highlighted in red).

These results show a Ru(II) metallo-intercalator can target nuclear DNA in living cells and successfully demonstrates the use of Ru(II)-based MLCT luminescence in biological imaging.

2.4.3.4 Toxicity

At longer incubation times the toxicity of the complex presents a problem, with the greater rate of cellular uptake and DNA staining by **[2.3]** being accompanied by an increase in cell death, as observable by positive staining by PI (Figure 2.13).

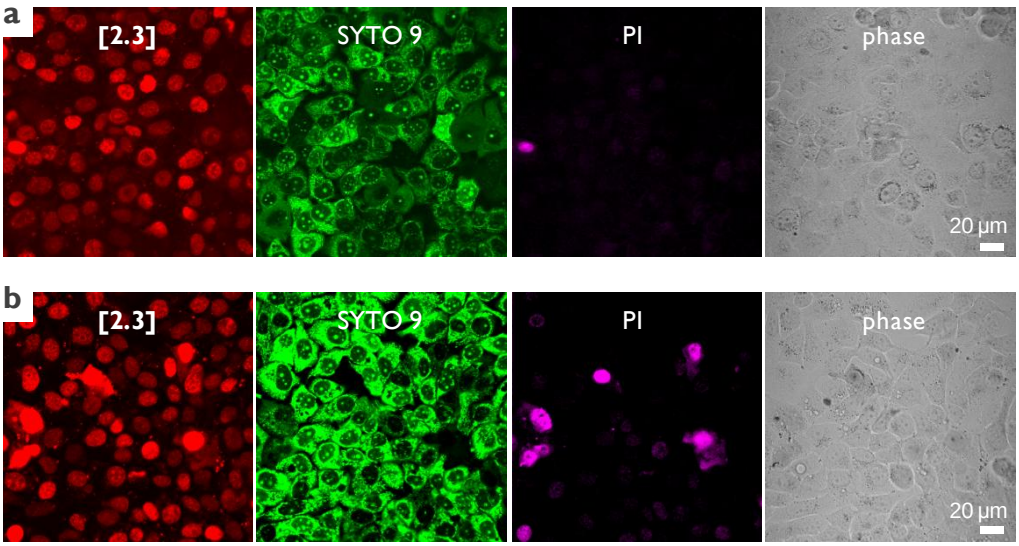

Figure 2.13 CLSM of MCF-7 cells incubated with 200 µM **[2.3]** in serum-free media for 1 hr (**a**) or 3 hrs (**b**). From left to right: luminescence emission of **[2.3]** (red), SYTO 9 (green), PI (purple) and phase contrast image.

When the concentration is increased even further (500 µM), this has the effect of killing all the cells in a short incubation time (~1 hr). This is evident by co-staining with PI, shown in Figure 2.14a. The co-staining with PI is in agreement with the DAPI co-staining data, providing further confirmation that **[2.3]** images cellular DNA. Using a shorter incubation time at this concentration (30 minutes), cells initially appear healthy but, after removal of the complex and subsequent CLSM imaging, cell death is then observed 20 minutes later (Figure 2.14b,c). This observation would suggest that it is the cellular internalisation of **[2.3]** that is directly responsible for the toxic effects observed.

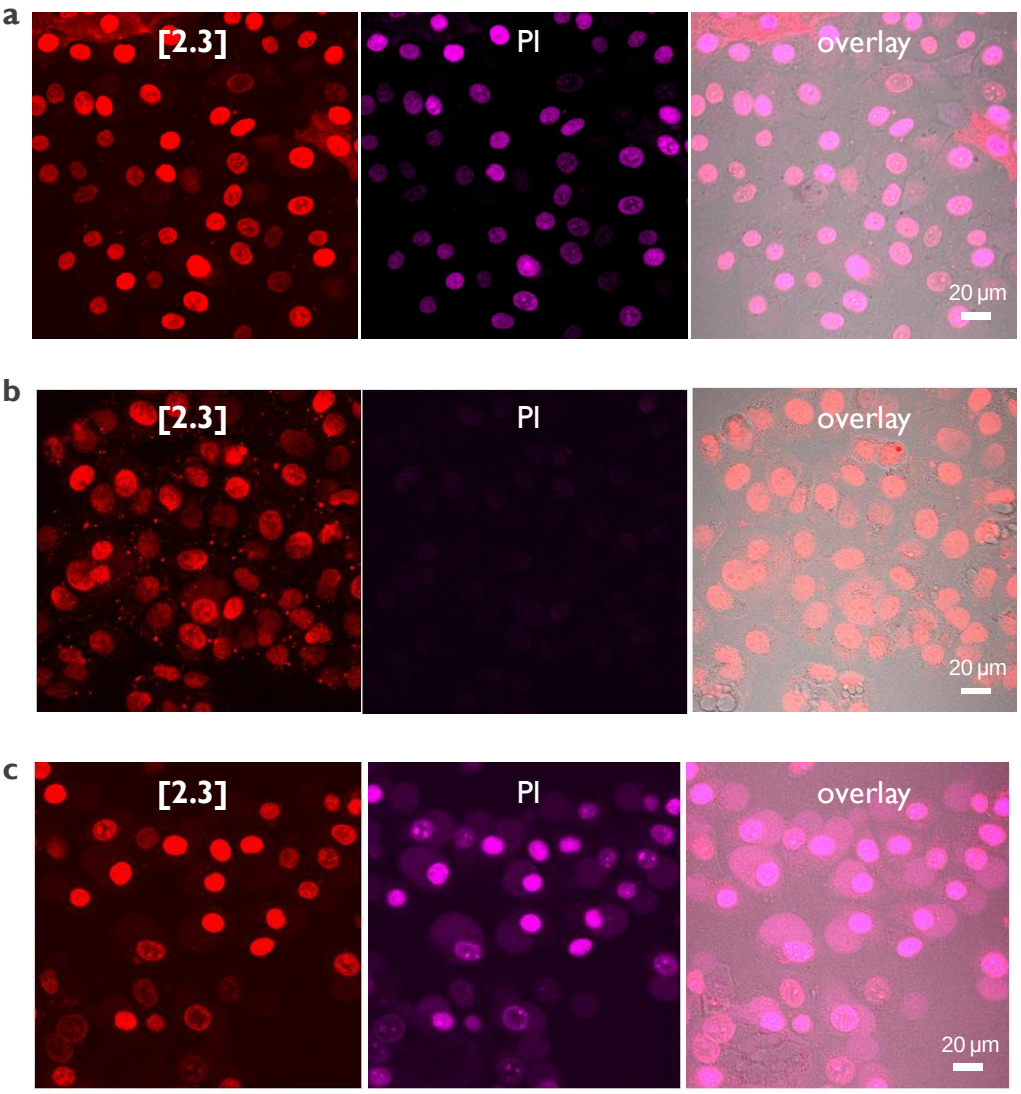

Figure 2.14 CLSM of MCF-7 cells incubated with **[2.3]**. **a,** 500 μM, 1 hr. **b,** 500 μM, 30 mins. **c,** 500 μM, 30 mins, cells then imaged 20 mins after removal of complex. From left to right: **[2.3]** (red), PI (purple), overlay (including phase contrast) image.

2.4.4 $[Ru(bpy)_2(tpphz)]^{2+}$

Applying the same strategy developed for $[Ru(phen)_2(tpphz)]^{2+}$ to achieve nuclear staining, cells were incubated with the bipyridine-analogous complex **[2.4]** at concentrations 200 μM or greater in serum-free medium. Although a much lower intensity luminescence is observed relative to **[2.3]**, MCF-7 cells incubated with **[2.4]** in these conditions do display nuclear staining (Figure 2.15a). A higher concentration (500 μM) improves the amount of nuclear staining observed (Figure 2.15b) but even under these conditions the intensity of staining is inconsistent, with some cells displaying much more intense staining than others. The reason for this is unclear, but may be due to cell-to-cell variation in uptake activity, perhaps dependent upon cell cycle stage. Co-staining with PI reveals **[2.4]** to be less toxic than **[2.3]**, with cells incubated with the former remaining viable using conditions that led to total cell death when **[2.3]** was used (Figure 2.15b and Figure 2.14a for **[2.4]** and **[2.3]** respectively).

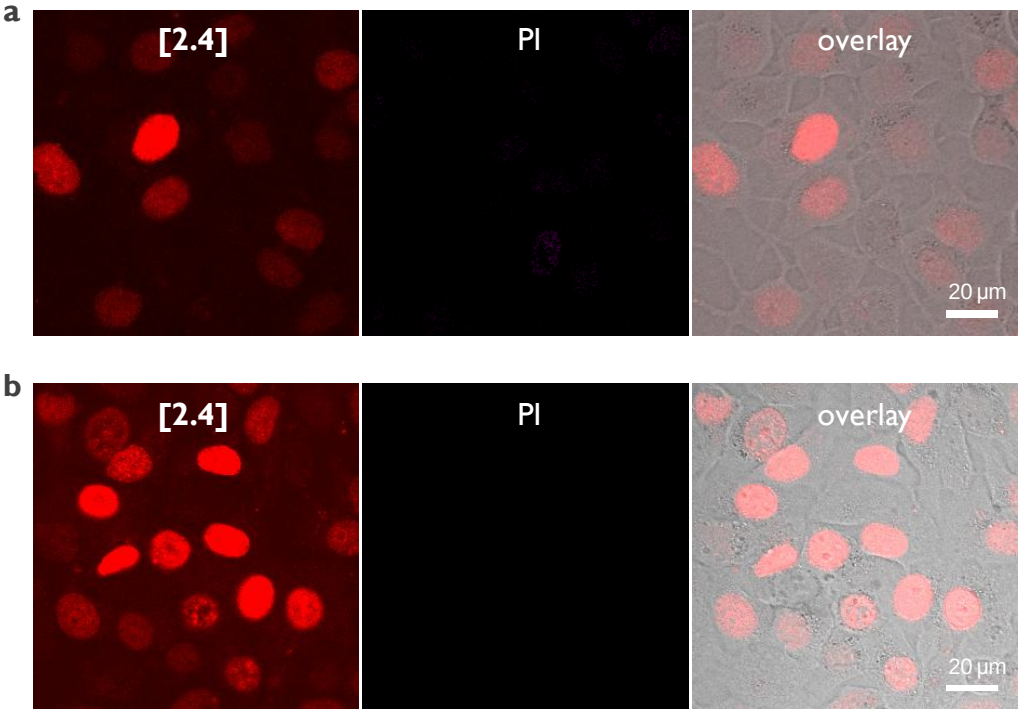

Figure 2.15 CLSM of MCF-7 cells incubated with **[2.4]**. **a,** 200 μM, 1 hr. **b,** 500 μM, 1 hour. From left to right: luminescence emission of **[2.4]** (red), PI (purple), and overlay (including phase contrast) image.

2.5 Fixed cell imaging

Ideally, imaging experiments should involve minimal cell preparation methods so that the natural internal structure that exists within living, functioning cells can be preserved and examined. However, fixing and permeablising cells prior to staining is a commonly used technique for DNA imaging. The great advantage of this procedure is that it allows the use of non membrane-permeable stains and, for example, this can be used to identify DNA damage or cell cycle phase or facilitate the evaluation of properties of a new DNA stain. With this in mind, the ability of each Ru(II) metallo-intercalator to bind to DNA in fixed, membrane-permeablised cells was investigated. The resultant DNA binding was assessed using CLSM, with the same excitation/emission wavelengths parameters used for live cell imaging being employed.

2.5.1 Ru(II)dppz complexes

Experiments on ethanol fixed and membrane-permeablised MCF-7 cells incubated with **[2.1]** or **[2.2]** showed zero luminescence emission (Figure 2.16), despite co-staining with propidium iodide confirming that cells had been rendered membrane-permeable. This was a surprising result considering that each compound is known to bind to DNA with a distinct luminescence signature. Experiments conducted without PI staining also displayed the same behaviour, eliminating the possibility that PI displaces the Ru(II)dppz complexes through competition for binding sites. The PI staining also shows the effect of fixation upon DNA structure, with the heterochromatin staining pattern appearing in a more condensed form around nucleoli than that observed in live cell staining.[17]

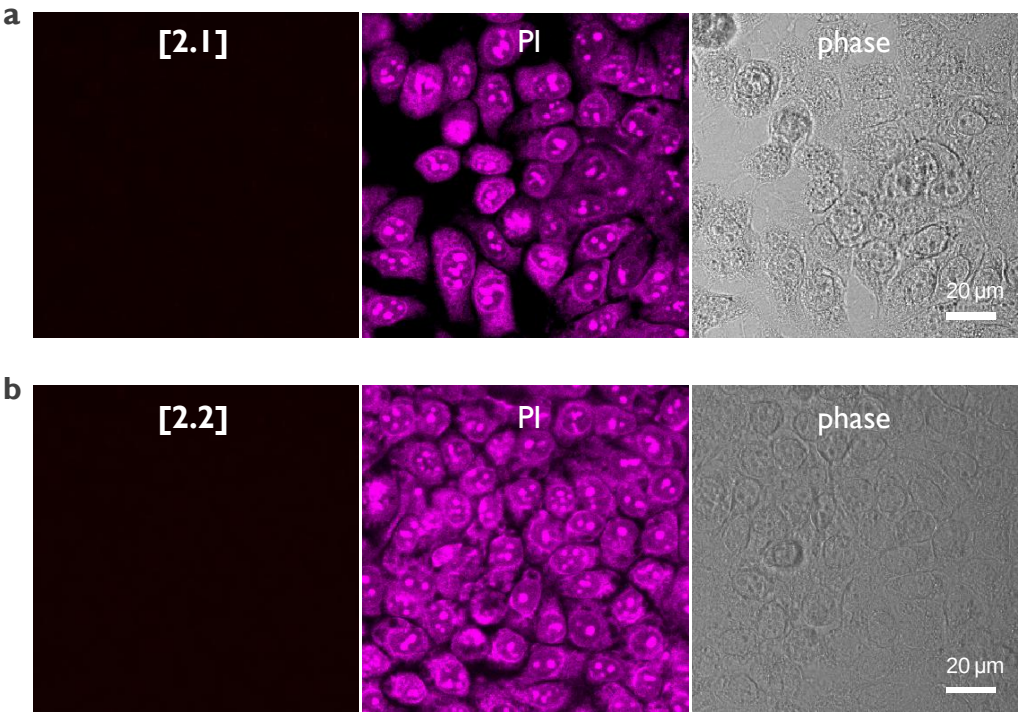

Figure 2.16 CLSM of fixed MCF-7 cells stained with **[2.1]** (a) or **[2.2]** (b) (100 µM, 10 mins). Propidium iodide staining is included as a positive control for membrane-permeablisation. From left to right: luminescence emission of Ru(II)dppz complex (red), PI (purple) and phase contrast image.

2.5.2 Organometallic Ru(II)dppz systems

Given the surprising lack of MLCT luminescence from **[2.1]** or **[2.2]** in fixed and membrane-permeablised cells, two further achiral Ru(II)dppz systems were investigated as DNA stains in fixed cells (Figure 2.17).

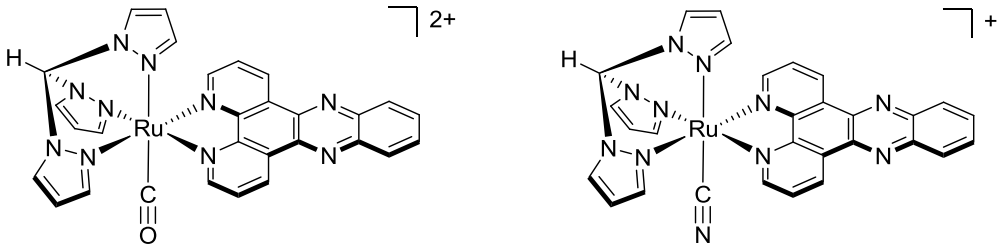

[2.5] **[2.6]**

Figure 2.17 Organometallic $[Ru(tpm)(L)(dppz)]^{n+}$ complexes, with L = CO (n = 2) **[2.5]** or CN^- (n = 1) **[2.6]**.

Synthesised by A. Mlitan, these organometallic complexes contain either carbon monoxide **[2.5]** or cyanide **[2.6]** ligands in the free coordination and were found to bind to DNA *via* intercalation with a characteristic light switch emission.[18] Both complexes emit at a lower wavelength than **[2.1]** and **[2.2]** and so the emission energy was adjusted to 600-650 nm accordingly. As shown in Figure 2.18, there is no luminescence from fixed, permeablised cells from either complex, strongly suggesting that neither complex is intercalated with cellular DNA and in agreement with the results observed for **[2.1]** and **[2.2]**.

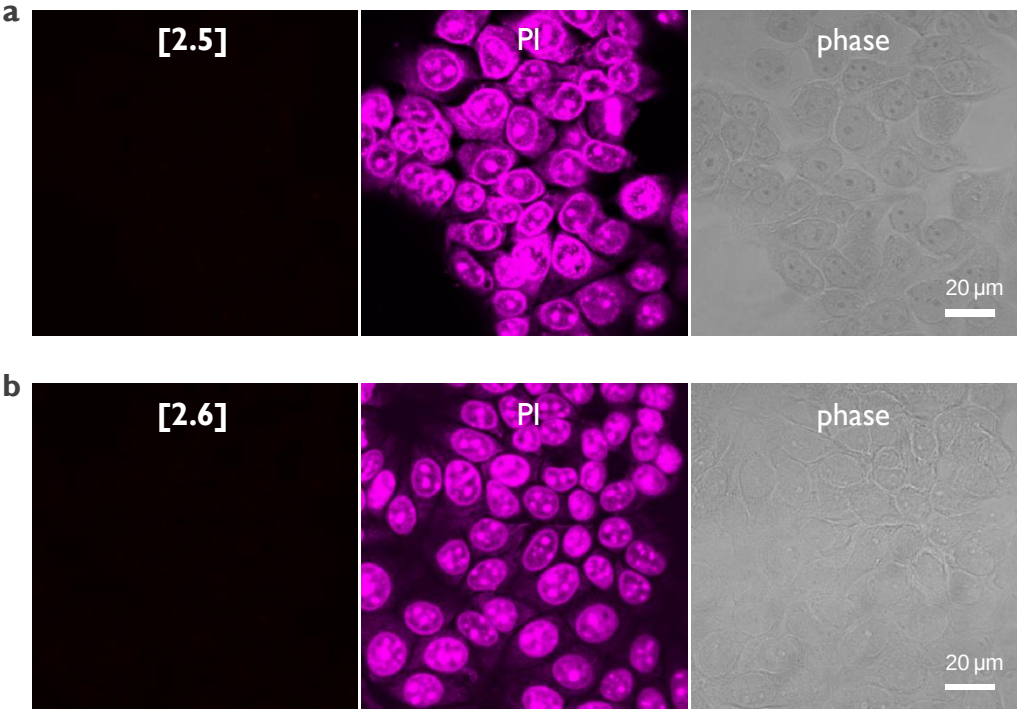

Figure 2.18 CLSM of fixed MCF-7 cells stained with **[2.5]** (a) or **[2.6]** (b) (100 µM, 10 mins). From left to right: luminescence emission of Ru(II)dppz organometallic complex (red), PI (purple) and phase contrast image.

These results indicate that the cellular location of these four Ru(II)dppz complexes is unobservable by CLSM even when the barrier of the cell membrane, and therefore a functional mechanism of cellular uptake, is

removed. The lack of MLCT emission is evidence that Ru(II)dppz complexes are not intercalating with cellular DNA. These experiments are also in agreement with the lack of emission of **[2.2]** observed in dead cells in Section 2.4.1. These experiments illustrate a significant drawback to using CLSM to investigate the cellular uptake of DNA light switch complexes: if there is no luminescence observed in fixed, permeablised cells then the complex clearly does not bind to cellular DNA with an associated light switch emission and therefore CLSM (or other fluorescence-based techniques) cannot be used reliably to investigate the cellular uptake of the molecule.

2.5.3 Ru(II)tpphz complexes

In contrast to Ru(II)dppz complexes, both **[2.3]** and **[2.4]** are excellent DNA stains in fixed cell conditions (Figure 2.19). When the barrier of transport across the cell membrane is eliminated, the luminescence emission of each complex is much brighter than that observed for live cell imaging and both complexes display similar levels of luminescence. This is in agreement with the hypothesis that it is the poorer rate of cellular uptake of **[2.4]** that is responsible for the lower staining observed in live cells in comparison to **[2.3]**.

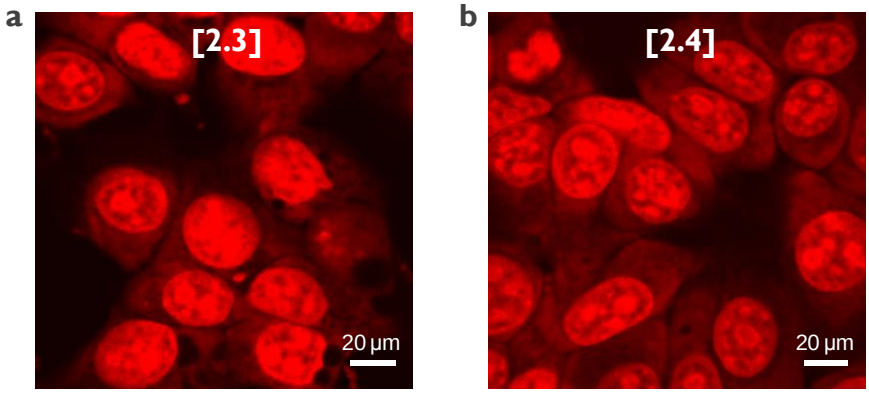

Figure 2.19 CLSM of fixed MCF-7 cells stained with Ru(II)tpphz complexes **[2.3]** (a) and **[2.4]** (b) (100 µM, 10 mins).

The addition of PI indicates that the cells are indeed permeablised and that the Ru(II)tpphz and PI signals show significant overlap, which would indicate that both molecules are bound to nuclear DNA (Figure 2.20). These experiments also demonstrate that Ru(II)tpphz complexes and PI may be used together without overlap of signals or quenching effects, which is a useful property as it allows the two stains to be used together in co-staining experiments. **[2.3]** and **[2.4]** additionally function as positive controls for the Ru(II)dppz experiments, suggesting that it is it is the difference between Ru(II)dppz and Ru(II)tpphz complexes that is responsible for the lack of MLCT luminescence observed for Ru(II)dppz complexes and not experimental error.

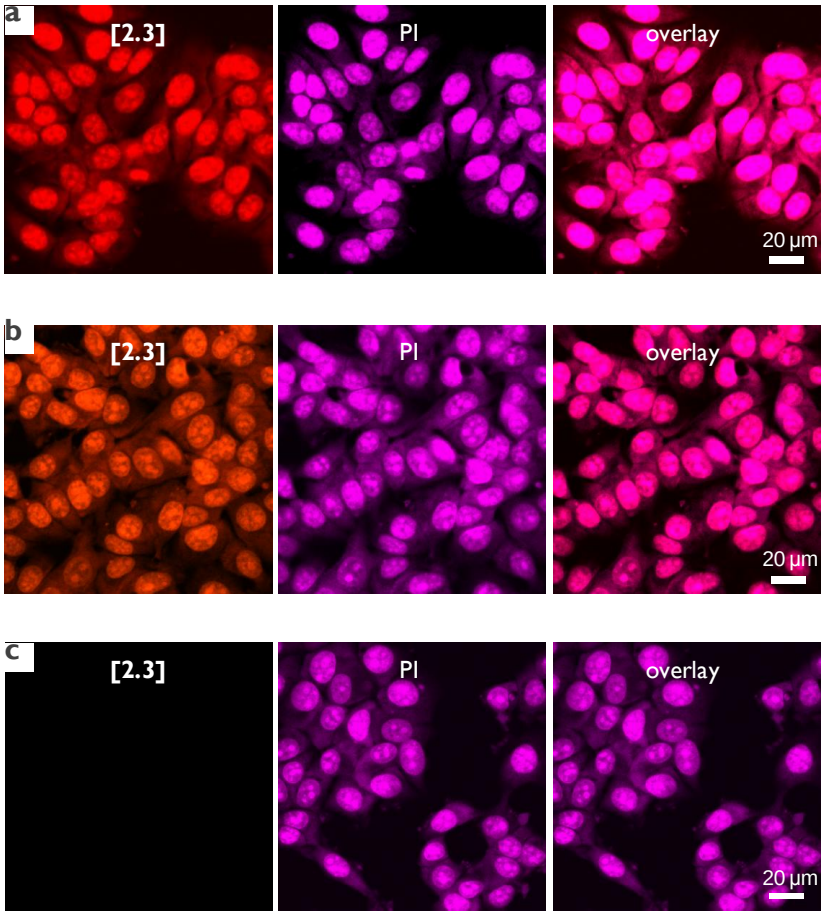

Figure 2.20 CLSM of fixed MCF-7 cells stained with Ru(II)tpphz complexes **[2.3]** (**a**) or **[2.4]** (**b**) (100 µM, 10 mins). From left to right: luminescence emission of Ru(II)tpphz complex (red), PI (purple) and overlay image. **c,** Negative control.

Other evidence that cellular DNA is successfully targeted includes the observation of condensed chromosomes of cells undergoing mitosis. Figure 2.21 shows four distinct phases of mitosis observed through staining by **[2.4]**; prophase, where the chromosomes condense from chromatin; prometaphase, containing highly condensed chromosomes; metaphase, where the chromosomes align themselves at the centre of the mitotic spindle and prepare for separation; anaphase, where the two sets of sister chromosomes break apart into two separate regions which will become two daughter cells after cytokinesis; and telophase, which occurs post-cytokinesis and involves the reversal of prometaphase and metaphase to form nuclei in each daughter cell. This is an example of how fixed cell imaging using luminescent DNA stains can be used to identify cell phase within a sample.

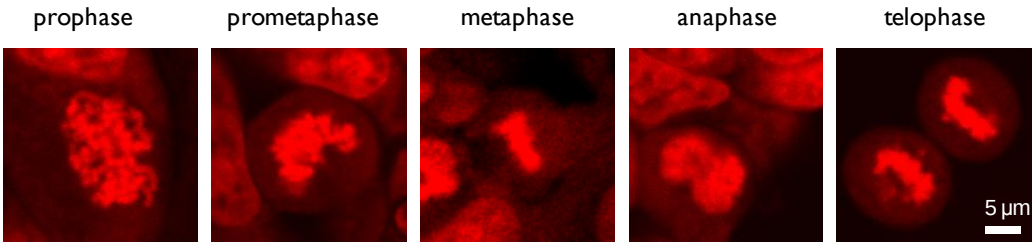

Figure 2.21 A collection of fixed M-phase MCF-7 cells stained by **[2.4]** (100 µM, 10 mins) showing the condensed chromosomes of several stages of mitosis.

These experiments show that Ru(II) metallo-intercalators based on the tpphz intercalating ligand can function as luminescence DNA probes using the MLCT light switch effect in fixed cell imaging applications. This is in contrast to the results in this thesis for complexes based on the dppz intercalating ligand.

2.6 Cellular uptake mechanism

As **[2.3]** and **[2.4]** are polar, positively charged and hydrophilic molecules, they are not predicted to passively permeate cell membranes. This is also suggested by the relatively high micromolar concentrations required for nuclear staining in live cells (200 μM or greater), compared to membrane-permeable dyes such as DAPI, which are employed on the nanomolar scale (typically 200 nM). As luminescence provides an indication of the successful internalisation of each complex, the mechanism of uptake was explored using inhibition treatment and CLSM.

MCF-7 cells incubated with **[2.3]** or **[2.4]** at 4°C resulted in no observable *in cellulo* luminescence in live cells, indicating active transport as the mechanism of cellular uptake for each and confirming neither molecule is membrane-permeable (Figure 2.22).

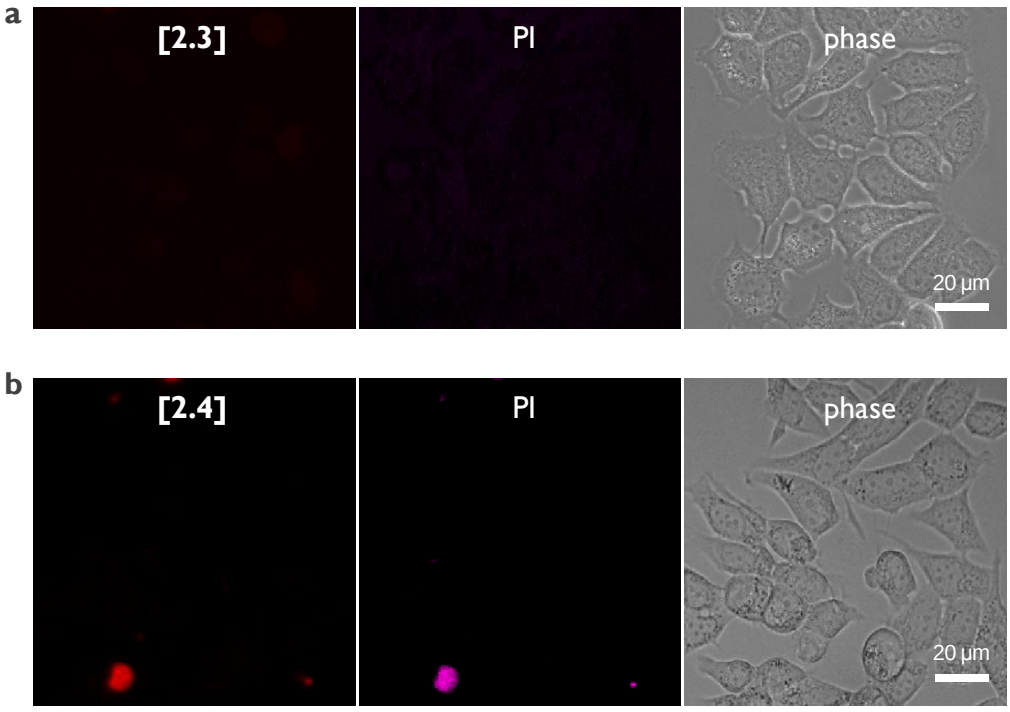

Figure 2.22 CLSM of MCF-7 cells incubated with 200 μM **[2.3]** (**a**) and **[2.4]** (**b**) at 4°C for 1 hr in serum-free media.

As one of the most common methods by which cells internalise membrane-impermeable molecules is endocytosis, this specific mechanism of uptake was briefly examined using an inhibitor of this process.

MCF-7 cells coincubated with **[2.3]** and the endocytosis inhibitor chloroquine, which prevents endosomal release by disturbing the pH balance between endosome and cytosol,[19] clearly demonstrate nuclear uptake (Figure 2.23). Considering the concentration-dependency described in Section 2.4.3.1, and the results observed when the complex was incubated at 4°C, if endocytosis were the main mechanism of uptake then complete inhibition and no staining would be predicted to be observed (as observed in Figure 2.22a). These results would therefore suggest that the main mechanism of uptake does not occur by a receptor-mediated endocytic pathway. However, the toxicity of **[2.3]** combined with inhibitor toxicity (as evident in Figure 2.23a) made further study problematic.

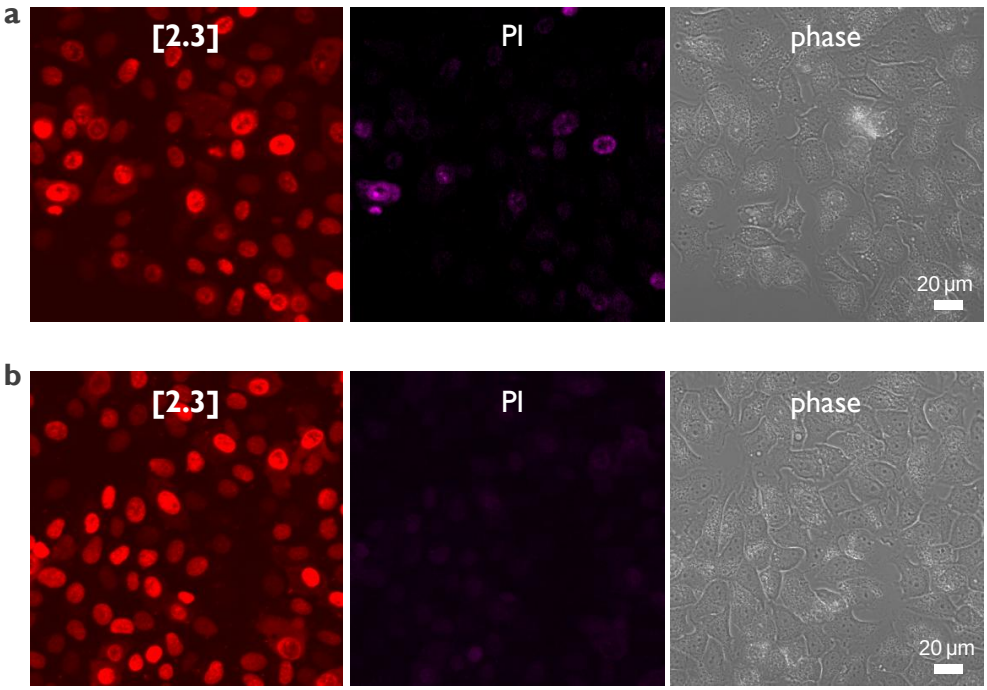

Figure 2.23 a, CLSM of MCF-7 cells coincubated with **[2.3]** (200 µM, 1hr) and endocytosis inhibitor chloroquine (100 µM). **b,** Negative control. PI staining is included to indicate cell viability.

Successful uptake of both these hydrophilic, polar molecules *via* non-passive diffusion means that designing molecules specifically to enhance lipophilicity is not always required for successful cellular internalisation and *in cellulo* DNA binding of metal complexes.

2.7 TEM studies

In addition to these luminescence microscopy studies, which rely on DNA binding and subsequent activation of the MLCT light switch effect to observe the *in cellulo* location of the Ru(II) complex, transmission electron microscopy (TEM) may be employed to examine the cellular distribution of each complex in both live and fixed samples.

TEM involves a sample being exposed to a beam of electrons: regions of high electronic density are able to scatter the electron beam while unscattered electrons pass through the sample and are detected by a fluorescent screen. This effect allows a contrast image of the specimen to be constructed. For biological imaging, ultra-thin cross-sections of cells are prepared and then stained with various staining agents, which usually contain a heavy metal capable of deflecting the electron beam. This enhances contrast and is the phenomenon exploited in the use of reagents such as immunogold labels, ruthenium red and osmium tetroxide. Figure 2.24a shows a cell stained with the lipid stain osmium tetroxide, where the molecule provides internal contrast by staining membranes. As would be predicted, in the absence of any contrast agent, no intracellular detail is observable (Figure 2.24b). Due to the smaller de Broglie wavelength of electrons than light, TEM is a higher resolution technique than light microscopy.

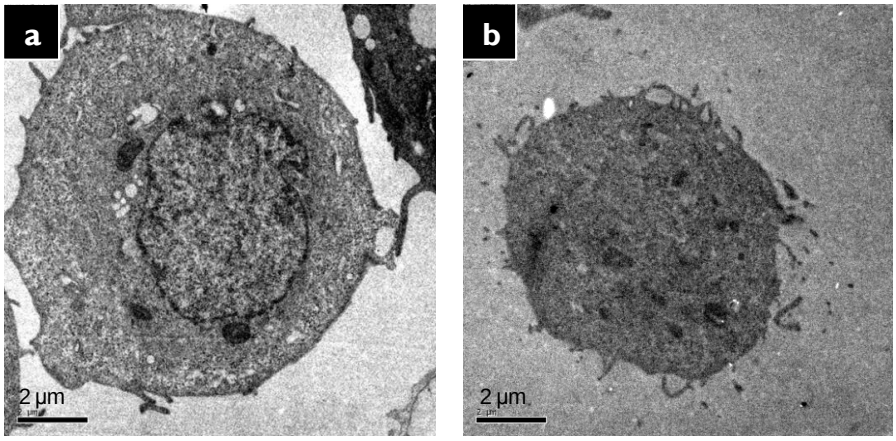

Figure 2.24 a, MCF-7 cell stained with osmium tetroxide. **b,** Negative control cell with no stain present.

Since Ru(II) complexes incorporate a second row transition metal with a high electron density, these complexes can scatter the TEM electron beam; hence the localisation of the Ru(II) complex within cells can be determined through TEM with high spatial resolution. The advantage of this technique over CLSM is that the cellular location of the metallo-intercalator can be observed without the requirement of a specific binding event such as intercalation to activate the light-switch effect.

2.7.1 Ru(II)dppz complexes

When MCF-7 cells are incubated with **[2.2]** using the same procedures used in live cell CLSM studies before preparation for TEM imaging no contrast effects are observable. This strongly suggests that the complex is not internalised by the cells. However, if the cells are fixed and permeablised *before* exposure to **[2.2]**, TEM imaging clearly reveals cellular staining (Figure 2.25). As no other contrast agent was used, the observable contrast effects must therefore be due to **[2.2]**. Figure 2.25 shows that **[2.2]** is distributed throughout the cytosol and clearly located within the nucleus.

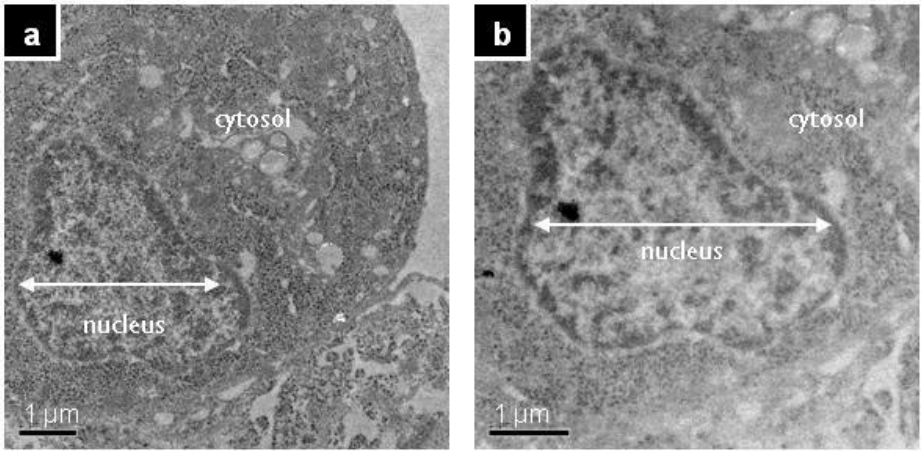

Figure 2.25 TEM micrographs of fixed MCF-7 cells stained with **[2.2]** (100 µM, 10 mins).

As outlined in Section 2.5.1, CLSM studies showed no luminescence using the same conditions and yet TEM studies confirm the complex is indeed within the nucleus. Taken together, these results indicate that Ru(II)dppz systems may bind to cellular DNA through a non-intercalative mode and/or target another nuclear binding site, such as histone proteins. In either case, this suggests that the mode of binding does not shield the phenazine nitrogen atoms of the dppz ligand from water so that the light switch effect is not activated. Although an unexpected result, these observations shed light on a recent study by Puckett and Barton in which related membrane permeable Ru(II)dppz complexes are clearly internalised by cells, yet no

nuclear MLCT luminescence is observed.[13] In a later study by the same group, a Ru(II)dppz complex was tagged with fluorescein and nuclear localisation demonstrated by fluorescein emission but no nuclear staining due to the Ru(II) complex was observed,[20] strongly suggesting that the molecule is not intercalated with cellular DNA. In this context, this work - showing that the two Ru(II)dppz complexes do not interact with nuclear DNA in cells in the manner documented using *in vitro* luminescence titrations - has significant implications as metallo-intercalators containing the dppz moiety have been much studied as putative DNA-binding substrates; if their *in cellulo* properties are different to their behaviour *in vitro,* the development of such systems will be considerably hampered.

2.7.2 Ru(II)tpphz complexes

As shown in Section 2.4, both **[2.3]** and **[2.4]** are taken up by live cells. To further probe the intracellular location of **[2.3]**, cells were incubated as for CLSM studies, and then fixed and examined using TEM. Figure 2.26 shows a MCF-7 cell strongly stained with **[2.3]**, revealing that the complex is evenly distributed throughout the cytosol of the cell. Notably, the nucleus shows strong heterochromatin staining (Figure 2.26a,b), indicating that **[2.3]** possesses a high affinity for densely-packed DNA. Interestingly, the TEM micrographs show contrast signal from mitochondrial regions in addition to nuclear staining (Figure 2.26c), indicating that **[2.3]** is located within these organelles. The CLSM studies showed minimal luminescence from cytosolic regions, including mitochondria, which implies that the complex is not located within a hydrophobic region, such as bound to DNA. This in turn suggests that **[2.3]** is not bound to mitochondrial DNA and that the luminescence is only activated upon delivery of the molecule, and subsequent intercalation, at the DNA-rich nucleus. This could indicate the complex is bound to a non-DNA target (for example, if it were protein-bound) or located within the space that divides the inner and outer membrane of mitochondria.

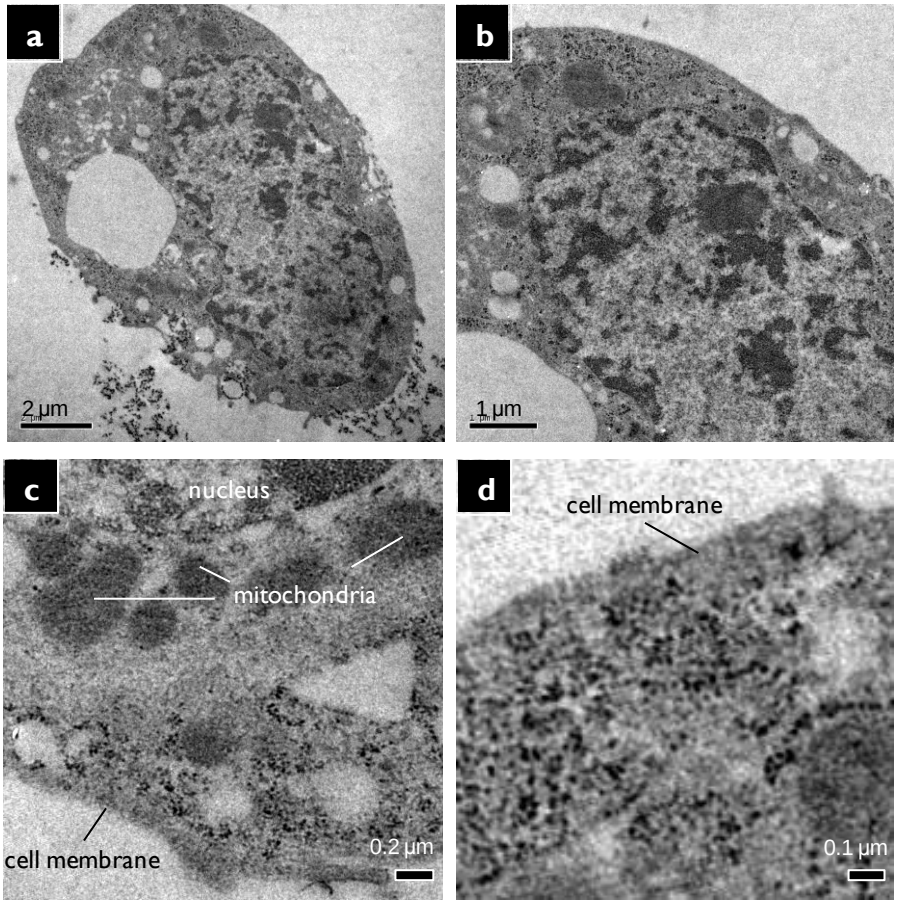

Figure 2.26 TEM micrographs of MCF-7 cells incubated with complex **[2.3]** (200 µM, 1 hr). **a,** Image showing even distribution of the stain throughout the cytosol. **b,** Detailed image of nucleus reveals clear heterochromatin staining. **c, d,** Detailed images revealing intracellular localisation and distinctive granular patterning of the distribution of **[2.3]** within the cytosol.

Furthermore, **[2.3]** can be observed in small, distinct regions of the cytosol (Figure 2.26c,d). High magnification reveals these "dots" to be ~10 nm in diameter (Figure 2.26d) and are localised close to membranes (Figure 2.26c). These dots also display evidence of internal structure, where they are aligned in rows, rather than dispersed randomly. This would suggest a relationship with a component of the cytoskeleton as opposed to the complex bound to free RNA or proteins within the cytosol. One suggestion would be that the dots are macromolecular-bound complex which are being

transported along microtubule networks, however, further work would be required to investigate and develop this hypothesis.

Cells fixed and permeablised *before* incubation with **[2.3]** show a similar distribution to that observed in live cells, although with less well-defined heterochromatin aggregation (Figure 2.27). Again, at high magnification, **[2.3]** can be seen to occupy distinct locations (as ~10 nm "dots") within the cytosol (Figure 2.27c,d).

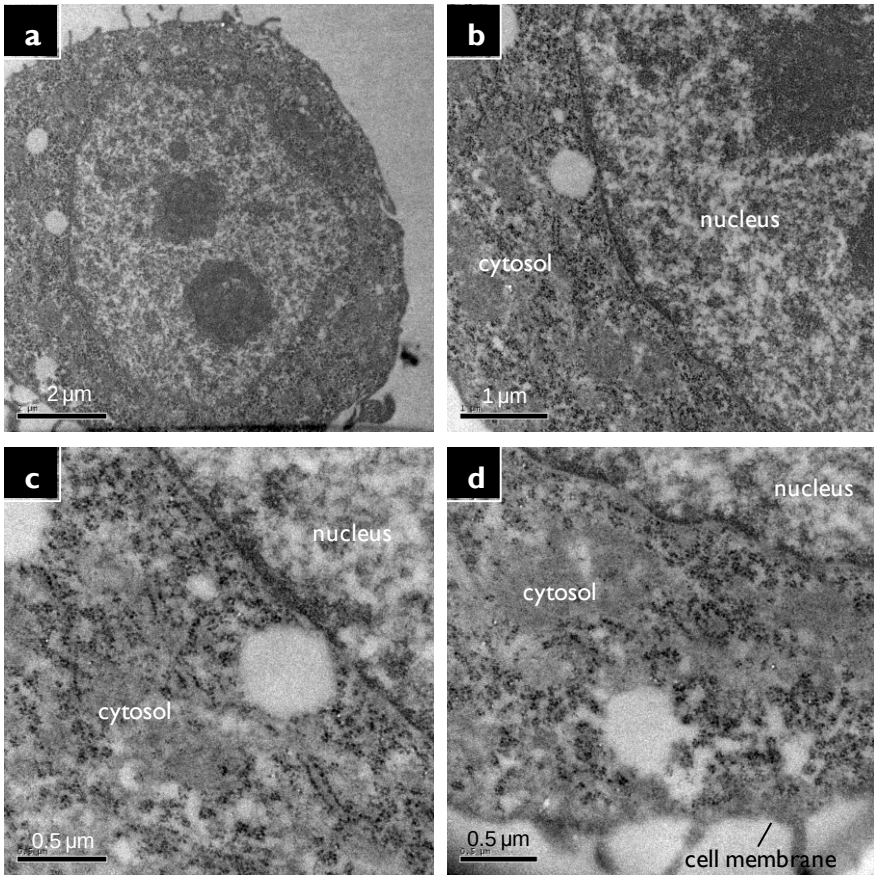

Figure 2.27 TEM micrographs of fixed MCF-7 cells stained with **[2.3]** (100 µM, 10 mins). **a,** Image showing even distribution of the stain throughout the cytosol and nucleoli are observable. **b, c, d,** Images revealing distinctive granular patterning of the distribution of **[2.3]** within the cytosol.

These results make **[2.3]** and **[2.4]** of interest as multifunctional DNA stains for use with both CLSM and TEM, a unique property of DNA-binding metal complexes. These results additionally demonstrate how TEM improves understanding of the intracellular location of the complex: as specific binding event need not occur for visualisation, the Ru(II) complex can be observed directly and at a higher resolution than offered by CLSM.

2.8 Cytotoxicity

2.8.1 MCF-7 cells

As complexes **[2.1]** – **[2.4]** bind to DNA with a high affinity and two of these, **[2.3]** and **[2.4]**, have been shown to target the nucleus upon cellular internalisation, they have potential to interfere with cellular process such as DNA repair, replication and transcription. Indeed, recent research has shown the recently commercialised DNA dye DRAQ5 (®) to adversely affect cellular function, with this intercalating organic molecule inhibiting DNA repair, replication and transcription by modifying the location and mobility properties of several DNA-binding proteins.[21] With this in mind, toxicity towards the MCF-7 human breast cancer cell line was assessed through MTT (3-(4,5-dimethylthiazol-2-yl)-2,5-diphenyltetrazolium bromide) assay and IC_{50} values (the concentration that would induce 50% cell death) thus obtained. The anti-cancer drug cisplatin was employed as a positive control.

As can be seen by Figure 2.28 and Table 2.4, neither **[2.1]** or **[2.2]** demonstrate significant toxicity towards MCF-7 cells over a 24 hour incubation time (IC_{50} values of 190 and >200 μM respectively), with **[2.1]** being the more toxic of the two complexes. In contrast, the anti-cancer drug cisplatin is much more toxic towards the cell line, as reflected by its low IC_{50} value (12 μM). These results are in agreement with the low rate of cellular

uptake, as observed by TEM, of each Ru(II)dppz complex. In contrast to **[2.1]** and **[2.2]**, complexes **[2.3]** and **[2.4]** show IC_{50} values that are more comparable to cisplatin (Figure 2.29 and Table 2.4), with complex **[2.3]** displaying the higher toxicity towards MCF-7 cells (IC_{50} values of 36 and 53 μM for **[2.3]** and **[2.4]** respectively). As the Ru(II)dppz complexes bind to DNA with a higher affinity than the Ru(II)tpphz complexes (Section 2.1), and this work has shown the Ru(II)tpphz complexes to demonstrate the greater rate of cellular uptake (Section 2.4), cytotoxicity therefore correlates more closely with the relative uptake of the complexes and not their overall binding affinity to DNA.

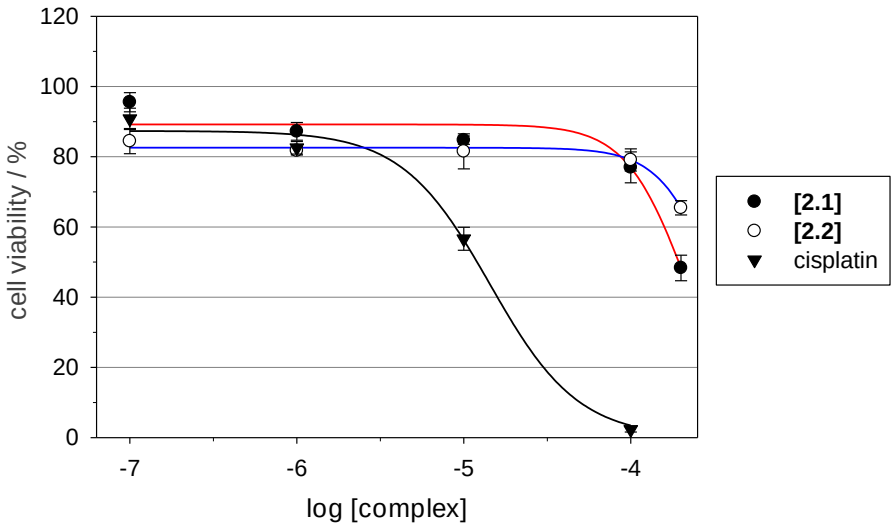

Figure 2.28 Cytotoxicity of Ru(II)dppz complexes **[2.1]** and **[2.2]** towards MCF-7 breast cancer cells (24 hour incubation time).

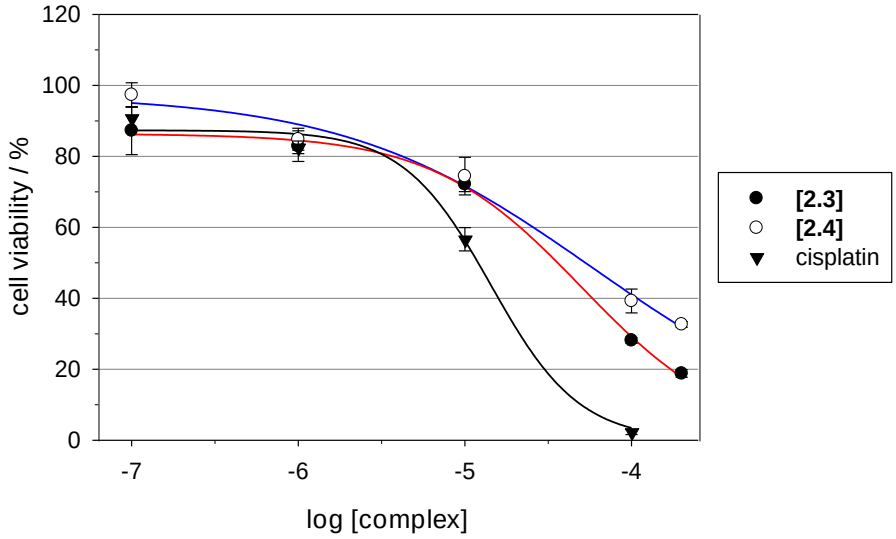

Figure 2.29 Cytotoxicity of Ru(II)tpphz complexes **[2.3]** and **[2.4]** towards MCF-7 breast cancer cells (24 hr incubation time).

Complex	IC_{50} / μM
[2.1]	190 ± 10
[2.2]	>200
[2.3]	36 ± 3
[2.4]	53 ± 7
cisplatin	12 ± 2

Table 2.4 IC_{50} values of Ru(II) metallo-intercalators towards the MCF-7 cell line (24 hour incubation time).

2.8.2 Cisplatin-resistant cancer cells

While cisplatin remains the first step in treating a variety of cancers, including ovarian cancers, acquired drug resistance represents a key challenge in cancer treatment. As the mechanism of DNA-binding by **[2.3]** is different to cisplatin, binding by a reversible mechanism rather than irreversible, this complex offers potential as a lead for a new class of therapeutics. With this in mind, the toxicity of **[2.3]** and **[2.4]** towards A2780 human ovarian cancer cells and the derived cisplatin-resistant A2780-CP70 daughter cell line[22] was investigated (Figure 2.30 and Table 2.5).

It was found that both complexes demonstrate a higher toxicity towards A2780 cells than that observed for MCF-7s, again with **[2.3]** demonstrating a greater toxicity than **[2.4]** (IC_{50} values of 11 and 36 μM respectively) with the IC_{50} value of **[2.3]** equal to that of cisplatin – Figure 2.29 and Table 2.5. Significantly, both **[2.3]** and **[2.4]** retain their cytotoxic potency towards the cisplatin-resistant A2780-CP70 cell line (IC_{50} values of 20 and 47 μM respectively) while, in contrast, cisplatin experiences a decrease in toxicity compared to the cisplatin-sensitive parental A2780 cell line (IC_{50} values of 55 and 12 μM respectively). The IC_{50} values obtained for cisplatin are in agreement with the values reported in the literature.[22]

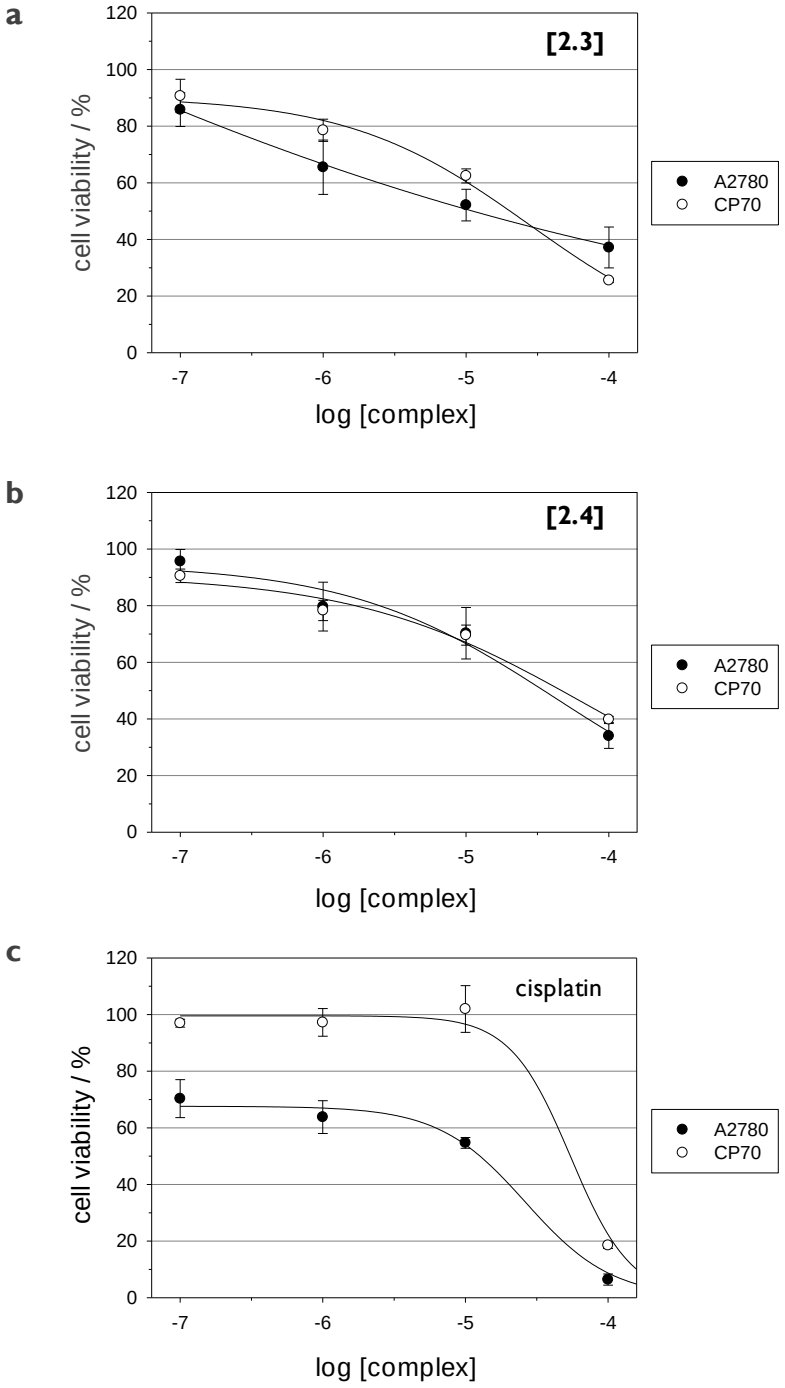

Figure 2.30 Cytotoxicity of Ru(II)tpphz complexes towards cisplatin-resistant cancer. **a, b,** Ru(II) tpphz complexes **[2.3]** (**a**) and **[2.4]** (**b**) show no decrease in toxicity for cisplatin-resistant CP70 ovarian cancer cells compared to parental cisplatin-sensitive A2780 cells. This behaviour is in contrast to cisplatin (**c**).

Complex	IC_{50} / μM	
	A2780	CP70
[2.3]	11 ± 2	20 ± 5
[2.4]	36 ± 6	47 ± 6
cisplatin	12 ± 2	55 ± 8

Table 2.5 IC_{50} values of Ru tpphz complexes and cisplatin towards MCF-7 human breast cancer, A2780 cisplatin-sensitive ovarian cancer and A2780-CP70 cisplatin-resistant ovarian cancer cell lines.

2.9 Conclusions and future work

In this chapter, the cellular DNA binding properties of four Ru(II) metallo-intercalators, containing either dppz or tpphz as the intercalating ligand, in both live and fixed cells were investigated by a combination of CLSM and TEM microscopy while the cytotoxicity towards cancer cell lines was assessed.

In contrast to their *in vitro* DNA binding, it was found that there was no observable *in cellulo* MLCT light switch effect from achiral Ru(II)dppz based systems in either live, non-viable or permeablised (fixed) cells. This is surprising as, even if they are not internalised by healthy cells, it would be expected that each complex would be able to intercalate and luminescence within non-viable and fixed cells. To further investigate the cellular location of Ru(II)dppz complexes, TEM studies on cells incubated before and after fixation, using the Ru(II)dppz complex as a contrast agent, were conducted. These studies revealed that, while there is no uptake in live cells, the complex was clearly located in the nucleus of fixed and permeablised cells.

Considering the absence of a luminescence light switch in fixed and permeablised cells (using CLSM) and evidence of nuclear location for cells treated using the same conditions using TEM, it was concluded that the complex is not intercalated with cellular DNA. These results indicate that the *in cellulo* DNA binding properties of the Ru(II)dppz complexes examined are different to their *in vitro* binding behaviour; this implies that only using CLSM to study the uptake properties of such complexes is not completely reliable.

In contrast to Ru(II)dppz systems, studies on two Ru(II)tpphz systems, $[Ru(bpy)_2(tpphz)]^{2+}$ and $[Ru(phen)_2(tpphz)]^{2+}$, reveals that they are successfully internalised by the MCF-7 cell line, where they function as imaging contrast agents for both CLSM and TEM, a unique property of this class of metal complexes. CLSM and co-localisation studies with the DNA stains DAPI and PI strongly suggests that both complexes bind to nuclear DNA in live and fixed cells. TEM studies clearly show nuclear localisation of both complexes in fixed cells and a strong association with nuclear heterochromatin. Cells incubated with $[Ru(phen)_2(tpphz)]^{2+}$ before fixation show that the complex is uptaken by live cells. TEM imaging reveals that, in addition to the expected nuclear staining, the complex is distributed throughout the cytosol. It was concluded that binding to DNA is responsible for the nuclear luminescence observable by CLSM and the emission energies are in agreement with an intercalative mode of binding.

Using CLSM in conjunction with inhibition treatment, the cellular uptake mechanism for each Ru(II)tpphz complex was shown to be *via* active transport, in agreement with the hydrophilicity of each complex, and a non-endocytic pathway was suggested as part of these uptake studies. It was found that the complex incorporating phen ancillary ligands display a greater rate of cellular uptake compared to the bpy-based complex, possibly

as a result of a molecule-specific binding event occurring during the uptake pathway.

Cell viability studies and IC_{50} values, summarised in Table 2.6, show that both Ru(II)tpphz complexes display a significantly higher toxicity than the Ru(II)dppz complexes towards MCF-7 cells, reflecting their more efficient cellular uptake and live cell DNA binding properties. As shown by the compiled IC_{50} values, the phen complex displays a greater toxicity than the bpy complex, again suggesting that uptake of the complex is responsible for the observed toxicity. The Ru(II)tpphz complexes display cytotoxicity comparable to cisplatin and furthermore they retain toxicity against cisplatin-resistant tumour cells, thus signifying the potential of these complexes as dual function imaging/therapeutic agents.

Complex	log P	IC_{50} / μM		
		MCF-7	A2780	CP70
[2.1]	-1.19	190 ± 10	-	-
[2.2]	-0.74	>200	-	-
[2.3]	-1.24	36 ± 3	11 ± 6	20 ± 5
[2.4]	-2.08	53 ± 7	36 ± 6	47 ± 6
cisplatin	-2.53*	12 ± 2	12 ± 2	55 ± 8

Table 2.6 Compiled octanol/water partition coefficient and IC_{50} values of Ru(II) metallo-intercalators towards the MCF-7, A2780 and CP70 cancer cell lines (24 hour incubation time). *Value obtained from Screnci *et al.*[23]

Metallo-intercalators, especially those containing the dppz moiety, have been subject to a large amount of research into their DNA-binding properties, and so these results are of significance to the development of metallo-intercalators in intracellular applications, specifically showing that Ru(II)tpphz systems hold much greater potential than Ru(II)dppz systems for both imaging and therapeutic applications.

The cytotoxicity properties of **[2.3]** and **[2.4]** are of great interest, particularly those of **[2.3]**. This complex, and further derivatives based on the tpphz intercalating ligand, offer great potential as leads for the development of a new class of multifunctional anti-cancer chemotherapy drug. Future work in this area will investigate the toxicity of **[2.3]** and **[2.4]** on a wider range of cancer cell lines. As both Ru(II)tpphz complexes bind to DNA *via* a different mechanism than platinum-based drugs, it seems that the mode of action is also different. To further investigate this hypothesis, studies into the mechanism of toxicity will be conducted. A starting point would be to establish if **[2.3]** induces apoptosis by using commercially available apoptosis staining kits, and further assessing the toxicity by cell counting techniques. Of additional interest is the ability of this class of Ru(II) complexes to generate singlet oxygen, a potent cytotoxic agent.[24] With this in mind, the phototoxicity of **[2.3]** would be examined and it would be hoped that toxicity would increase with exposure to light, a concept which would be of relevance to photodynamic therapy (PDT).

Since the uptake mechanism also proved to be an undetermined form of active transport, further work to establish the exact mechanism could prove useful in the development of cancer specific therapeutics and also provide a probe for the identified transport mechanism. In particular, the flexible substituent chemistry of these complexes allows the synthesis of many Ru(II)tpphz derivatives allowing modulation of the DNA binding,

photochemical, cellular uptake and toxicity properties of the complexes by ancillary ligand substitution. Thus, a series of dual imaging/therapeutic molecules active against a wide range of cancers may be developed.

2.10 References

1. A. E. Friedman, J. C. Chambron, J. P. Sauvage, N. J. Turro and J. K. Barton, A molecular light switch for DNA: $Ru(bpy)_2(dppz)^{2+}$, *J. Am. Chem. Soc.*, 1990, **112**, 4960-4962.
2. Y. Jenkins, A. E. Friedman, N. J. Turro and J. K. Barton, Characterization of dipyridophenazine complexes of ruthenium(II): The light switch effect as a function of nucleic acid sequence and conformation, *Biochemistry*, 1992, **31**, 10809-10816.
3. C. Metcalfe, H. Adams, I. Haq and J. A. Thomas, A ruthenium dipyridophenazine complex that binds preferentially to GC sequences, *Chem. Commun.*, 2003, 1152-1153.
4. P. Waywell, V. Gonzalez, M. R. Gill, H. Adams, A. J. H. Meijer, M. P. Williamson and J. A. Thomas, Structure of the Complex of $[Ru(tpm)(dppz)py]^{2+}$ with a B-DNA Oligonucleotide - A Single-Substituent Binding Switch for a Metallo-Intercalator, *Chem. Eur. J.*, 2010, **16**, 2407-2417.
5. S. A. Tysoe, R. Kopelman and D. Schelzig, Flipping the Molecular Light Switch Off: Formation of DNA-Bound Heterobimetallic Complexes Using $Ru(bpy)_2tpphz^{2+}$ and Transition Metal Ions, *Inorg. Chem.*, 1999, **38**, 5196-5197.
6. Y. Liu, A. Chouai, N. N. Degtyareva, D. A. Lutterman, K. R. Dunbar and C. Turro, Chemical Control of the DNA Light Switch: Cycling the Switch ON and OFF, *J. Am. Chem. Soc.*, 2005, **127**, 10796-10797.
7. H. Derrat, MPhil Thesis, University of Sheffield, 2009.
8. D. L. Reger, T. C. Grattan, K. J. Brown, C. A. Little, J. J. S. Lamba, A. L. Rheingold and R. D. Sommer, Syntheses of tris(pyrazolyl)methane ligands and $\{[tris(pyrazolyl)methane]Mn(CO)_3\}SO_3CF_3$ complexes: comparison of ligand donor properties, *J. Organomet. Chem.*, 2000, **607**, 120-128.

9. W. Paw and R. Eisenberg, Synthesis, Characterization, and Spectroscopy of Dipyridocatecholate Complexes of Platinum, *Inorg. Chem.*, 1997, **36**, 2287-2293.
10. A. Llobet, P. Doppelt and T. J. Meyer, Redox Properties of Aqua Complexes of Ruthenium(II) Containing the Tridentate Ligands 2,2':6',2"-Terpyridine and Tris(1-pyrazolyl)methane, *Inorg. Chem.*, 1988, **27**, 514-520.
11. J. Bolger, A. Gourdon, E. Ishow and J.-P. Launay, Mononuclear and Binuclear Tetrapyrido [3.2-a: 2', 3'-c: 3", 2"-h: 2"', 3"'-j] phenazine (tpphz) Ruthenium and Osmium Complexes, *Inorg. Chem.*, 1996, **35**, 2937-2944.
12. C. A. Lipinski, F. Lombardo, B. W. Dominy and P. J. Feeney, Experimental and computational approaches to estimate solubility and permeability in drug discovery and development settings, *Adv. Drug Delivery Rev.*, 2001, **46**, 3-26.
13. C. A. Puckett and J. K. Barton, Methods to Explore Cellular Uptake of Ruthenium Complexes, *J. Am. Chem. Soc.*, 2007, **129**, 46-47.
14. www.molinspiration.com
15. C. Mailaender, N. Reiling, H. Engelhardt, S. Bossmann, S. Ehlers and M. Niederweis, The MspA porin promotes growth and increases antibiotic susceptibility of both Mycobacterium bovis BCG and Mycobacterium tuberculosis, *Microbiology*, 2004, **150**, 853-864.
16. C. A. Puckett and J. K. Barton, Targeting a ruthenium complex to the nucleus with short peptides, *Bioorg. Med. Chem.*, 2010, **18**, 3564-3569.
17. C. Feijoo, C. Hall-Jackson, R. Wu, D. Jenkins, J. Leitch, D. M. Gilbert and C. Smythe, Activation of mammalian Chk1 during DNA replication arrest, *J. Cell Biol.*, 2001, **154**, 913-924.
18. A. Mlitan, MPhil Thesis, University of Sheffield, 2009
19. R. Wattiaux, N. Laurent, S. Wattiaux-De Coninck and M. Jadot, Endosomes, lysosomes: their implication in gene transfer, *Adv. Drug Delivery Rev.*, 2000, **41**, 201-208.
20. C. A. Puckett and J. K. Barton, Fluorescein Redirects a Ruthenium-Octaarginine Conjugate to the Nucleus, *J. Am. Chem. Soc.*, 2009, **131**, 8738-8739.
21. P.-O. Mari, V. Verbiest, S. Sabbioneda, A. M. Gourdin, N. Wijgers, C. Dinant, A. R. Lehmann, W. Vermeulen and G. Giglia-Mari, Influence of the live cell DNA marker DRAQ5 on chromatin-associated processes, *DNA Repair*, 2010, **9**, 848-855.

22. R. J. Parker, J. A. Vionnet, F. Bostick-Bruton and E. Reed, Ormaplatin sensitivity/resistance in human ovarian cancer cells made resistant to cisplatin, *Cancer Res.*, 1993, **53**, 242-247.

23. D. Screnci, M. J. McKeage, P. Galettis, T. W. Hambley, B. D. Palmer and B. C. Baguley, Relationships between hydrophobicity, reactivity, accumulation and peripheral nerve toxicity of a series of platinum drugs, *Br. J. Cancer*, 2000, **82**, 966-972.

24. K. E. Erkkila, D. T. Odom and J. K. Barton, Recognition and Reaction of Metallointercalators with DNA, *Chem. Rev.*, 1999, **99**, 2777-2796.

Chapter 3

Dinuclear Ru(II)tpphz complexes

Results within this chapter have been published as:

M. R. Gill, J. Garcia-Lara, S. J. Foster, C. Smythe, G. Battaglia and J. A. Thomas, A ruthenium(II) polypyridyl complex for direct imaging of DNA structure in living cells, *Nat. Chem.*, **2009**, *1*, 662-667.

The full paper is included in the Appendix.

3.1 Introduction

In the previous chapter, mononuclear Ru(II)tpphz intercalating systems were found to display cellular uptake and to stain the nuclear DNA of living and fixed cells. To build upon the success of these complexes, the two dinuclear Ru(II)tpphz systems $[\{Ru(phen)_2\}_2(tpphz)]^{4+}$ **[3.1]** and $[\{Ru(bpy)_2\}_2(tpphz)]^{4+}$ **[3.2]** (Figure 3.1), which contain the tpphz ligand as a ditopic linker for two Ru(II) centres, were synthesised and the *in cellulo* DNA-binding properties examined using a combination of CLSM and TEM by the methodology developed in Chapter 2.

Previous work conducted by the Thomas group has demonstrated both **[3.1]** and **[3.2]** to bind to duplex DNA with a higher affinity than any mono-intercalating complex (K_b = 1.1×10^7 and 3.3×10^8 M^{-1} for **[3.1]** and **[3.2]** respectively) and additionally displayed a high affinity for G3 quadruplex DNA (K_b = 4.4×10^6 and K_b = 9.6×10^6 M^{-1} for **[3.1]** and **[3.2]** respectively).[1]

The light-switch effect was observed with both forms of DNA upon MLCT excitation with a large luminescence enhancement (>60 times) and, intriguingly, binding to quadruplex results in blue-shifted emission and greater emission lifetime compared to duplex binding (Figure 3.2a). This indicates that the complex has the potential to discriminate between different DNA structures spectroscopically.

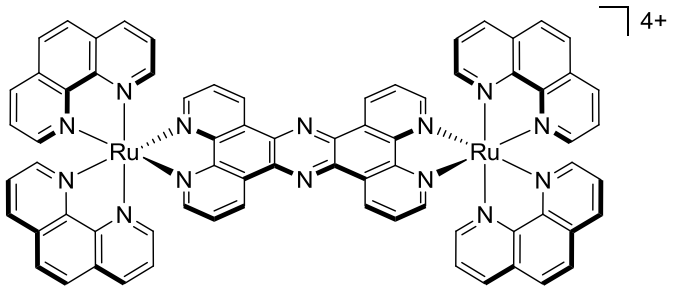

[3.1]

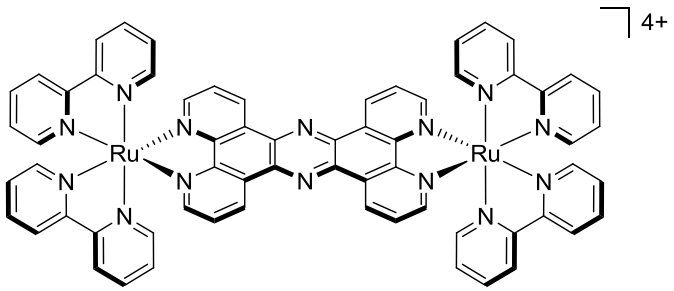

[3.2]

Figure 3.1 Dinuclear Ru(II)tpphz complexes, with either phen **[3.1]** or bpy **[3.2]** as the ancillary ligands.

While it was initially thought that these complexes bind to duplex DNA by intercalation,[1] a later study by C. Turro *et al.* demonstrated that **[3.2]** does not intercalate but binds to DNA *via* groove binding.[2] These results therefore confirm earlier studies that intercalation is not a requirement for light-switch behaviour.[3] Based upon these findings, the same mode of binding would be predicted for **[3.1]** due to the structural similarity of the two complexes.

As **[3.1]** and **[3.2]** each contain two chiral Ru(II) metal centres, three stereoisomers of each complex exist: ΛΔ (meso), ΛΛ and ΔΔ. 2D NMR binding studies on the resolved stereoisomers have provided evidence that the primary binding mode of these complexes to quadruplex DNA is by end stacking, with the central tpphz ligand of the complex bound to both the lateral and diagonal loop ends of the quadruplex structure (Figure 3.2b).[4] The high affinity for quadruplex DNA is of particular interest as small molecules able to induce/stabilise this non-duplex form of DNA hold particular attraction as a molecular target for new anti-cancer therapeutics, as previously discussed in Section 1.2.3.

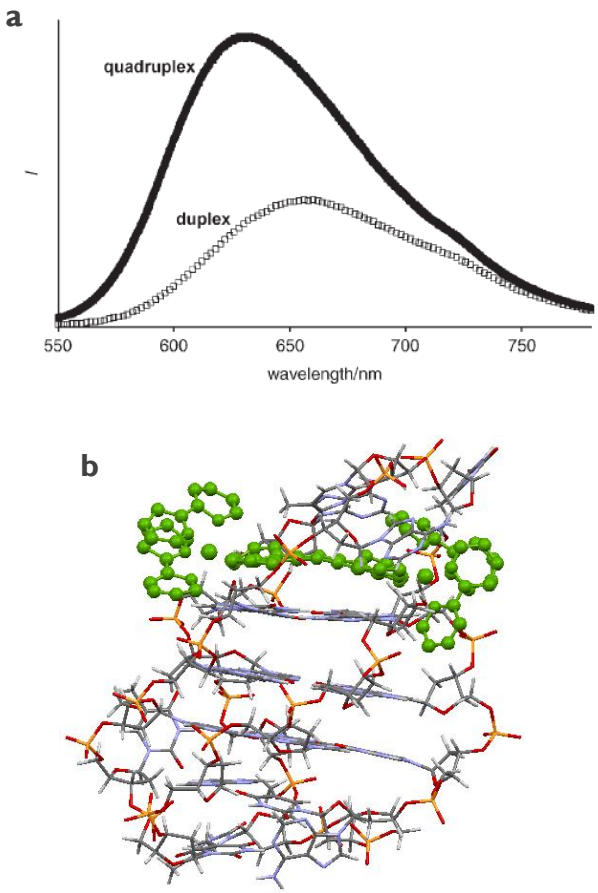

Figure 3.2 a, Luminescence emission for **[3.2]** when bound to duplex and quadruplex forms of DNA.[1] **b,** Structural model from 2D NMR binding studies of **[3.2]** bound to quadruplex DNA.[4]

3.2 Synthesis

3.2.1 Ligand synthesis

The tpphz ligand was synthesised by a method described by Bolger *et al.* (Scheme 3.1).[5]

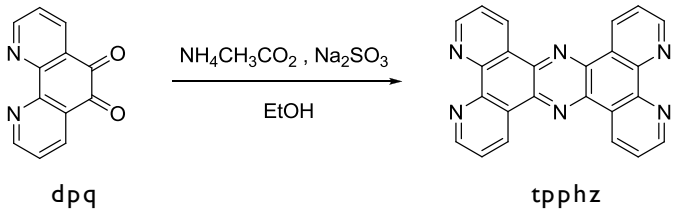

Scheme 3.1 Synthesis of tpphz ligand (yield = 34 %).

3.2.2 Complex synthesis

The two precursor complexes $Ru(phen)_2Cl_2$ and $Ru(bpy)_2Cl_2$ were prepared as described by Sullivan *et al.* (Scheme 3.2a).[6] They were then reacted with tpphz to produce the final products $[\{Ru(phen)_2\}_2(tpphz)]^{4+}$ **[3.1]** and $[\{Ru(bpy)_2\}_2(tpphz)]^{4+}$ **[3.2]** , shown by Scheme 3.2b.[1, 5]

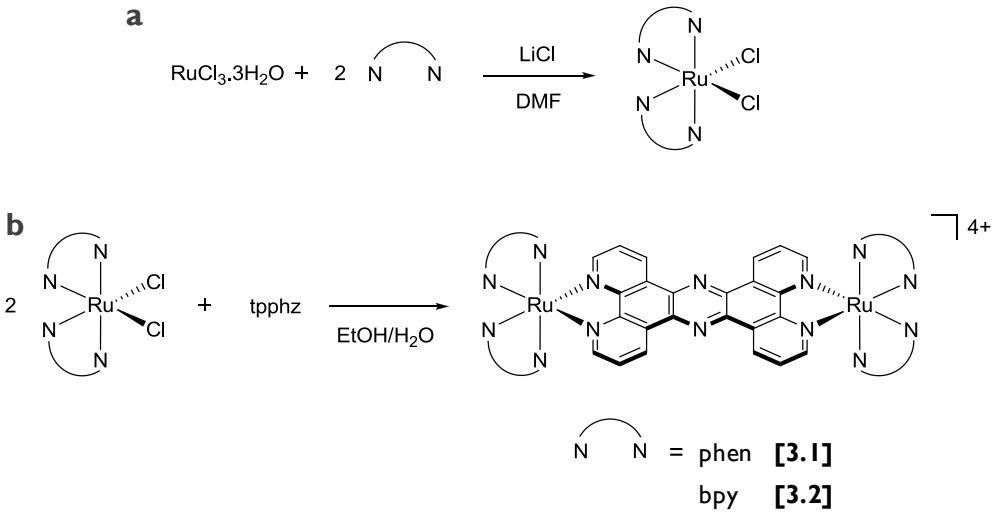

Scheme 3.2 a, Synthesis of [Ru(N^N)Cl2] precursors (yields ranged from 61 - 82 %). **b,** Synthesis of **[3.1]** and **[3.2]** (yields ranged from 64 – 85 %).

Both complexes were synthesised as their hexafluorophosphate salts and characterised by NMR and mass spectroscopy. They were converted into their water-soluble chloride salts by counter-ion metathesis using acetone solutions of tetrabuylammonium chloride. Each complex was used as a mixture of stereoisomers.

3.3 Partition coefficients

The octanol/water partition coefficients of **[3.1]** and **[3.2]** were measured using the "shake flask" method and the results are displayed in Table 3.1. The mass of each complex, excluding the counter-ion, is included to provide a measure of the relative size of each complex. The partition coefficients for the analogous mononuclear complexes $[Ru(phen)_2(tpphz)]^{2+}$ **[2.3]** and $[Ru(bpy)_2(tpphz)]^{2+}$ **[2.4],** as recorded in Chapter 2, are included for comparison.

Complex		Mass / Da	log P
$[\{Ru(phen)_2\}_2(tpphz)]^{4+}$	**[3.1]**	1308	-0.96 ± 0.09
$[\{Ru(bpy)_2\}_2(tpphz)]^{4+}$	**[3.2]**	1212	-1.61 ± 0.10
$[Ru(phen)_2(tpphz)]^{2+}$	**[2.3]**	846	-1.24 ± 0.12
$[Ru(bpy)_2(tpphz)]^{2+}$	**[2.4]**	798	-2.08 ± 0.15

Table 3.1 Measured octanol/water partition coefficients for **[3.1]** and **[3.2]**. The data for the analogous monometallic complexes **[2.3]** and **[2.4]** from Chapter 2 are included for comparison.

As shown by the log P values in Table 3.1, both **[3.1]** and **[3.2]** are hydrophilic molecules, with **[3.2]** the more hydrophilic of the two complexes. This is due to phen being a more hydrophobic ligand than bpy (log P = 1.44 and 1.90 for bpy and phen respectively[7]) as it has a greater aromatic surface area.

Even though **[3.1]** and **[3.2]** each possess a formal 4+ charge, both complexes are more hydrophobic than their respective monometallic 2+ complexes **[2.3]** and **[2.4]**. The presence of the second Ru(II) centre for the dinuclear complexes decreases overall hydrophilicity as the tpphz ligand is now ditopic, increasing hydrophobicity as there are no uncoordinated nitrogen atoms available for hydrogen-bonding, and further hydrophobicity is provided by the two additional ancillary ligands. These two effects counteract the increase in charge, resulting in each dinculear complex displaying a greater hydrophobicity than the respective mononuclear analogue.

Similarly to the complexes in Chapter 2, it would not be predicted that either **[3.1]** or **[3.2]** would be able to diffuse across the cell membrane as both are large, polar and hydrophilic molecules.

3.4 Live cell uptake and imaging

To examine the cellular uptake of the complexes MCF-7 cells were incubated with solutions of **[3.1]** and **[3.2]** and then imaged using CLSM. The excitation wavelength used was 458 nm and the emission measured at 670-700 nm (Stokes shift >212 nm), corresponding to the previously observed

MLCT luminescent "light switch" effect of each complex binding to DNA *in vitro*.[1]

MCF-7 cells incubated for 24 hrs with 100 μM of **[3.1]** or **[3.2]** displayed low levels of MLCT luminescence (Figure 3.3). The cellular location of the observed luminescence is clearly not from the nuclei of cells and these results are similar to the equivalent experiments for **[2.3]** and **[2.4]** (Section 2.4.2).

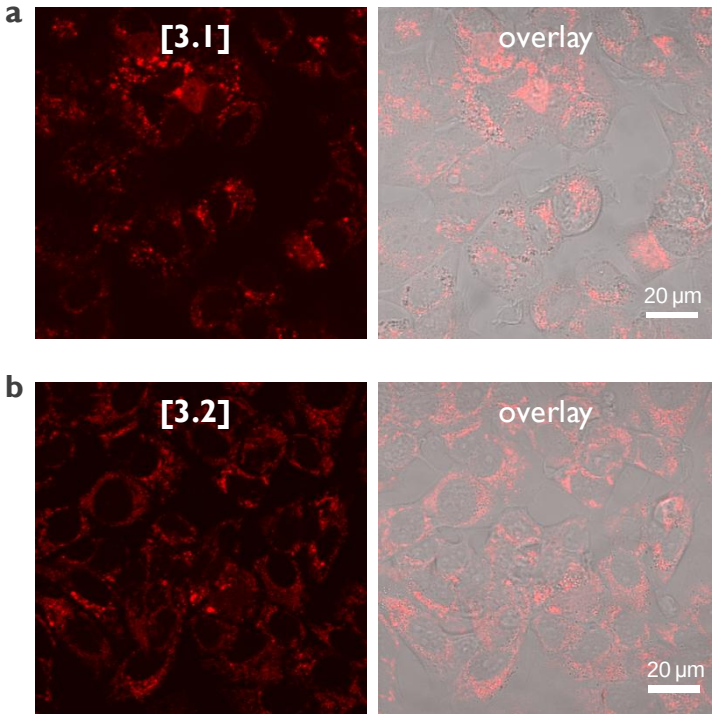

Figure 3.3 CLSM images of MCF-7 cells incubated with dinuclear Ru(II)tpphz complexes **[3.1]** (**a**) or **[3.2]** (**b**) (100 μM, 24 hrs). Left: Ru(II) emission. Right: Overlay image of Ru(II) emission and phase contrast.

3.4.1 $[\{Ru(phen)_2\}_2(tpphz)]^{4+}$

Chapter 2 showed how an increase in concentration along with incubation in serum-free media can result in nuclear staining in a short incubation time by the active molecule so, accordingly, MCF-7 cells were incubated with **[3.1]** at concentrations 200 μM or greater and without the presence of serum in the incubation media, with the aim of improving cellular uptake and nuclear staining by the complex.

3.4.1.1 Effects of serum and concentration

As shown by Figure 3.4, when the concentration is increased to 200 μM and serum-free conditions are employed low levels of nuclear staining by **[3.1]** are now observable.

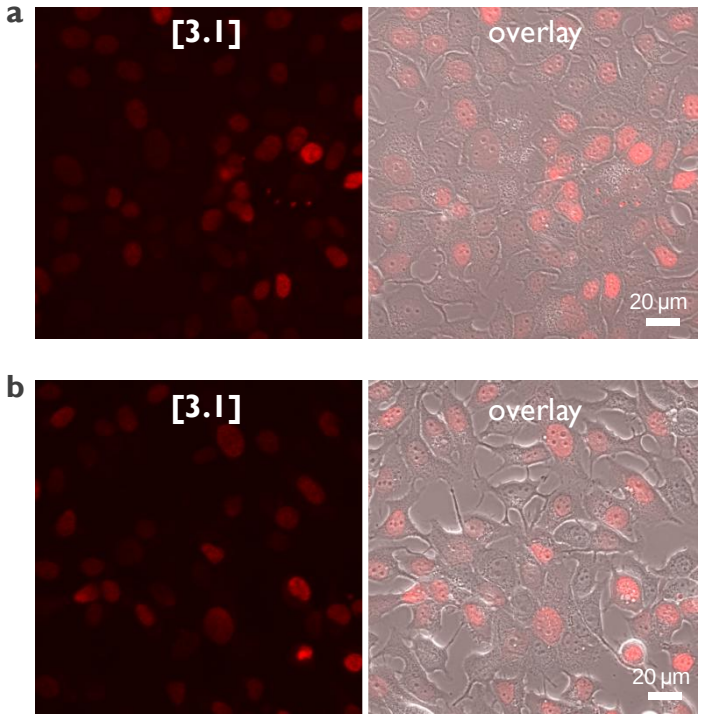

Figure 3.4 CLSM of MCF-7 cells incubated with 200 μM **[3.1]** in serum-free media for 1 hr (**a**) or 3 hrs (**b**). Left: **[3.1]** emission (red). Right: Overlay image of Ru(II) emission and phase contrast.

The luminescence intensity is much lower than that observed for the equivalent experiments for **[2.3]** (Section 2.4.3.1). As both complexes display a comparable increase in luminescence with the addition of DNA and similar binding affinities,[1, 8] this is therefore most likely due to a poorer rate of cellular uptake (resulting in a reduced nuclear accumulation) of **[3.1]** in comparison to **[2.3]**. As **[3.1]** is more hydrophobic than **[2.3]**, this effect therefore is not solely an effect of hydrophilicity – factors such as the higher charge and greater steric bulk of the molecule could well be responsible for the decreased uptake in comparison to **[2.3]**.

To attempt to further increase the uptake and improve the nuclear accumulation of **[3.1]**, the incubation concentration was increased to 500 μM and, as Figure 3.5 shows, at this high concentration there is now strong nuclear staining observable in MCF-7 cells. The emission at 670-700 nm corresponds to activation of the well-documented "light switch" effect upon reversible binding to DNA. This high incubation concentration does not compromise cell viability, as shown by the positive SYTO 9 and negative PI staining.

When cells were incubated with 500 μM **[3.1]** for 1 hr in either serum-containing or serum-free media the effect of serum inhibiting uptake is apparent (Figure 3.5 and Table 3.2). This effect was also observed for **[2.3]** although serum inhibition is more pronounced for **[3.1]**. These effects would be in agreement with an overall poorer rate of cellular uptake of the dinuclear complex compared to its mononuclear analogue and these results further establish the use of serum-free media in conjunction with a high incubation concentration as a successful strategy to attain nuclear localisation of Ru(II) complexes.

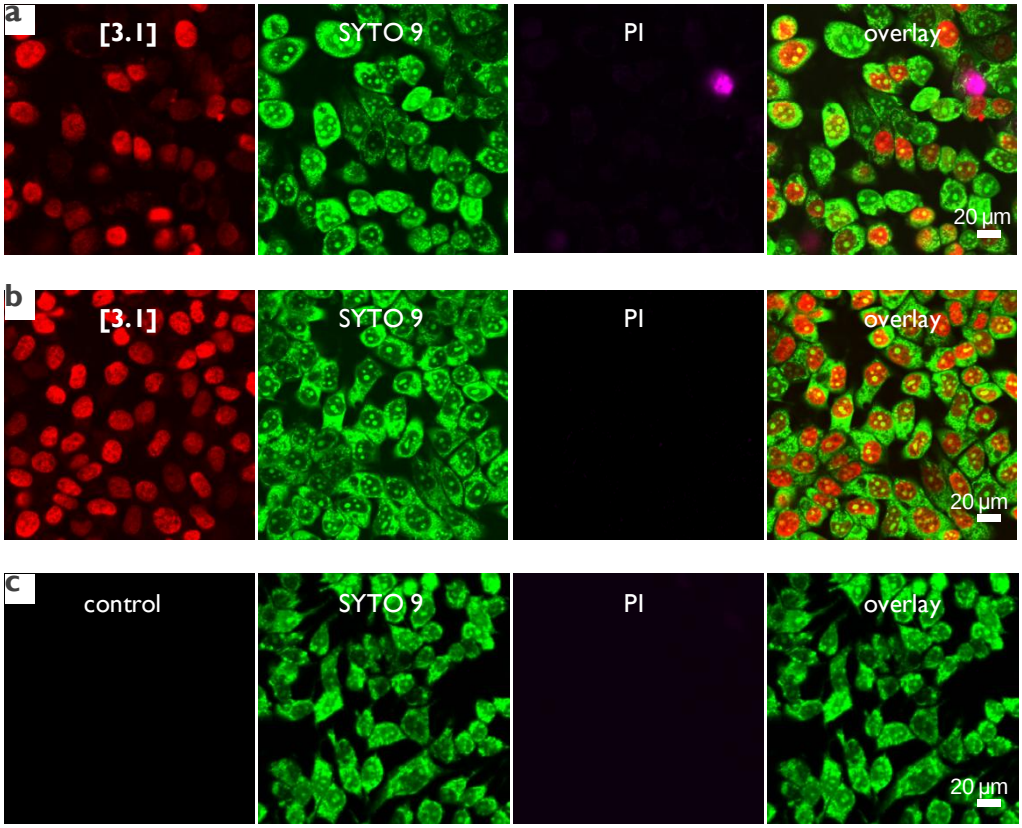

Figure 3.5 a, b, CLSM of MCF-7 cells incubated with 500 µM **[3.1]** in either serum-containing media (**a**) or serum-free media (**b**) for 1 hr. **c,** Negative control. From left to right: luminescence emission of **[3.1]** (red), SYTO 9 (green), PI (purple) and phase contrast image.

Conditions	Nuclei stained / %	Rel. emission intensity / % *
- serum	98 ± 3	100
+ serum	60 ± 4	35

Table 3.2 Extent of nuclear staining of MCF-7 cells by **[3.1]** (500 µM, 1 hr) in serum-free and serum-containing incubation conditions. Minimum of 200 cells counted for each experiment. *For relative emission intensity / cell, incubation in serum-free conditions used as 100 %.

The live/dead co-staining also demonstrates that the dinuclear complex **[3.1]** is less toxic than the mononuclear analogue **[2.3]**. The equivalent experiment for **[2.3]** caused total cell death (Section 2.4.3.4), in comparison to **[3.1]** which does not appear to compromise cell viability (Figure 3.5), as shown by the relevant PI co-staining after incubation with each complex. However, when cells were incubated with **[3.1]** for longer incubation times this did affect cell viability, indicating that there are more subtle toxic effects that need to be considered. As the ability not to induce cell death upon uptake and nuclear staining is an advantage in live cell microscopy, **[3.1]** therefore displays more favourable properties than **[2.3]** in this capacity.

3.4.1.2 3D luminescence location

To examine the location of the observed MLCT luminescence in 3 dimensions, a z-stack image, which takes a series of 2D images at different depths within the sample, was taken. Figure 3.6a shows that the observed **[3.1]** luminescence is near-spherical in three dimensions, corresponding to the cell nucleus. Co-staining with SYTO 9 was used as a reference stain to confirm the intracellular location of **[3.1]** (Figure 3.6b).

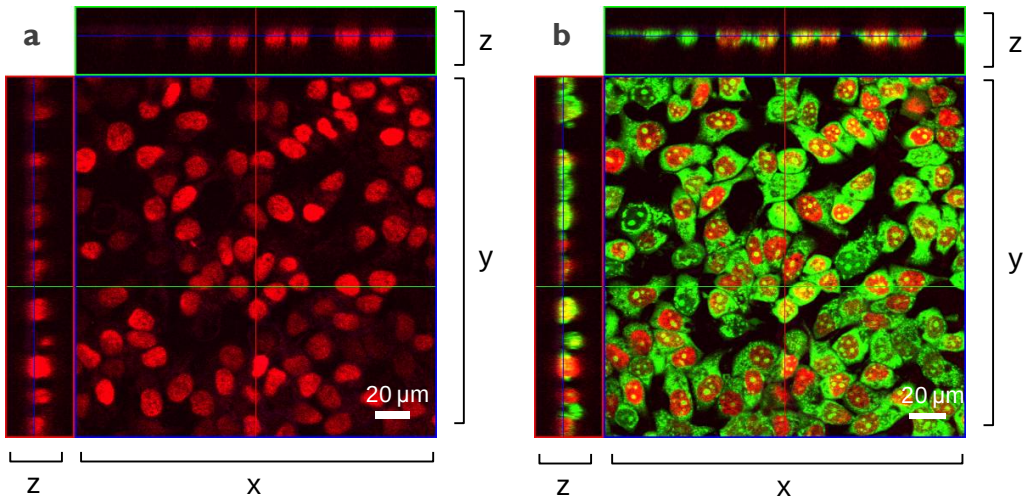

Figure 3.6 a, CLSM z-stack showing 3D location of *in cellulo* **[3.1]** luminescence. **b,** As for **a** with accompanying SYTO 9 staining for reference.

3.4.1.3 Co-staining with nucleic acid dyes

Higher resolution imaging and co-staining with other commercially available fluorescent nucleic acid stains suggest that **[3.1]** is targeting nuclear DNA. Incubation of MCF-7 cells with **[3.1]** and co-staining with the commonly used DNA dye DAPI shows a strong overlap of the two emission signals (Figure 3.7). This is confirmed in co-localisation studies, where the two emission signals show a high degree of co-localisation – as shown by the region labelled white in Figure 3.8.

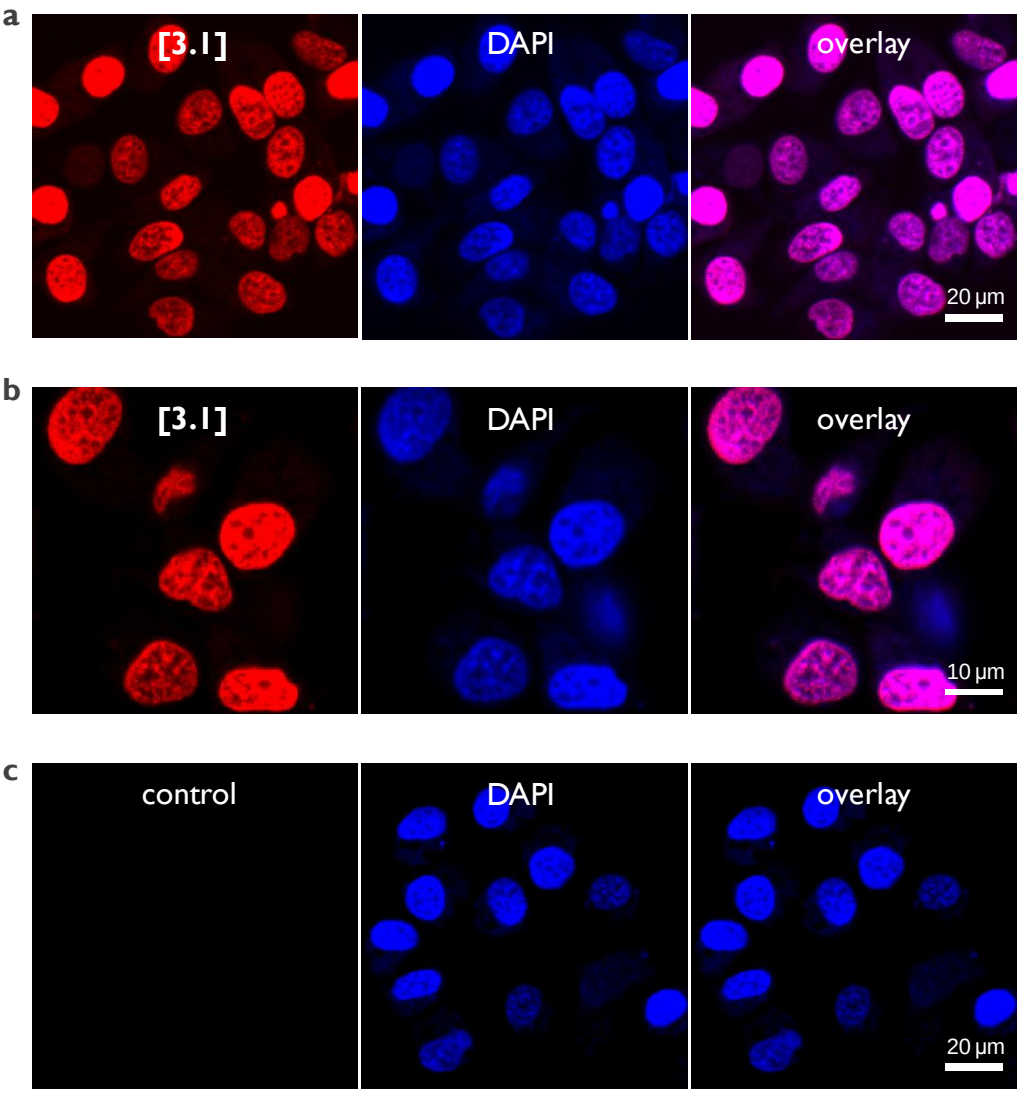

Figure 3.7 a, b, Co-staining of **[3.1]** (red) with DAPI (blue) and overlay image. **c,** Negative control.

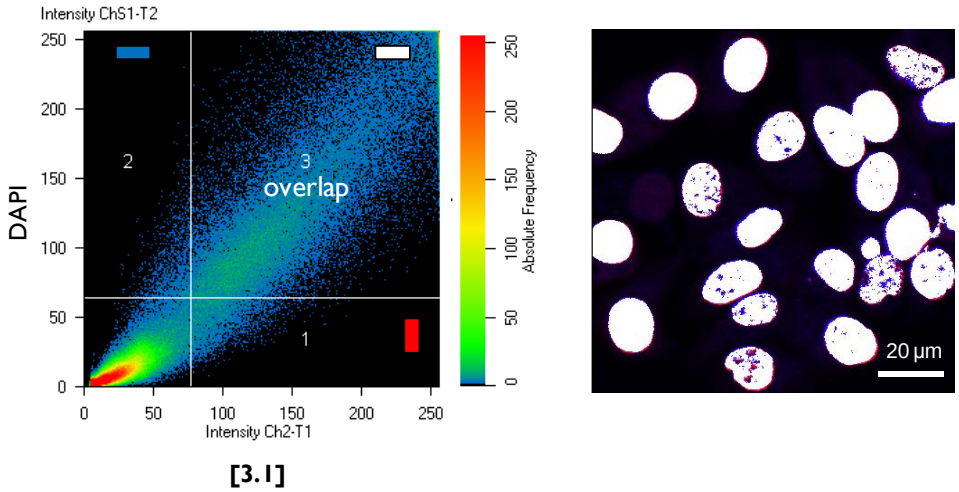

Figure 3.8 Co-localisation of **[3.1]** and DAPI emission signals (blue = region 2, DAPI, red = region 1, **[3.1]**, white = region 3, overlap).

Conversely, co-staining with the cyanine dye SYTO 9, a general nucleic acid stain, shows a clear difference in cellular localisation of the two emission signals (Figure 3.9). Notably SYTO 9 binds RNA in addition to DNA and, as a consequence, nucleoli, the site of rRNA synthesis and tRNA processing, are distinctly imaged through the dye's intense green emission. It is clear that **[3.1]** is a DNA-specific stain as, in contrast to SYTO 9, no emission from the complex is observed from nucleoli regions. SYTO 9 also labels mitochrondrial DNA and it is clear that there is no non-nuclear luminescence due to **[3.1]**, making **[3.1]** a nuclear DNA specific imaging agent when using these incubation conditions. The co-localisation studies with **[3.1]** and SYTO 9 clearly illustrate this behaviour; the overlap of the emissions from each molecule is minimal and is restricted to the nucleolus/nucleus boundary (Figure 3.10).

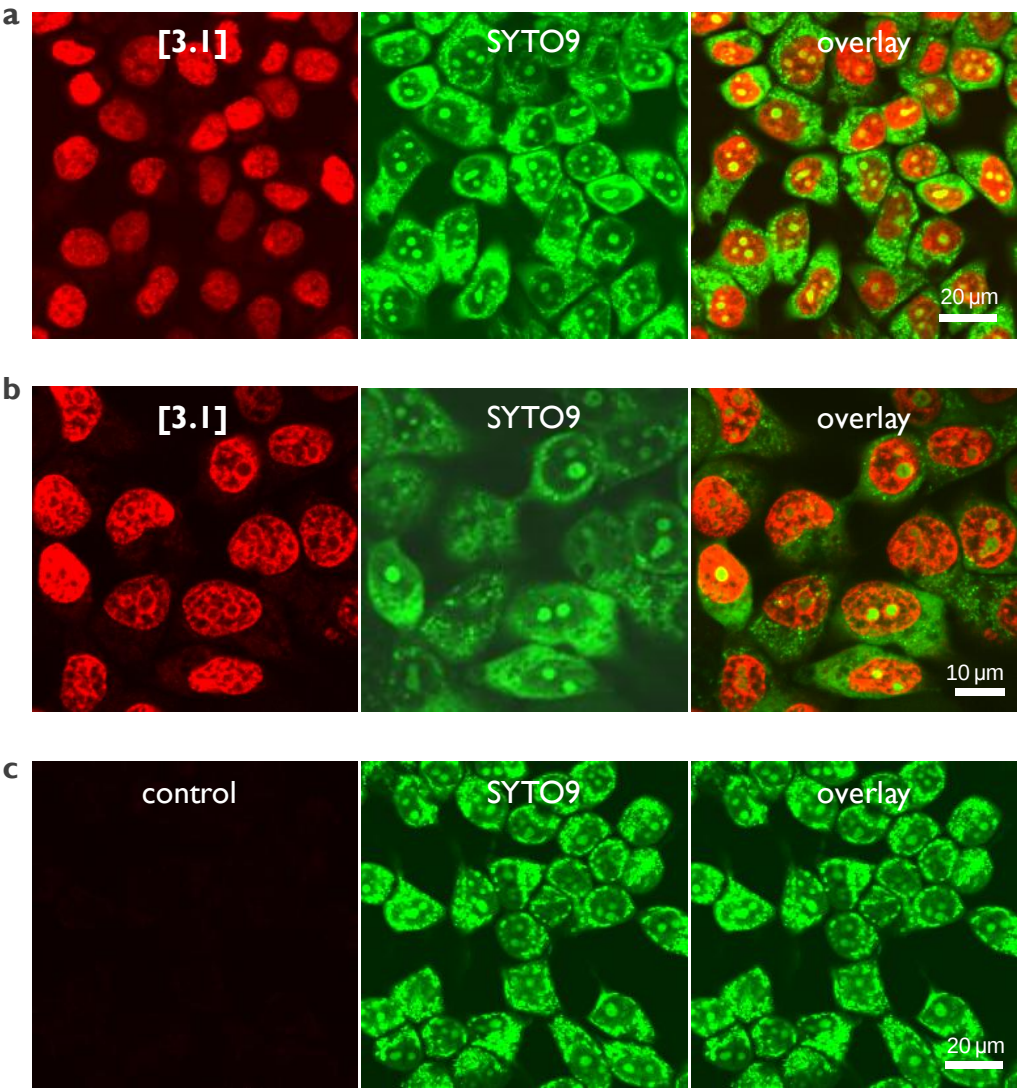

Figure 3.9 a, b, Co-staining of **[3.1]** (red) with SYTO 9 (green) and overlay image. **c,** Negative control.

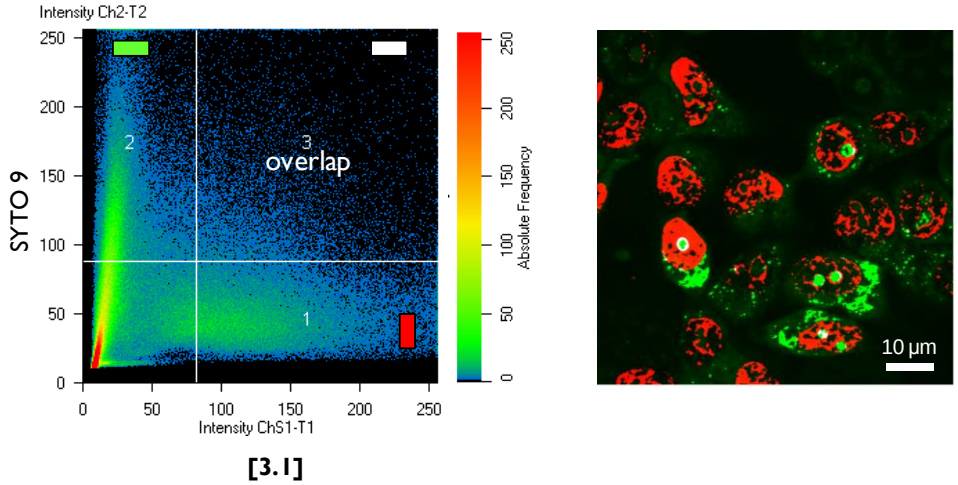

Figure 3.10 Co-localisation of **[3.1]** and SYTO 9 emission signals (green = region 2, SYTO 9, red = region 1, **[3.1]**, white = region 3, overlap).

3.4.1.4 Visualisation of mitotic chromosomes

In addition to these co-localisation studies, analysis of cells stained with **[3.1]** indicate that this molecule reports the characteristic structural changes in nuclear DNA as cells progress through the cell cycle, furthermore establishing the complex as a DNA-specific stain. When asynchronous cells are imaged the majority of labelled cells are in interphase but cells undergoing mitosis (~5%) are also clearly observed. Figure 3.11 shows the mitotic phases shown stained by **[3.1]** including; prophase, where the duplicated chromosomes begin to condense; prometaphase, where the nuclear envelope breaks down and sister chromatids may be visualised; and metaphase, where the chromosomes align themselves at the centre of the mitotic spindle and prepare for separation.

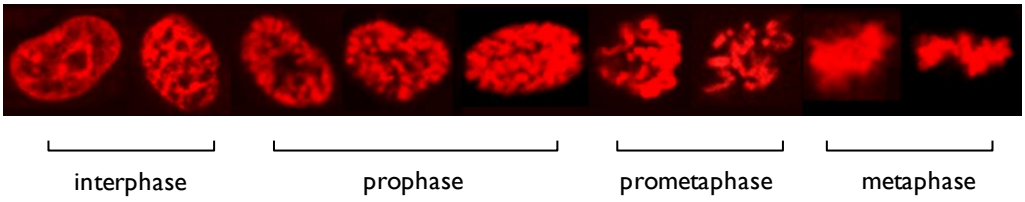

Figure 3.11 A collection of mitotic cells stained by **[3.1]** visualising chromosome aggregation through progression of m-phase.

To image condensed chromosomes in more detail, cells were halted in prometaphase using colchicine, which acts as a mitotic spindle poison and arrests mitosis,[9] stained with **[3.1]** and then mounted onto slides before imaging. This technique allows clear visualisation of the aggregated chromosomes (Figure 3.12).

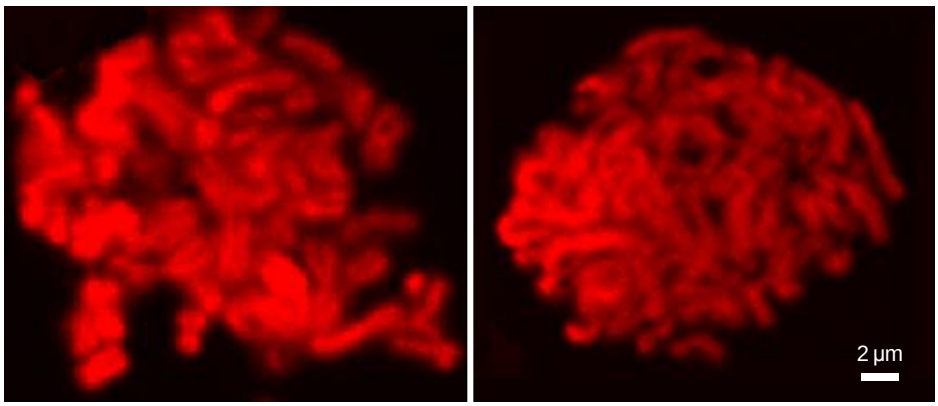

Figure 3.12 High magnification images of mitotic cells showing individual chromosomes stained by **[3.1]**.

3.4.1.5 A structure-sensitive DNA imaging agent

One application in using such systems as cellular DNA probes is their ability to display a high degree of sensitivity in their DNA binding. For example, there is currently a great deal of interest in four stranded DNA structures, such as quadruplexes. As discussed in Section 1.1.7, the induction/stabilisation of quadruplex DNA in G-rich sequences of DNA located at the ends of chromosomes (telomeres) is seen as a potential anti-cancer strategy but nevertheless, to date, the actual detection of quadruplex formation in living cells has remained elusive. Previous *in vitro* studies have demonstrated that **[3.1]** binds to both duplex and quadruplex DNA with a high affinity, displaying a distinctive blue-shifted "light-switch" emission for quadruplex binding in comparison to the analogous duplex effect (maxima of 630 nm and 660 nm respectively).[1] This indicates that **[3.1]** has the

ability to discriminate between different DNA structures and, along with the demonstration of successful nuclear uptake, the potential of **[3.1]** as a quadruplex DNA imaging tool was explored.

It was found that "light switch" emission due to the DNA bound complex within cells is comprised of *two* separate emission peaks. Lambda stacking experiments revealed maxima at approximately 680 and 630 nm respectively (Figure 3.13).

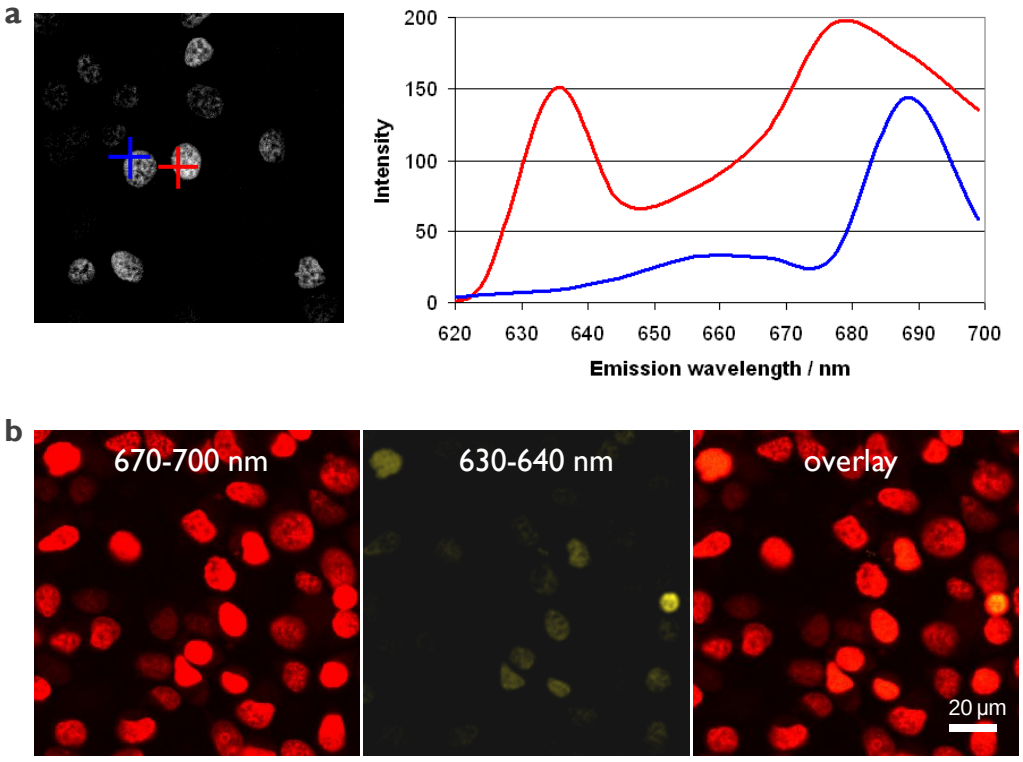

Figure 3.13 a, Lambda stacking experiments show the emission profile of **[3.1]** in live MCF-7 cells to be composed of multiple emission peaks. The emission profile of two separate cellular regions (labelled red and blue) show these peaks to have maxima of approximately 630 and 680 nm. **b,** CLSM using two separate detection channels 670-700 nm (red) and 630-640 nm (yellow) show the multiple emission profile of nuclear luminescence of **[3.1]** bound to DNA and the specific localisation of the 630-640 nm emission.

A representative Lambda stack displaying the emission profile of two separate regions in cells reveals the non-uniform specificity of the 630 peak in comparison with the prevalent 680 peak (Figure 3.13a), suggesting that the 630 emission is from a different source. In order to observe the cellular localisation of each of the signals the image acquisition process was calibrated by defining separate 670-700 nm (coloured red) and 630-640 nm (coloured yellow) channels. Figure 3.13b shows that, using this setup, it is clear that while the red emission shows the expected nuclear chromatin staining, the yellow emission is localised in specific areas within nuclei and is not co-localised with the red emission.

To determine whether this effect was due to a non-duplex structure of DNA being imaged we explored the ability of **[3.1]** to induce/stabilise alternative forms of DNA by using formaldehyde fixation. This produces DNA-protein crosslinks and has the effect of "freezing" DNA structure.[10] Using the novel imaging properties of the complex as a marker stain, fixed cell experiments were conducted; with MCF-7 cells being exposed to **[3.1]** before and after fixation. The incubation of fixed, permeablised cells with **[3.1]** resulted in only the 680 nm emission being visible, with no detectable 630 nm peak (Figure 3.14). This would be in agreement with **[3.1]** being incapable of inducing DNA structural changes after fixation, resulting in the single 680 nm emission arising from **[3.1]** binding to native duplex DNA observed.

In contrast to this behaviour, when cells were fixed in an identical manner *after* incubation with **[3.1]** the distinctive multiple emission profile is maintained (Figure 3.15). We suggest that these results show that **[3.1]** induces/stabilises multiple structures of DNA *in cellulo* and that the 630 nm emission is due to an alternative non-duplex DNA structure.

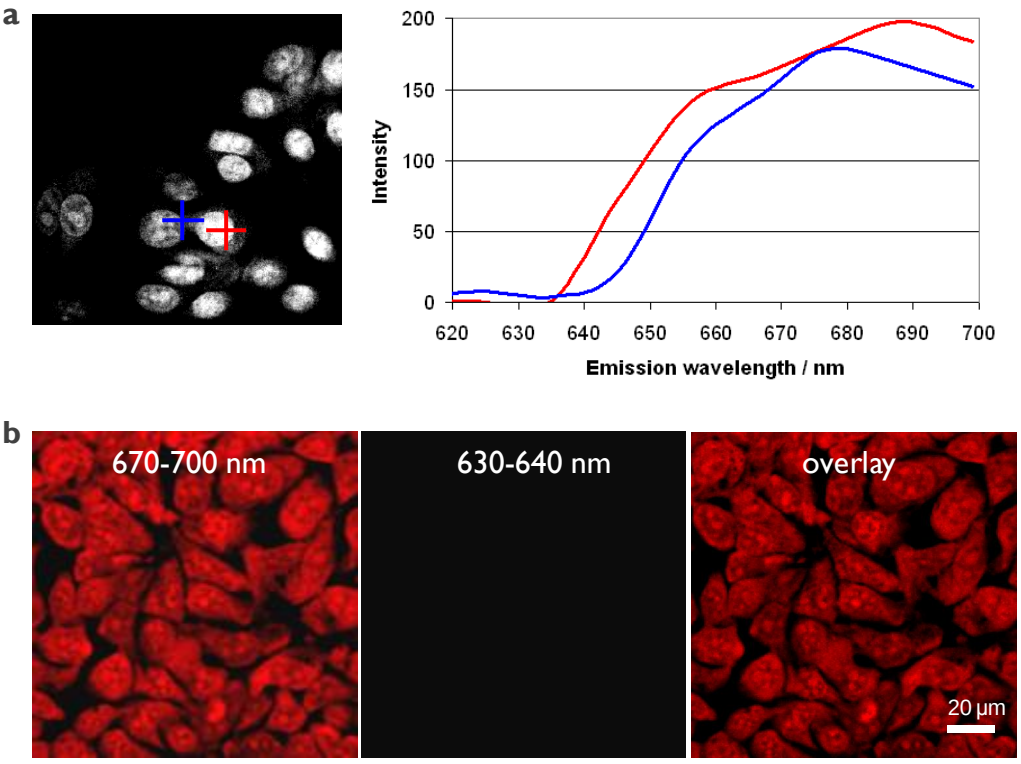

Figure 3.14 a, Lambda stacking experiment of **[3.1]** in fixed MCF-7 cells displays only the 680 nm emission peak. **b,** CLSM imaging experiment for fixed cells show only the 670-700 nm red emission is present.

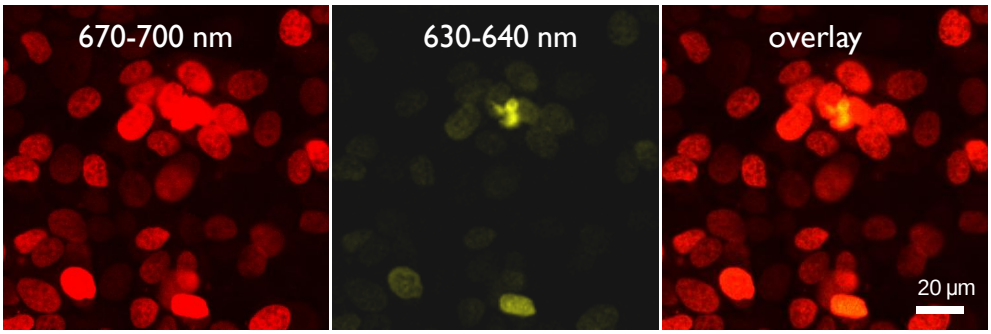

Figure 3.15 MCF-7 cells fixed *after* incubation with **[3.1]** show the distinctive multiple emission properties as for live cell imaging is retained.

In an attempt to further define the nature of the 630 nm emission, we selected the L5178Y-R mouse lymphoma cell line for further imaging experiments. This cell line has a large average length of G-rich telomeric DNA (80 kb compared to 2 kb in MCF-7 cells)[11] and therefore exhibits a greater potential for quadruplex formation. As shown in Figure 3.16a, the staining of these cells by **[3.1]** results in a large increase in the yellow 630-640 nm emission compared to the MCF-7 cell line. Interestingly, this image also includes a mitotic cell showing three intense yellow points, apparently located at specific regions on the chromosomes (Figure 3.16b). This data would be in agreement with **[3.1]** functioning as a luminescent marker for quadruplex DNA, representing the exciting possibility that **[3.1]** can be used as an *in cellulo* imaging agent for this DNA structure.

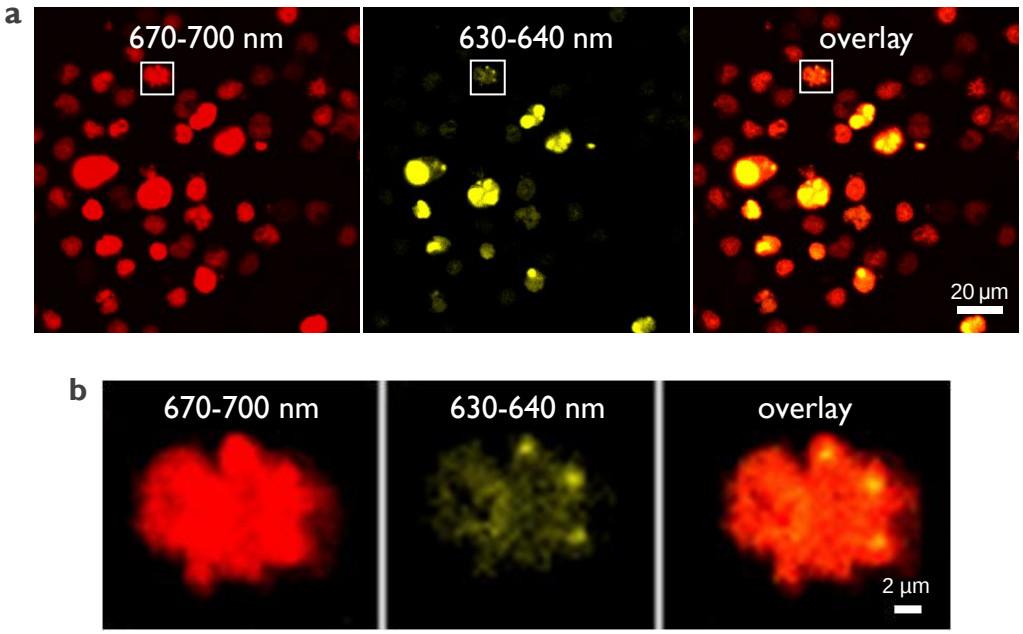

Figure 3.16 a, CLSM of L5178Y-R cells incubated with **[3.1]** (200 µM, 30 mins) display a large increase in 630-640 nm emission. **b,** L5178Y-R metaphase chromosomes showing specific localisation of the 630-640 nm emission peaks.

3.4.1.6 Cell adherence and extended imaging time

An unexpected property of **[3.1]** is that the complex causes strong cell adherence: cells treated with the complex are then unable to be detached from the surface - even the application of 1% v/v Trypsin/PBS a for a period of 1 hr (usually used at 0.1% for 2 minutes) failed to detach the cells. In an imaging context, this adhesion effect is an advantage: cells incubated with **[3.1]** were imaged at regular intervals for 4 hours after removal of the complex and cell media. To preserve cell hydration, the cells were covered with a layer of PBS and Figure 3.17 shows that the majority of cells remained attached with minimal loss in the imaging quality and the nuclei of cells appear to remain intact. Untreated control cells were observed to detach in approximately 1 hour under these conditions.

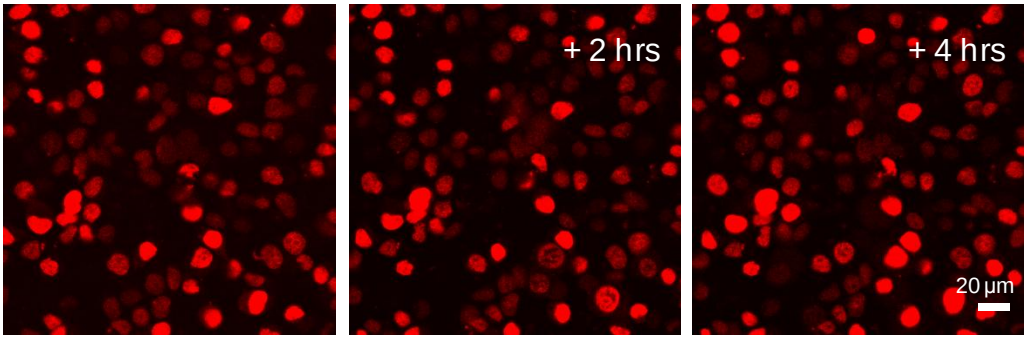

Figure 3.17 CLSM of MCF-7 cells incubated with **[3.1]** (500 μM, 1 hour) showing luminescence emission 2 and 4 hours after removal of the complex.

This cell adherence effect was also observed by Schatzschneider *et al.* for the Ru(II) DNA binding system $[Ru(bpy)_2(dppn)]^{2+}$, which contains the extended intercalating ligand dppn (benzo[*i*]-dipyrido[3,2-a:2',3'-*c*]phenazine) - Figure 3.18.[12] Strong cell adherence was observed in their studies and they suggested that the complex may modify the cell-cell or cell-matrix adhesion properties. Considering the same effect was observed for **[3.1]**, this effect may be a general property of metal polypyridyl complexes.

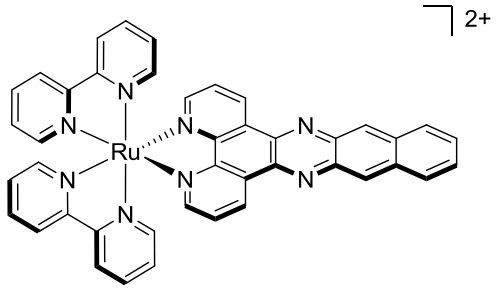

Figure 3.18 Metallo-intercalator $[Ru(bpy)_2(dppn)]^{2+}$

3.4.1.7 Bacterial imaging

In addition to these studies on the uptake of **[3.1]** by eukaryotic cells, experiments performed by Dr J. Garcia-Lara are also able to show that **[3.1]** is internalised by the bacteria *Staphylococcus aureus* (*S. aureus*) *in vivo*; the first time prokaryotic cells have been directly imaged using a metal-based system (Figure 3.19).

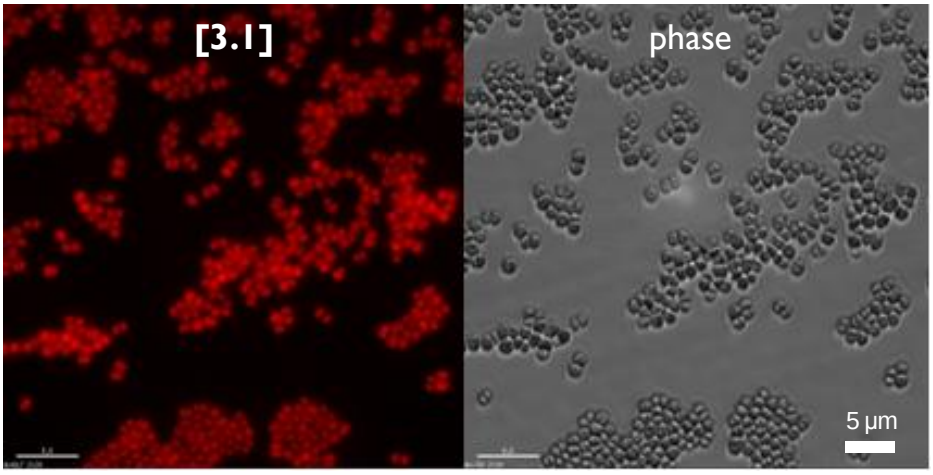

Figure 3.19 *S. aureus* bacteria cells stained by **[3.1]**. Experiment performed by Dr J. Garcia-Lara.

3.4.2 $[\{Ru(bpy)_2\}(tpphz)]^{4+}$

In contrast to **[3.1]**, the incubation of MCF-7 cells with **[3.2]** and subsequent imaging showed no staining of live cells under the same conditions (Figure 3.20). Using these conditions, **[3.2]** is an efficient indicator of cell mortality, as shown by co-staining with PI in Figure 3.20b. Indeed, in live/dead staining applications it functions in a manner identical to PI but with novel excitation/emission wavelengths.

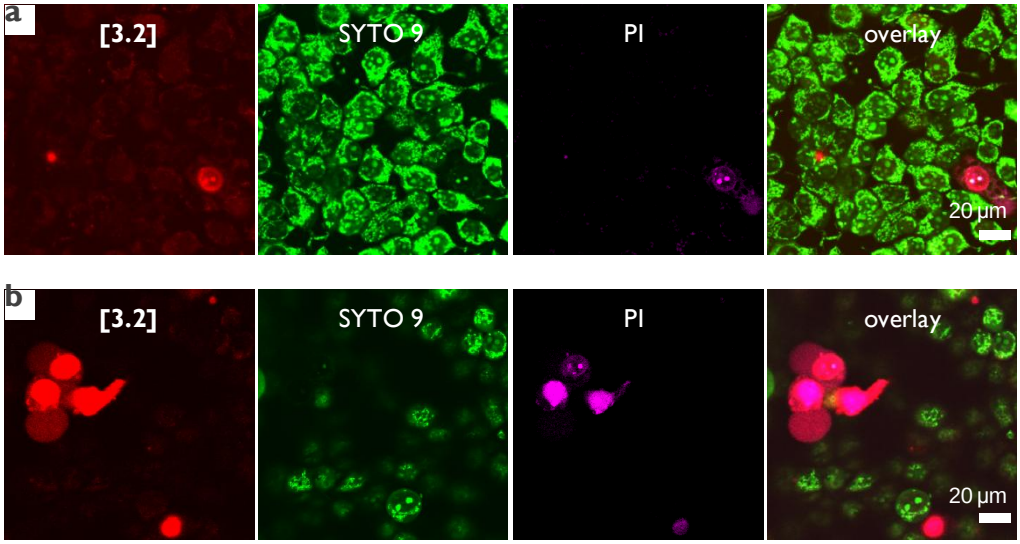

Figure 3.20 CLSM of MCF-7 cells incubated with 500 µM **[3.2]** for 1 hr. **a,** No uptake of **[3.2]** is observed in live cells. **b, [3.2]** is an effective dead cell stain by co-localisation with PI emission. From left to right: luminescence emission of **[3.2]** (red), SYTO 9 (green), PI (purple) and phase contrast image.

At longer incubation times (500 µM, 6 hrs) nuclear staining by **[3.2]** is observed the intensity of this staining is inconsistent, with only a small number of cells observed to be stained weakly (Figure 3.21). As both **[3.1]** and **[3.2]** display a comparable increase in luminescence when bound to DNA, along with similar affinities for DNA (in fact **[3.2]** binds DNA more strongly than **[3.1]**),[1] the poorer nuclear staining properties of **[3.2]** are therefore most likely due to a lower rate of cellular uptake of **[3.2]** compared to **[3.1]**.

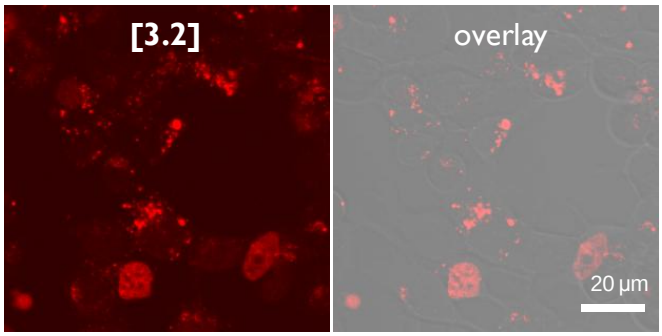

Figure 3.21 CLSM images of MCF-7 cells incubated with 500 µM **[3.2]** for 6 hrs. Left: Ru(II) emission. Right, Overlay image of Ru(II) emission and phase contrast.

3.5 Fixed cell imaging

The ability of each dinuclear Ru(II)tpphz complex to bind DNA in fixed and membrane-permeablised cells was investigated using CLSM to observe the resultant DNA binding. The same excitation/emission wavelength parameters as for live cell imaging were used.

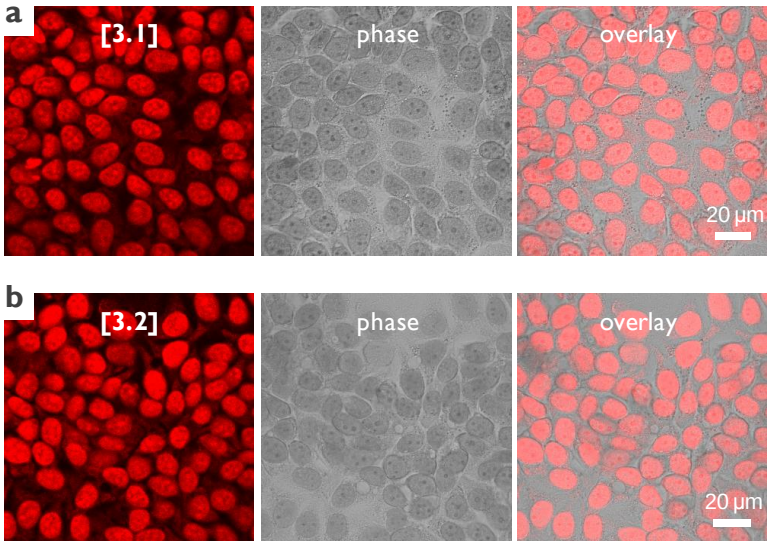

Figure 3.22 CLSM of fixed MCF-7 cells stained with **[3.1]** (**a**) or **[3.2]** (**b**) (100 µM, 10 mins). From left to right: luminescence emission of Ru(II) complex (red), phase contrast and overlay image.

As shown by Figure 3.22, both **[3.1]** and **[3.2]** are excellent DNA stains for fixed, permeablised cells. Figure 3.23 shows fixed MCF-7 cells stained with either **[3.1]** or **[3.2]** at a higher magnification and sub-nuclear chromatin structure is clearly observed. These results make both complexes of interest as DNA stains in fixed cell applications. As both complexes display similar levels of luminescence when bound to DNA *in vitro*[1] and Figure 3.23c shows this to be the case in fixed and permeablised cells, this strongly suggests that it is the reduced efficiency of cellular uptake of **[3.2]** that is responsible for the lower staining observed in live cell experiments in comparison to **[3.1]** and not an inability of **[3.2]** to bind to DNA with activation of luminescence.

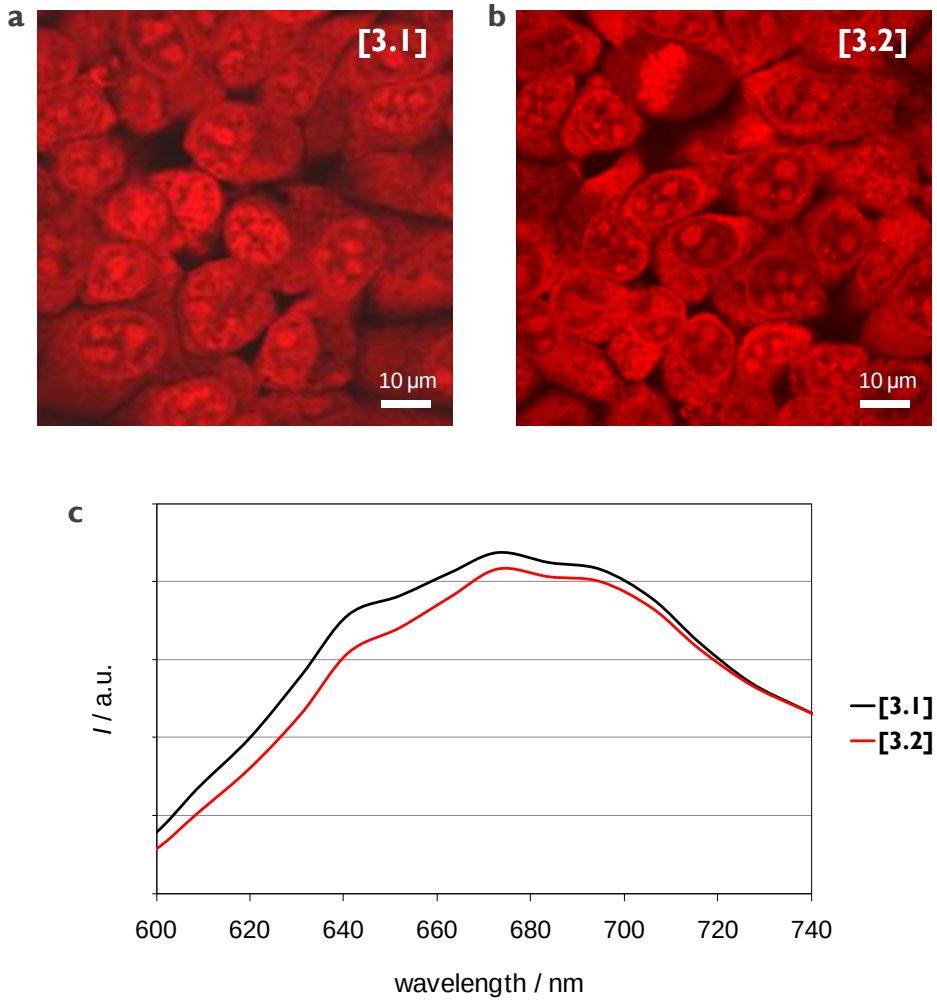

Figure 3.23 CLSM of fixed MCF-7 cells stained with Ru(II) complexes **[3.1]** (**a**) or **[3.2]** (**b**) (100 µM, 10 mins). **c,** Relative emission intensity of **[3.1]** and **[3.2]** in fixed cells.

3.6 Cellular uptake mechanism

The hydrophilicity and high charge of **[3.1]** would imply that the molecule does not freely diffuse across the cell membrane, a property reflected by the relatively high concentration required for efficient uptake. With this in mind, the mechanism of cellular uptake of **[3.1]** was investigated using the luminescent properties of the complex as an indication of successful cellular uptake.

3.6.1 Temperature-dependence

To probe whether **[3.1]** was taken up by a passive- or active-transport mechanism, MCF-7 cells were incubated with **[3.1]** at a temperature of 4°C. Figure 3.24 shows that no luminescence is observed when the cells are incubated with the complex at this temperature, indicating that **[3.1]** enters cells and targets the nucleus by a temperature-dependent pathway and confirming **[3.1]** is not a membrane-permeable molecule.

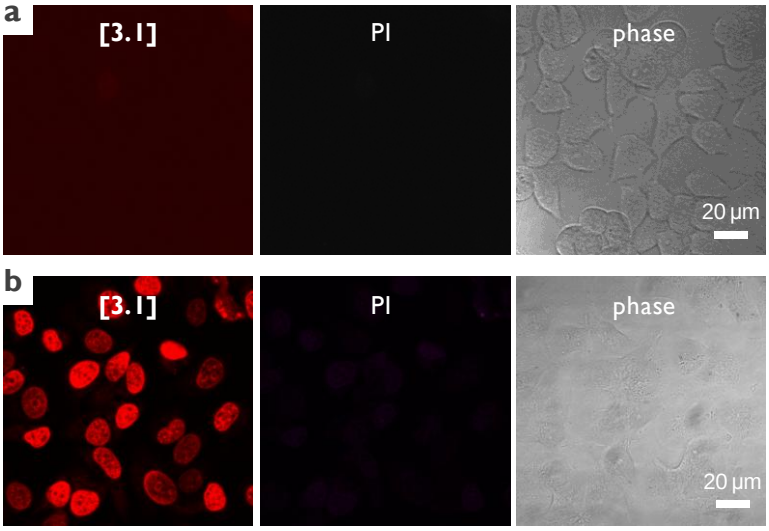

Figure 3.24 Temperature-dependence studies of uptake of **[3.1]** by MCF-7 cells. **a,** Cells incubated with **[3.1]** (500 µM, 1 hour) at 4°C display no *in cellulo* luminescence. **b,** 37°C control. The phase contrast image is included for reference.

3.6.2 Endocytosis inhibitors

To investigate if the mechanism of uptake involved an endocytic pathway, cells were co-incubated with **[3.1]** and several well-documented inhibitors of this process. Cellular uptake was then assessed by the extent of resultant nuclear staining by luminescence microscopy (Figure 3.25).

Co-incubation with **[3.1]** and the general endocytosis inhibitors chloroquine or ammonium chloride (two lysosomotropic agents which prevent the maturation of endosomes)[13, 14] had no effect on the ability of **[3.1]** to function as a nuclear stain (Figure 3.25a,c,d). Co-incubation with the specific endocytosis inhibitors chlorpromazine (which disrupts the assembly of clathin lattices)[15] or filipin (which prevents the formation of caveolae)[16], which inhibit clathrin- and caveolae-mediated endocytosis respectively, do not inhibit the uptake of **[3.1]**, showing that these two well-studied endocytic pathways are not responsible for the uptake of **[3.1]** (Figure 3.25a,e,f) Furthermore, neither colchicine or nocodazole, which disrupt the polymerisation of microtubules and thus prevent membrane and endosomal trafficking,[17] showed any inhibition of uptake (Figure 3.25a,g,h), suggesting that membrane trafficking in any form does not contribute to the process by which **[3.1]** is taken up into MCF-7 cells. Consistent with these observations, our measurements of the lipophilicity of **[3.1]** show that the molecule remains hydrophilic under the mildly acidic conditions found in early endosomes (log P = -0.77 at pH 5 – Table 3.3) and would be unlikely therefore to diffuse across an endosomal membrane to gain access to the cytosol and subsequently the nucleus. Taken together, these results suggest a non-endocytic mechanism of cellular uptake by MCF-7 cells.

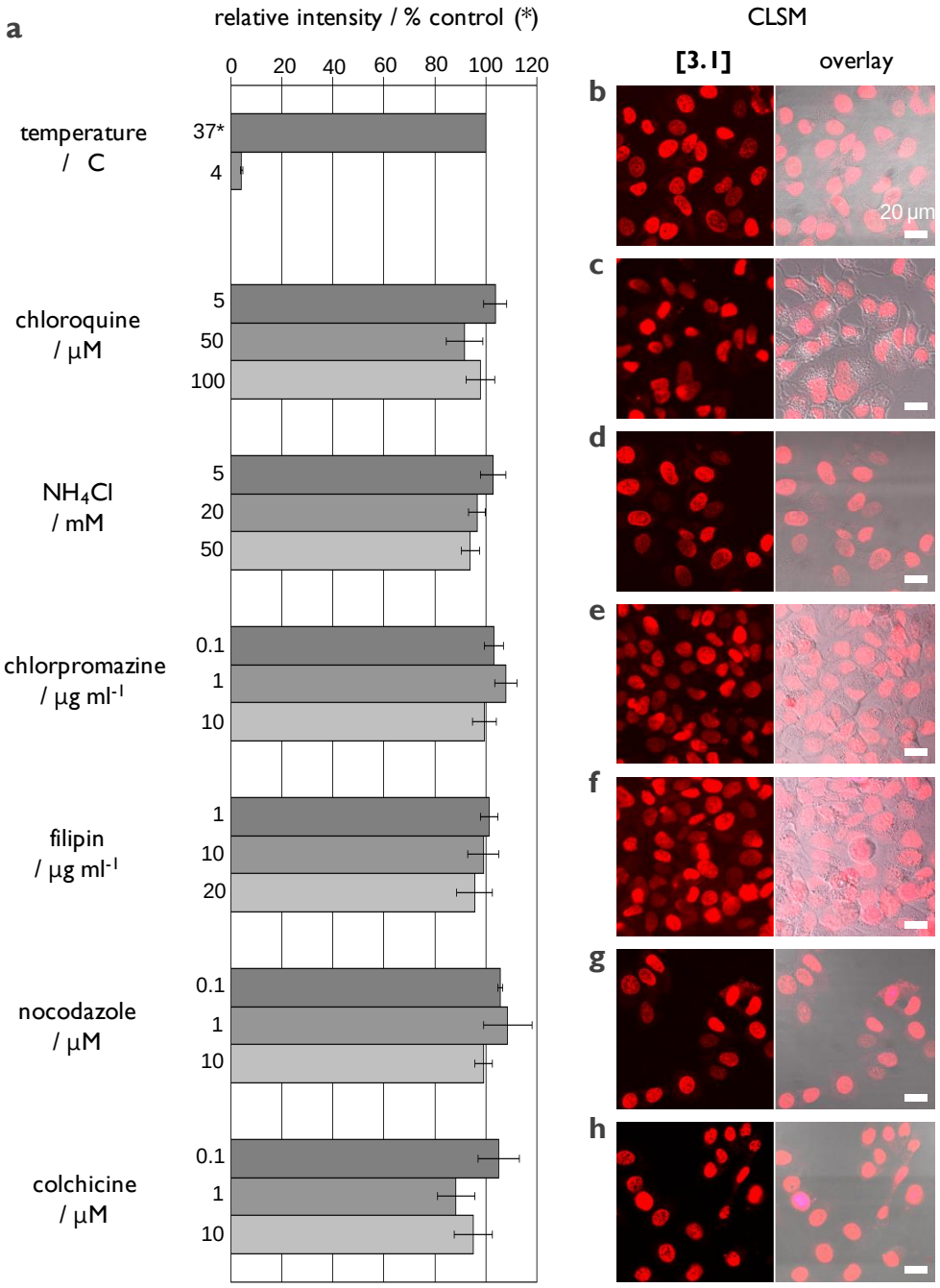

Figure 3.25 a, Relative luminescence intensity of **[3.1]** in MCF-7 cells after inhibition treatment (500 μM, 1 hour). *Error bars represent ± standard error of the mean (SEM) with n = 3. **b - h,** CLSM images of MCF-7 cells incubated with **[3.1]** (500 μM, 1 hour) and inhibitor: **b,** Negative control. **c,** 100 μM chloroquine. **d,** 50 mM NH_4Cl. **e,** 10 μg/ml chlorpromazine. **f,** 20 μg/ml filipin. **g,** 20 μM nocodazole. **h,** 20 μM colchicine. Left: **[3.1]** emission. Right: Overlay image including PI staining to indicate cell viability and phase contrast image.

pH	log P
3	-0.47 ± 0.01
4	-0.57 ± 0.14
5	-0.77 ± 0.02
6	-0.94 ± 0.01
7	-0.96 ± 0.09

Table 3.3 Measured octanol/water partition coefficients for **[3.1]** at various water-phase pH values.

In addition to the uptake studies on MCF-7 cells, Section 3.4.1.7 showed that **[3.1]** is internalised by the bacteria *S. Aureus*. As these cells do not undergo endocytosis, this indicates that **[3.1]** is able to enter cells through a non-endocytic mechanism of uptake. This would be in agreement with the uptakes studies on MCF-7 cells, although the exact uptake mechanism could well vary depending upon cell type.

3.6.3 Effects of media

The staining experiments initiated using MCF-7 cells were repeated for multiple cell lines: including FaDu (human hypopharyngeal carcinoma), Saos-2 (human osteosarcoma) and HeLa (human cervical cancer) cancer cell lines. In these cell lines, however, no nuclear staining was observed using the same incubation conditions (500 μM, 1 hour) that resulted in the well-characterised luminescence in MCF-7 cells described in Section 3.4.1. These data raised the possibility that the lack of staining was due to cell-specificity in the cellular uptake properties of **[3.1]**. However, when we consider the ability of serum to inhibit cellular uptake and nuclear staining has been well documented for both **[3.1]** and the related monometallic Ru(II)tpphz

complexes described in Chapter 2 and that the cell lines which were not readily stained required distinct medium (DMEM compared with RPMI for MCF-7 cells) for optimal growth, the possibility that the media composition might affect uptake efficiency also existed.

To explore this idea further, HeLa human ovarian cancer cells, a cell line that may be cultured in both DMEM and RPMI cell media, were incubated with solutions of **[3.1]** in either DMEM or RPMI serum-free media and the extent of the resultant staining assessed by CLSM (Figure 3.26).

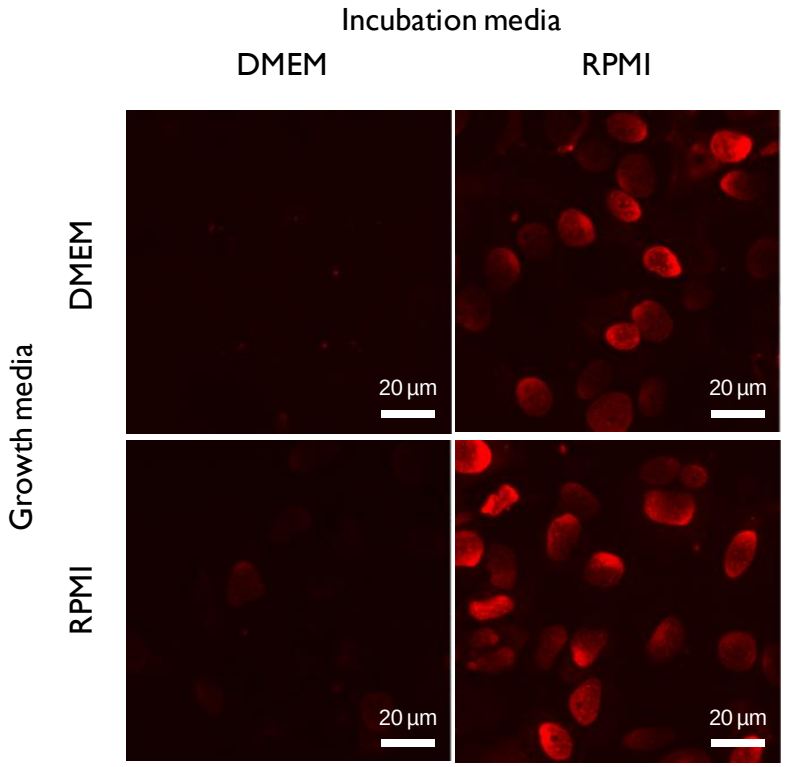

Figure 3.26 CLSM of HeLa cells incubated with **[3.1]**. Cells were cultured either in DMEM or RPMI media before incubation with solutions of **[3.1]** in each media formulation (500 µM, 1 hour).

Growth media	Incubation media	Rel. emission intensity / %
RPMI	RPMI	100
DMEM	RPMI	61
RPMI	DMEM	14
DMEM	DMEM	12

Table 3.4 Relative emission intensities of HeLa cells incubated with **[3.1]** (500 μM, 1 hour). Growth media = RPMI, incubation media = RPMI used as 100%.

As Figure 3.26 and Table 3.4 show, HeLa cells display much greater nuclear staining when the incubation medium is RPMI compared to DMEM. A greater intensity is observed for cells cultured in RPMI, indicating that the growth medium is a factor in the uptake of the complex, although not to the same extent as the incubation medium.

These results indicate that DMEM inhibits the uptake of **[3.1]** and show that the medium is not merely acting as a solvent for the active molecule – it can interfere with the uptake and application, positively or negatively. These data demonstrate how, in addition to the variables (cell line/concentration/time/serum) described previously, the incubation medium is a crucial factor which needs to be considered when measuring the uptake of this class of membrane-impermeable complexes into live cells.

3.6.3.1 Folic acid

The observation that DMEM inhibits the uptake of **[3.1]** is of particular interest as this media formulation contains 4x the folic acid concentration of RPMI.[18] Folate receptors are cell membrane receptors that are highly

expressed by numerous cancer cells and display a high affinity for their target ligands of folic acid and reduced folates.[19] Due to this, folic acid conjugation is a frequently employed targeting strategy for the delivery of drugs to folate receptor-positive tumour cells.[20] Thus, the possibility that the mechanism of uptake in MCF-7 cells may involve a folate receptor was explored by using the principle that this would be predicted to involve folic acid competition. To assess the effects of folic acid upon the rate of cellular uptake of **[3.1]**, MCF-7 cells were therefore incubated with **[3.1]** in RPMI containing various concentrations of folic acid and the effect upon the resultant staining measured by CLSM.

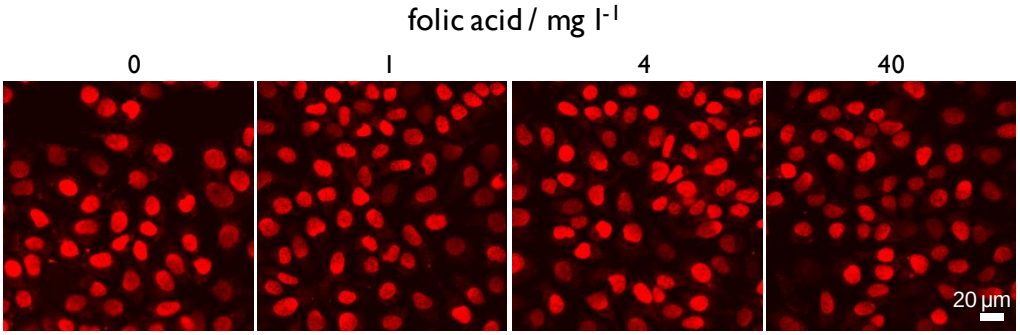

Figure 3.27 CLSM of MCF-7 cells incubated with **[3.1]** (500 μM, 1 hour) in RPMI media with increasing folic acid concentration.

It can be see that as the concentration of folic acid is increased from 0 mg/l to concentrations as high as 40 mg/l, there is no reduction in the nuclear staining due to **[3.1]**, indicating that folic acid does not inhibit the uptake of **[3.1]** in MCF-7 cells (Figure 3.27). Since DMEM media contains 4 mg/l folic acid,[18] it seems unlikely that the increased folic acid concentration is responsible for DMEM media inhibiting the cellular uptake of **[3.1]**. These results show that the mechanism of uptake does not involve competition with folic acid which in turn implies that cellular entry is not facilitated by the folate receptor.

3.6.4 Concentration-dependence

An intriguing aspect of the mechanism by which **[3.1]** is internalised by cells is the apparent threshold concentration of **[3.1]** required to obtain nuclear staining. When cells are incubated at lower concentrations, there is evidence of cytoplasmic luminescence and only weak nuclear staining is observed, even at extended incubation times (Figure 3.28a). At an intermediate concentration, there is a mix of localisation and both cytoplasmic and nuclear staining can now be observed (Figure 3.28b). A higher concentration and substantially shorter incubation time results in nuclear staining as previously described and, under these conditions, cytoplasmic staining is not readily observed, presumably because it is substantially weaker than the nuclear signal under these incubation conditions (Figure 3.28c).

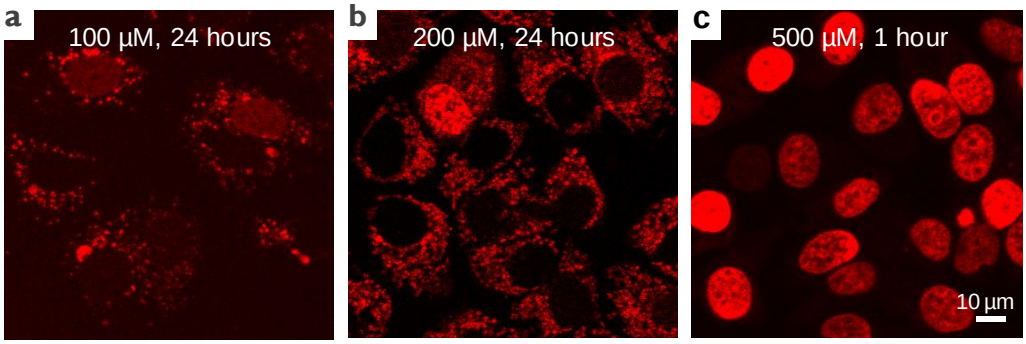

Figure 3.28 CLSM of MCF-7 cells incubated with **[3.1]**.

That a threshold concentration of **[3.1]** is required to obtain nuclear staining also suggests that nuclear uptake is a two step process: the first step resulting in the observable cytosol luminescence and the second to achieve nuclear uptake. As the nuclear pore diffusion limit is ~40 kD (diameter <39 nm),[21] this would imply that the molecule is not present as the free complex diffused within the cytosol and is bound to a macromolecule or within an organelle.

In an attempt to characterise the cellular location of the non-nuclear luminescence observed for cells incubated with lower concentrations of **[3.1]**, MCF-7 cells were co-stained with the specific organelle dyes Mitotracker Red, a thiol-reactive chloromethyl based probe which labels active mitochondria, and Lysotracker Yellow, an acidotropic probe used to label and track the acidic lysosomes in live cells.

Figure 3.29 shows the co-staining of **[3.1]** with Mitotracker, which shows an apparently small co-localisation between the emission signals (Figure 3.29b).

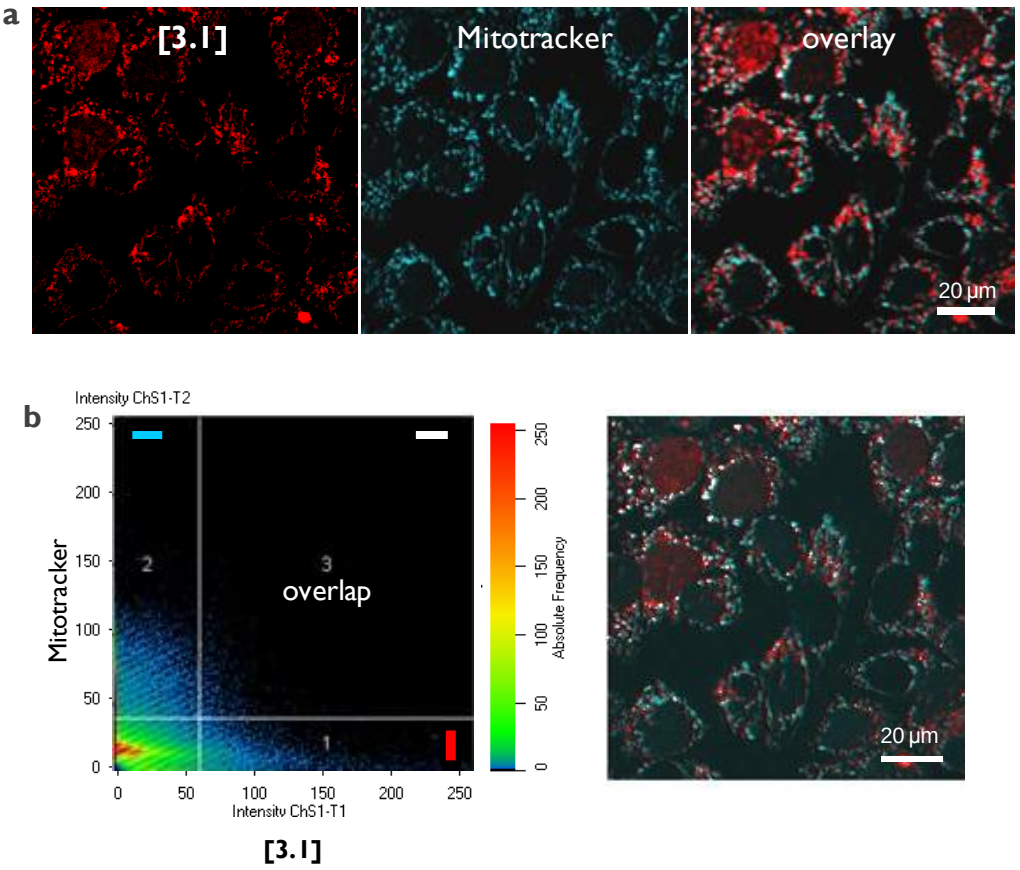

Figure 3.29 CLSM of MCF-7 cells incubated with **[3.1]** (200 μM, 24 hrs). **a,** Co-staining of **[3.1]** (red) with Mitotracker Red (cyan) and overlay image. **b,** Co-localisation of **[3.1]** and Mitotracker emission signals (cyan = region 2, Mitotracker, red = region 1, **[3.1]**, white = region 3, overlap).

Figure 3.30 shows the equivalent co-staining and co-localisation of **[3.1]** and Lysotracker, which again shows a small amount of overlap between the two signals, suggesting that a small amount of the signal from **[3.1]** is in acidic lysosomes.

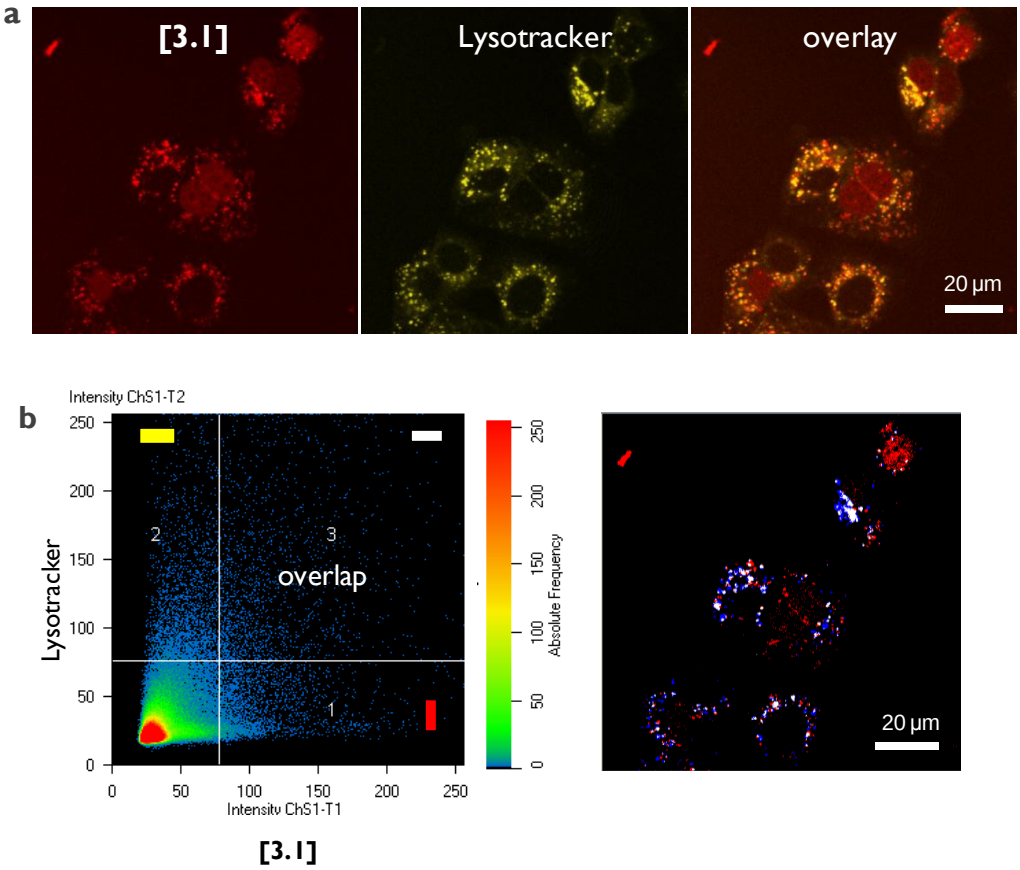

Figure 3.30 CLSM of MCF-7 cells incubated with **[3.1]** (200 μM, 24 hrs). **a,** Co-staining of **[3.1]** (red) with Lysotracker Yellow (yellow) and overlay image. **b,** Co-localisation of **[3.1]** and Lysotracker emission signals (yellow = region 2, Lysotracker, red = region 1, **[3.1]**, white = region 3, overlap).

Taken together, the non-uniform appearance of cytoplasmic **[3.1]** staining together with its partial co-localisation with both mitochondria and lysosomal compartments suggests that **[3.1]** may stain membrane-bound cellular compartments including mitochondria and lysosomes. In the case of mitochondria it is conceivable that luminescence arises from DNA binding.

If **[3.1]** is indeed located within lysosomes or other organelles, the question of what is activating the luminescence of **[3.1]** arises. The light switch effect is not uniquely dependent on **[3.1]** binding to DNA, but is predicted to occur whenever **[3.1]** is in an environment where the phenazine nitrogen ligands are shielded from water. In cells, this could occur if **[3.1]** was protein- or RNA-bound, or within a hydrophobic environment such as any cellular membranes, as examples. The corollary of this is that a lack of luminescence does not inherently imply the absence of **[3.1]** from other organelles, as it is possible the complex is within such compartments but the light switch emission is deactivated as it is present in an aqueous environment.

From these co-staining experiments, the majority of the signal localisation remains undefined; showing no clear overlap with either Mitotracker or Lysotracker, and the relatively low emission intensity makes any conclusions problematic.

3.6.5 Cell-specific uptake

In contrast to MCF-7 cells, **[3.1]** proved to be a very poor stain of primary human dermal fibroblast (HDF) cells. As Figure 3.31a shows, only low levels of nuclear luminescence are observable in HDF cells (labelled with CelltrackerRed – falsely coloured cyan) whereas the MCF-7 cells display the expected nuclear staining due to **[3.1]** (Figure 3.31b). This cell type-specific staining is still observed when the two types of cell were co-cultured together (Figure 3.31c); MCF-7 cells are clearly distinguishable by the emission due to **[3.1]** whereas the Celltracker-labelled HDF show poor staining by the complex, eliminating the possibility that differences in media composition or content are responsible for the failure of **[3.1]** to stain HDF cells.

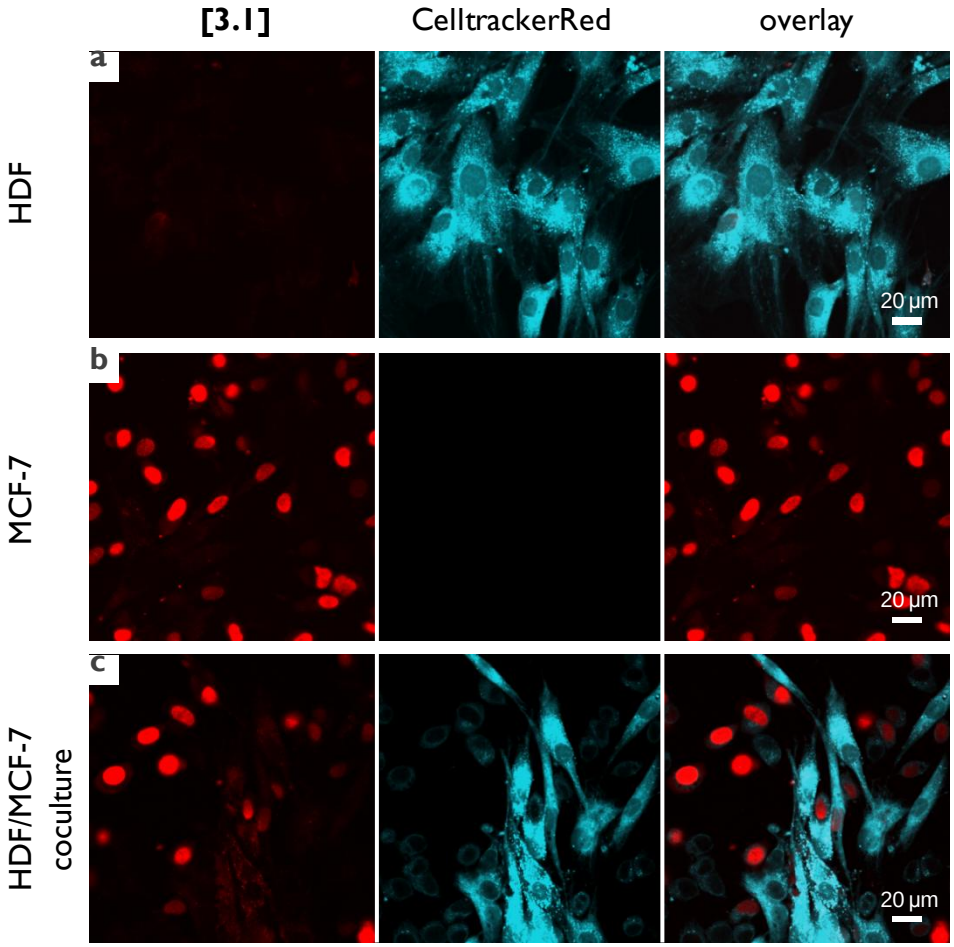

Figure 3.31 CLSM of HDF cells (**a**), MCF-7 cells (**b**) and HDF/MCF-7 coculture (**c**) incubated with **[3.1]** (500 μM, 1 hour). HDF cells were incubated with CelltrackerRed prior to seeding. From left to right: luminescence emission of **[3.1]** (red), CelltrackerRed (cyan) and overlay image.

These data confirm **[3.1]** as a non-membrane permeable imaging agent and strongly suggest that a specific uptake mechanism, whose components are differentially expressed in distinct cell types, operates for nuclear DNA staining by **[3.1]**. The selective staining of immortalised cancer cell lines derived from distinct tissues raises the possibility that **[3.1]** has potential as either a cell-type or tumour-cell specific discrimination reagent or diagnostic tool.

3.7 TEM studies

As shown in Chapter 2, Ru(II) complexes are able to scatter the electron beam used in TEM imaging and therefore act as contrast agents for this high resolution technique. This provides a significant advantage over CLSM as the cellular location of each complex can be determined without requiring the complex to be present in an environment that causes activation of its luminescent properties.

For comparison to the results achieved with each dinuclear Ru(II)tpphz complex, the control experiments, with and without phospholipid contrast reagent osmium tetroxide staining, are shown in Figure 3.32.

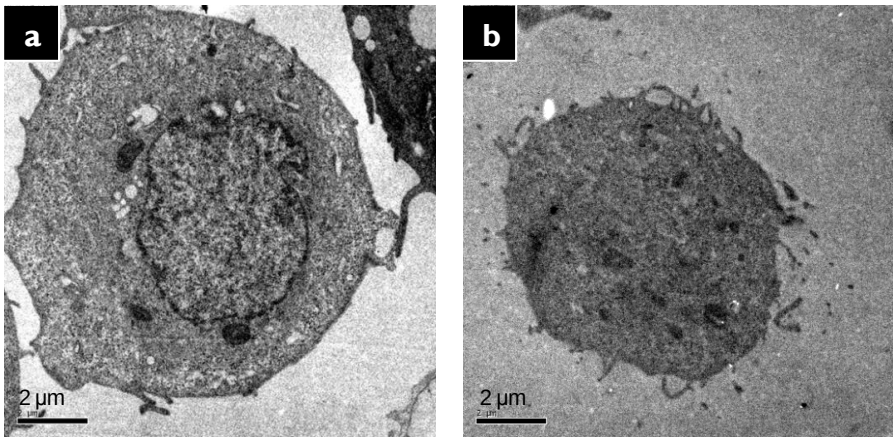

Figure 3.32 a, MCF-7 cell stained with osmium tetroxide. **b,** Negative control cell with no stain present.

3.7.1 $[\{Ru(phen)_2\}(tpphz)]^{4+}$

MCF-7 cells incubated with solutions of **[3.1]** as for luminescence microscopy before fixation and sectioning for TEM imaging show that, while **[3.1]** is located throughout the cell cytoplasm, it is found in much higher concentration within the nucleus, where it localises to heterochromatin, as evidenced by the strong contrast in regions close to the nuclear envelope.

(Figure 3.33a,b). Interestingly, TEM images also reveal that significant levels of **[3.1]** are present in mitochondria (Figure 3.33c). Examining the sub-mitochondrial localisation of **[3.1]** in more detail, it is apparent that the complex is located in the intermembrane space (Figure 3.33d). As mitochondrial DNA is located within the central lumen of the organelle[22] and these TEM images show that the complex is not located there, then this suggests that the observed CLSM luminescence for the same incubation conditions is not a result of the complex bound to mitochondrial DNA.

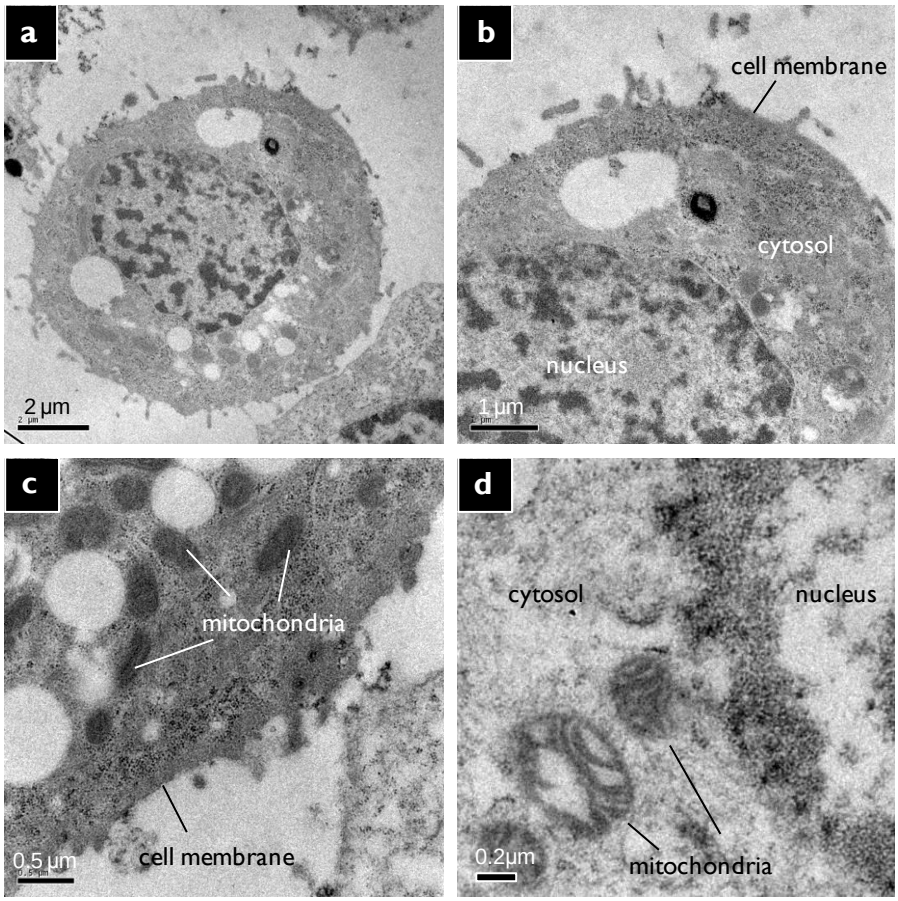

Figure 3.33 TEM micrographs of MCF-7 cells incubated with complex **[3.1]** (500 µM, 1 hr). **a,** Image showing **[3.1]** especially associates within the nucleus where it displays strong heterochromatin staining. **b,** Detailed image of nucleus reveals clear heterochromatin staining. **c, d,** Mitochondria stained by **[3.1]**.

Sub-nuclear localisation is further confirmed by co-staining with osmium tetroxide. As shown in Figure 3.34, cells co-stained with **[3.1]** and osmium tetroxide display highly contrasted nuclear heterochromatin and again the endosomal compartments show no presence of compound **[3.1]**. As expected, the negative control micrograph of a cell stained only with osmium tetroxide shows a much less contrasted nuclear area (Figure 3.32a).

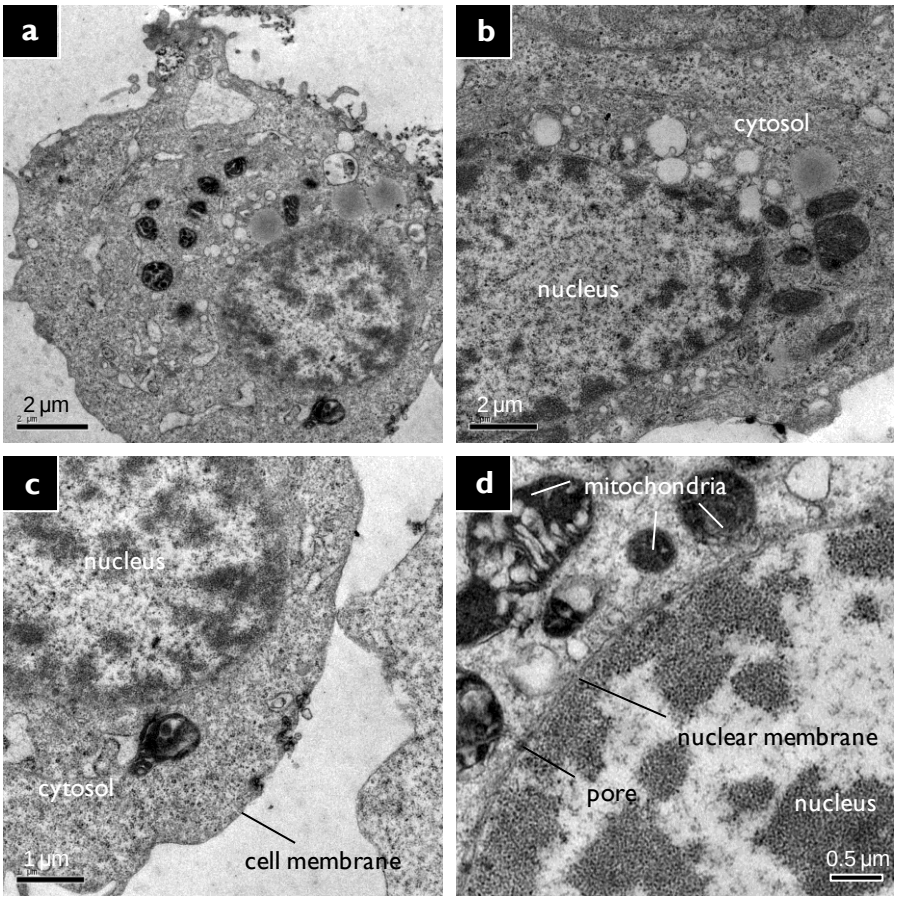

Figure 3.34 TEM micrographs of MCF-7 cells incubated with complex **[3.1]** (500 µM, 1 hr) and stained with osmium tetroxide to show greater cellular detail. **a,** Image showing highly contrasted nuclear heterochromatin due to **[3.1]**. **b, c,** Detailed images of nuclei reveals clear heterochromatin staining. **d,** Image showing heterochromatin and nuclear membrane detail (membrane stained with osmium tetroxide).

3.7.2 $[\{Ru(bpy)_2\}_2(tpphz)]^{4+}$

MCF-7 cells incubated with **[3.2]** before preparation for TEM show very limited contrast effects from within cells, making viewing problematic (Figure 3.35a,b). This supports the view that **[3.2]** is not readily internalised by MCF-7 cells, in agreement with the CLSM data. As TEM is a higher resolution technique and one that does not require a specific mode of binding to DNA for observation, these results provide the strongest indication that poor cellular uptake is responsible for the minimal nuclear staining observed for **[3.2]** in MCF-7 cells and not intracellular factors, such as a non-DNA target, for example.

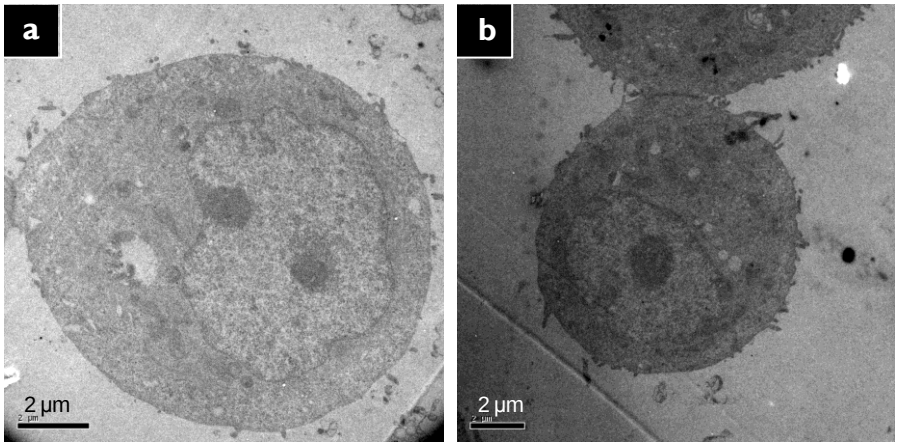

Figure 3.35 a, b, TEM micrographs of MCF-7 cells incubated with complex **[3.2]** (500 µM, 1 hr) display minimal intracellular contrast signal.

When MCF-7 cells are incubated with **[3.2]** *after* fixation, TEM micrographs clearly show contrast within the cell, including strong contrast from the nucleus (Figure 3.36a,b). This makes **[3.2]** of interest as a DNA imaging agent in permeablised cells for transmission election microscopy.

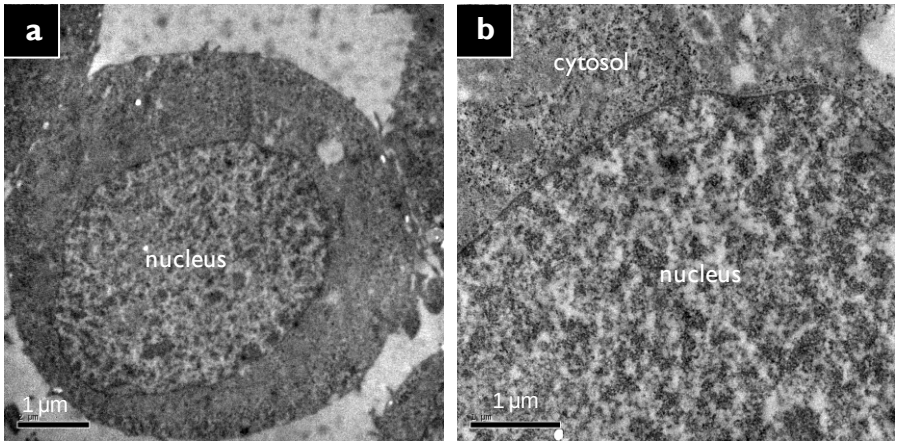

Figure 3.36 a, b, Fixed MCF-7 cells stained with **[3.2]** (100 µM, 10 mins.) show intracellular contrast signal and clear heterochromatin staining.

3.8 Cytotoxicity

3.8.1 MCF-7 cells

As **[3.1]** demonstrates successful cellular internalisation and the ability to bind to nuclear DNA in live cells, the cytotoxic properties of both **[3.1]** and **[3.2]** towards the MCF-7 human breast cancer cell line was determined by MTT assay and the IC_{50} value for each complex thus determined. As for Chapter 2, the anti-cancer drug cisplatin was included for comparison.

As can be seen by Figure 3.37 and Table 3.5, neither **[3.1]** or **[3.2]** demonstrate significant toxicity towards MCF-7 cells over a 24 hour incubation time (IC_{50} values of 138 and >500 µM respectively) and cisplatin demonstrates a toxicity one order of magnitude greater than **[3.1]** (IC_{50} value = 12 µM). The dinuclear complex which displays the greater cellular uptake, **[3.1]**, also displays the greater toxicity and both dinuclear complexes are an order of magnitude less cytotoxic than their monometallic analogues **[2.3]** and **[2.4]** (IC_{50} values of 36 and 53 µM respectively –

Section 2.8.1). The mononuclear complexes bind to DNA with a lower affinity but CLSM studies reveal a greater degree of nuclear staining. Thus, toxicity correlates better with the relative uptake of the complexes into cells and not their overall binding affinity to DNA. However, it should be noted that determination of the exact intracellular concentration of each complex would be required to confirm this.

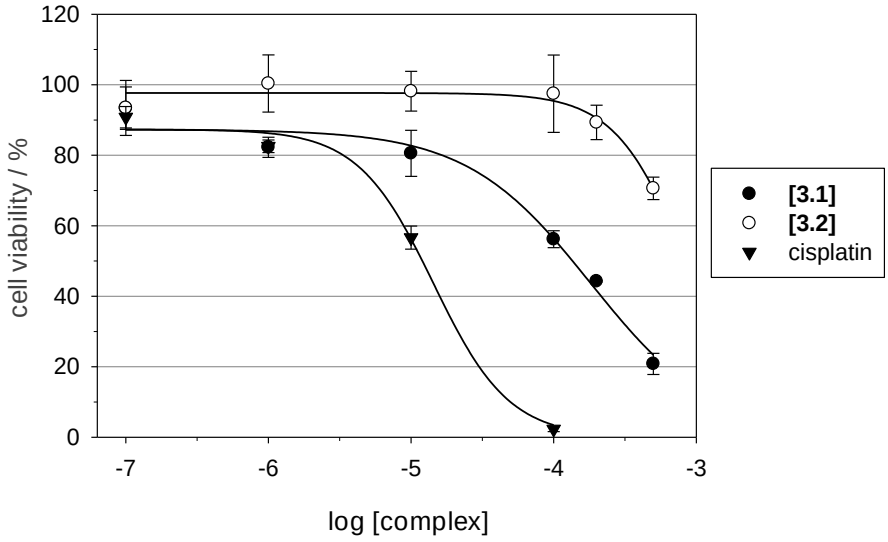

Figure 3.37 Cytotoxicity of dinuclear Ru(II)tpphz complexes **[3.1]** and **[3.2]** towards MCF-7 breast cancer cells (24 hr incubation time).

As the doubling time for MCF-7 cells is ~37 hours,[23] the incubation time was increased to 72 hours, to allowing time for cells to divide, and the cytotoxicity of each complex over this extended time period determined (Figure 3.38 and Table 3.5). Cisplatin is again included for comparative purposes.

With the greater exposure time of 72 hours, **[3.1]** now demonstrates much greater cytotoxicity and displays a similar potency to cisplatin (an IC_{50} value of 6 μM was obtained for each molecule - Table 3.5). A difference in behaviour between each complex is that cisplatin exhibits a greater

cytotoxicity at submicromolar concentrations. **[3.2]** also demonstrated an increase in toxicity but is two orders of magnitude less toxic than **[3.1]** and cisplatin (IC_{50} value of 168 μM – Table 3.5).

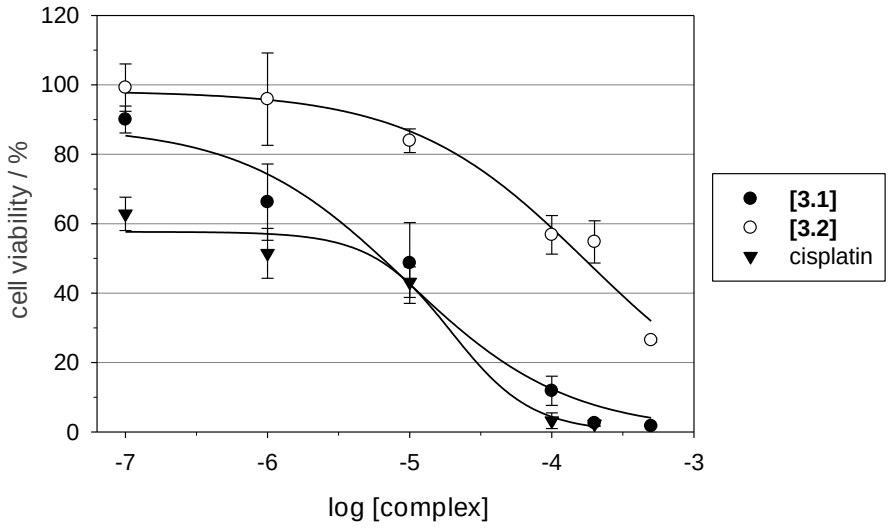

Figure 3.38 Cytotoxicity of dinuclear Ru(II)tpphz complexes **[3.1]** and **[3.2]** towards MCF-7 breast cancer cells (72 hr incubation time).

Complex	24 hr IC_{50} / μM	72 hr IC_{50} / μM
[3.1]	138 ± 6	6 ± 2
[3.2]	>500	168 ± 9
cisplatin	12 ± 3	6 ± 2

Table 3.5 IC_{50} values of dinuclear Ru(II) complexes towards MCF-7 cells.

As discussed in Section 1.1.7, interference with the processes that maintain telomere length is a current strategy for the development of novel chemotherapeutics in anti-cancer research. Small molecules that induce or stabilise quadruplexes at G-rich telomeric locations (specifically the 3'

overhang) are considered to be promising anti-cancer candidates and they have been shown to interfere with the process of telomere maintenance.[24, 25] Quadruplex formation at the telomeres of the chromosomes would be predicted to interfere with the process of cellular division, affecting long term viability of a population, not causing instant cell mortality.[26] The cytotoxicity results for **[3.1]** towards MCF-7 cells show exactly this behaviour; the complex shows a low short-term toxicity but, over a longer incubation time, it demonstrates cytotoxicity comparable to cisplatin. These results therefore make **[3.1]** of interest as a molecule that inhibits cancer cell growth. As **[3.1]** and **[3.2]** bind to quadruplex DNA with high affinity, and luminescent imaging experiments with **[3.1]** *in cellulo* reveal the presence of a peak that corresponds to complex binding to quadruplex DNA, the cytotoxicity of these complexes are of great interest. Many anti-cancer drugs, such as cisplatin, are limited by their toxic side effects, thus the low short-term toxicity of **[3.1]** may be an advantage in this context.

3.8.2 Cellular uptake and cytotoxicity

As CLSM and TEM studies have shown **[3.1]** to be successfully internalised by live cells and the molecule has been shown to demonstrate toxic effects against the MCF-7 cell line which increase with exposure time, the relationship between the cellular internalisation properties of the molecule and cytotoxicity of the molecule were explored.

3.8.2.1 Effects of media

It was shown in Section 3.6.3 that incubation of MCF-7 cells in DMEM media had the effect of inhibiting the uptake of **[3.1]** in comparison to RPMI. This property therefore provides an easy method by which to investigate the effect of cellular uptake efficiency upon the cytotoxic properties of **[3.1]**. HeLa cells, which may be cultured in either DMEM or RPMI media, were

incubated with solutions of **[3.1]** in DMEM or RPMI media and the effect upon cell viability of the complex in each media formulation determined.

Figure 3.39 and Table 3.6 show that **[3.1]** displays a low cytotoxicity towards HeLa cells when the incubation medium used is DMEM (IC_{50} value = 219 μM). However, when the incubation medium is RPMI, there is now a substantial increase in cytotoxicity (IC_{50} = 12 μM).

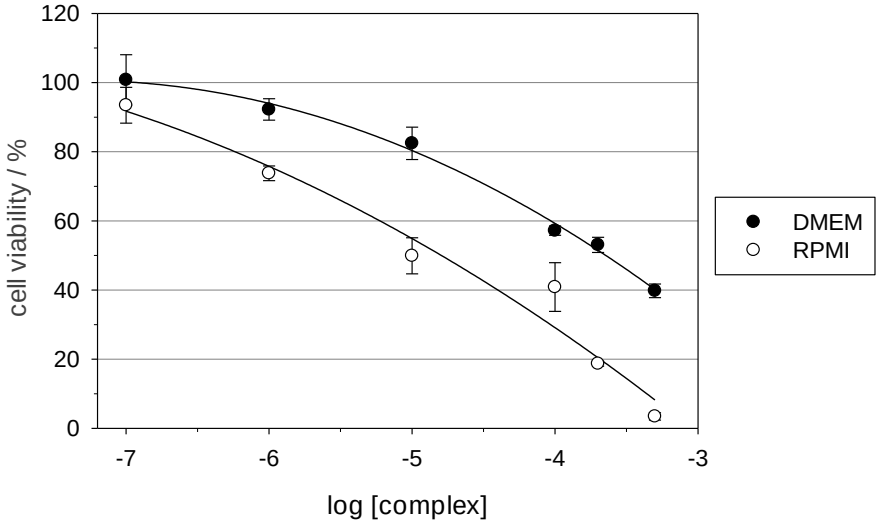

Figure 3.39 Cytotoxicity of **[3.1]** towards HeLa cervical cancer cells in either DMEM or RPMI growth/incubation media (24 hr incubation time).

Complex	DMEM IC_{50} / μM	RPMI IC_{50} / μM
[3.1]	219 ± 10	12 ± 2

Table 3.6 IC_{50} values of **[3.1]** towards the HeLa cell line in either DMEM or RPMI growth/incubation media (24 hour incubation time).

As the efficiency of **[3.1]** uptake was previously shown to be greater when HeLa cells were exposed to complexes in RMPI media compared to DMEM, these results reveal that an increase in cellular uptake of **[3.1]** is accompanied by an increase in cytotoxicity. This indicates that an intracellular mechanism is most likely to be responsible for the associated toxicity of the molecule.

It is interesting to note that **[3.1]** demonstrates a much greater cytotoxicity towards the HeLa cell line than MCF-7 cells over the same time period (IC_{50} values of 12 and 138 μM for HeLa and MCF-7 cells respectively). As HeLa cells divide more rapidly than MCF-7 cells (doubling times of 22 hrs and 37 hours for HeLa and MCF-7 cells respectively[27,23]) this would be in agreement with the toxicity of the molecule increasing as a function of increasing frequency of cell division.

3.8.2.2 IT_{50} values

In a similar fashion to the use of IC_{50} values (where the viability is measured at different concentrations for a given incubation time), the toxicity of a molecule may also be described by an IT_{50} value. This involves the viability being measured at different time points for a given concentration and the IT_{50} value is therefore the time at which a specific concentration would induce 50 % viability within the cell population.

As **[3.1]** displays significantly different *in cellulo* localisation at different concentrations, displaying nuclear staining after incubation with 500 μM in contrast to no observable nuclear staining after incubation with 100 μM, MCF-7 cells were incubated with solutions of **[3.1]** (10, 100 or 500 μM **[3.1]**) and the viability of the cells determined at time points. IT_{50} values

calculated for each concentration allows a direct comparison of the toxicity at each concentration.

Figure 3.40 shows the effect of cells incubated with three different concentrations of **[3.1]** and exponential decay relationships were plotted (data were fit to $y = ae^{-bx}$, where a and b are constants, R^2 >0.95). Table 3.7 shows the derived IT_{50} values.

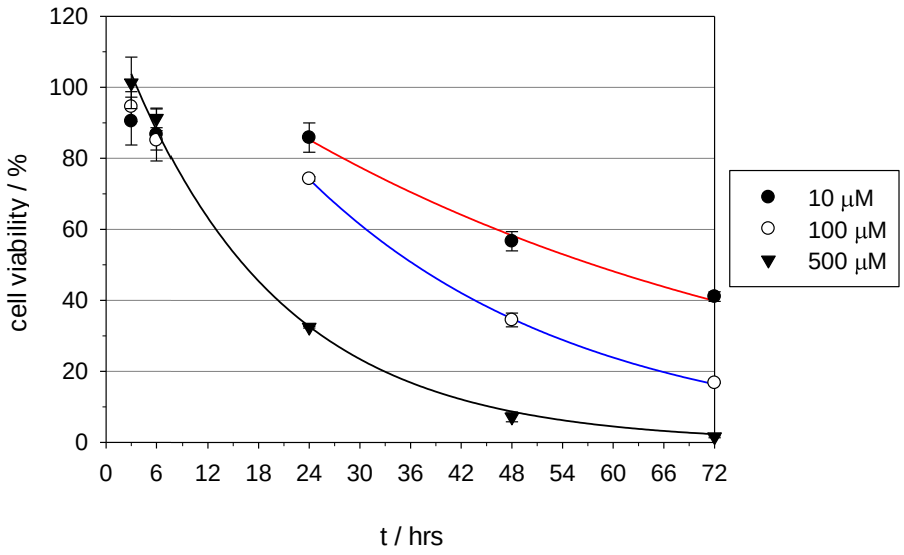

Figure 3.40 Cytotoxicity of **[3.1]** (incubation concentration 10, 100 or 500 μM) towards MCF-7 cells.

When these experiments are repeated for HeLa cells, a similar trend is observed (Figure 3.41). As for Section 3.8.2.1, a greater toxicity of **[3.1]** towards HeLa cells is observed, with each IT_{50} value being approximately half of that recorded for the MCF-7 cell line (Table 3.7), indicating that half the time is required to achieve 50% cell viability for each concentration measured.

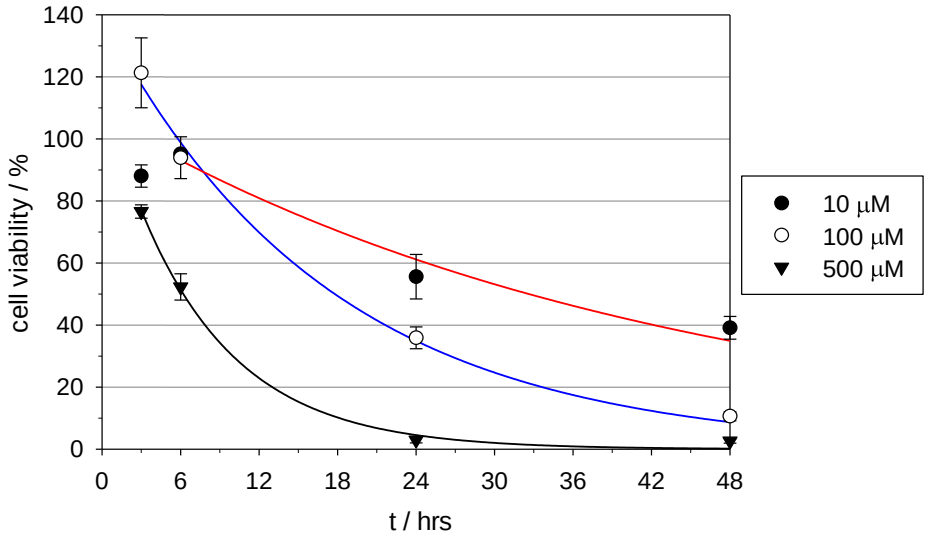

Figure 3.41 Cytotoxicity of **[3.1]** towards HeLa cells (incubation concentration 10, 100 or 500 μM).

[3.1] / μM	IT_{50} / hrs	
	MCF-7	HeLa
10	63 ± 3	33 ± 6
100	35 ± 3	18 ± 2
500	16 ± 1	6 ± 1

Table 3.7 IT_{50} values for **[3.1]** towards MCF-7 and HeLa cell lines.

These IT_{50} values clearly show the toxic effects of **[3.1]** – when the concentration is increased a decrease in the IT_{50} value is observed, as would be expected, and a non-linear relationship between IT_{50} value and concentration is apparent.

3.8.2.3 Nuclear uptake and toxicity

The cytotoxic effects demonstrated by **[3.1]** in Section 3.8.1 are of interest because the complex: a) binds to DNA with a high affinity and b) has been shown to bind to DNA in the nucleus of cells. These properties indicate that **[3.1]** has the potential to induce cell death by interfering with cellular process such as DNA replication and transcription.

However, in Section 3.4.1 it was noted that a high concentration (> 200 μM) and a short incubation time (1 hr) in serum-free media were factors required to achieve nuclear staining by **[3.1]** of MCF-7 cells. When MCF-7 cells were incubated with lower concentrations of **[3.1]** (100 μM, 24 hours), cells displayed minimal cellular uptake (Figure 3.3) yet these same incubation conditions cause the cell viability to be reduced to 56 % (Figure 3.37). When the incubation concentration is increased to 500 μM, a concentration shown to demonstrate significant nuclear staining (60% of cell nuclei stained after 1 hr – Figure 3.5), the cell viability now is 21 % after 24 hours exposure (Figure 3.37). These toxicity studies therefore raise the question of how the nuclear uptake properties of **[3.1]** are related to cellular viability and particularly the rate by which **[3.1]** can induce cell death after it has reached the nucleus.

To assess the effects of nuclear uptake of **[3.1]** upon cell health over an extended time period, MCF-7 cells were incubated with solutions of **[3.1]** (100 or 500 μM) in either serum-free or serum-containing media for 1 hr and the complex-containing solution was replaced with normal cell media. The viability of the cells was then determined at numerous time points after removal. An IT_{50} value for each experiment was thus obtained from these results and these values can be used to directly compare the toxicity effects for each of the incubation conditions.

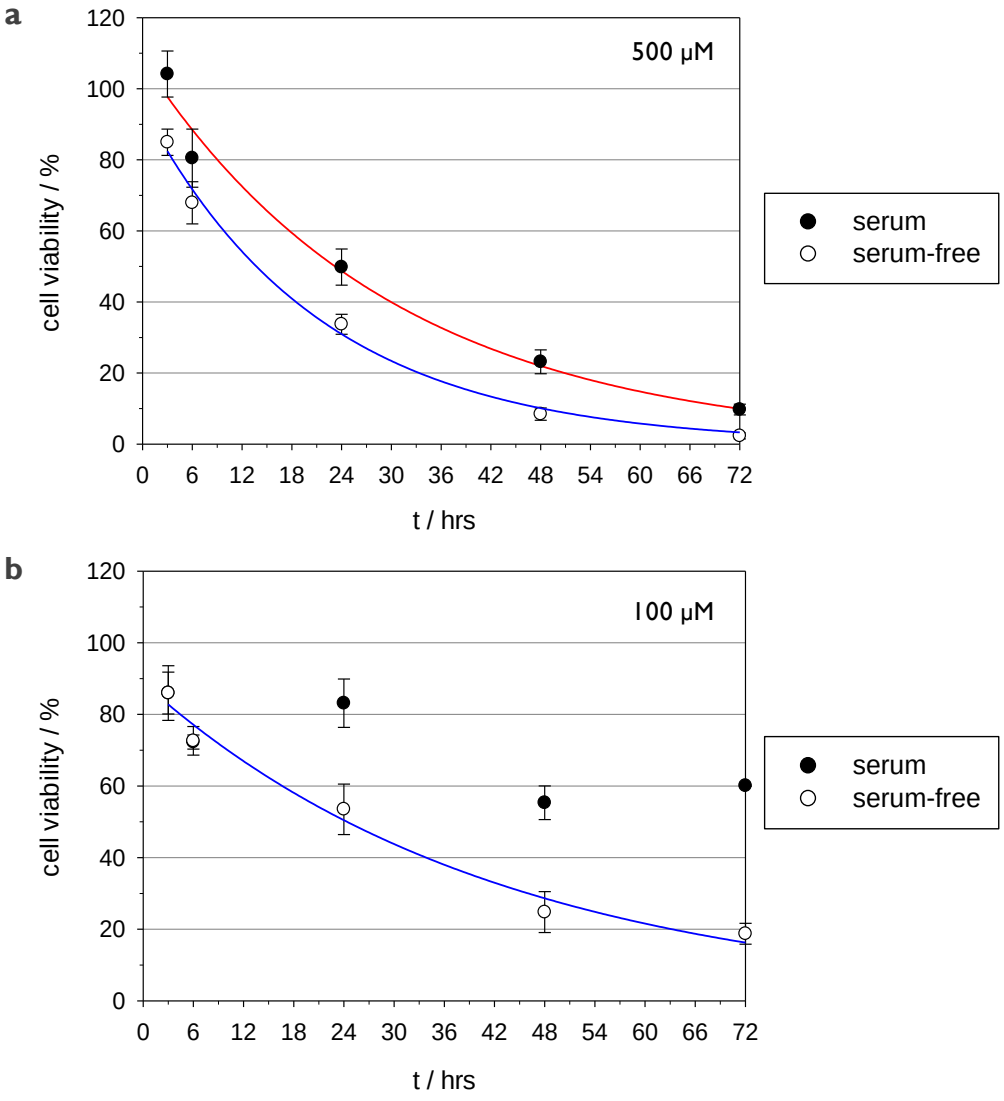

Figure 3.42 Effect on viability of MCF-7 cells incubated with 500 µM (**a**) or 100 µM (**b**) **[3.1]** for 1 hour in either serum-containing or serum-free media. Complex-containing media was removed and replaced with standard growth media.

Incubation conc. / μM	Incubation conditions	IT_{50} / hrs
500	+ serum	23 ± 2
500	- serum	14 ± 1
100	+ serum	>72
100	- serum	25 ± 2

Table 3.8 IT_{50} values for MCF-7 cells incubated with **[3.1]** for 1 hr towards MCF-7. Complex-containing media was removed and replaced with standard growth media.

Figure 3.42a and Table 3.8 show that the effect of incubating MCF-7 cells with 500 μM **[3.1]** for 1 hour significantly affects the viability of the cell population over time. An exponential decay in viability is again observed for incubation with 500 μM **[3.1]** in both serum and serum-free conditions and 100 μM **[3.1]** in serum-free conditions.

When the uptake of **[3.1]** is improved by using serum-free media during the incubation period (previously shown to achieve 98% nuclear staining of the population) this has the effect of significantly increasing the toxicity, with cells experiencing a more rapid decay in viability than those incubated in serum-containing media (IT_{50} = 14 hrs and 23 hrs respectively for 500 μM **[3.1]**). Cells incubated for 1 hour in serum-free media now display a greater toxicity (IT_{50} = 14 hrs) than cells incubated *continuously* with the complex at the same concentration in serum-containing media (IT_{50} = 16 hrs). When it is considered that Section 3.4.1 demonstrated that serum inhibits uptake, this provides further evidence that cellular uptake of **[3.1]** is responsible for the toxic effects demonstrated by the complex and that the toxicity of **[3.1]**

is achieved in a relatively short exposure time to the complex at this concentration.

When these experiments were repeated using a lower concentration (100 μM), and one which does not lead to successful nuclear luminescence, a significantly reduced toxicity is observed (Figure 2.42b, Table 3.8). The difference between cells incubated in serum and serum-free conditions is more pronounced (IT_{50} values >72 hours and 25 hrs respectively) and again, cells incubated for 1 hr in serum-free media display a greater toxicity than *constant* incubation with the same concentration in serum-containing media (IT_{50} value = 35 hours).

As cell imaging experiments using incubation of MCF-7 cells under these conditions display no evidence of DNA staining, these results show that nuclear uptake (at least to a level observable by CLSM) is not a requirement for **[3.1]** to demonstrate cytotoxicity properties.

With this in mind, two things that would explain the observed toxicity at 100 μM would be:

a) A small amount of **[3.1]** (unobservable by CLSM) bound to nuclear DNA is able to achieve significant cytotoxicity, which would be in agreement with the high binding affinity shown by the molecule.
b) Cytotoxicity is achieved by a non-nuclear DNA-binding mechanism. Given that **[3.1]** has also been shown to target mitochondria by TEM imaging, this would then represent the most likely cause of toxicity. Indeed, mitochondrial accumulation with associated toxicity has been observed for related DNA-binding Ru(II) polypyridyl complexes.[28, 29]

The previous observation that toxicity increases as a function of an increased frequency of cell division would support the premise that **[3.1]** achieves toxicity by interference with DNA metabolism, but a model where mitochondria are compromised would not be in agreement with this. These results raise the question of the exact mechanism by which **[3.1]** causes cell death and the possibility that more than one mechanism of cytotoxicity is occurring cannot be discounted. Clearly, further work in this area is required.

3.9 Conclusions and future work

In this chapter, the cellular DNA binding properties of two dinuclear Ru(II) tpphz light switch complexes in both live and fixed cells were investigated by a combination of CLSM and TEM microscopy. In addition, the cytotoxicity towards cancer cell lines was assessed.

The complex containing phen as the ancillary ligand, $[\{Ru(phen)_2\}_2(tpphz)]^{4+}$ **[3.1]**, was found to be internalised by the MCF-7 cell line, where it functions as an imaging agent for both CLSM and TEM. In CLSM studies, colocalisation with DAPI, clear visualisation of condensed chromosomes of mitotic cells and excitation/emission energies were all shown to be in agreement with previous *in vitro* DNA binding studies, strongly suggesting that the complex binds to DNA *in cellulo*, while TEM studies showed strong heterochromatin staining by the complex. Perhaps the most fascinating attribute of **[3.1]** as a DNA imaging tool is the existence on DNA binding of multiple emission peaks suggesting that this complex may find future application as an *in cellulo* DNA structural probe, specifically for quadruplex DNA. Using CLSM in conjunction with the use of specific cell process inhibitors, the cellular uptake mechanism was found to be *via* a

concentration-dependent, but non-endocytic, mechanism of active transport. In contrast to **[3.1]**, the bypyridine analogue, $[\{Ru(bpy)_2\}_2(tpphz)]^{4+}$ **[3.2]**, displayed a significantly lower cellular uptake, however, the complex was shown to stain DNA efficiently in fixed cells and thus may have application as a dead cell stain.

It is interesting to note that a similar behaviour for the mononuclear Ru(II)tpphz complexes in Chapter 2 was observed, where the bpy analogue, $[Ru(bpy)_2(tpphz)]^{2+}$ **[2.4]**, displayed lower levels of nuclear staining and cytotoxicity in live cells, presumably due to poorer cellular uptake of the complex in comparison to the complex containing phen as the ancillary ligand, $[Ru(phen)_2(tpphz)]^{2+}$ **[2.3]**. The results within this Chapter further demonstrate the effect of the ancillary ligand upon cellular uptake – with much reduced uptake for the bipyridine mononuclear and dinuclear complexes in comparison to the phen analogue. As the mechanism by which these molecules access their cellular targets involves an active uptake mechanism, rather than passive diffusion, this would suggest the existence of at least one specific receptor, and that the structural difference between bpy and phen determines the efficiency of cell internalisation rather than a physical (i.e. hydrophobic or lipophilic) effect.

Cell viability studies show that **[3.1]** displays a low toxicity towards the MCF-7 cell line after 24 hour incubation but when the incubation time is increased to 72 hours, the toxicity of the complex is equal to that of the anticancer drug cisplatin (IC_{50} values summarised in Table 3.9). Complex **[3.2]** demonstrated a significantly lower toxicity than **[3.1]**, suggesting that the greater efficiency of uptake of **[3.1]** is responsible for these toxic effects. **[3.1]** was shown to demonstrate a substantially greater toxicity towards HeLa cells when the incubation medium was RPMI compared to DMEM (IC_{50} values of 12 and 219 μM respectively). As DMEM had previously been

shown to inhibit cellular uptake of the complex, this further establishes that cellular uptake is responsible for the toxic properties of **[3.1]** and implies an intracellular mechanism of toxicity. Each dinuclear complex is significantly less cytotoxic than the monometallic metallo-intercalator. This would be in agreement with a greater rate of cellular uptake of **[2.3]** and **[2.4]** but it should also be noted that a different DNA binding mechanism (intercalative compared to groove-binding) could be responsible for the difference in toxicity. The toxic properties of **[3.1]** are particularly intriguing as **[3.1]** possesses a high affinity for quadruplex DNA *in vitro.* Along with the successful cellular uptake of the complex, this signifies the potential of the complex to interfere with cell proliferation by the disruption of telomere maintenance[25] making **[3.1]** of interest as the basis for the development of an anti-cancer therapeutic agent.

Complex	log P	IC_{50} / μM	
		MCF-7 (24 hr)	MCF-7 (72 hr)
[3.1]	-0.96 ± 0.09	138 ± 6	6 ± 2
[3.2]	-1.61 ± 0.10	>500	168 ± 9
cisplatin	-2.53*	12 ± 3	6 ± 2
[2.3]	-1.24 ± 0.12	36 ± 3	-
[2.4]	-2.08 ± 0.15	53 ± 7	-

Table 3.9 Compiled octanol/water partition coefficient and IC_{50} values of Ru(II) complexes towards MCF-7 cells. *Value obtained from Screnci *et al.*[30]

Future work in this area will investigate the toxicity of **[3.1]** towards a range of cancer and non-cancer cell lines. As the mechanism of DNA-binding of **[3.1]** is radically different to cisplatin, a reversible interaction rather than

direct coordination to DNA, it would be predicted that the mechanism of toxicity is also very different. This in turn would indicate that **[3.1]** will remain active against cisplatin-resistance cancer. Therefore, future work will focus on the toxicity of **[3.1]** towards cisplatin-resistance cancer cell lines and the mechanism by which **[3.1]** induces cell death. As the use of cisplatin is restricted by its high toxicity and associated side-effects, it would be hoped that the low short-term toxicity of **[3.1]** would be advantageous in this capacity.

3.10 References

1. C. Rajput, R. Rutkaite, L. Swanson, I. Haq and J. A. Thomas, Dinuclear Monointercalating Ru(II) Complexes That Display High Affinity Binding to Duplex and Quadruplex DNA, *Chem. Eur. J.*, 2006, **12**, 4611-4619.
2. D. A. Lutterman, A. Chouai, Y. Liu, Y. Sun, C. D. Stewart, K. R. Dunbar and C. Turro, Intercalation Is Not Required for DNA Light-Switch Behavior, *J. Am. Chem. Soc.*, 2008, **130**, 1163-1170.
3. C. G. Coates, J. J. McGarvey, P. L. Callaghan, M. Coletti and J. G. Hamilton, Probing the Interaction of $[Ru(phen)_2(dppz)]^{2+}$ with Single-Stranded DNA: What Degree of Protection Is Required for Operation of the "Light-Switch Effect"?, *J. Phys. Chem. B*, 2001, **105**, 730-735.
4. T. Wilson, PhD Thesis, University of Sheffield, 2009.
5. J. Bolger, A. Gourdon, E. Ishow and J. P. Launay, Mononuclear and Binuclear Tetrapyrido[3,2-a:2',3'-c:3",2"-h:2"',3"'-j]phenazine (tpphz) Ruthenium and Osmium Complexes, *Inorg. Chem.*, 1996, **35**, 2937-2944.
6. B. P. Sullivan, D. J. Salmon and T. J. Meyer, Mixed phosphine 2,2'-bipyridine complexes of ruthenium, *Inorg. Chem.*, 1978, **17**, 3334-3341.
7. www.molinspiration.com
8. H. Derrat, MPhil Thesis, University of Sheffield, 2009.
9. E. W. Taylor, The mechanism of colchicine inhibition of mitosis, *J. Cell Biol.*, 1965, **25**, 145-160.

10. M. P. Douglas and S. O. Rogers, DNA damage caused by common cytological fixatives, *Mutat. Res.*, 1998, **401**, 77-88.
11. A. Canela, E. Vera, P. Klatt and M. A. Blasco, High-throughput telomere length quantification by FISH and its application to human population studies, *Proc. Natl. Acad. Sci. U. S. A.*, 2007, **104**, 5300-5305.
12. U. Schatzschneider, J. Niesel, I. Ott, R. Gust, H. Alborzinia and S. Wölfl, Cellular Uptake, Cytotoxicity, and Metabolic Profiling of Human Cancer Cells Treated with Ruthenium(II) Polypyridyl Complexes $[Ru(bpy)_2(N\text{-}N)]Cl_2$ with N-N=bpy, phen, dpq, dppz, and dppn., *ChemMedChem*, 2008, **3**, 1104-1109.
13. R. Wattiaux, N. Laurent, S. Wattiaux-De Coninck and M. Jadot, Endosomes, lysosomes: their implication in gene transfer, *Adv. Drug Delivery Rev.*, 2000, **41**, 201-208.
14. H. K. Ziegler and E. R. Unanue, Decrease in macrophage antigen catabolism caused by ammonia and chloroquine is associated with inhibition of antigen presentation to T cells, *Proc. Natl. Acad. Sci. U.S.A.*, 1982, **79**, 175-178.
15. L. H. Wang, K. G. Rothberg and R. G. Anderson, Mis-assembly of clathrin lattices on endosomes reveals a regulatory switch for coated pit formation, *J. Cell Biol.*, 1993, **123**, 1107-1117.
16. J. E. Schnitzer, P. Oh, E. Pinney and J. Allard, Filipin-sensitive caveolae-mediated transport in endothelium: reduced transcytosis, scavenger endocytosis, and capillary permeability of select macromolecules, *J. Cell Biol.*, 1994, **127**, 1217-1232.
17. M. L. Elkjaer, H. Birn, P. Agre, E. I. Christensen and S. Nielsen, Effects of microtubule disruption on endocytosis, membrane recycling and polarized distribution of Aquaporin-1 and gp330 in proximal tubule cells, *Eur. J. Cell Biol.*, 1995, **67**, 57-72.
18. www.sigmaaldrich.com
19. N. Parker, M. J. Turk, E. Westrick, J. D. Lewis, P. S. Low and C. P. Leamon, Folate receptor expression in carcinomas and normal tissues determined by a quantitative radioligand binding assay, *Anal. Biochem.*, 2005, **338**, 284-293.
20. J. Sudimack and R. J. Lee, Targeted drug delivery via the folate receptor, *Adv. Drug Delivery Rev.*, 2000, **41**, 147-162.
21. N. Pante and M. Kann, Nuclear Pore Complex Is Able to Transport Macromolecules with Diameters of ~39 nm, *Mol. Biol. Cell*, 2002, **13**, 425-434.
22. B. Alberts, A. Johnson, J. Lewis, M. Raff, K. Roberts and P. Walter, *Molecular Biology of the Cell*, 5th edn., Garland Science, New York, 2007.

23. H. D. Soule, J. Vasquez, A. Long, S. Albert and M. Brennan, A human cell line from a pleural effusion derived from a breast carcinoma, *J. Natl. Cancer Inst.*, 1973, **51**, 1409-1416.

24. H. Han and L. H. Hurley, G-quadruplex DNA: a potential target for anti-cancer drug design, *Trends Pharmacol. Sci.*, 2000, **21**, 136-142.

25. S. Neidle and G. N. Parkinson, Telomere maintenance as a target for anticancer drug discovery, *Nat. Rev. Drug Discovery*, 2002, **1**, 383-393.

26. A. De Cian, L. Lacroix, C. Douarre, N. Temime-Smaali, C. Trentesaux, J.-F. Riou and J.-L. Mergny, Targeting telomeres and telomerase, *Biochimie*, 2008, **90**, 131-155.

27. Z. M. Mu, X. F. Le, S. Vallian, A. B. Glassman and K. S. Chang, Stable overexpression of PML alters regulation of cell cycle progression in HeLa cells, *Carcinogenesis*, 1997, **18**, 2063-2069.

28. T. Chen, Y. Liu, W.-J. Zheng, J. Liu and Y.-S. Wong, Ruthenium Polypyridyl Complexes That Induce Mitochondria-Mediated Apoptosis in Cancer Cells, *Inorg. Chem.*, 2010, **49**, 6366-6368.

29. M. J. Pisani, D. K. Weber, K. Heimann, J. G. Collins and F. R. Keene, Selective mitochondrial accumulation of cytotoxic dinuclear polypyridyl ruthenium(ii) complexes, *Metallomics*, 2010, **2**, 393-396.

30. D. Screnci, M. J. McKeage, P. Galettis, T. W. Hambley, B. D. Palmer and B. C. Baguley, Relationships between hydrophobicity, reactivity, accumulation and peripheral nerve toxicity of a series of platinum drugs, *Br. J. Cancer*, 2000, **82**, 966-972.

Chapter 4

A series of substituted dinuclear Ru(II)tpphz complexes

4.1 Introduction

In the previous chapter, a dinuclear Ru(II) complex with a ditopic tpphz ligand and phen as the ancillary ligand, **[3.1]**, was shown to be internalised by cells and bind to nuclear DNA. This was observable by CLSM and TEM as the molecule acts a DNA imaging agent for both of these techniques. In addition to the imaging properties displayed by the complex, **[3.1]** also demonstrated cytotoxicity equal to that of cisplatin over an extended incubation time. In contrast, the dinuclear Ru(II)tpphz containing bpy as the ancillary ligand in place of phen, **[3.2]**, demonstrated significantly lower cellular uptake and cytotoxicity. This highlights the importance of ancillary ligands in the bioactivity of the complex. To further explore this effect and with the aim of generating further bioactive molecules, a series of derivatives of **[3.1]** were prepared using ligand substitution (Figure 4.1) and the DNA binding, cellular imaging and cytotoxic properties of the series was investigated.

The ligands selected were the methyl-substituted phenanthrolines 5mp (5-methyl-1,10-phenanthroline) and dmp (2,9-dimethyl-1,10-phenanthroline) and the phenyl-substituted DIP (4,7-diphenyl-1,10-phenanthroline) ligand. Methyl-substitution offers a method by which to subtly tailor the properties of a molecule including the *in vitro* DNA binding affinity, luminescent

emission wavelength and hydrophobicity whereas the use of DIP as an ancillary ligand has been shown to promote cellular uptake as its high hydrophobicity often increases the membrane-permeability of complexes.[1-4]

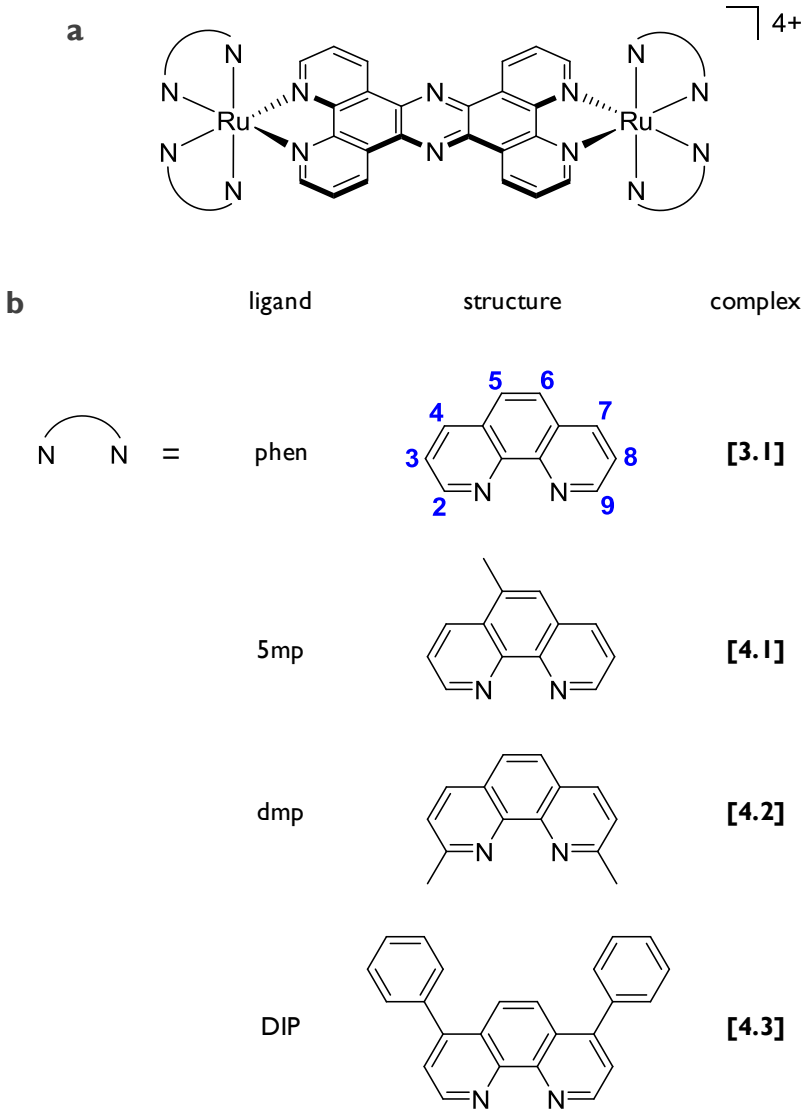

Figure 4.1 a, Structure of dinuclear Ru(II)tpphz complexes. **b,** Structure of ancillary ligands: phen, including substitution site numbers, 5-methyl-phen (5mp), 2,9-dimethyl-phen (dmp) and 4,7-diphenyl-phen (DIP).

4.2 Synthesis

4.2.1 Ligand synthesis

The tpphz ligand was synthesised using the same method described in Chapter 3 (Scheme 3.1). [5]

4.2.2 Complex synthesis

The final products $[\{Ru(5mp)_2\}_2(tpphz)]^{4+}$ **[4.1]**, $[\{Ru(dmp)_2\}_2(tpphz)]^{4+}$ **[4.2]** and $[\{Ru(DIP)_2\}_2(tpphz)]^{4+}$ **[4.3]** were prepared using the same method as described in Chapter 3 for the synthesis of **[3.1]** with either 5mp, dmp or DIP replacing phen as the ancillary ligand - Scheme 4.1.[5-7] One advantage to this approach is that all three ancillary ligands are available from commercial sources, eliminating the need for additional synthetic steps.

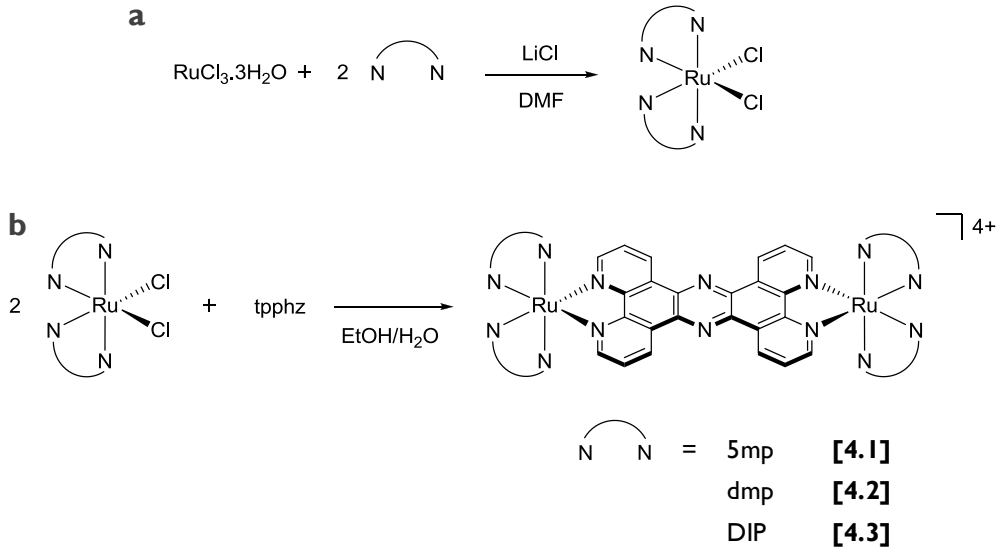

Scheme 4.1 a, Synthesis of $[Ru(N^N)Cl_2]$ precursors (yields ranged from 47 - 56 %). **b,** Synthesis of **[4.1]** - **[4.3]** (yields ranged from 74 - 86 %).

All complexes were synthesised as their hexafluorophosphate salts and characterised by NMR, mass spectroscopy and elemental analysis. Unless stated otherwise, each complex was used as the chloride salt. They were converted into their water-soluble chloride salts by counter-ion metathesis using acetone solutions of tetrabuylammonium chloride. Each complex was used as a mixture of stereoisomers.

4.3 Photochemistry

4.3.1 Absorption spectra

UV-visible absorption spectra for the PF_6^- salt of each complex were recorded in acetonitrile at room temperature. Figure 4.2 shows an example spectrum for **[4.1]** and Table 4.1 displays the full spectroscopic details for complexes **[4.1]** – **[4.3]**. The high energy peaks (< 370 nm) can be assigned to ligand-centred $\pi \rightarrow \pi^*$ transitions and the broad, low energy emission (~350 – 550 nm) is characteristic of metal-to-ligand charge-transfer from the Ru(II) metal centre(s) to the polypyridyl ligand(s).[8]

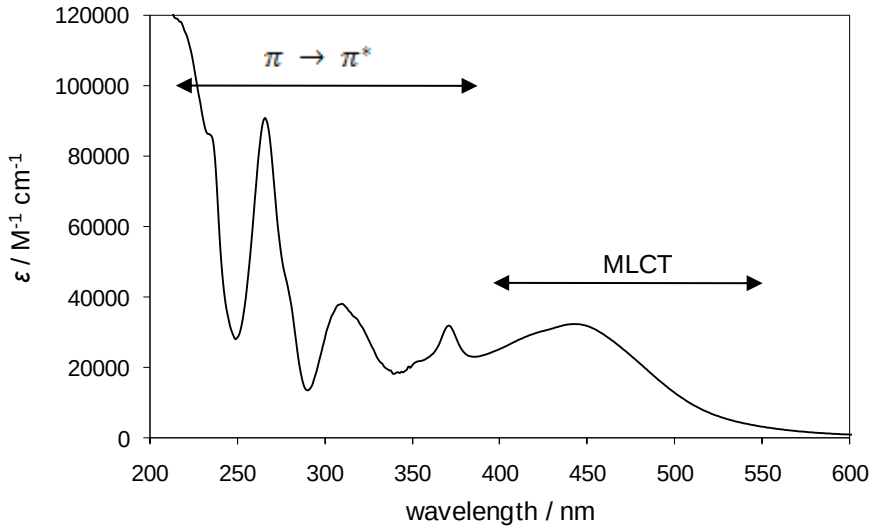

Figure 4.2 UV-vis absorbance spectra of **[4.1]** in acetonitrile at room temperature. MLCT = metal to ligand charge transfer.

Complex	Absorption peak		Assignment
	λ_{max} / nm	ε / M^{-1} cm^{-1}	
[4.1]	202	156000	$\pi \rightarrow \pi^*$
	266	93700	$\pi \rightarrow \pi^*$
	311	37900	$\pi \rightarrow \pi^*$
	371	31400	$\pi \rightarrow \pi^*$
	443	32200	MLCT
[4.2]	206	168400	$\pi \rightarrow \pi^*$
	268	68700	$\pi \rightarrow \pi^*$
	311	53500	$\pi \rightarrow \pi^*$
	374	33100	$\pi \rightarrow \pi^*$
	449	22700	MLCT
[4.3]	202	220800	$\pi \rightarrow \pi^*$
	271	105500	$\pi \rightarrow \pi^*$
	311	77100	$\pi \rightarrow \pi^*$
	372	31800	$\pi \rightarrow \pi^*$
	454	45700	MLCT

Table 4.1 UV-vis spectroscopy data for **[4.1]** – **[4.3]** in acetonitrile at room temperature.

From Figure 4.2 and Table 4.1 it can be seen that each dinuclear Ru(II) complex exhibits ligand-centred $\pi \rightarrow \pi^*$ transitions originating from the polypyridyl ligands (peaks located at ~206, ~268, ~311 and ~371 nm). In addition to these transitions, broad Ru → N^N and Ru → tpphz MLCT absorptions in the visible region of the spectrum are also observed (~450

nm). The equivalent peaks were described for the both the parent phen complex **[3.1]** and the bipyridine analogue **[3.2]**.[9-11]

Examining each peak in more detail, it can be seen that the molar extinction coefficient for the peak at ~371 nm is equal for each complex (ε = 31400 ± 1600 M^{-1} cm^{-1}). As each molecule posses a single tpphz ligand, this band can therefore be assigned to a $\pi \rightarrow \pi^*$ transition primarily located on the tpphz ligand. The wavelength and intensity of bands at ~206, ~268 and ~311 nm correlate with the nature of the ancillary ligand – for example, the complex containing DIP as the ancillary ligand, **[4.3]**, displays the largest molar extinction coefficient for each absorption peak. As the DIP ligand possesses the most extended delocalised π system of the ancillary ligands investigated, this implies that these absorption bands are due to $\pi \rightarrow \pi^*$ transitions predominantly located on the ancillary (N^N) ligand.

The UV-visible absorption spectra for the Cl^- salt of **[4.1]** and **[4.2]** were recorded in water and the data is summarized in Table 4.2. No results for **[4.3]** were obtained as the complex was found to be insoluble in pure water. Unsurprisingly, each complex displays essentially the same peaks as for the PF_6^- salt in acetonitrile, although a small red shift of the MLCT absorptions in the visible region (450 to 455 nm) and a significant increase in the absorbance at 266 nm that subsumes the peak at 371 nm are observed when the complex is dissolved in water.

Complex	Absorption peak		Assignment
	λ_{max} / nm	ε / M^{-1} cm^{-1}	
[4.1]	202	217400	$\pi \rightarrow \pi^*$
	266	162800	$\pi \rightarrow \pi^*$
	371	31400	$\pi \rightarrow \pi^*$
	445	34000	MLCT
[4.2]	206	114300	$\pi \rightarrow \pi^*$
	268	137500	$\pi \rightarrow \pi^*$
	374	34600	$\pi \rightarrow \pi^*$
	454	25300	MLCT
[4.3]	not water-soluble		-

Table 4.2 UV-vis spectroscopy data for **[4.1]** and **[4.2]** in water at room temperature.

4.3.2 Excitation and emission spectra

^{1}MLCT excitation in acetonitrile (λ_{ex} = 450 nm) results in observable luminescence for all three complexes (600 – 750 nm), characteristic of emission from a ^{3}MLCT state.[8] Given the structural similarity of the complexes and the fact that the excited state involves ^{1}MLCT and ^{3}MLCT states located on the tpphz ligand, the excitation/emission spectra for each complex display very similar properties. An example of the excitation/emission spectra observed for **[4.1]** is shown in Figure 4.3 and Table 4.3 summarises the full spectroscopic details for complexes **[4.1]** – **[4.3]**.

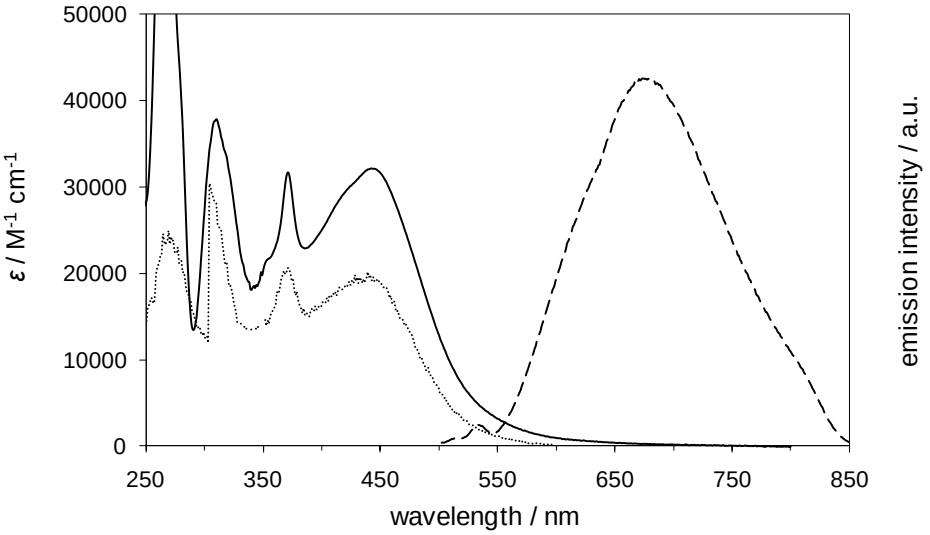

Figure 4.3 Absorption (——), excitation (·····) and emission (– – –) spectra of 5 μM **[4.1]** in acetonitrile at room temperature. λ_{em} = 660 nm and λ_{ex} = 450 nm for excitation and emission spectra respectively. a.u. = arbitrary units.

The quantum yields were calculated using Equation 4.1 and are summarised in Table 4.3. The quantum yield for **[3.1]** is included for comparison.[9]

$$\varphi_x = \varphi_{ref}\left(\frac{A_{ref}}{I_{ref}}\right)\left(\frac{I_x}{A_x}\right)\left(\frac{\eta_x}{\eta_{ref}}\right)^2$$

Equation 4.1 Quantum yield. Φ = quantum yield, *A* = absorbance at the excitation wavelength, *I* = integrated emission intensity, *η* = solvent refractive index for the reference (*ref*) and sample (*x*).

As Table 4.3 shows, when the ancillary ligand is changed from phen to 5mp, each dinuclear ruthenium complex displays comparable levels of luminescence, with **[4.1]** displaying the greater emission intensity (Φ = 5×10^{-3} and 6.9×10^{-3} for **[3.1]** and **[4.1]** respectively). However, when the ancillary ligand is changed to dmp, the complex now demonstrates much lower emission intensity and the quantum yield of **[4.2]** (Φ = 3×10^{-4}) is now an order of magnitude weaker than that of **[3.1]** in the same solvent. The

complex that contains DIP as the ancillary ligand, **[4.3]**, displays a significant increase in emission intensity (Φ = 1.7×10^{-2}) compared to the parent complex **[3.1]** and 5-methyl derivative **[4.1]**.

Complex	λ_{ex} / nm (λ_{em} / nm)	λ_{em} max / nm (λ_{ex} = 450 nm)	Φ (λ_{ex} / nm)
[4.1]	263, 302, 366, 440 (670)	670	$6.9 \pm 0.7 \times 10^{-3}$ (450)
[4.2]	372, 450 (670)	670	$3 \pm 2 \times 10^{-4}$ (450)
[4.3]	271, 303, 370, 440 (640)	640	0.017 ± 0.002 (450)
[3.1]	-	710	5×10^{-3} (439)

Table 4.3 Luminescence data for **[4.1]** – **[4.3]** in acetonitrile at room temperature. Data for **[3.1]** is included for reference.[9]

As the DIP ligand possesses the greatest delocalised π system of the ancillary ligands for **[4.1]** – **[4.3]**, this increase in emission intensity would suggest that the observed MLCT emission of **[4.3]** is comprised of a significant Ru → N^N MLCT emission in addition to the Ru → tpphz MLCT emission, a factor that would additionally be responsible for the broad and blue-shifted peak. The large size of the DIP ligand may also act to sterically protect the tpphz ligand from the bulk solvent meaning the MLCT excited state would interact less with solvent molecules which would cause an enhancement in emission intensity. These results indicate that the addition of a methyl group at the 5 position of the phen ligand does not significantly alter the luminescent properties of the dinuclear complex in acetonitrile whereas, in contrast, the addition of two methyl groups at the 2 and 9

positions decreases the luminescent properties. The addition of two phenyl groups at the 4 and 7 positions acts to improve the luminescent properties. This shows how the choice of ancillary ligand can alter the luminescent properties of the molecule as a whole.

In water, upon ^{1}MLCT excitation (λ_{ex} = 450 nm), **[4.1]** displays reduced emission in water ($\Phi = 1.62\times10^{-3}$) and the emission maximum is blue-shifted by ~70 nm to 600 nm (Figure 4.4 and Table 4.4) – this large solvent shift is a well-documented effect in agreement with related work.[10] **[4.2]** displayed no observable luminescence. The decrease of luminescence for each complex in aqueous conditions in comparison to acetonitrile solvent is due to the well documented effect of water quenching the ^{3}MLCT $\rightarrow$ ^{1}GS transition by hydrogen bonding to the phenazine nitrogen atoms of the tpphz ligand.[12]

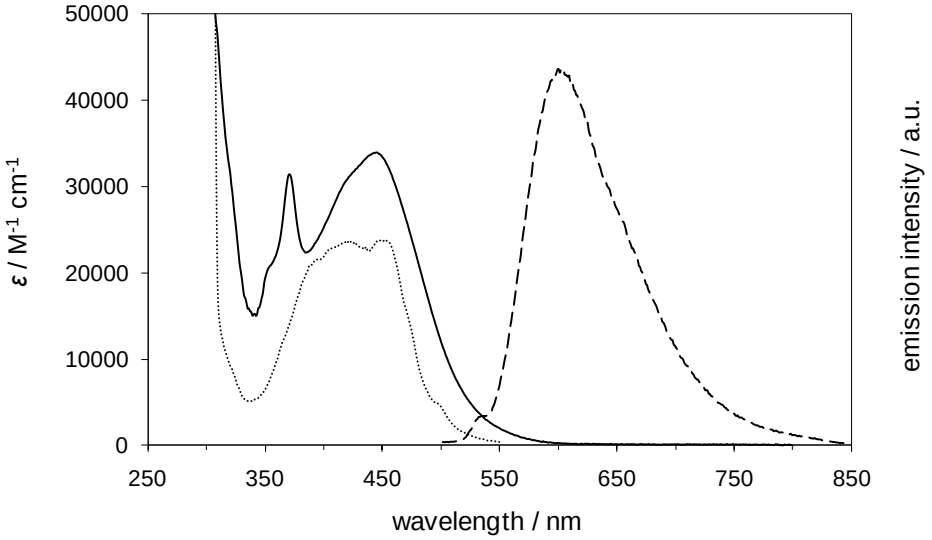

Figure 4.4 Absorption (——), excitation (·····) and emission (– – –) spectra of 5 μM **[4.1]** in water at room temperature. λ_{em} = 660 nm and λ_{ex} = 450 nm for excitation and emission spectra respectively. a.u. = arbitrary units.

Complex	λ_{ex} / nm (λ_{em} / nm)	λ_{em} max / nm (λ_{ex} = 450 nm)	Φ (λ_{ex} / nm)
[4.1]	263, 450 (600)	600	$1.6 \pm 0.5 \times 10^{-3}$ (450)
[4.2]	non-emissive	-	-

Table 4.4 Luminescence data for **[4.1]** and **[4.2]** in water at room temperature.

The luminescence from **[4.1]** in water was unexpected and not observed for the parent complex **[3.1]**.[7] C. Turro *et al.* suggest that relatively small amounts of the monometallic complex $[Ru(N^N)_2(tpphz)]^{2+}$ as an impurity can result in shifted luminescence peaks[10] but this would not explain the behaviour of **[4.1]** observed in water as the Ru → tpphz MLCT emission of these impurities in water would be predicted to be quenched by hydrogen bonding. The possibility that the observed emission at 600 nm of **[4.1]** is due to a Ru → N^N MLCT transition cannot be discounted. Indeed, work by Barton and N. Turro show the aqueous emission spectra of $[Ru(phen)_3]^{2+}$ is comprised of two peaks – one of which occurs at 600 nm[13] – in agreement with the peak observed for **[4.1]** in water (600 nm). Why this peak is not observed for the parent complex **[3.1]** remains unclear.

To fully establish the exact nature of this emission, further work involving purification of **[4.1]** by exacting separation methods such as HPLC (high performance liquid chromatography) and a comparison of its photochemical properties with related complexes such as $[Ru(5mp)_3]^{2+}$ would be required.

4.4 DNA binding studies

As the interaction between the parent complex **[3.1]** and DNA results in the characteristic light switch effect,[7] the ability of **[4.1]** and **[4.2]** to similarly bind to DNA *in vitro* with an accompanying increase in luminescence was investigated.

As can be seen in Figure 4.5, the addition of calf thymus DNA (CT-DNA) to aqueous solutions of **[4.1]** or **[4.2]** resulted in a significant enhancement of the ^{3}MLCT luminescence emission for each, indicating that both complexes are behaving as DNA light switch systems. The emission maximum for both **[4.1]** and **[4.2]** (~665 nm) is the same as that reported for **[3.1]**.[7] This light switch effect is the result of binding to DNA shielding the tpphz phenazine nitrogen atoms from hydrogen bonding with water, activating luminescence, as opposed to the quenched emission of the free complex.

In addition to this being an advantageous property in an imaging context, the increase in luminescence intensities of each complex upon the addition of CT-DNA can be used to assess the binding affinity of each complex with DNA. This technique involves a known concentration of DNA being titrated into a known concentration of the complex and the intensity of the resultant ^{3}MLCT emission DNA measured until the emission intensity reaches a maximum and does not increase when further DNA is added.

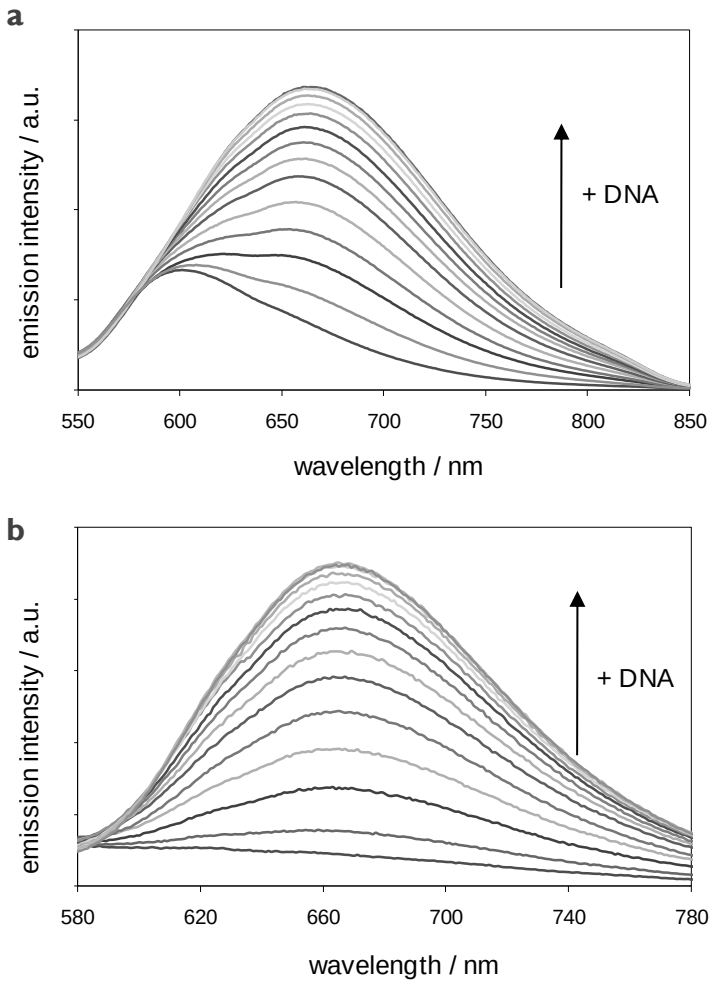

Figure 4.5 Increase of luminescence of **[4.1]** (**a**) and **[4.2]** (**b**) in aqueous buffer solution (25 mM NaCl, 5 mM Tris, pH 7.0) on addition of CT-DNA.

The data obtained from these luminescent titrations can then be used to calculate the fraction of the complex bound by the following equation:

$$\chi = \frac{\left(I_{obs} - I_f\right)}{\left(I_b - I_f\right)} \qquad \textbf{Equation 4.2}$$

Where χ is the fraction of the complex bound and I_{obs}, I_b and I_f are the emission intensities of the observed, fully bound and free complex respectively.

The ratio of the bound complex, C_b, to the concentration of DNA (in base pairs), r, may be given by:

$$r = \frac{C_b}{[\text{DNA}]} \qquad \textbf{Equation 4.3}$$

$$\text{where} \qquad C_b = \chi[\text{complex}] \qquad \textbf{Equation 4.4}$$

And it follows that the concentration of the free complex, C_f, is given by:

$$C_f = C_i - C_b \qquad \textbf{Equation 4.5}$$

Where C_i is the initial concentration.

The Scatchard equation is a commonly used equation for determining the affinity constant of a ligand with a receptor (Equation 4.6) and a plot of r/C_f v. r (the Scatchard plot) can be used to determine the equilibrium binding constant, K_b, and the number of binding sites per molecule, n.[14]

$$\frac{r}{C_f} = K_b(n - r) \qquad \textbf{Equation 4.6}$$

The Scatchard binding model works well with 1:1 binding systems but when the binding is more complicated, such as for small molecules binding to DNA, the relationship between r/C_f and r is non-linear and, as a result, the Scatchard equation is an inaccurate model. To more accurately fit the data the McGhee-von Hippel model – Equation 4.7 - is used to fit the data.[15] From this equation, the y-intercept yields the equilibrium binding constant K_b and the reciprocal of the x-intercept is equal to n, which is the number of DNA binding sites (in base pairs) occupied by the small molecule.

$$\frac{r}{C_f} = K_b(1 - nr)\left(\frac{1 - nr}{1 - (n-1)r}\right)^{n-1} \qquad \textbf{Equation 4.7}$$

As the binding reaches saturation, the number of free binding sites smaller than n increases significantly and an effective concentration of the complex up to two orders of magnitude can be required to increase the occupancy of binding sites from 90-100%. This has the effect of artificially increasing the binding constant for the molecule and so, to minimise these effects, the model is fit to the experimental data for 30 – 90% of the complex bound.[16]

To measure the binding of **[4.1]** and **[4.2]** with DNA, I_{obs}, I_b and I_f were obtained from the luminescence binding titration of each complex with CT-DNA and a binding curve for each complex was constructed, which is shown in Figure 4.6. The equilibrium binding constant for each complex with CT-DNA was calculated by displaying the data as Scatchard plots (χ = 30 – 90%) and the data fit to the McGhee-von Hippel model (Figure 4.6). The model fitted the data well and in each case the R^2 value was >0.95. Table 4.5 contains the values for K_b and n value obtained for each complex.

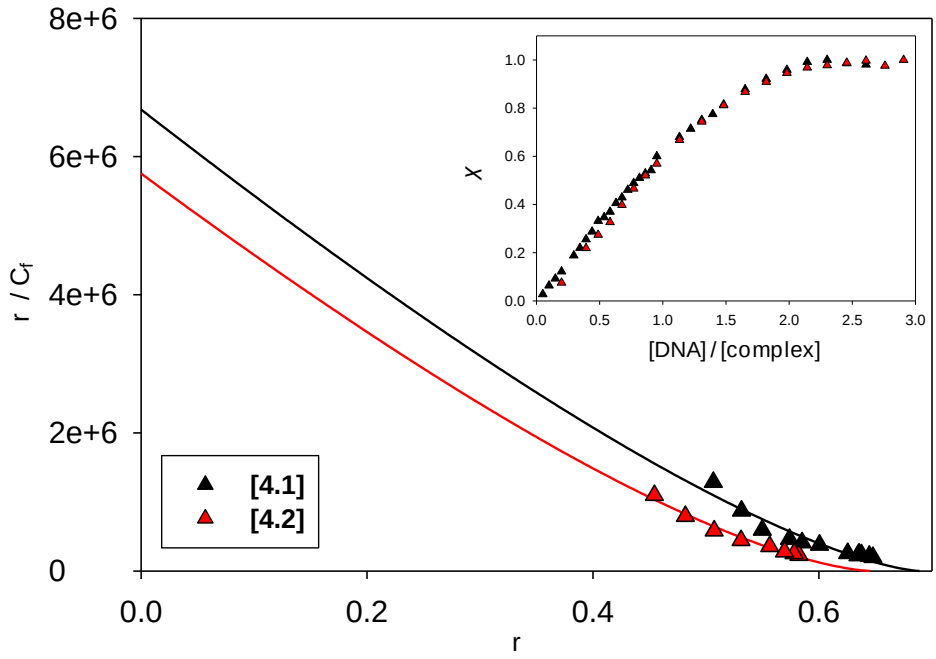

Figure 4.6 Binding curves (inset) and Scatchard plots with McGhee-von Hippel best fit (outset) obtained by luminescent titrations of **[4.1]** or **[4.2]** with DNA (25 mM NaCl, 5 mM Tris, pH 7.0).

Complex	I_b / I_f	K_b / M^{-1}	n
[4.1]	27	$6.7 \pm 0.8 \times 10^6$	1.45 ± 0.02
[4.2]	62	$5.8 \pm 0.4 \times 10^6$	1.55 ± 0.02
[3.1]	~60*	1.1×10^{7}*	2.9*

Table 4.5 Luminescent properties, equilibrium binding constant K_b and binding site size *n* (in base pairs) for **[4.1]** and **[4.2]** binding with CT-DNA (25 mM NaCl, 5 mM Tris, pH 7.0). *Data for **[3.1]** is included for reference.[7]

As shown by Table 4.5, both **[4.1]** and **[4.2]** display a similar binding affinity for DNA as the parent complex **[3.1]** and the DNA binding affinities of all three complexes lies in the 10^6 M^{-1} range. This is the same order of magnitude as a classical metallo-intercalator such as $[Ru(phen)_2(dppz)]^{2+}$.[17] As the binding affinity of the mononuclear intercalator $[Ru(phen)_2(tpphz)]^{2+}$ was found to be an order of magnitude lower ($K_b = 3.0\times10^5$ M^{-1}) [18] than that observed for **[4.1]** and **[4.2]** and considering that the related dinuclear tpphz complex $[\{Ru(bpy)_2\}_2(tpphz)]^{4+}$ **[3.2]** interacts with DNA by a groove binding mechanism,[10] the binding affinities of **[4.1]** and **[4.2]** with CT-DNA in this work are therefore in agreement with a groove binding mode of action accompanied by a significant electrostatic contribution due to the high charge (4+) of each molecule although further binding studies would be required to confirm this hypothesis.

Other work has shown the effect of methyl-substitution on the DNA binding properties of metallo-intercalators to be location dependent; the addition of a methyl group(s) on the ancillary ligand can either display a minimal effect or inhibition of binding, depending upon the substitution position.[19, 20] This implies it is the steric properties of the methyl-substituted derivative that govern the DNA affinity of the molecule as a whole. The results in Table 4.5

show that this behaviour is observed for these dinuclear Ru(II)tpphz systems.

4.5 Partition coefficients

The octanol/water partition coefficients of **[4.1]** and **[4.2]** were measured using the "shake flask" method and the log P value for each complex determined (Table 4.6). The mass of each complex, excluding the counter-ion, is included to provide a measure of the relative size of each complex. The partition coefficient for the parent complex $[\{Ru(phen)_2\}_2(tpphz)]^{4+}$ **[3.1],** as recorded in Chapter 3, is included for comparison. The octanol/water partition coefficient for $[\{Ru(DIP)_2\}_2(tpphz)]^{4+}$ **[4.3]** could not be assessed by this method due to the extremely poor water-solubility of the complex, which, by definition, indicates that the molecule is strongly hydrophobic.

Complex		Mass / atomic units	log P
$[\{Ru(5mp)_2\}_2(tpphz)]^{4+}$	**[4.1]**	1364	-0.81 ± 0.08
$[\{Ru(dmp)_2\}_2(tpphz)]^{4+}$	**[4.2]**	1420	-0.69 ± 0.06
$[\{Ru(DIP)_2\}_2(tpphz)]^{4+}$	**[4.3]**	1916	hydrophobic
$[\{Ru(phen)_2\}_2(tpphz)]^{4+}$	**[3.1]**	1308	-0.96 ± 0.09

Table 4.6 Measured octanol/water partition coefficients for **[4.1]** and **[4.2]**. The data for **[3.1]** from Chapter 3 is included for comparison.

The molecular volume and log P value for the relevant ancillary ligands, as shown in Table 4.7, is in agreement with the measured log P value for each Ru(II) complex with the order of hydrophobicity increasing phen → 5mp → DIP. In particular, it can be seen that the high hydrophobicity of the DIP ligand is clearly responsible for the strong hydrophobic nature of **[4.3]**.

Ligand	Mass / atomic units	Volume / Å^3	log P
phen	180	163	1.90
5mp	194	180	2.58
dmp	208	197	2.00
DIP	332	307	5.95

Table 4.7 Calculated ligand octanol/water partition coefficients, masses and molecular volumes. Log P and molecular volume values calculated using molinspiration property calculation software.[21]

One anomaly that arises from these results is that the log P value for the dmp ligand is lower than that for 5mp. This is not in agreement with the principle that the addition of a methyl group would increase the hydrophobicity of the molecule, therefore calculations for an equivalent series of ligands bound to a single ruthenium atom (Figure 4.7) were carried out (Table 4.8). These calculations show that the 2,9-dimethyl derivative has a greater log P value than the 5-methyl derivative, suggesting that the result obtained for the free dmp ligand is due to software inaccuracies.

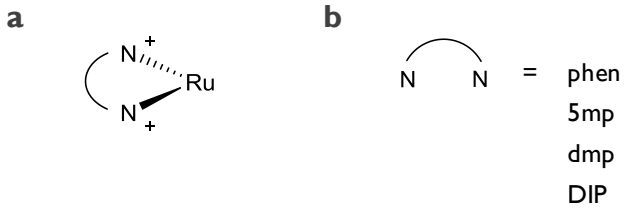

Figure 4.7 a, Revised model for ligand log P comparison entered into molinspiration software. **b,** Relevant N^N ligands.

Ligand model	log P
$Ru(phen)^{2+}$	-4.90
$Ru(5mp)^{2+}$	-4.73
$Ru(dmp)^{2+}$	-4.70
$Ru(DIP)^{2+}$	-2.00

Table 4.8 Calculated octanol/water partition coefficients using molinspiration property calculation software[21] for the revised ligand models.

From these values, **[4.1]** and **[4.2]** would not be predicted to be internalised by cells through passive diffusion whereas the strong hydrophobicity of **[4.3]** would indicate that the complex would not accumulate in hydrophilic cellular regions. The lack of water-solubility of **[4.3]** also presents a significant problem as potentially toxic organic solvents, such as dimethyl sulphoxide (DMSO), must be employed to aid dissolution, a factor which will affect cell viability.

4.6 Live cell uptake and imaging

As Section 4.4 showed that **[4.1]** and **[4.2]** bind to DNA with high binding affinities and increases in luminescence, their cellular uptake and *in cellulo* DNA binding properties can be studied using luminescence microscopy.

To examine cellular internalisation of each complex, MCF-7 cells were incubated with solutions of **[4.1]** and **[4.2]** and then imaged using CLSM. The excitation wavelength used was 458 nm and the emission measured at 650-700 nm, corresponding to the previously observed ^{3}MLCT luminescence emission maxima for each complex when bound to DNA *in vitro* (Section 4.4).

4.6.1 $[\{Ru(5mp)_2\}_2(tpphz)]^{4+}$

MCF-7 cells incubated for 24 hours with 100 μM of **[4.1]** displayed low levels of non-nuclear *in cellulo* MLCT luminescence (Figure 4.8).

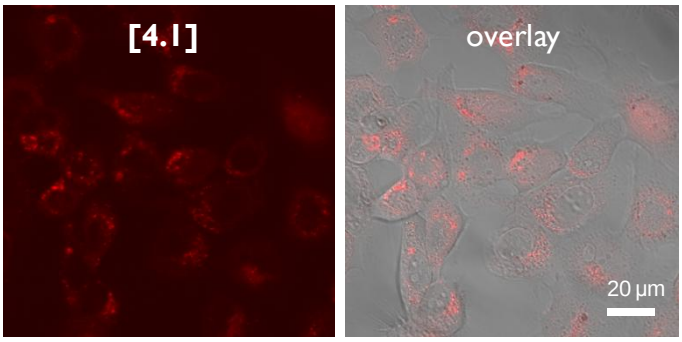

Figure 4.8 CLSM images of MCF-7 cells incubated with complexes **[4.1]** (100 μM, 24 hrs). Left: Ru(II) emission. Right, Overlay image of Ru(II) emission and phase contrast.

Chapter 3 demonstrated how the use of a high incubation concentration, short incubation time and serum-free media achieved more efficient cellular uptake. Accordingly, MCF-7 cells were incubated with 500 μM solutions of **[4.1]** in serum-free cell media, with the aim of improving cellular internalisation and achieving nuclear uptake with the associated DNA staining.

Under these conditions, **[4.1]** is shown to be internalised by live cells and the nuclei of cells are clearly stained by the complex (Figure 4.9). The accompanying live/dead staining shows the viability of the cells to be uncompromised whereby viable cells, as indicated by SYTO 9 staining, are clearly stained by **[4.1]**.

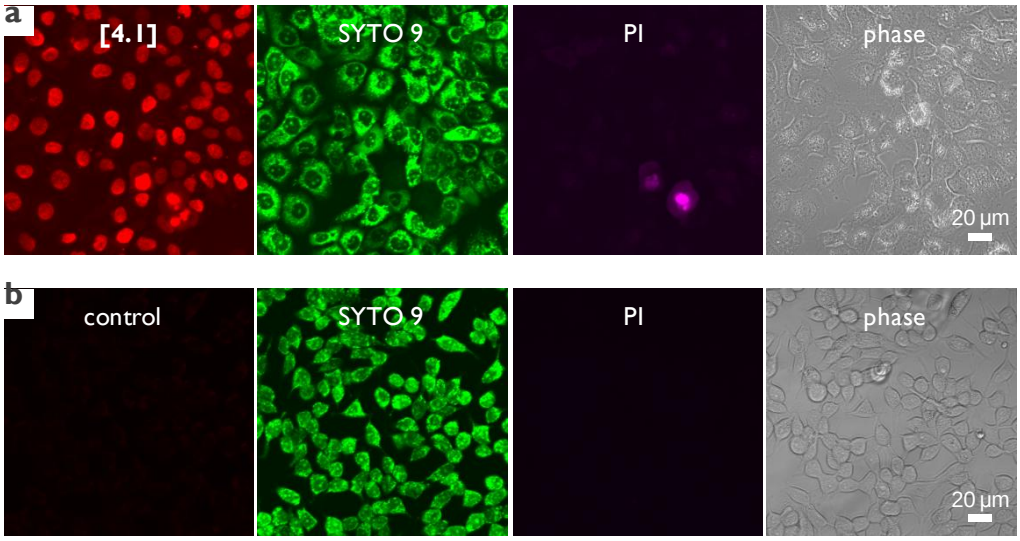

Figure 4.9 a, CLSM of MCF-7 cells incubated with 500 μM **[4.1]** in serum-free media for 1 hr. **b,** Negative control. From left to right: luminescence emission of Ru(II) complex (red), SYTO 9 (green), PI (purple) and phase contrast image.

Figure 4.9 shows **[4.1]** to display a similar behaviour to the parent complex **[3.1]**; both are internalised by cells and nuclear location is observable by CLSM in a concentration-dependent manner with no observable short-term toxicity.

To further compare the behaviour of **[4.1]** and **[3.1]**, and specifically to attempt to identify whether **[4.1]** is targeting DNA in cells, the cellular location of the complex and mechanism of internalisation of **[4.1]** was examined using a combination of CLSM and TEM by the methods described in Chapters 2 and 3.

4.6.1.1 Co-staining with nucleic acid dyes

Incubation of MCF-7 cells with **[4.1]** and co-staining with the commonly used DNA dye DAPI shows the distinct overlap of the two emission signals in MCF-7 cells (Figure 4.10a). This is clearly shown in the co-localisation image (Figure 4.10b), where the two emission signals display overlap in the majority of cells, which is a strong indication that both molecules are bound to nuclear DNA. Interestingly, co-staining with DAPI reveals that not all cells are stained by **[4.1]**; there are clearly cells stained by DAPI that show poor signal from **[4.1]**.

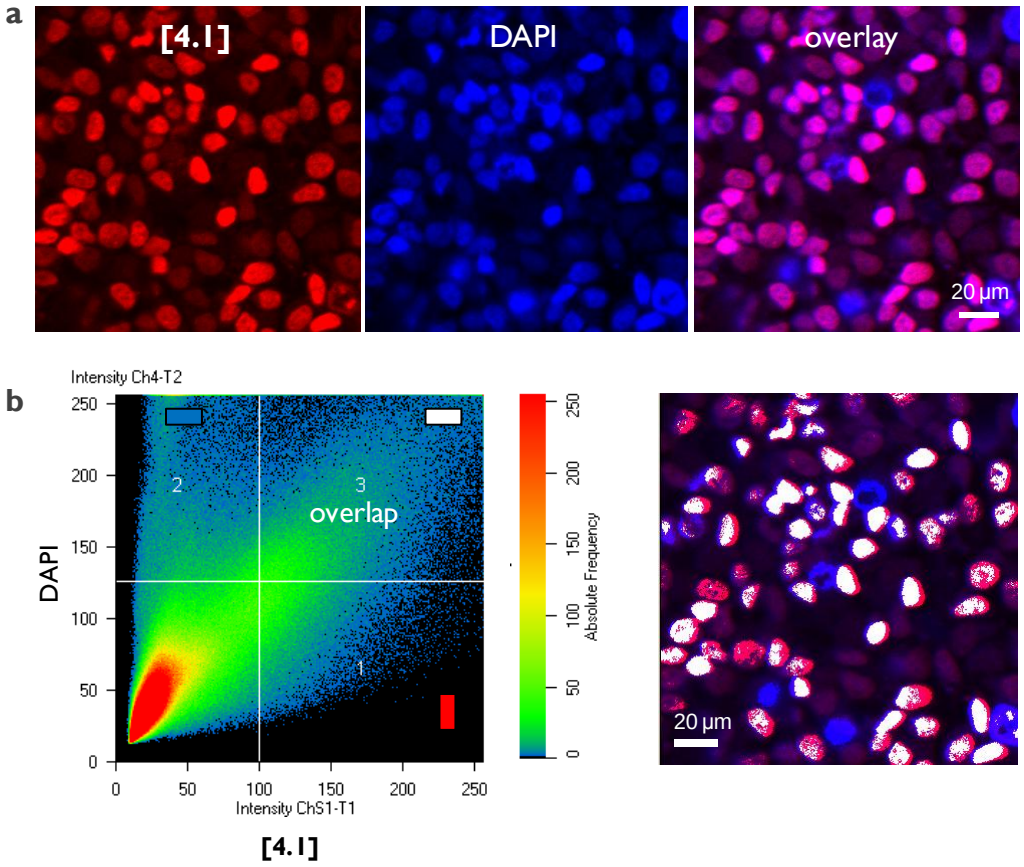

Figure 4.10 CLSM of MCF-7 cells incubated with **[4.1]** (500 µM, 1 hr). **a,** Co-staining of **[4.1]** (red) with DAPI (blue) and overlay image. **b,** Co-localisation of **[4.1]** and DAPI emission signals (blue = region 2, DAPI, red = region 1, **[4.1]**, white = region 3, overlap).

Co-staining experiments with **[4.1]** and SYTO 9 show a much lower co-localisation of the two emission signals than that observed with DAPI (Figure 4.11). As SYTO 9 fluorescently labels RNA and mitochondrial DNA, this indicates that **[4.1]** is a nuclear-specific stain in a manner analogous to **[3.1]**.

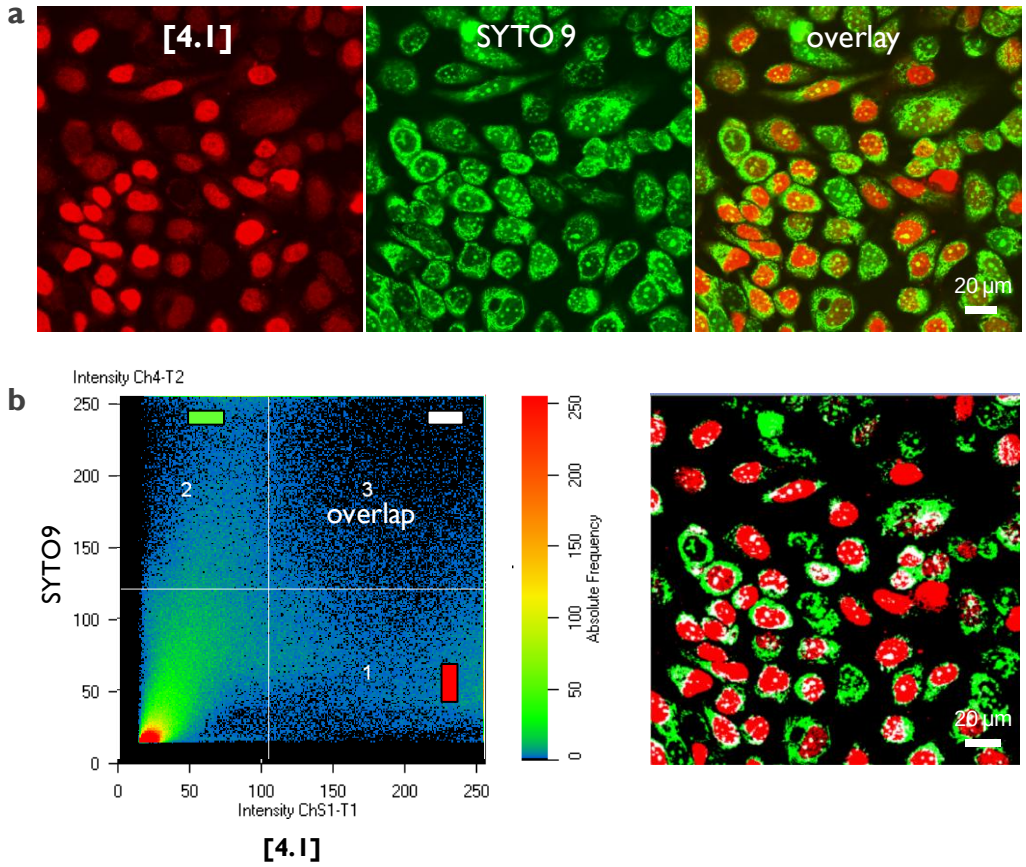

Figure 4.11 CLSM of MCF-7 cells incubated with **[4.1]** (500 µM, 1 hr). **a,** Co-staining of **[4.1]** (red) with SYTO 9 (green) and overlay image. **b,** Co-localisation of **[4.1]** and SYTO 9 emission signals (green = region 2, SYTO 9, red = region 1, **[4.1]**, white = region 3, overlap).

These co-staining experiments and the observation of condensed chromosomes of mitotic cell phases stained by **[4.1]** (Figure 4.12) present clear evidence that cellular DNA is successfully targeted by the ruthenium complex.

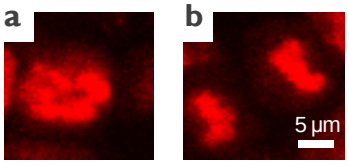

Figure 4.12 Prometaphase (**a**) and late-anaphase (**b**) MCF-7 cells stained by **[4.1]** showing condensed chromosome structure.

The co-staining experiments with SYTO 9 also displayed the non-uniform nature of the cellular internalisation of **[4.1]:** the majority of cells stained by SYTO 9 also show emission due to **[4.1]** but clearly there are also SYTO 9-stained cells which display minimal Ru(II) signal. This effect is summarised in Table 4.9 and the results for **[3.1]** are included for comparison.

Complex	Cell nuclei stained / %
[4.1]	77 ± 12
[3.1]	98 ± 3

Table 4.9 Extent of nuclear staining of MCF-7 cells by **[4.1]** or **[3.1]** (500 μM 1 hr in serum-free conditions). Minimum of 200 cells counted for each experiment.

The conclusion from this work is that a methyl group at the 5 position of the phen ligand alters the cellular uptake properties of Ru(II)tpphz systems and provides a cell selectivity on the basis of an as yet unknown parameter.

4.6.1.2 TEM studies

To examine the cellular location of each complex in more detail, MCF-7 cells were incubated with solutions of **[4.1]**, as for luminescence microscopy, and then the cells were fixed and sectioned for TEM imaging.

Figure 4.13 shows that **[4.1]** accumulates within the nucleus of MCF-7 cells where it associates with heterochromatin, observable by the strong contrast signal from these regions of densely-packed DNA. This makes **[4.1]** of interest as a DNA-imaging agent for both CLSM and TEM.

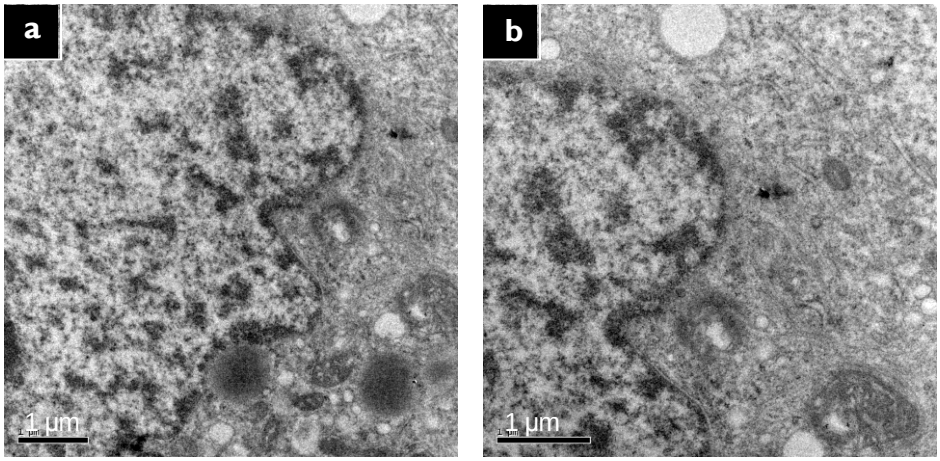

Figure 4.13 TEM micrographs of MCF-7 cells incubated with **[4.1]** (500 µM, 1 hr). **a, b,** Images showing **[4.1]** associates within the nucleus where it displays strong heterochromatin contrast.

4.6.1.3 Mechanism of uptake

The negative (hydrophilic) octanol/water partition log P value, 4+ charge and large size of **[4.1]** would suggest that **[4.1]** is not a membrane-permeable molecule. With this in mind, the uptake mechanism of **[4.1]** for MCF-7 cells was examined using inhibition studies, using the luminescence properties of **[4.1]** as an indication of the degree of cellular internalisation of the complex.

As shown by Figure 4.14, MCF-7 cells incubated with **[4.1]** at 4°C resulted in no observable *in cellulo* luminescence from the complex in viable cells. This result indicates that **[4.1]** is not able to freely diffuse across the cell membrane and therefore is internalised by cells *via* a temperature-dependent pathway (active transport). This is in agreement with the live cell uptake studies of **[4.1]** which have shown that a high concentration is required to achieve internalisation and the observation of non-uniform nuclear staining: neither effect would be predicted for a membrane-permeable DNA dye.

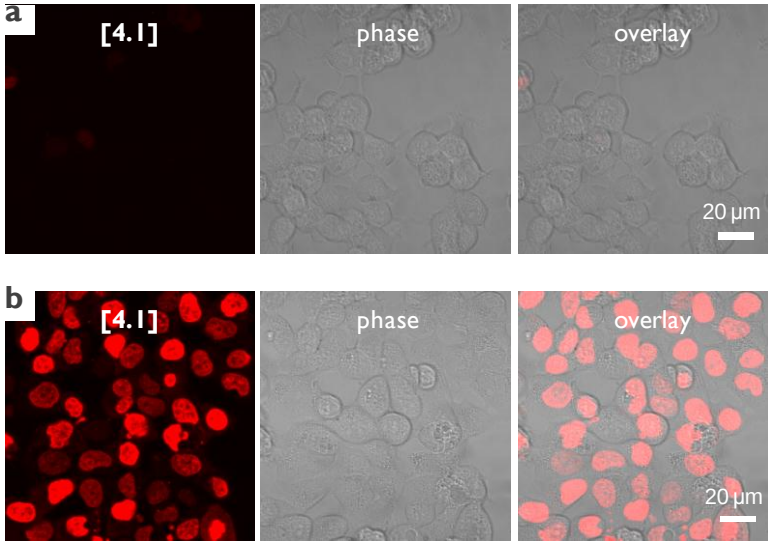

Figure 4.14 Temperature-dependence studies of uptake of **[4.1]** by MCF-7 cells. **a,** Cells incubated with **[4.1]** (500 µM, 1 hour) at 4°C display no *in cellulo* luminescence. **b,** 37 °C control. The phase contrast image is included for reference.

To investigate the exact mechanism of active transport in more detail, MCF-7 cells were co-incubated with **[4.1]** and chloroquine or ammonium chloride, which are two lysosomotropic agents which prevent the maturation of endosomes by disturbing the pH balance between endosome and cytosol,[22, 23] and thus inhibit endocytosis.

Figure 4.15 shows that there is no reduction of nuclear staining due to **[4.1]** for either inhibition treatment, suggesting that the complex is not internalised by MCF-7 cells *via* an endocytic pathway. Chapter 3 showed how **[3.1]** was found to be internalised by cells through a non-endocytic mechanism of active transport and - considering the structural similarity of **[4.1]** to the parent complex **[3.1]** - the results for the cellular uptake mechanism of **[4.1]** are not surprising.

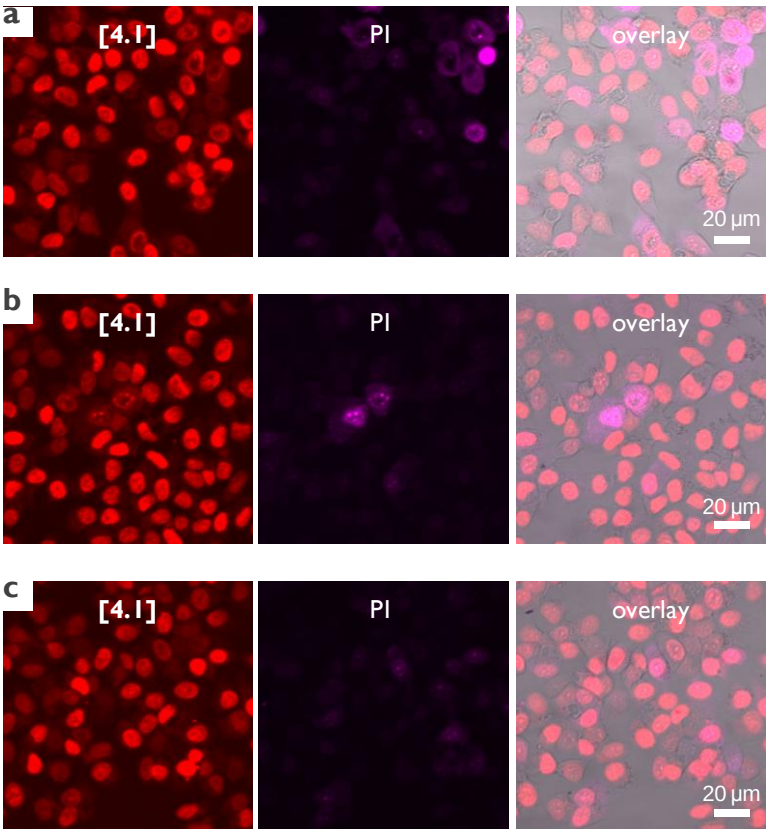

Figure 4.15 a, b, CLSM of MCF-7 cells coincubated with **[4.1]** and endocytosis inhibitors chloroquine (**a**) and NH4Cl (**b**). **c,** Negative control. PI staining is included to indicate cell viability.

4.6.2 $[\{Ru(dmp)_2\}_2(tpphz)]^{4+}$

MCF-7 cells incubated for 24 hours with 100 μM of **[4.2]** displayed no observable luminescence but, in a similar fashion as for **[4.1]**, MCF-7 cells incubated with **[4.2]** at a high concentration are observed to display very low levels of MLCT luminescence (Figure 4.16).

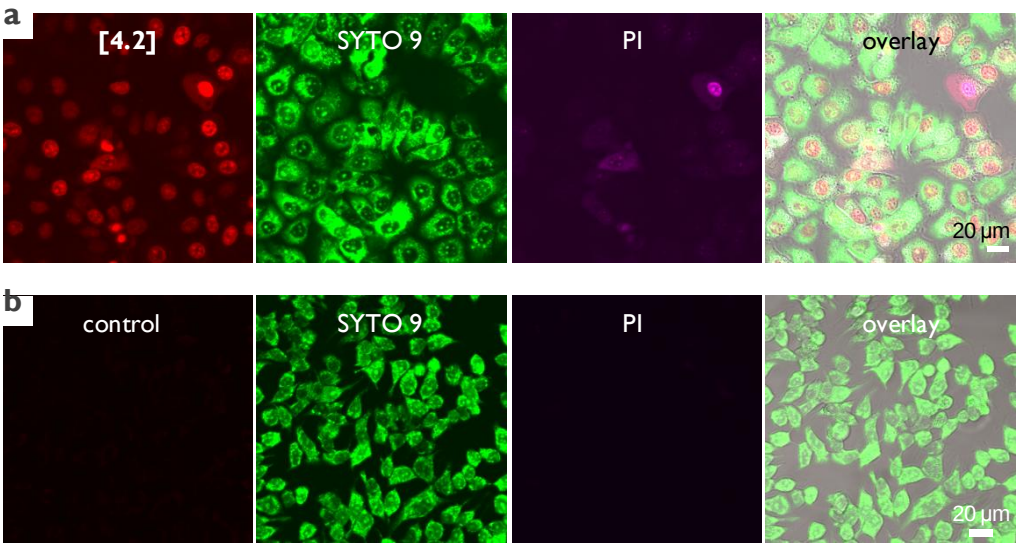

Figure 4.16 a, CLSM of MCF-7 cells incubated with 500 μM **[4.2]** in serum-free media for 1 hr. **b,** Negative control. From left to right: luminescence emission of Ru(II) complex (red), SYTO 9 (green), PI (purple) and phase contrast image.

This luminescence is located in the nuclei of cells (Figure 4.17) and provides evidence of the successful cellular uptake of **[4.2]**. The requirement of a high concentration to achieve live cell staining would indicate that the complex is not membrane-permeable, in agreement with the hydrophilic log P value recorded, although the low luminescence makes further study into the exact mechanism of uptake and intracellular target problematic.

The low emission of **[4.2]** from the nuclei of cells is due to the generally poor luminescent properties of the molecule – both free complex and when

bound to DNA - in comparison to other light switch complexes. Although these properties make **[4.2]** a poor imaging agent in comparison to **[3.1]** and **[4.1]**, this is still one of the few examples of using an MLCT light switch complex to image live cells.

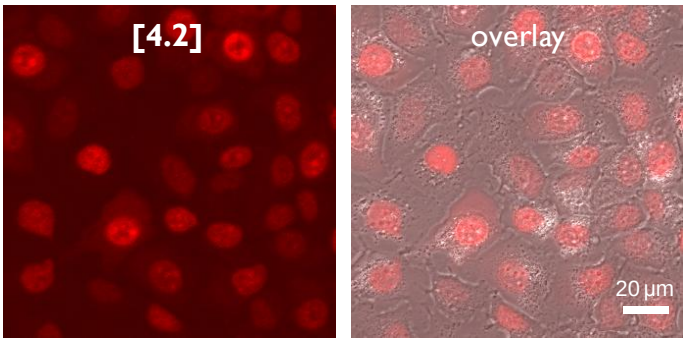

Figure 4.17 CLSM of MCF-7 cells incubated with 500 µM **[4.2]** in serum-free media for 1 hr. Left: Ru(II)tpphz emission (red). Right: Overlay image of Ru(II)tpphz emission and phase contrast.

4.6.3 $[\{Ru(DIP)_2\}_2(tpphz)]^{4+}$

The lack of water-solubility displayed by **[4.3]** required the complex to be dissolved in DMSO (dimethyl sulphoxide) to prevent precipitation. A high concentration of DMSO (> 20%) was required to achieve a concentration of 5 µM in PBS, reflecting the strong hydrophobicity of the complex. This concentration of DMSO is toxic to cells and not advantageous in a live cell imaging application however CLSM experiments were conducted to provide an indication of the intracellular target of the complex.

[4.3] displays a markedly different intracellular localisation than **[4.1]** and **[4.2]** where, in contrast to the nuclear staining displayed by the methyl-substituted complexes, luminescence emission from **[4.3]** is clearly observed from the nuclear envelope as well as distinct regions within the cytosol (Figure 4.18). It is possible that this complex is targeting the entire

endomembrane system - an extensive membrane system that comprises organelles such as the Golgi apparatus, nucleus and the endoplasmic reticulum (ER) in cells. Indeed, the staining pattern demonstrated by **[4.3]** is similar to that obtained by $DiOC_6$ (3,3′-dihexyloxacarbocyanine iodide), a fluorescent organic molecule used to stain the ER, vesicle membranes and mitochondria of cells.[24]

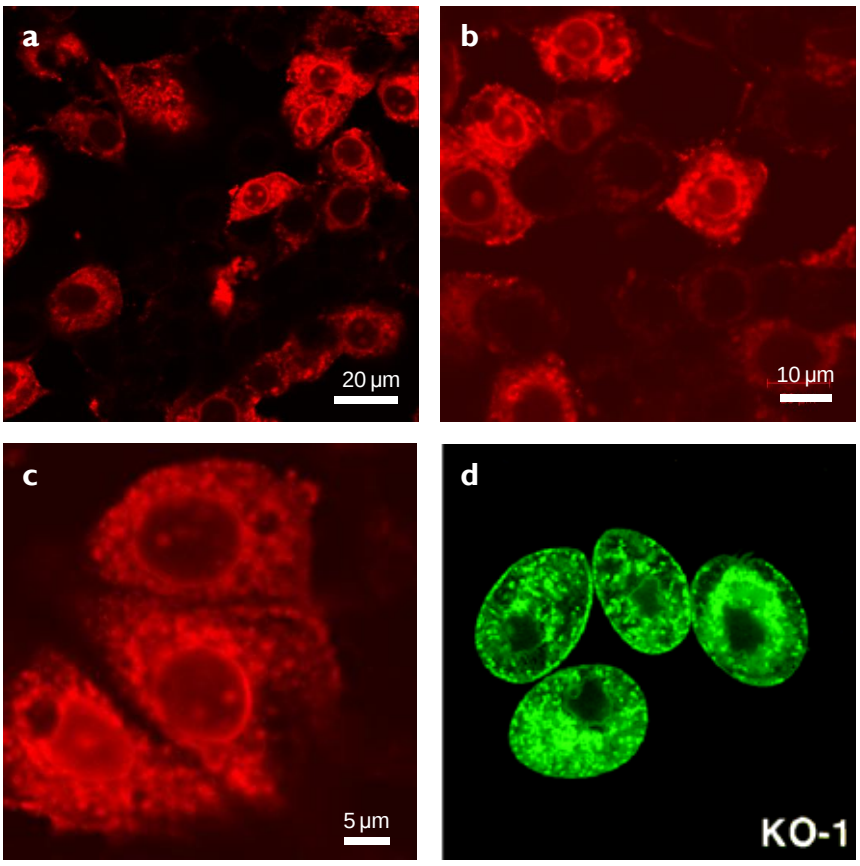

Figure 4.18 a, b, c, CLSM images of MCF-7 cells incubated with 10 µM **[4.3]** in serum-free media for 10 mins. **d,** Internal membrane structure of protozoa stained with $DiOC_6$.[25]

As **[4.3]** is a strongly hydrophobic molecule, it seems reasonable to suggest that the molecule is associating within hydrophobic regions (i.e. membranes) in the cell. To determine the exact intracellular target stained by **[4.3]**, co-staining experiments with specific organelle stains such as the

previously mentioned membrane stain $DiOC_6$ or ER-Tracker Dyes, which are designed for live-cell endoplasmic reticulum labelling, would be required. However, it should be noted that the insolubility of **[4.3]** in aqueous media presents a significant challenge in the development of this molecule for imaging applications.

These results do illustrate one drawback in designing metal complexes for the specific property of hydrophobicity - a molecule that is too hydrophobic will associate within hydrophobic regions such as membranes and the intended target (such as DNA) will not be imaged. This effect can also be observed in work by the Barton group, with their membrane-permeable $[Ru(DIP)_2(dppz)]^{2+}$ system displaying no evidence of targeting cellular DNA after it has traversed the cell membrane.[1, 2]

4.7 Fixed cell imaging

After the demonstration of live cell internalisation and nuclear staining by each complex in MCF-7 cells, the ability of **[4.1]** and **[4.2]** to stain fixed and membrane-permeabilised MCF-7 cells was investigated using CLSM. The same excitation/emission wavelength parameters used for live cell imaging were applied.

As shown by Figure 4.19a, **[4.1]** is an excellent nuclear stain for fixed and permeablised cells. **[4.2]** does show some ability in this capacity but the low luminescence of the complex decreases the signal/noise ratio and the images obtained are of poorer quality (Figure 4.19b).

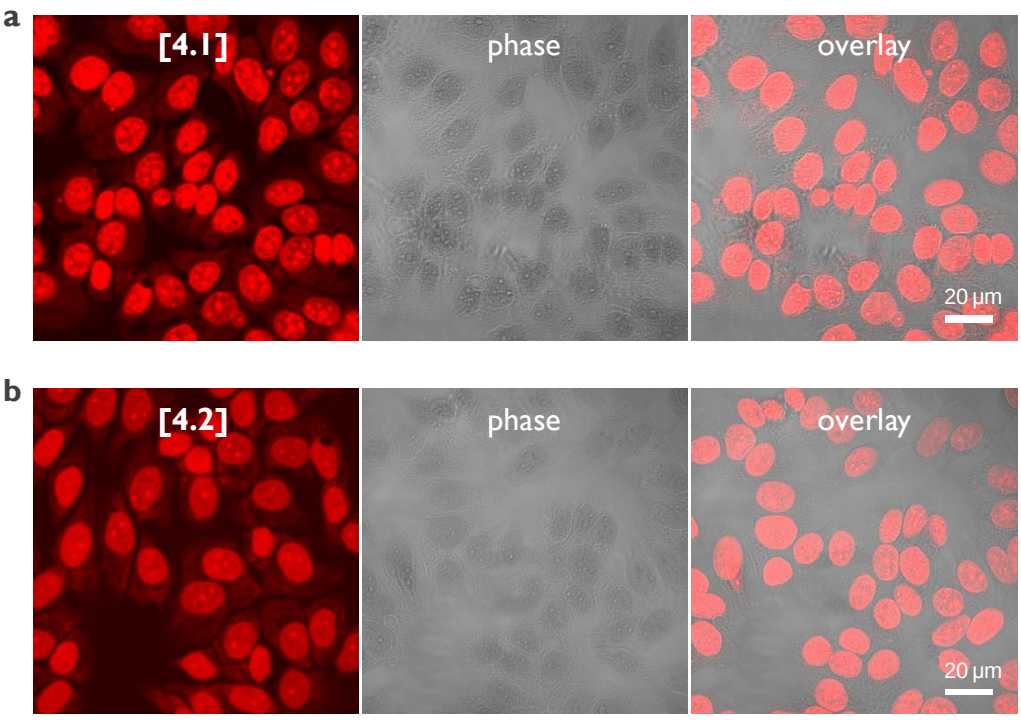

Figure 4.19 CLSM of fixed MCF-7 cells stained with **[4.1]** (a) or **[4.2]** (b) (100 µM, 10 mins.). From left to right: luminescence emission of Ru(II) complex (red), phase contrast and overlay image.

4.7.1 Relevant emission intensity

To directly compare the emission intensity of the methyl-substituted derivatives **[4.1]** and **[4.2]** and the parent complex **[3.1]** in fixed cell imaging conditions, micrographs of each complex staining fixed and membrane-permeablised MCF-7 cells were obtained where the incubation concentration/time and microscope settings (laser power, pinhole and detector gain) for each set of images were equal.

Using this approach, **[4.1]** and **[3.1]** each display comparable levels of luminescence in fixed, membrane-permeablised cells whereas **[4.2]** displays a significantly lower emission (Figure 4.20). This observation is agreement with the luminescent properties of each molecule when bound to DNA: **[3.1]**

and **[4.1]** display a similar luminescence and are each an order of magnitude more luminescent than **[4.2]** (Section 4.4).

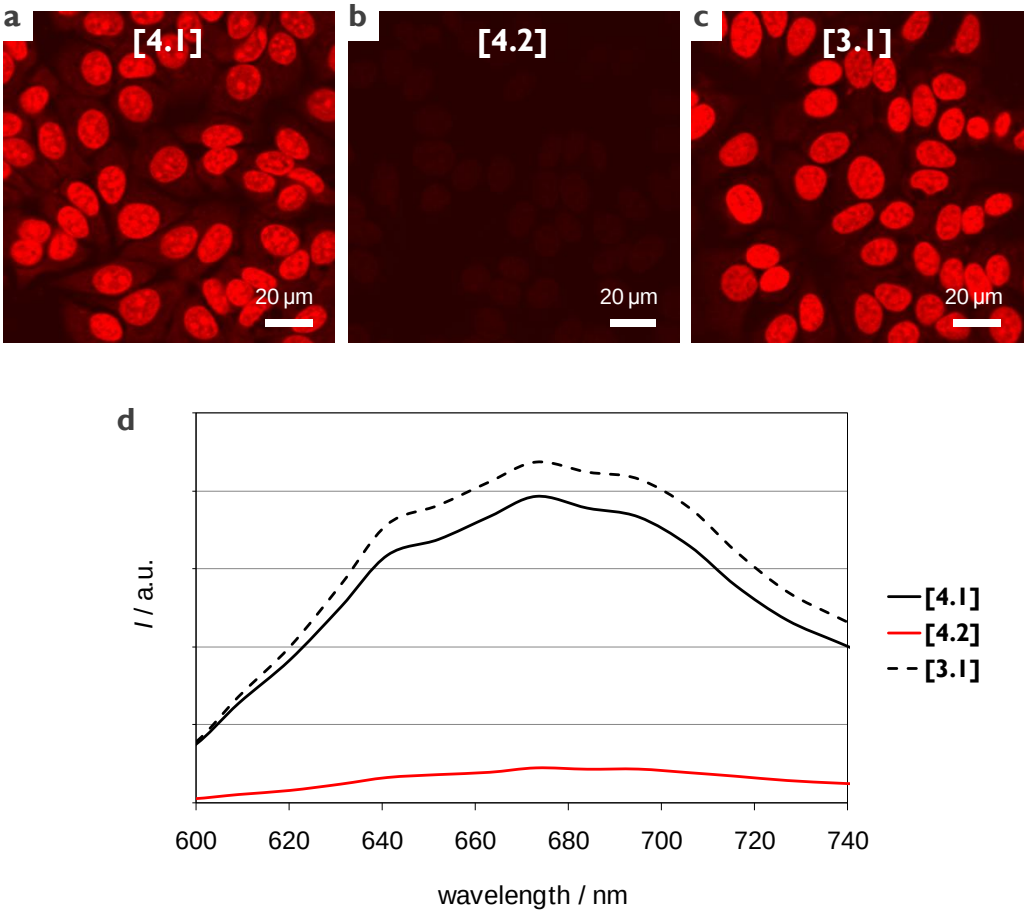

Figure 4.20 CLSM of fixed MCF-7 cells stained with Ru(II) complexes **[4.1]** (a), **[4.2]** (b) or **[3.1]** (c) (100 µM, 10 mins.). d, Relative emission intensity of **[4.1]**, **[4.2]** and **[3.1]** in fixed cells.

4.8 Cytotoxicity

As both **[4.1]** and **[4.2]** have been shown to demonstrate successful cellular uptake and the ability to bind to nuclear DNA in live MCF-7 cells the cytotoxicity of both complexes towards MCF-7 cells was investigated.

Chapter 3 showed how the quadruplex DNA-binding complex **[3.1]** demonstrated a low cytotoxicity for an incubation time of 24 hours but cytotoxicity equal to that of the anti-cancer drug cisplatin over a 72 hour incubation time, indicating that the complex possesses potential as the basis for an anti-cancer therapeutic. With this in mind, the cytotoxicity for **[4.1]** and **[4.2]** towards MCF-7 cells for both 24 and 72 hour incubation time periods was determined by MTT assay and the IC_{50} value for each experiment obtained.

As can be seen in Figure 4.21a and Table 4.10, **[4.1]** demonstrates a low cytotoxicity towards MCF-7 cells over a 24 hour incubation time (IC_{50} = 246 μM) but a significantly higher cytotoxicity over a 72 hours (IC_{50} = 16 μM), which, under these conditions, is now of a similar potency to that of cisplatin (IC_{50} = 6 μM). The methyl-substituted complex **[4.1]** displays a lower cytotoxicity than **[3.1]** (IC_{50} = 138 μM) and, as **[3.1]** has been shown to demonstrate superior cellular uptake properties than **[4.1]** (Section 4.6), this would suggest that it is the cellular uptake of the complex responsible for the cytotoxic properties.

[4.2] demonstrates a three-fold increase of cytotoxic potency over **[4.1]** for a 24 hour incubation time (IC_{50} = 80 μM) and a cytotoxicity equal to that of

cisplatin for a 72 hour incubation time period (IC_{50} = 5 μM) – Figure 4.21b and Table 4.10.

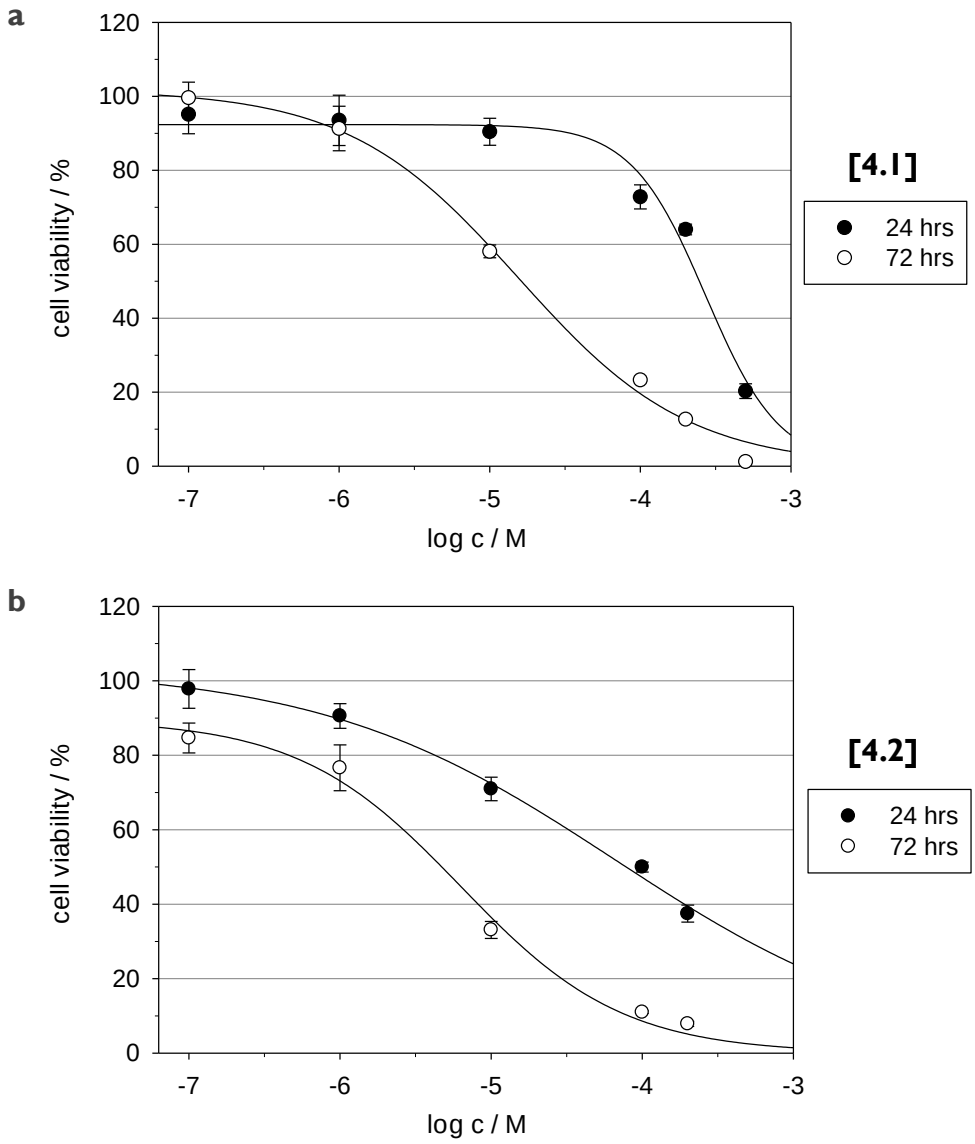

Figure 4.21 Cytotoxicity of methyl-substituted dinuclear Ru(II)tpphz complexes **[4.1]** (**a**) and **[4.2]** (**b**) towards MCF-7 breast cancer cells (24 and 72 hr incubation times).

Complex	24 hr IC_{50} / μM	72 hr IC_{50} / μM
[4.1]	246 ± 12	16 ± 2
[4.2]	80 ± 4	5 ± 2
[3.1]	138 ± 6	6 ± 2
cisplatin	12 ± 3	6 ± 2

Table 4.10 IC_{50} values of methyl-substituted dinuclear Ru(II) complexes towards the MCF-7 cell line. The data for **[3.1]** and cisplatin are included for reference.

It is interesting to note that **[4.1]** and **[4.2]** display the same anti-cancer toxicity behaviour previously observed for **[3.1]**: a modest IC_{50} value for MCF-7 cells incubated with each complex for 24 hours but cytotoxicity similar to that of cisplatin when the incubation time is increased to 72 hours (Table 4.10). These results therefore make **[4.1]** and **[4.2]** of interest as potential anti-cancer therapeutic agents.

4.9 Conclusions and future work

In this chapter, three derivatives of $[\{Ru(phen)_2\}_2(tpphz)]^{4+}$ **[3.1]** were synthesised by ancillary ligand substitution: $[\{Ru(5mp)_2\}_2(tpphz)]^{4+}$ **[4.1]**, $[\{Ru(dmp)_2\}_2(tpphz)]^{4+}$ **[4.2]** and $[\{Ru(DIP)_2\}_2(tpphz)]^{4+}$ **[4.3]**. The luminescent properties of each complex were characterised and the *in vitro* DNA binding, cellular uptake and *in cellulo* DNA binding properties of **[4.1]** and **[4.2]** investigated by CLSM microscopy while the cytotoxicity towards a human breast cancer cell line was assessed.

The complex containing the ancillary ligand with the greatest delocalised π system, **[4.3]**, was shown to demonstrate a significantly greater luminescence than **[4.1]** while **[4.2]** displayed a low emission in acetonitrile. This shows how the ancillary ligand can influence the luminescent properties of the molecule as a whole.

DNA binding studies demonstrated **[4.1]** and **[4.2]** to be DNA light switch complexes; demonstrating a significant increase of luminescence when bound to DNA in comparison to free complex (a 27- and 62-fold increase in luminescence for **[4.1]** and **[4.2]** respectively), and luminescence binding titrations showed each complex to bind to DNA with a high affinity (K_b = 6.7 × 10^6 M^{-1} and K_b = 6.7 × 10^6 M^{-1} for **[4.1]** and **[4.2]** respectively) – Table 4.11.

Complex	MLCT absorption / nm (ε / M^{-1} cm^{-1}) *	Φ * (λ_{ex} / nm)	K_b / M^{-1}
[4.1]	443 (32182)	6.9 ± 0.7 × 10^{-3} (450)	6.7 ± 0.8 × 10^6
[4.2]	449 (22716)	3 ± 2 × 10^{-4} (450)	5.8 ± 0.4 × 10^6
[4.3]	454 (45712)	0.017 ± 0.002 (450)	water-insoluble

Table 4.11 Summary of the photochemical and *in vitro* DNA binding properties of **[4.1]** – **[4.3]**. * In acetonitrile.

Cellular studies revealed **[4.1]** to be internalised by the MCF-7 cell line by a non-endocytic mechanism of active transport where the complex functions as an imaging agent for both CLSM and TEM. The co-localisation of the

emission signal of **[4.1]** with DAPI, clear visualisation of condensed chromosomes of mitotic cells stained by the complex and the emission energy were all shown to be in agreement with the *in vitro* DNA binding data, strongly suggesting that the complex binds to DNA *in cellulo*, while TEM studies showed strong heterochromatin staining by the complex. **[4.2]** also stains the nuclei of live MCF-7 cells but the poor luminescence of the complex made further study problematic. Both **[4.1]** and **[4.2]** were shown to stain fixed and membrane-permeablised cells and the relative emission for each complex was in agreement with the *in vitro* DNA binding emission data.

It is interesting to note that **[4.1]** displays reduced uptake properties compared to **[3.1]** – the majority of cells were stained by **[4.1]** but there were clearly cells not stained by the complex. This structure-specificity (in this case favouring phen as the ancillary ligand over 5mp) further suggests that at least one specific receptor-binding event is likely to occur at some point during the uptake process into the nucleus. In particular, if the cellular uptake of **[3.1]** is facilitated by binding to a specific protein, then it is possible that methyl-substitution at the 5 position of the phen ancillary could reduce the affinity of the complex for the protein and thus inhibit cellular uptake.

Cytotoxicity studies demonstrated that **[4.1]** and **[4.2]** show the same behaviour as **[3.1]**; a low toxicity towards the MCF-7 cell line after 24 hour incubation but when this incubation time is increased to 72 hours a significantly greater toxicity is observed (IC_{50} values summarised in Table 4.12). **[4.1]** demonstrated a reduced cytotoxicity in comparison to the parent complex **[3.1]**. This would be in agreement with the reduced cellular uptake demonstrated by **[4.1]** which in turn implies an intracellular mechanism of toxicity. Complex **[4.2]** demonstrated a greater toxicity than

[4.1] and **[3.1]**, making it the most toxic of the dinuclear Ru(II)tpphz complexes studied within this thesis. As **[3.1]** binds DNA with a greater affinity than **[4.2]** this is further evidence that it is the cellular uptake properties, rather than DNA binding affinity, that is the most important factor which governs the toxicity of the complex. Combined with the results from Chapter 3, the cytotoxicity of dinuclear Ru(II)tpphz complexes is, in decreasing cytotoxicity, **[4.2]** > **[3.1]** > **[4.1]** > **[3.2]**. This shows how the cytotoxicity of a metal complex can be subtly modified by the choice of ancillary ligand, where the order of toxicity was shown to be: dmp > phen > 5mp > bpy. It would be interesting to synthesise further derivatives and to expand this "toxicity series".

Complex	Ancillary ligand	log P	IC_{50} / μM	
			MCF-7 (24 hr)	MCF-7 (72 hr)
[4.1]	5mp	-0.81 ± 0.08	246 ± 12	16 ± 2
[4.2]	dmp	-0.69 ± 0.06	80 ± 4	5 ± 2
[3.1]	phen	-0.96 ± 0.09	138 ± 6	6 ± 2
[3.2]	bpy	-1.61 ± 0.10	>500	168 ± 9
cisplatin	-	-2.53*	12 ± 3	6 ± 2

Table 4.12 Compiled octanol/water partition coefficient and IC_{50} values of dinuclear Ru(II)tpphz complexes towards MCF-7 cells. Data for **[3.1]** and **[3.2]** from Chapter 3 is included for reference. *Value obtained from Screnci *et al.*[26]

Future work would focus on the DNA binding properties of **[4.1]** and **[4.2]**, specifically examining the ability of each complex to bind quadruplex DNA. Previous work has shown the parent complex **[3.1]** binds to quadruplex DNA *in vitro* with a greater affinity than duplex[7] and the wavelength and

intensity of the emission has recently been shown to be dependent on the exact structure of the DNA quadruplex to which it binds.[27] In this context, it would be hoped that the equivalent studies on **[4.1]** and **[4.2]** would provide new quadruplex-interactive molecules, of particular relevance considering that each molecule has demonstrated anti-cancer cytotoxic potential.

4.10 References

1. C. A. Puckett and J. K. Barton, Methods to Explore Cellular Uptake of Ruthenium Complexes, *J. Am. Chem. Soc.*, 2007, **129**, 46-47.
2. C. A. Puckett and J. K. Barton, Mechanism of Cellular Uptake of a Ruthenium Polypyridyl Complex, *Biochemistry*, 2008, **47**, 11711-11716.
3. E. Musatkina, H. Amouri, M. Lamoureux, T. Chepurnykh and C. Cordier, Mono- and dicarboxylic polypyridyl-Ru complexes as potential cell DNA dyes and transfection agents, *J. Inorg. Biochem.*, 2007, **101**, 1086-1089.
4. K. K.-W. Lo, T. K. M. Lee, J. S. Y. Lau, W. L. Poon and S. H. Cheng, Luminescent Biological Probes Derived from Ruthenium(II) Estradiol Polypyridine Complexes, *Inorg. Chem.*, 2008, **47**, 200-208.
5. J. Bolger, A. Gourdon, E. Ishow and J.-P. Launay, Mononuclear and Binuclear Tetrapyrido [3.2-a: 2', 3'-c: 3", 2"-h: 2"', 3"'-j] phenazine (tpphz) Ruthenium and Osmium Complexes, *Inorg. Chem.*, 1996, **35**, 2937-2944.
6. B. P. Sullivan, D. J. Salmon and T. J. Meyer, Mixed phosphine 2,2'-bipyridine complexes of ruthenium, *Inorg. Chem.*, 1978, **17**, 3334-3341.
7. C. Rajput, R. Rutkaite, L. Swanson, I. Haq and J. A. Thomas, Dinuclear Monointercalating Ru(II) Complexes That Display High Affinity Binding to Duplex and Quadruplex DNA, *Chem. Eur. J.*, 2006, **12**, 4611-4619.
8. A. Juris, V. Balzani, F. Barigelletti, S. Campagna, P. Belser and A. Von Zelewsky, Ru(II) polypyridine complexes: photophysics, photochemistry, electrochemistry, and chemiluminescence, *Coord. Chem. Rev.*, 1988, **84**, 85-277.
9. S. Campagna, S. Serroni, S. Bodige and F. M. MacDonnell, Absorption Spectra, Photophysical Properties, and Redox Behavior of Stereochemically Pure

Dendritic Ruthenium(II) Tetramers and Related Dinuclear and Mononuclear Complexes, *Inorg. Chem.*, 1999, **38**, 692-701.

10. D. A. Lutterman, A. Chouai, Y. Liu, Y. Sun, C. D. Stewart, K. R. Dunbar and C. Turro, Intercalation Is Not Required for DNA Light-Switch Behavior, *J. Am. Chem. Soc.*, 2008, **130**, 1163-1170.
11. C. Rajput, PhD Thesis, University of Sheffield, 2005.
12. C. Turro, S. H. Bossmann, Y. Jenkins, J. K. Barton and N. J. Turro, Proton Transfer Quenching of the MLCT Excited State of $Ru(phen)_2dppz^{2+}$ in Homogeneous Solution and Bound to DNA, *J. Am. Chem. Soc.*, 1995, **117**, 9026-9032.
13. C. V. Kumar, J. K. Barton and N. J. Turro, Photophysics of ruthenium complexes bound to double helical DNA, *J. Am. Chem. Soc.*, 1985, **107**, 5518-5523.
14. G. Scatchard, The attraction of proteins for small molecules, *Proc. Natl. Acad. Sci. U.S.A.*, 1949, **51**, 660-672.
15. J. D. McGhee and P. H. von Hippel, Theoretical aspects of DNA-protein interactions: Co-operative and non-co-operative binding of large ligands to a one-dimensional homogeneous lattice, *J. Mol. Biol.*, 1974, **86**, 469-489.
16. C. Metcalfe, PhD Thesis, University of Sheffield, 2002.
17. C. Metcalfe and J. A. Thomas, Kinetically inert transition metal complexes that reversibly bind to DNA, *Chem. Soc. Rev.*, 2003, **32**, 215-224.
18. H. Derrat, MPhil Thesis, University of Sheffield, 2009.
19. S. Mahadevan and M. Palaniandavar, Spectral and Electrochemical Behavior of Copper(II)-Phenanthrolines Bound to Calf Thymus DNA. $[(5,6\text{-dimethyl-OP})_2Cu]^{2+}$ (5,6-dimethyl-OP = 5,6-Dimethyl-1,10-phenanthroline) Induces a Conformational Transition from B to Z DNA, *Inorg. Chem.*, 1998, **37**, 3927-3934.
20. P. Waywell, V. Gonzalez, M. R. Gill, H. Adams, A. J. H. Meijer, M. P. Williamson and J. A. Thomas, Structure of the Complex of $[Ru(tpm)(dppz)py]^{2+}$ with a B-DNA Oligonucleotide - A Single-Substituent Binding Switch for a Metallo-Intercalator, *Chem. Eur. J.*, 2010, **16**, 2407-2417.
21. www.molinspiration.com
22. R. Wattiaux, N. Laurent, S. Wattiaux-De Coninck and M. Jadot, Endosomes, lysosomes: their implication in gene transfer, *Adv. Drug Delivery Rev.*, 2000, **41**, 201-208.

23. H. K. Ziegler and E. R. Unanue, Decrease in macrophage antigen catabolism caused by ammonia and chloroquine is associated with inhibition of antigen presentation to T cells, *Proc. Natl. Acad. Sci. U.S.A.*, 1982, **79**, 175-178.

24. A. J. Koning, P. Y. Lum, J. M. Williams and R. Wright, DiOC6 staining reveals organelle structure and dynamics in living yeast cells, *Cell Motility and the Cytoskeleton*, 1993, **25**, 111-128.

25. S. Lee, J. C. Wisniewski, W. L. Dentler and D. J. Asai, Gene Knockouts Reveal Separate Functions for Two Cytoplasmic Dyneins in Tetrahymena thermophila, *Mol. Biol. Cell*, 1999, **10**, 771-784.

26. D. Screnci, M. J. McKeage, P. Galettis, T. W. Hambley, B. D. Palmer and B. C. Baguley, Relationships between hydrophobicity, reactivity, accumulation and peripheral nerve toxicity of a series of platinum drugs, *Br. J. Cancer*, 2000, **82**, 966-972.

27. T. Wilson, M. P. Williamson and J. A. Thomas, Differentiating quadruplexes: binding preferences of a luminescent dinuclear ruthenium(II) complex with four-stranded DNA structures, *Org. Biomol. Chem.*, 2010, **8**, 2617-2621.

Chapter 5

Future perspective

5.1 Introduction

A major aim of this work was to examine the cellular DNA binding properties of Ru(II) DNA light switch complexes. The demonstration of successful internalisation, nuclear DNA staining and cytotoxicity of several Ru(II) complexes within this thesis represents a significant advance towards the use of such systems in biological applications.

This work has shown the application of such complexes for both live and fixed cell DNA luminescent imaging and that these complexes are compatible with fluorescent microscopy techniques, including CLSM. In addition to this, these complexes are also able to act as contrast agents for TEM and thus are dual imaging agents; a unique property of metal-based DNA binding systems. In particular, luminescent mono- and dinuclear Ru(II)tpphz systems which bind to DNA reversibly have shown great potential as DNA imaging agents and also as potential anti-cancer therapeutics; specifically offering an alternative to platinum-based chemeotherapeutics (and other derivatives), which bind to DNA irreversibly.

Future work based on the results and ideas developed in this thesis will be discussed within this chapter.

5.2 Quantitative uptake studies

The work within this thesis has used qualitative techniques to assess cellular uptake of luminescent Ru(II) complexes. Importantly, this has provided information the cellular localisation of each complex but it has not shown the relevant *total* cellular ruthenium accumulation for each complex.

Therefore, future work would carry out a systematic quantitative evaluation of the cellular uptake of each Ru(II) complex. Using techniques such as AAS (atomic absorption spectroscopy) or ICP-MS (inductively coupled plasma mass spectroscopy), the amount of complex internalised by cells can be accurately quantified and the effects of ligand substitution, incubation concentration, serum, incubation time upon cellular uptake and cytotoxicity may be more accurately described.

Indeed, Schatzschneider *et al.* used this approach for a series of Ru(II) complexes and showed that the complex that displays the greatest cellular uptake also displays the greatest cytotoxicity.[1] It would be hoped that this approach would provide further illumination of the relationship between the rate of cellular uptake and cytotoxicity of the systems within this thesis which in turn would provide a measure of the potency of each complex.

5.3 Chirally resolved complexes

In Chapter 3, the cellular uptake, DNA imaging and cytotoxicity studies of **[3.1]** used the complex as a mixture of stereoisomers. **[3.1]** is a dinuclear

complex which contains two chiral Ru(II) metal centres and therefore three stereoisomers of the complex exist: ΛΔ (meso), ΛΛ and ΔΔ (Figure 5.1).

When we consider that many currently used drugs are chiral molecules and that frequently only one enantiomer is active, with the other being responsible for unwanted side-effects, this makes the separation and related cellular studies of the stereoisomers of **[3.1]** of key importance.

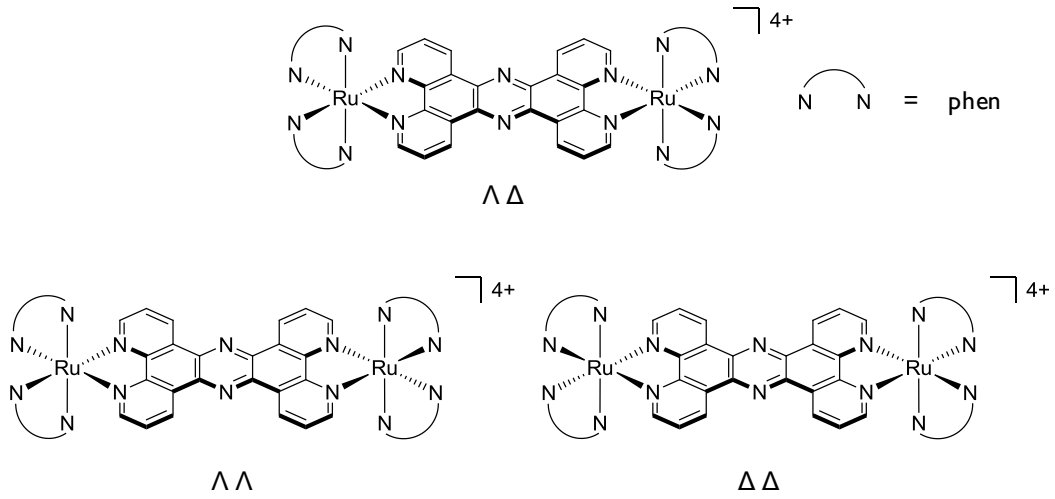

Figure 5.1 Stereoisomers of **[3.1]**.

5.3.1 Synthesis of chirally resolved dinuclear Ru(II) complexes

Preparation of **[3.1]** using the synthetic route described in Scheme 3.2 results in the mixture of stereoisomers ΛΔ: ΛΛ: ΔΔ in the ratio of 2:1:1. As this is a mixture of both diastereomers (ΛΔ vs. ΛΛ and ΔΔ) and enantiomers (ΛΛ vs. ΔΔ), this makes the resolution of each stereoisomer more difficult.

Using an approach developed by Norden and Lincoln[2] and utilised by MacDonnell and co-workers,[3] work by the Thomas group has instead

concentrated on synthesising the enantiomerically pure starting complexes $[Ru(phen)_2(dpq)]^{2+}$ (dpq = 1,10-phenanthroline-5,6-dione) and $[Ru(phen)_2(dap)]^{2+}$ (dap = 5,6-diamino-1,10-phenanthroline), which then may be reacted together to form the three required stereoisomers of **[3.1]** – Scheme 5.1.[3, 4] This method involves the resolution of $[Ru(phen)_2(dpq)]^{2+}$ using the bulk resolution procedure of coprecipitation with sodium arsenyl (+)-tartrate or sodium arsenyl (−)-tartrate salts.[2] The resolved complex may then be reacted with hydroxylamine and $BaCO_3$ before reduction using 10% Pd-C to give $[Ru(phen)_2(dap)]^{2+}$.[5]

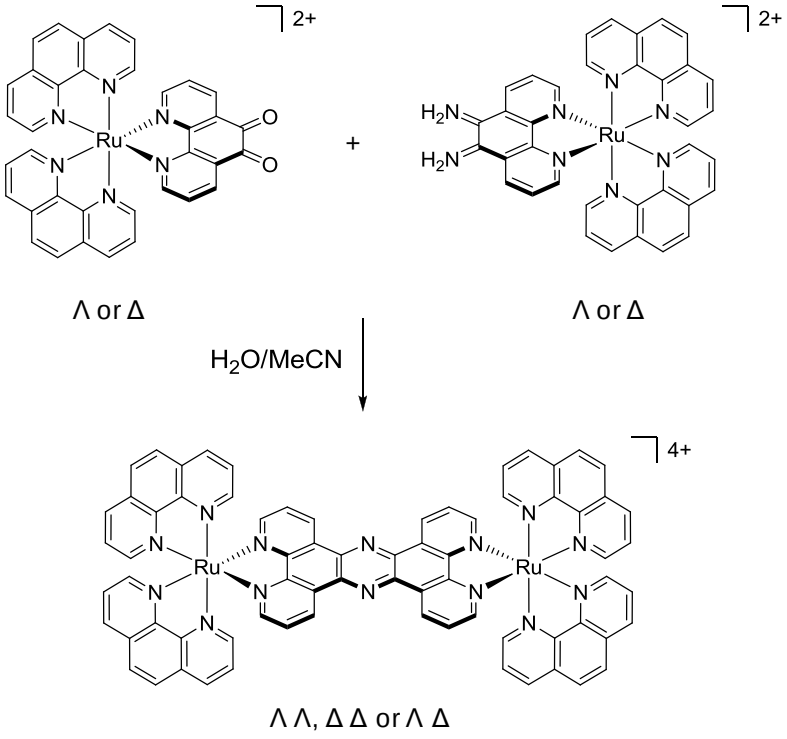

Scheme 5.1 Synthesis of resolved stereoisomers of **[3.1]**.

In related research, MacDonnell *et al.* also show how resolution of the stereoisomers of **[3.1]** can be achieved with a high efficiency by using HPLC with a chiral stationary phase[6] while Keene and co-workers have developed cation exchange chromatography with a utilising a chiral eluent to separate the diastereomers of numerous dinuclear Ru(II) metal species.[7, 8] Both

techniques offer an alternative strategy if the proposed approach is unsuccessful.

5.3.2 DNA binding properties

All three stereoisomers are DNA light switch complexes and binding studies into the DNA affinities of the stereoisomers have shown that the binding of the ΛΛ isomer to G3 quadruplex DNA to be three orders of magnitude strong than that observed for ΔΔ, whereas a similar affinity for duplex DNA (CT-DNA) is observed (Table 5.1).[4] These results indicate that the chirality of the complex plays a large part in the binding to quadruplex DNA.

Stereoisomer	CT-DNA K_b / M^{-1}	G3 DNA K_b / M^{-1}
Mixture (25% ΔΔ, 25% ΛΛ, 50% ΔΛ)	$6.68 \pm 2.21 \times 10^6$	$1.77 \pm 2.85 \times 10^6$
ΔΔ	$1.99 \pm 0.29 \times 10^6$	$2.95 \pm 5.52 \times 10^4$
ΛΛ	$6.73 \pm 2.21 \times 10^6$	$1.16 \pm 0.66 \times 10^7$

Table 5.1 Equilibrium binding constants of different diastereoisomers of **[3.1]** with CT-DNA and G3 quadruplex DNA.[4]

5.3.3 Proposed cellular studies

Future work will investigate the effect of the chirality of **[3.1]** upon the cellular internalisation and cytotoxicity. In a similar manner to the studies within this thesis on the unresolved complex, the MLCT luminescent properties of each stereoisomer can be used to directly compare the rate of cellular uptake and DNA binding properties for each stereoisomer. In particular, there is the question of how the chirality of the molecule affects the cellular uptake and if the stereoisomer that displays the higher affinity

for quadruplex DNA also displays the greatest ability to interfere with cell proliferation.

5.4 Mechanism of toxicity

Cisplatin, which remains the predominant treatment for hormone-independent breast and ovarian tumours, irreversibly creates intra-strand DNA cross links, provoking a cell's DNA damage response and ultimately inducing apoptosis.[9] Cisplatin selectively kills cancer cells because tumour cells, unlike normal counterparts in the same tissue, have lost the ability to carry out homologous recombination (HR), which is used to repair the DNA lesion. However, tumour cells have very high rates of DNA mutation and can recover their HR capability to become cisplatin-resistant.[10]

As shown in this work, the monometallic complex **[2.3]** demonstrates a cytotoxicity comparable to cisplatin, while the dinuclear complexes **[3.1]**, **[4.1]** and **[4.2]** each demonstrate a similar potency to cisplatin over an extended incubation time; signifying that each complex displays the ability to interfere with cancer cell proliferation.

However, the biological mechanism by which these complexes induce cell death is unknown. As the mechanism of DNA-binding of each complex is radically different to cisplatin, a reversible association rather than direct coordination to the DNA double helix, it would be predicted that the mechanism of toxicity is also very different. This in turn would indicate that such complexes will remain active against cisplatin-resistance cancer, as demonstrated for **[2.3]** in Chapter 2, and thus may represent an entirely new class of therapeutics.

These complexes may photosensitise reactive species such as singlet oxygen, thus inducing cytotoxic effects by damaging DNA or other critical cellular components. Alternatively, binding of these complexes to DNA may interfere with some key aspect of DNA metabolism leading directly or indirectly to cell death. With this in mind, the mechanism of toxicity is of great interest and future work would be concentrated in the following areas:

5.4.1 Mechanism of induced cell death

Molecules which bring about irreparable forms of DNA damage (such as cisplatin) induce a defined cell death programme or apoptosis. In order to establish whether these Ru(II) complexes could act to induce apoptotic or necrotic cell death, complex-treated cells will be monitored for the timely appearance of key markers of apoptosis, including specific proteases such as activated caspase 3, the appearance of DNA single-strand breaks and plasma membrane-associated Annexin V, all of which may be detected by direct fluorescence or indirect immunofluorescence microscopy.[11]

Something of specific interest is the possibility that **[3.1]** binds to quadruplex DNA *in vivo* and that this is responsible for the toxic properties of the complex. If so, this would be predicted to inhibit telomerase function. The enzymatic activity of telomerase would be quantified using the telomerase TRAP (telomere repair amplification protocol) assay and would be predicted to decrease with increasing exposure to **[3.1]**.

5.4.2 Comparative analysis of complex cytotoxicity in cisplatin-resistant and sensitive cell-lines

Recent evidence has indicated that one major mechanism for the emergence of platinum resistance in ovarian cancers involves the re-acquisition of function in the breast/ovarian cancer sensitivity gene BRCA2 by mutational

reversion.[12] Therefore, a series of experiments using BRCA2-deficient ovarian cancer cell lines and their wild-type BRCA2 derivatives would be used to establish the relationship between sensitivity to the Ru(II) complexes and HR capability. It would be hoped that the toxicity of the Ru(II) complexes is independent of cell HR capability, which would signify their potential as an exciting new class of anti-cancer therapeutics.

5.5 Cellular uptake mechanism

An exciting finding which emerges from the studies in this thesis is the observation of cell-specific uptake of **[3.1]**, where MCF-7 breast cancer cells display increased staining by the complex compared to HDF primary human skin cells when grown together in co-culture. This raises the question of how the molecule enters cells and, along with the structure-specificity observed for the Ru(II) complex, this suggests the involvement of a specific (most likely, protein) receptor and internalisation pathway. The uptake mechanism has important implications for the activity, optimisation and mechanism of toxicity of this class of molecule; something of relevance to the role of **[3.1]** both as an imaging agent and novel anti-cancer therapeutic.

Interestingly, **[3.1]** is internalised by *Drosophila S2 tissue culture* cells (Figure 5.2). The availability of whole genome information, and minimal redundancy of function, makes Drosophila an attractive system for the identification of gene products involved in any biological function. The technique of RNA interference (RNAi) in cells involves the introduction of a small RNA molecule whose base sequence is complementary to the coding sequence of a messenger RNA encoding a particular protein, resulting in the specific elimination of that protein from cells. The availability of the entire Drosophila genome sequence allows for the design of a complete set of RNAi

molecules for every gene (~16,000) in the organism.[13] The emergence of software and hardware to analyse datasets arising from the elimination of each gene product separately in one single experiment makes this the approach of choice for the identification of components of the pathway involved in the cellular uptake and nuclear targeting of the Ru(II) complexes described here.

Future work would employ the RNAi screening facility at the University of Sheffield for a systematic genome-wide screen in *Drosophila* with the aim to identify the genes which regulate the uptake pathway of **[3.1]**. This would use the same principle as for the inhibition studies on MCF-7 cells; the *in cellulo* luminescence of **[3.1]** would be used as an indication of successful cellular uptake in a genome-wide fluorescence assay, utilising an automated high content microscope to process and quantify the luminescence obtained in each case. Identification of a putative receptor for Ru(II) complexes uptake in Drosophila cells would require subsequent validation in a human cell line, involving the identification of human homologue(s) of the Drosophila gene, and comparative analysis of Ru(II) complex uptake into cell populations which retain or lack the putative receptor.

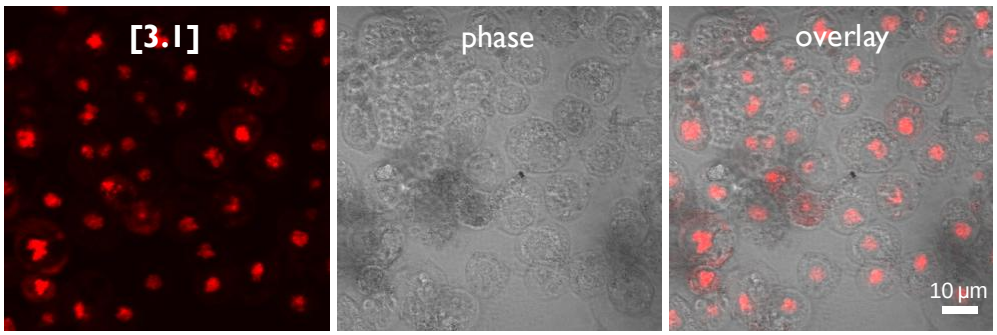

Figure 5.2 CLSM images of *Drosophila* cells incubated with dinuclear Ru(II)tpphz complex **[3.1]** (500 µM, 80 mins). Left: Ru(II) emission. Centre: Phase contrast. Right: Overlay image of Ru(II) emission and phase contrast.

5.6 Application of IT_{50} values

The use of IC_{50} values (that is, the concentration required to induce 50% cell death for a given incubation time) is frequently used to compare the toxic properties of molecules. Due variance in experimental protocols (such as incubation time), comparisons between research groups can be problematic.

As time is a fixed quantity for a given experiment, two complexes that have the same IC_{50} value may also display significantly different toxic behaviour over an extended time period – this was observed where **[3.1]** displays an IC_{50} value an order of magnitude larger than cisplatin when cells are exposed to it for 24 hours, but an equal IC_{50} with 72 hour exposure.

Another drawback is that an IC_{50} value does not describe the behaviour above and below this concentration. So two complexes may have the same IC_{50} value but one may be significantly more toxic at other concentrations – for example, cisplatin and **[3.1]** have the same IC_{50} value for 72 hour incubation time but cisplatin demonstrates a higher toxicity at sub-IC_{50} concentrations than **[3.1]**; something not reflected by the IC_{50} value for each complex.

The use of IT_{50} values (that is, the time required to induce 50% cell death for a given concentration) within this thesis demonstrates an alternative to the IC_{50} method and one specific advantage of this method is it takes time as a variable into account, allowing a more detailed assessment to be made of the toxicity of a molecule.

When the IT_{50} values recorded in this thesis (Section 3.8) are plotted on a graph of log C vs. IT_{50} and an exponential relationship is observed and therefore the data may be fit by a standard exponential decay curve (Figure 5.3). As the incubation time for an IC_{50} experiment is equal to the IT_{50} value for the IC_{50} concentration obtained, IC_{50} values may be plotted onto the same graph. These results show that the IC_{50} values for 24 and 72 hour incubation times are in agreement with the IT_{50} values measured for **[3.1]**, indicating that both experimental techniques can be combined together.

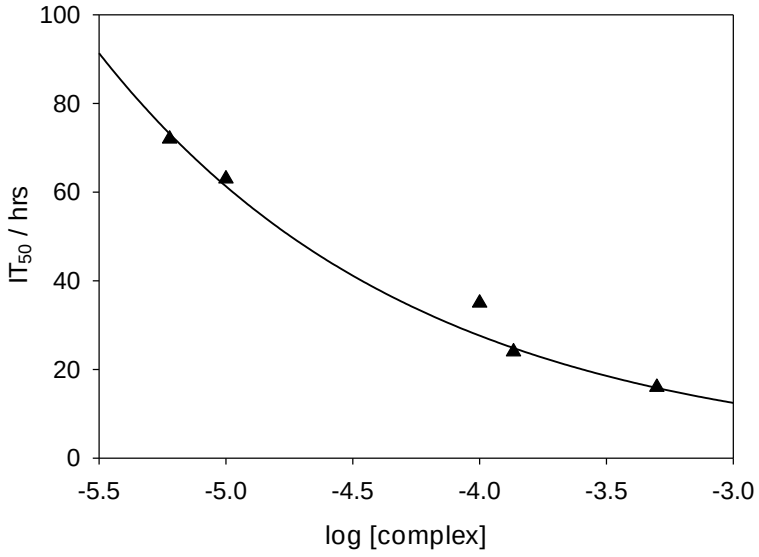

Figure 5.3 Plot of IT_{50} vs. log [complex] for **[3.1]** in MCF-7 cells. Data fit by $y = ae^{-bx}$ (a = 1.139, b = 0.797). $R^2 = 0.998$ by least squares analysis.

This approach also means that, for any given time, the associated IC_{50} value may be calculated by interpolation. For example, the IC_{50} value for MCF-7 cells exposed to **[3.1]** for 48 hours can be determined to be 20 μM from the fit plotted in Figure 5.3.

The rate of toxicity, *b*, is a measurement of how toxicity varies with concentration: a large rate of toxicity value indicates a large variation of toxicity with concentration.

The use of IT_{50} values can thus be applied in conjunction with the standard concentration/viability IC_{50} assay to describe the toxic properties of a molecule more completely and future work would develop this idea further by measuring the IT_{50} values for more molecules. It would be interesting to compare the decay curves of currently used anti-cancer drugs to those of potential candidates and, indeed, if there is any potential of this concept to be used as a model that is able to predict the drug-likeness of a molecule.

5.7 References

1. U. Schatzschneider, J. Niesel, I. Ott, R. Gust, H. Alborzinia and S. Wölfl, Cellular Uptake, Cytotoxicity, and Metabolic Profiling of Human Cancer Cells Treated with Ruthenium(II) Polypyridyl Complexes $[Ru(bpy)_2(N\text{-}N)]Cl_2$ with N-N=bpy, phen, dpq, dppz, and dppn., *ChemMedChem*, 2008, **3**, 1104-1109.
2. C. Hiort, P. Lincoln and B. Norden, DNA binding of Δ-and Λ-$[Ru(phen)_2dppz]^{2+}$, *J. Am. Chem. Soc.*, 1993, **115**, 3448-3454.
3. F. M. MacDonnell and S. Bodige, Efficient Stereospecific Syntheses of Chiral Ruthenium Dimers, *Inorg. Chem.*, 1996, **35**, 5758-5759.
4. T. Wilson, PhD Thesis, University of Sheffield, 2009.
5. S. Bodige and F. M. MacDonnell, Synthesis of free and ruthenium coordinated 5,6-diamino-1,10-phenanthroline, *Tetrahedron Lett.*, 1997, **38**, 8159-8160.
6. P. Sun, A. Krishnan, A. Yadav, S. Singh, F. M. MacDonnell and D. W. Armstrong, Enantiomeric Separations of Ruthenium(II) Polypyridyl Complexes Using High-Performance Liquid Chromatography (HPLC) with Cyclodextrin Chiral Stationary Phases (CSPs), *Inorg. Chem.*, 2007, **46**, 10312-10320.
7. F. R. Keene, Isolation and characterisation of stereoisomers in di- and tri-nuclear complexes, *Chem. Soc. Rev.*, 1998, **27**, 185-194.

8. B. T. Patterson and F. R. Keene, Isolation of Geometric Isomers within Diastereoisomers of Dinuclear Ligand-Bridged Complexes of Ruthenium(II), *Inorg. Chem.*, 1998, **37**, 645-650.
9. Z. H. Siddik, Cisplatin: mode of cytotoxic action and molecular basis of resistance, *Oncogene*, 2003, **22**, 7265-7279.
10. R. Agarwal and S. B. Kaye, Ovarian cancer: strategies for overcoming resistance to chemotherapy, *Nat. Rev. Cancer*, 2003, **3**, 502-516.
11. C. Stadelmann and H. Lassmann, Detection of apoptosis in tissue sections, *Cell Tissue Res.*, 2000, **301**, 19-31.
12. A. Ashworth, Drug Resistance Caused by Reversion Mutation, *Cancer Res.*, 2008, **68**, 10021-10023.
13. R. Dasgupta and N. Perrimon, Using RNAi to catch Drosophila genes in a web of interactions: insights into cancer research, *Oncogene*, 2004, **23**, 8359-8365.

Chapter 6

Experimental methods

6.1 General

6.1.1 Chemicals

All chemicals and solvents were purchased from commercial sources and were used as supplied unless stated otherwise. All Ru(II) complexes were treated as toxic.

6.1.2 Nuclear magnetic resonance (NMR) spectroscopy

^{1}H NMR spectra were recorded on a Bruker AM250 machine working in Fourier transform mode. The following abbreviations are used in the annotation of ^{1}H spectra: s = singlet, d = doublet, dd = doublet of doublets, t = triplet and m = multiplet.

6.1.3 Mass spectroscopy

Fast-atom bombardment (FAB) mass spectra (MS) were recorded on a Kratos MS80 mass spectrometer working in positive ion mode.

6.1.4 Elemental analysis

Microanalyses for carbon, hydrogen and nitrogen were obtained using a Perk-Elmer 2400 analyser working at 975 °C.

6.2 Synthesis

6.2.1 Tris(1-pyrazoyl)methane (tpm)[1]

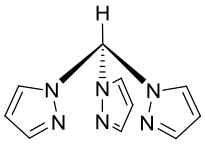

Pyrazole (20 g, 294 mmol) and tetra-n-butylammonium bromide (4.7 g, 14.7 mmol) were both added to distilled water (300 ml). With vigorous stirring using mechanical agitation sodium carbonate (187 g, 1.8 mol) was added. After cooling to room temperature, chloroform (150 ml) was added and the mixture boiled under reflux for three days. The solution was cooled to room temperature and filtered to remove excess base. An extraction with ether and water carried out. The combined organic layers were washed with saturated brine (200 ml) and dried over magnesium sulphate. The solvent was removed by rotary evaporation and the solid dried *in vacuo*. Mass = 6.24 g (294 mmol, 33.3 % yield) orange solid. ^{1}H NMR (acetone-d^{6}) δ (splitting, integration): 6.40 (dd, 3H), 7.62 (d, 3H), 7.86 (d, 3H) 8.73 (s, 1H).

6.2.2 1,10-phenanthroline-5,6-dione (dpq)[2]

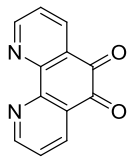

1,10-phenanthroline (5 g, 27.8 mmol) was dissolved into concentrated sulphuric acid (30 mL). Sodium bromide (2.6 g) and nitric acid (15 mL) were then carefully added and the mixture boiled under reflux for 40 minutes. The solution was cooled and poured over ice (400 g) and neutralised to pH 7.0 by addition of aqueous sodium hydroxide. An extraction with chloroform was carried out. The collected organic layers were dried with magnesium sulphate and the solvent removed by rotary evaporation. The yellow product was recrystallised using water/methanol (1:50). Mass = 2.83 g (13.4 mmol, 48.2 %) yellow solid. ^{1}H NMR ($CDCl_3$) δ (splitting, integration): 7.56 (dd, 2H), 8.47 (dd, 2H), 9.07 (dd, 2H).

6.2.3 Dipyrido[3,2-a:2',3'-c]phenazine (dppz)[2]

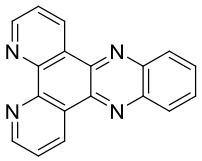

o-Phenylenediamine (0.6 g, 5.46 mmol) and dpq (1 g, 4.76 mmol) were boiled under reflux in ethanol (60 mL) for twenty minutes. The brown solid formed was recrystallised from ethanol/water (1:1). The solid was collected by filtration and dried under vacuum. Mass = 0.85 g (3.01 mmol, 63.2 %) pale yellow solid. ^{1}H NMR (acetone-d^6) δ (splitting, integration): 7.90 (dd, 2H), 8.10 (dd, 2H), 8.40 (dd, 2H), 9.20 (dd, 2H), 9.65 (dd, 2H).

6.2.4 Tetrapyrido[3,2-a:2',3'-c:3'',2''-h:2''',3'''-j]phenazine (tpphz)[3]

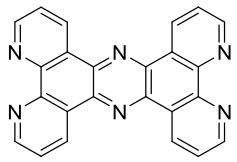

Ammonium acetate (15 g, 194.6 mmol), dpq (2.90 g, 13.8 mmol) and sodium sulfite (300 mg, 1.72 mmol) were boiled under reflux in ethanol (50 mls) for 2 hrs at 180°C under nitrogen. The solution was cooled and water (20 ml) was added resulting the formation of a yellow precipitate which was collected and washed with water, methanol and acetone. The crude product was added to boiling EtOH (100 ml), filtered while hot and dried *in vacuo*. Mass = 0.906 g (2.36 mmol, 34.2 %) yellow solid. ^{1}H NMR (TFA-d^6) δ (splitting, integration): 8.9 (t, 4H), 9.85 (dd, 4H), 10.8 (dd, 4H). MS; m/z (%): 385 (100) [M+].

6.2.5 [Ru(tpm)(Cl)$_3$][4]

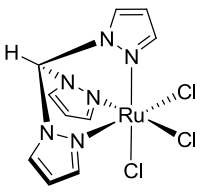

$RuCl_3.3H_2O$ (1.22 g, 4.67 mmol) and tpm (1 g, 4.67 mmol) were boiled under reflux in ethanol (50 mL) for three hours. After cooling the dark precipitate was filtered and washed with cold ethanol and ethyl ether then dried under vacuum. Mass = 1.32 g (3.14 mmol, 67.2 %) brown solid. MS m/z (%) 389 (100) $[M\text{-}Cl]^+$.

6.2.6 [Ru(tpm)(Cl)(dppz)]$^{+}$ [5]

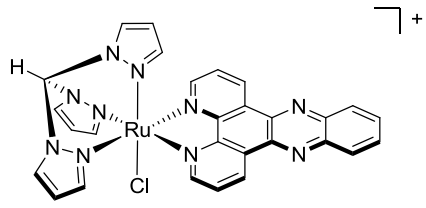

[Ru(tpm)Cl_3] (1.11 g, 2.61 mmol), dppz (0.75 g, 2.66 mmol) and LiCl (0.40 g) were boiled under reflux in ethanol/water (3:1, 100 mL) for ten minutes. Twelve drops of triethylamine were added and the solution boiled under reflux for 30 minutes under a nitrogen atmosphere. The solution was cooled and the solvent removed. The residue was dissolved in methanol (20 mL) and the fine dark solid was filtered out. The product was precipitated by addition of aqueous NH_4PF_6 and collected by filtration. The crude product was chromatographed on grade l alumina with acetonitrile/toluene (1:1). The purple band was collected and concentrated by rotary evaporation. Addition of diethyl ether precipitated the product as a dark solid. Mass= 0.66 g (0.85 mmol, 25.3 %) purple solid. ^{1}H NMR (acetone-d^6) δ (splitting, integration): 6.30 (td, 1H), 6.87 (m, 3H), 8.06 (dd, 2H), 8.17 (dd, 2H), 8.42 (dd, 2H), 8.52 (dd, 2H), 8.57 (m, 3H), 9.17 (dd, 2H), 9.57 (dd, 2H), 9.63 (s, 1H). MS m/z (%): 633 (100) $[M]^+$, 597 (30) $[M\text{-}Cl]^+$.

6.2.7 [Ru(tpm)(NCMe)(dppz)]$^{2+}$ [2.1][5]

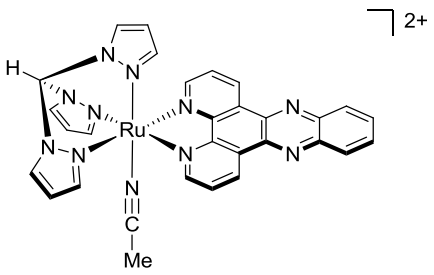

[Ru(tpm)(Cl)(dppz)](PF$_6$) (0.1 g, 0.13 mmol) and AgCF$_3$SO$_3$ (0.36 g, 0.14 mmol, 1.1 eq.) were heated at reflux in freshly distilled acetonitrile (50 mL) for fourteen hours. After cooling, the solvent was removed and the residue was taken up into methanol (20 mL). The solution was filtered through Celite and treated with aqueous NH_4PF_6 to precipitate the product, which was collected by filtration and dried under vacuum. Mass = 0.054 g (0.06 mmol, 44.7 %) red solid. ^{1}H NMR (acetone-d^6) δ (splitting, integration): 2.29 (s, 3H), 6.37 (dd, 1H), 6.95 (dd, 2H), 7.07 (dd, 1H), 8.22 (dd, 2H), 8.27 (dd, 2H), 8.56 (t, 2H), 8.62 (dd, 1H), 8.80 (dd, 2H), 9.42 (dd, 2H), 9.86 (dd, 2H), 9.87 (dd, 2H), 10.01 (s, 1H). MS m/z (%): 784 (100) [M-PF$_6$]$^+$, 638 (70) [M]$^+$, 597 (80) [M-(MeCN)-2(PF$_6$)]$^+$.

6.2.8 [Ru(tpm)(py)(dppz)]$^{2+}$ [2.2][5]

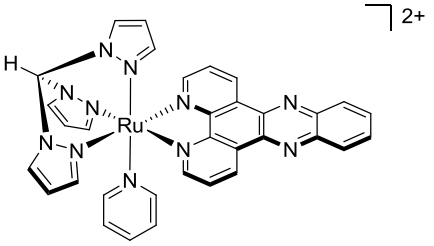

[Ru(tpm)(Cl)(dppz)](PF$_6$) (0.10g, 0.13 mmol) and AgNO$_3$ (0.035 g, 0.22 mmol) were boiled at reflux in ethanol: water (3:1) (40 mL) for five hours. After cooling to room temperature the solution was filtered through Celite to remove solid AgCl. Pyridine (1 mL) was added and the solution boiled at reflux overnight. After cooling to room temperature the solution was filtered again through Celite and aqueous NH_4PF_6 was added. The precipitate was collected by filtration and washed with water and diethyl ether then dried under vacuum. Mass = 0.10 g (0.10 mmol, 76.9 %) orange solid. ^{1}H NMR (acetone-d^6) δ (splitting, integration): 6.30 (dd, 1H), 6.93 (dd, 1H), 6.98 (m, 2H), 7.15 (dd, 2H), 7.76 (dd, 2H), 7.80 (t, 1H), 8.21 (dd, 2H), 8.24 (dd, 2H), 8.52 (dd, 2H), 8.56 (m, 2H), 8.58 (dd, 1H), 8.85 (dd, 2H), 9.42 (dd, 2H), 9.87 (dd, 2H), 9.93 (s, 1H). MS m/z (%): 965 (45) [M]$^+$, 597 (55) [M-py-2(PF$_6$)]$^{2+}$.

6.2.9 $[Ru(phen)_2(Cl)_2]$[6]

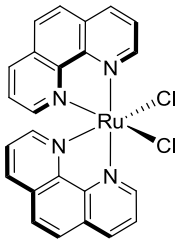

$RuCl_3.3H_2O$ (3 g, 11.53 mmol), 1,10-phenanthrolene (4.1 g, 22.7 mmol) and LiCl (3.1 g, 73.8 mmol) were heated at reflux in dimethylformamide (40 ml) for 8 hours. After cooling to room temperature, 200 ml of acetone was added and then the solution was stored at 4°C for 16 hours. The precipitate was collected by filtration, washed with water and ether before drying *in vacuo*. Mass = 3.75 g (7.05 mmol, 62.1 %) brown-green solid. MS m/z (%): 532 (65) $[M]^+$.

6.2.10 $[\{Ru(phen)_2\}_2(tpphz)]^{4+}$ [3.1][3, 7]

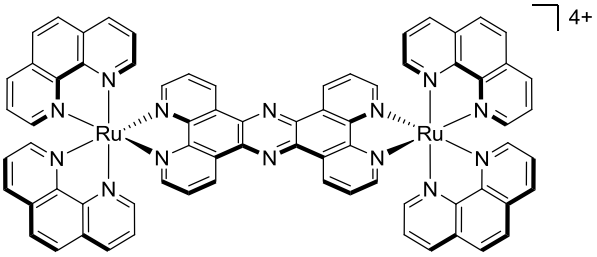

$[Ru(phen)_2Cl_2]$ (0.922g, 1.73 mmol) and tpphz (0.267g, 0.70 mmol) were added to a 1:1 solution of EtOH/water (80 mls) and heated at reflux for 12 hours under nitrogen. The solution was cooled to room temperature then a further 16 hours at 4°C. The brown solution was filtered and the ethanol removed by rotary evaporation. The addition of NH_4PF_6 caused the formation of a dark brown precipitate which was collected by filtration, washed with water, recrystallised in acetonitrile by addition of diethyl ether and dried *in vacuo*. Mass = 1.13g (0.60 mmol, 85.7 %) orange/brown solid. ^1H NMR (acetone-d^6) δ (splitting, integration): 7.8 (t, 8H), 8.0 (t, 4H), 8.4 (d, 4H), 8.4 (s, 8H), 8.6 (dd, 8H), 8.8 (dd, 8H), 10.1 (dd, 4H). MS; m/z (%): 1742 (65) $[M\text{-}PF_6]^+$, 1598 (100) $[M\text{-}2(PF_6)]^+$, 1453 (45) $[M\text{-}3(PF_6)]^+$.

6.2.11 $[Ru(bpy)_2(Cl)_2]$[6]

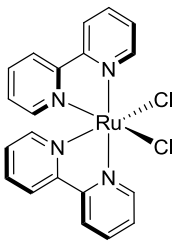

$RuCl_3.3H_2O$ (3 g, 11.53 mmol), bipyridine (3.6 g, 22.8 mmol) and LiCl (3.12 g, 73.8 mmol) were heated at reflux in dimethylformamide (30 ml) for 8 hours. After cooling to room temperature, 200 ml of acetone was added and then the solution was stored at 4°C for 16 hours. The precipitate was collected by filtration and washed with water and ether before drying *in vacuo*. Mass = 4.513 g (9.32 mmol, 81.8 %) brown-green solid. MS m/z (%): 484 (100) $[M]^+$.

6.2.12 $[\{Ru(bpy)_2\}_2(tpphz)]^{4+}$ [3.2][3, 7]

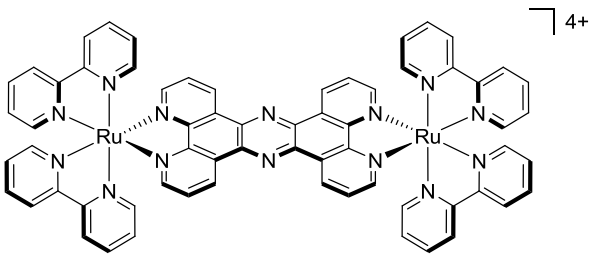

$[Ru(bpy)_2Cl_2]$ (1.012 g, 2.09 mmol) and tpphz (0.267g, 0.70 mmol) were added to a 1:1 solution of EtOH/water (80 mls) and heated at reflux for 12 hours under nitrogen. The solution was cooled to room temperature then a further 16 hours at 4°C. The brown solution was filtered and the ethanol removed by rotary evaporation. The addition of NH_4PF_6 caused the formation of a red/brown precipitate which was collected by filtration and washed with water. The crude product was recrystallised from acetonitrile/ether and dried *in vacuo*. Mass = 0.8 g (0.45 mmol, 64.3 %) red solid. ^1H NMR (MeCN-d^6) δ (splitting, integration): 7.5 (m, 8H), 7.7 (m, 8H), 7.9 (d, 4H), 8.0 (m, 8H), 8.3 (dd, 4H), 8.5 (m, 8H), 10.0 (dd, 4H). MS; m/z (%): 1647 $[M\text{-}PF_6]^+$, 1502 $[M\text{-}2(PF_6)]^+$, 1357 $[M\text{-}3(PF_6)]^+$, 1212 $[M\text{-}4(PF_6)]^+$. Elemental analysis for **[3.2]**$(PF_6)_4$, $C_{64}H_{44}F_{24}N_{14}P_4Ru_2$: Calcd: C; 42.92, H; 2.48, N; 10.95. Found: C; 42.18, H; 2.57, N; 10.58.

6.2.13 $[Ru(5mp)_2(Cl)_2]$

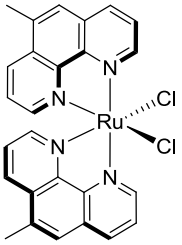

$RuCl_3.3H_2O$ (1.3 g, 5 mmol), 5-methyl-1,10-phenanthroline (5mp) (2 g, 10 mmol) and LiCl (1.4 g, 33.3 mmol) were heated at reflux in dimethylformamide (40 ml) for 8 hours under a nitrogen atmosphere. After cooling to room temperature, 100 ml of acetone was added and then the solution was stored at 4°C for 24 hours. The precipitate was collected by filtration, washed with water and ether before drying *in vacuo*. Mass = 1.526g (2.73 mmol, 54.5 %) brown solid. MS; m/z (%): 525 (100) $[M\text{-}Cl]^+$.

6.2.14 $[\{Ru(5mp)_2\}_2(tpphz)]^{4+}$ [4.1]

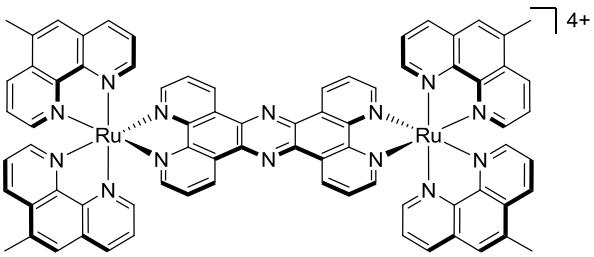

$[Ru(5mp)_2(Cl)_2]$ (0.9g, 1.61 mmol) and tpphz (0.263g, 0.68 mmol) were added to a 1:1 solution of EtOH/water (80 mls) and heated at reflux for 12 hours under nitrogen. The solution was cooled to room temperature then a further 24 hours at 4°C. The ethanol removed by rotary evaporation. The addition of NH_4PF_6 caused the formation of a red/brown precipitate which was collected by filtration and washed with water. The crude product was recrystallised from acetonitrile/ether and dried *in vacuo*. Mass = 1.134g (0.65 mmol, 85.6 %) orange/brown solid. ^1H NMR (MeCN-d^6) δ (splitting, integration): 2.9 (s, 12H), 7.7 (m, 8H), 7.9 (m, 4H), 8.1 (m, 4H), 8.2 (s, 4H), 8.3 (m, 8H), 8.5 (m, 8H), 10.0 (dd, 4H). MS; m/z (%): 827 (100%) $[M\text{-}2(PF_6)]^{2+}$, 503 (35%) $[M\text{-}3(PF_6)]^{3+}$. Elemental analysis for **[4.1]**$(PF_6)_4.4.5H_2O$, $C_{76}H_{61}F_{24}N_{14}O_{4.5}P_4Ru_2$: Calcd: C; 45.09, H; 3.04, N; 9.69. Found: C; 45.04, H; 3.03, N; 9.66.

6.2.15 $[Ru(dmp)_2Cl_2]$

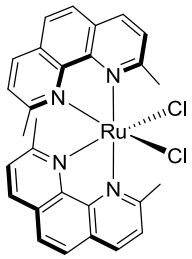

$RuCl_3.3H_2O$ (3.12 g, 12 mmol), neocuproine (dmp) (5 g, 24 mmol) and LiCl (3.1 g, 73.8 mmol) were heated at reflux in dimethylformamide (40 ml) for 8 hours under a nitrogen atmosphere. After cooling to room temperature, 100 ml of acetone was added and then the solution was stored at 4°C for 24 hours. The precipitate was collected by filtration, washed with water and ether before drying *in vacuo*. Mass = 3.98 g (6.8 mmol, 56.4 %) dark brown solid. MS m/z (%): 590 (80) $[M]^+$.

6.2.16 $[\{Ru(dmp)_2\}_2(tpphz)]^{4+}$ [4.2]

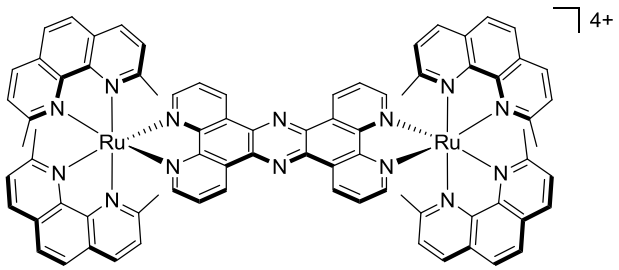

$[Ru(dmp)_2(Cl)_2]$ (1.02g, 1.73 mmol) and tpphz (0.267g, 0.7 mmol) were added to a 1:1 solution of EtOH/water (50 mls) and heated at reflux for 12 hours under nitrogen. The solution was cooled to room temperature then a further 24 hours at 4°C. The ethanol was removed by rotary evaporation. The addition of NH_4PF_6 caused the formation of a red/brown precipitate which was collected by filtration and washed with water. The crude product was recrystallised from acetonitrile/ether and dried *in vacuo*. Mass = 1.216 g (0.11 mmol, 86.9 %) brown solid. ^1H NMR (MeCN-d^6) δ (splitting, integration): 2.9 (s, 24H), 7.7 (t, 8H), 7.9 (t, 4H), 8.1(m, 8H), 8.2 (s, 8H), 8.5 (dd, 4H), 10.0 (dd, 4H). MS; m/z (%): 855 (20%) $[M\text{-}2(PF_6)]^+$, 537 (100%) $[M\text{-}3(PF_6)]^{3+}$. Elemental analysis for **[4.2]**$(PF_6)_4.2H_2O$, $C_{80}H_{64}F_{24}N_{14}O_2P_4Ru_2$: Calcd: C; 47.21, H; 3.17, N; 9.63. Found: C; 46.27, H; 3.17, N; 9.69.

6.2.17 $[Ru(DIP)_2Cl_2]$

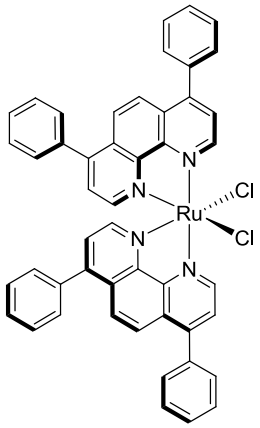

$RuCl_3.3H_2O$ (2.1 g, 8.03 mmol), 4-7-diphenyl-1,10-phenanthrolene (DIP) (5 g, 15 mmol) and LiCl (2.08 g, 49 mmol) were heated at reflux in dimethylformamide (20 ml) for 8 hours under a nitrogen atmosphere. After cooling to room temperature, 100 ml of acetone was added and then the solution was stored at 4°C for 24 hours. The precipitate was collected by filtration, washed with water and ether before drying *in vacuo*. Mass = 2.95g (3.5 mmol, 46.7 %) brown solid. MS; m/z (%): 836 (100%) $[M]^+$.

6.2.18 $[\{Ru(DIP)_2\}_2(tpphz)]^{4+}$ [4.3]

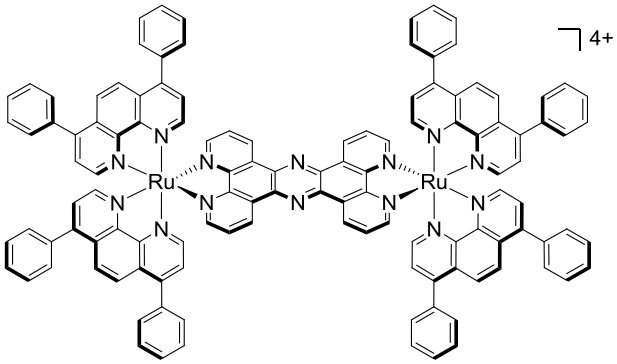

$[Ru(DIP)_2(Cl)_2]$ (1.47g, 1.76 mmol) and tpphz (0.34g, 0.88 mmol) were added to a 1:1 solution of EtOH/water (50 mls) and heated at reflux for 12 hours under nitrogen. The solution was cooled to room temperature then a further 24 hours at 4°C. The ethanol removed by rotary evaporation. The addition of NH_4PF_6 caused the formation of a red/brown precipitate which was collected by filtration and washed with water. The crude product was recrystallised from acetonitrile/ether and dried *in vacuo*. Mass = 1.62 g (0.65 mmol, 73.8 %) red solid. ^1H NMR (MeCN-d^6) δ (splitting, integration): 7.5 (d, 16H), 7.6 (d, 16H), 7.8 (m, 16H), 8.0 (m, 4H), 8.2 (s, 8H), 8.3 (dd, 4H), 8.4 (d, 8H), 8.5 (d, 8H), 10.1 (dd, 4H). MS; m/z (%): 1103 (55%) $[M-2(PF_6)]^{2+}$, 686 (100%) $[M-3(PF_6)]^{3+}$. Elemental analysis for **[4.3]**$(NO_3)_4.10H_2O$, $C_{120}H_{96}N_{18}O_{22}Ru_2$: Calcd: C; 61.48, H; 4.12, N; 10.75. Found: C; 61.83, H; 4.36, N; 10.50.

6.2.19 Anion metatheses

The hexafluorophosphate salt of each complex was dissolved in the minimum volume of acetone and a saturated solution of ammonium chloride in acetone added. The resultant precipitated chloride salt was collected by filtration, washed with cold acetone and dried *in vacuo*.

6.2.20 Complex preparation for cellular studies

Stock solutions of the chloride salts of each complex were made in PBS (typically 5 mM). Sonication and gentle heating were used to aid dissolution, as required. Stock solutions were filter sterilised with a 0.20 μm filter.

6.3 Photochemistry

6.3.1 Absorption spectra

A quartz cuvette was loaded with solutions of the complex dissolved in acetonitrile (as the PF_6^- salt) or water (at the Cl^- salt) and absorption spectra were collected using a Cary 500 Scan UV-vis-NIR Spectrophotomer working in double beam mode (spectral band width = 2 nm) at a scan speed of 600 nm/min and baseline corrected.

6.3.2 Molar extinction coefficients

The absorbance, A, for each peak was recorded (path length, l = 1 cm) and an average value for the molar extinction coefficient, , over a range of concentrations, c, was calculated using the Beer-Lambert law (Equation 6.1).

$$A = \varepsilon l c$$

Equation 6.1 The Beer-Lambert law.

6.3.3 Excitation and emission spectra

Deoxygenation for the luminescence experiments was performed by bubbing the solvent used for each sample with nitrogen for 30 mins. Solutions of each complex (5, 10, 20 μM) were dissolved in acetonitrile, loaded into a cuvette and the excitation and emission spectrum was recorded using a Fluoromax-3 Spectrophotometer (excitation and emission slit = 5 nm, scan speed = 100 nm/min).

6.3.4 Quantum yields

For each complex and reference sample, the emission spectra (λ_{ex} = 463 nm) was recorded and the integrated emission intensity calculated using the Fluoromax-3 Spectrophotometer software. The absorbance at 463 nm was measured by UV-vis spectrophotometry. The quantum yield value for each complex calculated using Equation 4.1, where Φ_x and Φ_{ref} are the quantum yields of the sample and reference respectively, A_x and A_{ref} the measured absorbance of the sample and reference at the excitation wavelength, I_x and I_{ref} the integrated emission intensities of the sample and η_x and η_{ref} are the refractive index of the solvent of the sample and reference respectively. $[Ru(bpy)_3](PF_6)_2$ in CH_3CN (Φ = 0.062) was used as the reference.[8] A graph of A vs. I was plotted for each complex and $[Ru(bpy)_3](PF_6)_2$. The quantum yield was calculated using each gradient and Equation 4.1. At least 5 data points were used in the construction of each graph.

$$\varphi_x = \varphi_{ref}\left(\frac{A_{ref}}{I_{ref}}\right)\left(\frac{I_x}{A_x}\right)\left(\frac{\eta_x}{\eta_{ref}}\right)^2$$

Equation 4.1 Quantum yield. Φ = quantum yield, A = absorbance at the excitation wavelength, I = integrated emission intensity, η = solvent refractive index for the reference (*ref*) and sample (*x*).

6.4 DNA binding studies

6.4.1 DNA preparation

Calf thymus DNA (CT-DNA) was dissolved in aqueous buffer (25 mM NaCl, 5 mM Tris, pH = 7) and broken into an average of 150-200 base pair fragments by sonication (2 × 15 mins). The purity of the sample was determined by UV-vis spectroscopy, with A260/A290 > 1.9 indicating a protein-free sample. The concentration of CT-DNA was determined by UV-vis spectroscopy (ε_{280nm} = 13200 M^{-1} cm^{-1}).

6.4.2 Luminescence titration

A 5 μM solution of the complex was dissolved in aqueous buffer (25 mM NaCl, 5 mM Tris, pH = 7) and loaded into a quartz cuvette. This was allowed to equilibrate at 25°C for 30 mins and the emission spectra recorded. 0.5 -2 μL of a concentrated stock CT-DNA solution in aqueous buffer (typically 200 μM) was added and the solution mixed by pipette. The emission spectrum was recorded, showing an enhancement in emission, and this procedure was continued until the emission became constant. The emission intensity *I* for each addition of DNA was calculated using the Fluoromax-3 Spectrophotometer software and the binding constant calculated using the binding model described in detail in Section 4.4.

6.5 Octanol/water partition coefficients

Calculated octanol/water partition coefficients for organic molecules and ligands were obtained using the "Molinspiration" software.[9] Experimentally determined octanol/water partition coefficients for each Ru(II) complex were obtained using the "shake-flask" method described as follows: A sample of the chloride salt of each complex was dissolved in deionised water (100 μM) and the absorbance recorded. A known volume of water was then mixed with an equal volume of n-octanol by inversion (x 50) and the two layers were allowed to separate overnight. The concentration of complex in each phase was quantified by absorbance at 450 nm and interpolated with the calibration graph of absorbance v. concentration of the complex in each solvent. The partition coefficient, log P, was calculated using Equation 2.1 (n = 3).

$$\log P_{octanol/\,water} = \log\left(\frac{[complex]_{octanol}}{[complex]_{water}}\right)$$

Equation 2.1 Calculation of octanol/water partition coefficient log P.

6.6 Cell Culture

MCF-7 (human breast carcinoma), A2780 and CP70 (human ovarian carcinoma) cell lines were cultured in RMPI-1640 medium. FaDu (human hypopharyngeal carcinoma), Saos-2 (human osteosarcoma) cell lines and primary HDF (human dermal fibroblast) cells were cultured in Dulbecco's modified Eagle's medium (DMEM). HeLa (cervical carcinoma) cells were cultured in either RMPI-1640 or DMEM media, as specified by the experiment. All growth media was supplemented with 2 mM L-glutamine, 100 IU ml^{-1} penicillin, 100 μg ml^{-1} streptomycin and 10% fetal calf serum (FCS). Cultures were grown as monolayers and maintained at 37°C in an atmosphere of 5 % CO_2 / 95 % air. Cultures were subcultured routinely using Trypsin (0.1 % v/v in PBS) once 80-95 % confluence was achieved. L5178Y-R (mouse lymphoma) cells were cultured in suspension in RPMI-1640 medium, supplemented with 2 mM L-glutamine, 100 IU ml^{-1} penicillin, 100 μg ml^{-1} streptomycin and 10% FCS and subcultured *via* centrifugation. Cell lines were used between passage numbers 5-40 and primary cell cultures were used between passage numbers 3-6.

6.7 Confocal laser scanning microscopy (CLSM)

6.7.1 Sample preparation for live cell microscopy

For live cell microscopy, cell cultures were grown on 6 well plates for upright microscopy or microdishes (Thistle Scientific) for inverted microscopy and allowed to grow for a minimum of 24 hours. Cell cultures were then incubated with solutions of Ru(II) complex at the stated conditions, concentration and time for the relevant experiment. After incubation, the complex-containing medium was removed and the cells washed with PBS.

6.7.2 Sample preparation for fixed cell microscopy

For fixed cell experiments, monolayers were treated with 10% formaldehyde (10 minutes) or 70% cooled ethanol before incubation with Ru(II) complex (typically 100 μM in PBS for 10 minutes). For staining after fixation, cells fixed using formaldehyde were additionally permeablised with Triton (10 minutes) before exposure to the complex. After incubation, the solution was removed and the cells were washed with PBS.

6.7.3 Co-staining

Where stated, co-staining was performed using the following commercially available stains (Invitrogen), which were dissolved in PBS unless otherwise indicated: SYTO9 (2 μM, 2 minutes), PI (10 μM, 10 minutes), DAPI (500 nM, 2 minutes), Mitotracker Red (1 μM, 20-45 minutes, serum-free culture medium) and Lysotracker Yellow (100 nM, 45–60 minutes, normal culture medium). After co-staining, cells were washed with PBS before imaging.

6.7.3 Image acquisition

Cell cultures were luminescently imaged on Zeiss LSM 510 META upright and Zeiss LSM 510 META inverted confocal laser scanning microscopes equipped with Argon (λ_{ex} = 458 nm, 488 nm, 514 nm), He-Ne (λ_{ex} = 543 nm, 643 nm) lasers and a blue diode laser (λ_{ex} = 405 nm, inverted microscope only). Objectives used were: 40x, 63x and 100x long-range water-dipping lenses (upright microscope) or 40x and 63x oil-immersion lenses (inverted microscope). Ru(II) complexes were excited with an Ar-ion laser at 458 nm and emission collected using META detection within a 600-700 nm (red) range; the exact wavelengths used for each complex as stated by the specific experiment. SYTO9 was excited at 488 nm (Ar-ion) and emission collected using a 500-530 nm BP (bandpass) filter. PI was excited at 543 nm (He-Ne) and emission collected using META detection at 565-615 nm. DAPI was excited using a 405 nm diode laser and emission detected using a 420 nm LP (long-pass) filter. Mitotracker Red was excited at 543 nm (He-Ne) and emission detected using META detection at 580-620 nm. Lysotracker Yellow was excited at 458 nm (Ar-ion) and emission detected using a 500-560 nm BP filter. Image data acquisition and processing was performed using Zeiss LSM Image Browser. Co-localisation was performed using histogram analysis, with the two emissions as the parameters selected (Figure 6.1). Emission signals were unmixed, where appropriate.

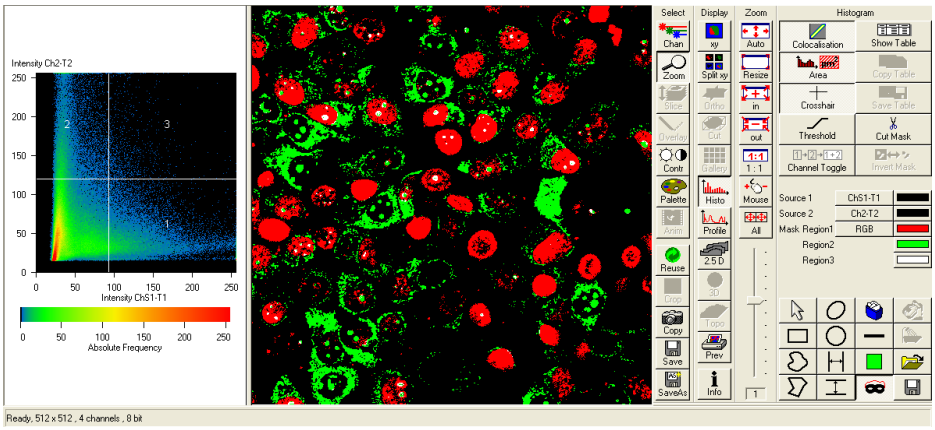

Figure 6.1 Colocalisation set-up.

6.8 Transmission Electron Microscopy (TEM)

Sample preparation involved MCF-7 cells being grown in 6 well plates then incubated with Ru(II) complex at the stated concentration and time, the solution removed and the cells fixed using 3% glutaraldehyde. For fixed cellular location TEM studies, cells were fixed with cooled 70% ethanol prior to exposure with the complex. For both methods, cell cultures were dehydrated using a series of ethanol washes (70 – 100 % ethanol) and TEM samples sectioned in Araldite resin by microtome. Samples were examined on a FEI Tecnai instrument operating at 80 kV equipped with a Gatan 1 k CCD Camera.

6.9 Inhibition treatment (uptake mechanism)

Temperature-dependence used cells that had been cooled at 4°C for 30 minutes then incubated with Ru(II) complex at 4°C for 1 hour. For treatment with endocytosis inhibitors, cells were treated with: chloroquine (5 – 100 μM),[10] NH_4Cl (5 – 50 mM),[11] chlorpromazine (0.1 – 10 μg ml^{-1}),[12] filipin (1 – 20 μg ml^{-1}),[13] nocodazole (0.1 – 10 μM)[14] or colchicine (0.1 – 10 μM)[14] for 30 minutes then with Ru(II) complex plus each inhibitor for 1 hour before analysis. Each inhibitor treatment required serum-free conditions throughout. For qualitative uptake analysis, cells were examined using CLSM. For quantitative uptake analysis, the luminescence intensity (% 37 °C control, n = 3) was measured by ImageXpress 5000A (Axon instruments, Inc.) cellular screening platform data acquisition hardware and software. Excitation wavelength = 465 nm, emission band pass filter 600 - 680 nm.

6.10 Cytotoxicity (MTT assay)

The basis of the MTT assay is that yellow MTT (3-(4,5-dimethylthiazol-2-yl)-2,5-diphenyltetrazolium bromide) is reduced to a purple formazan product in the mitochondria of living cells by reductase enzymes. As the reduction of MTT can only occur within active mitochondria, this amount of formazan produced is directly related to the number of viable cells within a sample. The amount of formazan may be quantified by absorbance between 500-600 nm and the toxicity of a sample may be deduced by comparison of the formazan content for cells exposed to the sample to that of an untreated control. As different cell samples can show different relationships between enzyme activity and cell number, the assay is only valid for comparative purposes within the same sample of cells.

6.10.1 IC_{50} values

Cell cultures were grown on 24 or 48 well plates and allowed to grow for 24 hours. Cell cultures were then treated with solutions of Ru(II) complex at various concentrations (10% PBS: 90% medium) for the given incubation time in triplicate. Solutions were removed and the cells incubated with 0.5 mg ml^{-1} MTT dissolved in PBS for 30-40 minutes. The formazan product was eluted using 200 µl/well of acidified propan-2-ol, 150 µl of this was transferred to a 96 well plate and the absorbance quantified by spectrophotometer (540 nm, referenced at 640 nm). An average absorbance for each concentration was obtained and cell viability was determined as a percentage of untreated negative control wells (10% PBS: 90% medium). Using Sigmaplot 11.0 software, a 3 parameter sigmoidal curve was used to fit each data set ($R^2 > 0.97$ for each fit) and the IC_{50} value (the concentration corresponding to 50% viability) calculated by interpolation.

6.10.2 IT_{50} values

Cell cultures were grown on 24 or 48 well plates and allowed to grow for 24 hours. Cell cultures were then treated with solutions of Ru(II) complex (10% PBS: 90% medium) at the given concentration in triplicate. Cell viability was assessed by MTT assay at various time points. IT_{50} data was fit by a 2 parameter exponential decay curve ($R^2 > 0.98$ for each fit) and the IT_{50} value (the time corresponding to 50% viability) calculated by interpolation.

6.11 References

1. D. L. Reger, T. C. Grattan, K. J. Brown, C. A. Little, J. J. S. Lamba, A. L. Rheingold and R. D. Sommer, Syntheses of tris(pyrazolyl)methane ligands and {[tris(pyrazolyl)methane]$Mn(CO)_3$}SO_3CF_3 complexes: comparison of ligand donor properties, *J. Organomet. Chem.*, 2000, **607**, 120-128.
2. W. Paw and R. Eisenberg, Synthesis, Characterization, and Spectroscopy of Dipyridocatecholate Complexes of Platinum, *Inorg. Chem.*, 1997, **36**, 2287-2293.
3. J. Bolger, A. Gourdon, E. Ishow and J.-P. Launay, Mononuclear and Binuclear Tetrapyrido [3.2-a: 2', 3'-c: 3", 2"-h: 2"', 3"'-j] phenazine (tpphz) Ruthenium and Osmium Complexes, *Inorg. Chem.*, 1996, **35**, 2937-2944.
4. A. Llobet, P. Doppelt and T. J. Meyer, Redox Properties of Aqua Complexes of Ruthenium(II) Containing the Tridentate Ligands 2,2':6',2"-Terpyridine and Tris(1-pyrazolyl)methane, *Inorg. Chem.*, 1988, **27**, 514-520.
5. C. Metcalfe, H. Adams, I. Haq and J. A. Thomas, A ruthenium dipyridophenazine complex that binds preferentially to GC sequences, *Chem. Commun.*, 2003, 1152-1153.
6. B. P. Sullivan, D. J. Salmon and T. J. Meyer, Mixed phosphine 2,2'-bipyridine complexes of ruthenium, *Inorg. Chem.*, 1978, **17**, 3334-3341.
7. C. Rajput, R. Rutkaite, L. Swanson, I. Haq and J. A. Thomas, Dinuclear Monointercalating Ru(II) Complexes That Display High Affinity Binding to Duplex and Quadruplex DNA, *Chem. Eur. J.*, 2006, **12**, 4611-4619.

8. J. M. Calvert, J. V. Caspar, R. A. Binstead, T. D. Westmoreland and T. J. Meyer, Metallopolymer photochemistry. Photophysical, photochemical and photoelectrochemical properties of $(bpy)_2Ru(II)$ sites bound to poly(4-vinylpyridine), *J. Am. Chem. Soc.*, 1982, **104**, 6620-6627.

9. www.molinspiration.com

10. R. Wattiaux, N. Laurent, S. Wattiaux-De Coninck and M. Jadot, Endosomes, lysosomes: their implication in gene transfer, *Adv. Drug Delivery Rev.*, 2000, **41**, 201-208.

11. H. K. Ziegler and E. R. Unanue, Decrease in macrophage antigen catabolism caused by ammonia and chloroquine is associated with inhibition of antigen presentation to T cells, *Proc. Natl. Acad. Sci. U.S.A.*, 1982, **79**, 175-178.

12. L. H. Wang, K. G. Rothberg and R. G. Anderson, Mis-assembly of clathrin lattices on endosomes reveals a regulatory switch for coated pit formation, *J. Cell Biol.*, 1993, **123**, 1107-1117.

13. J. E. Schnitzer, P. Oh, E. Pinney and J. Allard, Filipin-sensitive caveolae-mediated transport in endothelium: reduced transcytosis, scavenger endocytosis, and capillary permeability of select macromolecules, *J. Cell Biol.*, 1994, **127**, 1217-1232.

14. M. L. Elkjaer, H. Birn, P. Agre, E. I. Christensen and S. Nielsen, Effects of microtubule disruption on endocytosis, membrane recycling and polarized distribution of Aquaporin-1 and gp330 in proximal tubule cells, *Eur. J. Cell Biol.*, 1995, **67**, 57-72.

Appendix

M. R. Gill, J. Garcia-Lara, S. J. Foster, C. Smythe, G. Battaglia and J. A. Thomas, A ruthenium(II) polypyridyl complex for direct imaging of DNA structure in living cells, *Nat. Chem.*, **2009**, *1*, 662-667.

nature chemistry

ARTICLES

PUBLISHED ONLINE: 18 OCTOBER 2009 | DOI: 10.1038/NCHEM.406

A ruthenium(II) polypyridyl complex for direct imaging of DNA structure in living cells

Martin R. Gill[1,3], Jorge Garcia-Lara[2], Simon J. Foster[2], Carl Smythe[3], Giuseppe Battaglia[3]* and Jim A. Thomas[1]*

In the search for new biological imaging agents, metal coordination compounds able to emit from triplet metal-to-ligand charge transfer (MLCT) states offer many advantages as luminescent probes of DNA structure. However, poor cellular uptake restricts their use in live cells. Here, we present a dinuclear ruthenium(II) polypyridyl system that works as a multifunctional biological imaging agent staining the DNA of eukaryotic and prokaryotic cells for both luminescence and transition electron microscopy. This MLCT 'light switch' complex directly images nuclear DNA of living cells without requiring prior membrane permeabilization. Furthermore, inhibition and transmission electron microscopy studies show this to be via a non-endocytotic, but temperature-dependent, mechanism of cellular uptake in MCF-7 cells, and confocal microscopy reveals multiple emission peaks that function as markers for cellular DNA structure.

Since the identification of DNA as the carrier of genetic material, work towards the understanding of DNA organization and structure within the cell nucleus has become of great importance. Fluorescent microscopy using luminescent, cell membrane-permeable organic DNA-binding molecules as marker stains is a well established technique towards achieving this goal[1]. However, many of the currently available set of fluorescent dyes suffer from low water solubility, high toxicity and photobleaching[2]. Many of the DNA dyes traditionally used by the cell biologist, such as 4′,6-diamidino-2-phenylindole (DAPI) or the Hoechst stains, also require ultraviolet (UV) light as illumination, which can induce extensive DNA photodamage[3]. In addition to these points, the difference between emission and excitation energies (the Stokes shift) is small (typically less than 50 nm) and this can lead to unwanted background signal due to autofluorescence of endogenous fluorophores[1].

In this context, metal ion complexes offer a very attractive set of optical imaging properties and recent studies have seen the development of long-lifetime cell-permeable lanthanide and platinum based systems as effective nuclear imaging agents[4,5]. Ever since the discovery that $[Ru(bpy)_2(dppz)]^{2+}$ (bpy = 2,2′-bipyridine, dppz = dipyrido[3,2-a:2′,3′-c]phenazine) functions as a molecular 'light switch' for DNA upon metal-to-ligand charge transfer (MLCT) excitation[6], there has been great attention drawn to the DNA-binding properties of polypyridyl coordination complexes of d^6 octahedral metal ions, specifically towards the development of highly sensitive and structure-specific DNA probes[7,8]. As DNA imaging tools, such complexes offer several advantages over existing systems: MLCT excitations occur in the visible region of the spectrum, they possess high Stokes shifts (typically greater than 150 nm) along with chemical and photostability. Until recently research has largely focused on the development of *in vitro* probes; the few studies involving direct imaging of DNA in living cells with such systems has had limited success, with poor membrane permeability being ascribed as the limiting factor[9–15].

In this study, we explore the potential of two dinuclear ruthenium(II) systems as cellular DNA stains, showing one of these to be successfully taken up by living cells and to act as a structure-sensitive probe of DNA.

Using previously reported methods[16,17], the dinuclear Ru(II) complexes $[(phen)_2Ru(tpphz)Ru(phen)_2]^{4+}$ **1** and $[(bpy)_2Ru(tpphz)Ru(bpy)_2]^{4+}$ **2** (phen = 1,l0-phenanthroline, tpphz = tetrapyrido[3,2-a:2′,3′-c:3″,2″-h:2‴,3‴-j]phenazine; Fig. 1a) were synthesized as their water-soluble chloride salts, and their potential as cellular DNA stains was investigated. As both **1** and **2** are non-emissive in water but display intense luminescence when bound to DNA they are ideal candidates for such a role. Like in the related dppz systems, this light switch effect arises due to the shielding of the phenazine nitrogen atoms of the ditopic tpphz ligand from water and resultant emission from the ^{3}MLCT state[16–19].

The cytotoxicity of each complex towards the MCF-7 human breast cancer cell line was determined by MTT (MTT = (3-(4,5-dimethylthiazol-2-yl)-2,5-diphenyltetrazolium bromide) assay and the derived IC_{50} values showed that neither **1** or **2** demonstrates high toxicity over a 24 hour incubation period (IC_{50} values of 138 μM and >500 μM respectively), with **1** being the more toxic of the two complexes.

To examine the cellular uptake of the complexes, we incubated MCF-7 cells with solutions of **1** and **2**, and then imaged them using confocal microscopy. The excitation wavelength used was 458 nm and the emission measured at 670–700 nm, corresponding to the previously observed MLCT luminescent 'light switch' effect of each complex upon binding to DNA *in vitro*. To determine the health of the cells after incubation, a standard live/dead staining procedure using two commercially available dyes—SYTO 9 and propidium iodide (PI)—was performed. SYTO 9 (octanol/water partition coefficient, log$P$ = 0.93)[20] is a membrane-permeable nucleic acid dye, which stains the RNA of living cells; and the intercalator PI (log$P$ = –3.73) is a non-membrane-permeable DNA stain. As the membrane of a dead cell is highly damaged, positive staining by PI indicates cell mortality. Figure 1b shows that **1** (log$P$ = –0.96) displays intense *in cellulo* luminescence in live cells—apparently located in the cell nucleus—and does not affect cell viability, which is a critical factor in live cell imaging applications. The emission at 670–700 nm corresponds to activation of the well-documented 'light switch' effect upon reversible binding to DNA, and z-stack experiments involving co-localization with SYTO 9 clearly show that the

[1]Department of Chemistry, [2]Department of Molecular Biology and Biotechnology, [3]Department of Biomedical Science, University of Sheffield, Sheffield, UK.
*e-mail: james.thomas@sheffield.ac.uk; g.battaglia@sheffield.ac.uk

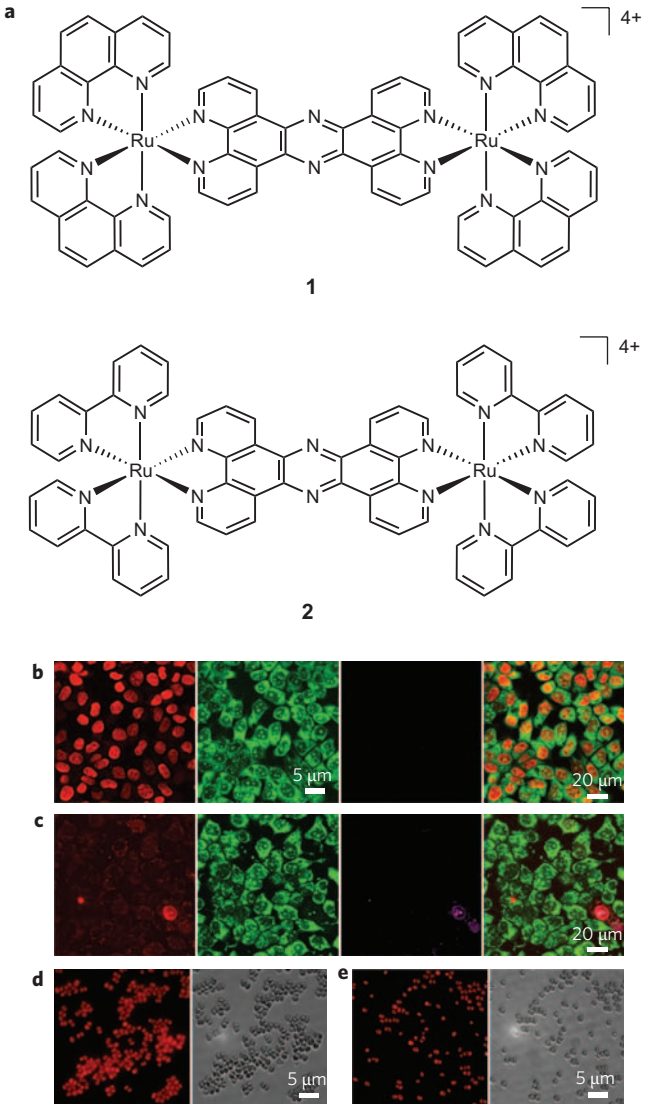

Figure 1 | The cellular uptake properties of dinuclear Ru(II) tpphz complexes. a, The two dinuclear ruthenium(II) tpphz systems relevant to this study, with either phen (**1**) or bpy (**2**) as ancillary ligands. **b**, Uptake and nuclear staining of MCF-7 breast cancer cell line by **1** (500 μM, 1 h). From left to right: luminescence emission of **1** (red), live cell stain SYTO 9 (green), dead cell stain propidium iodide (PI) (purple) and overlay image. **c**, Incubation with **2** (500 μM, 1 h) shows no staining of live cells and the co-localization with PI emission shows **2** to act as a dead cell stain. **d**, Staining of *S. Aureus* by **1** (200 μM, 45 min) showing the cellular uptake and *in cellulo* luminescence of **1** (left) with phase-contrast image (right). **e**, Fixed *S. Aureus* cells stained by **1** showing the condensed nucleoid structure (left) again with phase-contrast image (right).

observed luminescence is spherical in three dimensions, corresponding to the cell nucleus (Supplementary Fig. 1).

In contrast to **1**, the incubation of MCF-7 cells with **2** ($\log P = -1.61$) and subsequent imaging showed no staining of live cells under the same conditions (Fig. 1c), which would correspond with the lower cytotoxicity displayed by **2**. Further studies have revealed that complex **2** is an efficient DNA stain in fixed cell applications and is an indicator of cell mortality (Supplementary Fig. 2). Indeed, in live/dead staining it functions in a manner identical to PI but with novel excitation/emission wavelengths. Complex **1** displays similar advantages over conventional probes for living cells; it is highly water soluble, photostable (Supplementary Fig. 3) and

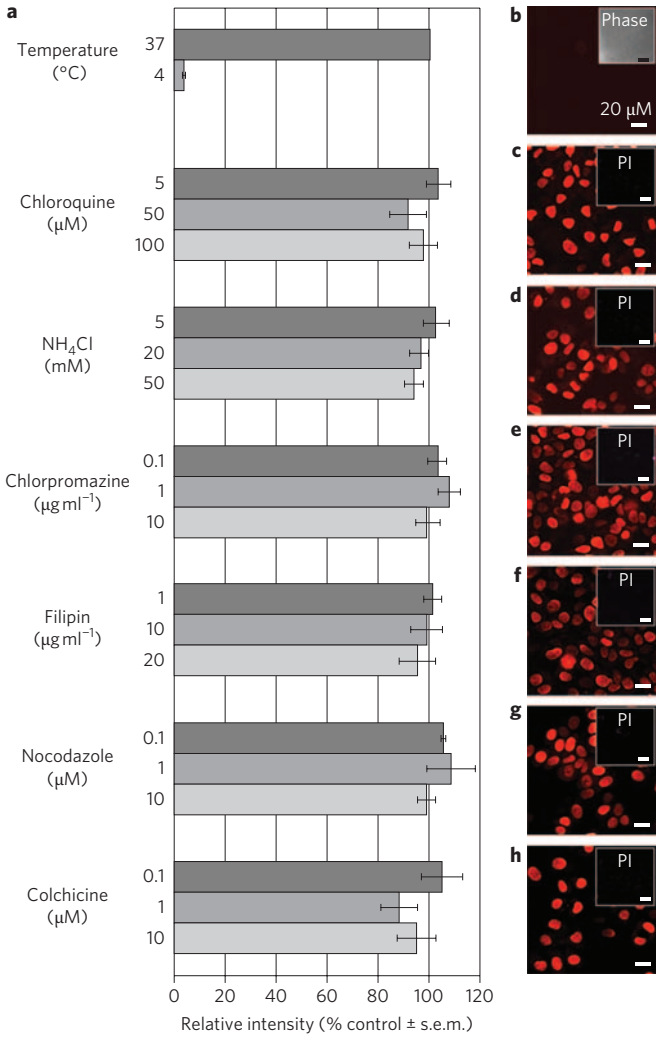

Figure 2 | Mechanism of cellular uptake of Ru(II) tpphz complex. a, Relative luminescence intensity of **1** in MCF-7 cells after inhibition treatment (500 μM, 1 h). Error bars represent standard error of the mean (s.e.m.) with $n = 3$. **b**, Temperature-dependence studies of uptake of **1** by MCF-7 cells at 4 °C (500 μM, 1 h) displays no *in cellulo* luminescence. The phase-contrast image is included for reference. **c**–**h**, Treatment with the endocytosis inhibitors chloroquine (100 μM) (**c**), NH_4Cl (50 mM) (**d**), chlorpromazine (10 μg ml^{-1}) (**e**), filipin (20 μg ml^{-1}) (**f**), nocodazole (20 μM) (**g**), and colchicine (20 μM) (**h**) show no inhibition of uptake of **1** by MCF-7 cells. PI staining is included for each to indicate cell viability. All scale bars represent 20 μM.

displays a large Stokes shift value with a long lifetime far-red emission—a factor that makes it extremely compatible with other imaging agents, such as the heavily-used green fluorescent protein (GFP). We are also able to show that **1** clearly images bacteria such as *Staphylococcus aureus in vivo*; the first time prokaryotic cells have been directly imaged using a metal-based system (Fig. 1d). For visualization of the nucleoid structure, fixed-cell experiments were performed and the condensed chromosome was clearly observable in cells (Fig. 1e).

The hydrophilicity and high charge of **1** would imply that the molecule does not freely diffuse across the cell membrane, as reflected by the relatively high concentration (>200 μM) required for efficient uptake. With this in mind, the mechanism of cellular uptake of the complex was investigated.

To probe whether **1** was taken up by a passive or active transport mechanism, MCF-7 cells were incubated with **1** at a temperature of

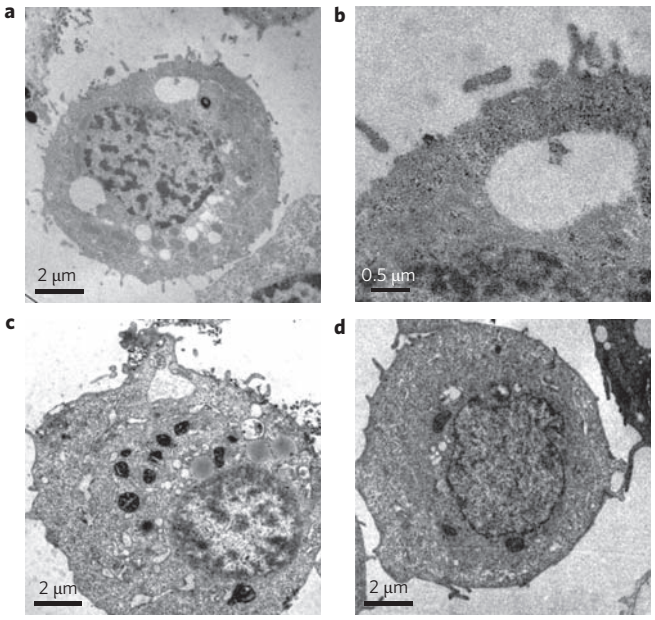

Figure 3 | Cellular localization of Ru(II) tpphz complex characterized by transition electron microscopy. a, TEM micrograph showing the cellular uptake of **1** by MCF-7 cells (500 μM, 1 h), directly using Ru(II) tpphz complex as a contrast agent to show cellular localization where **1** especially associates within the nucleus and shows strong heterochromatin staining. Note complete lack of contrast within cellular vesicles. **b**, The absence of **1** within an intracellular vesicle (large scale). **c**, MCF-7 cells incubated with **1** (500 μM, 1 h) and additionally stained with osmium tetroxide to show greater cellular detail. **d**, Negative control MCF-7 cell stained solely with osmium tetroxide.

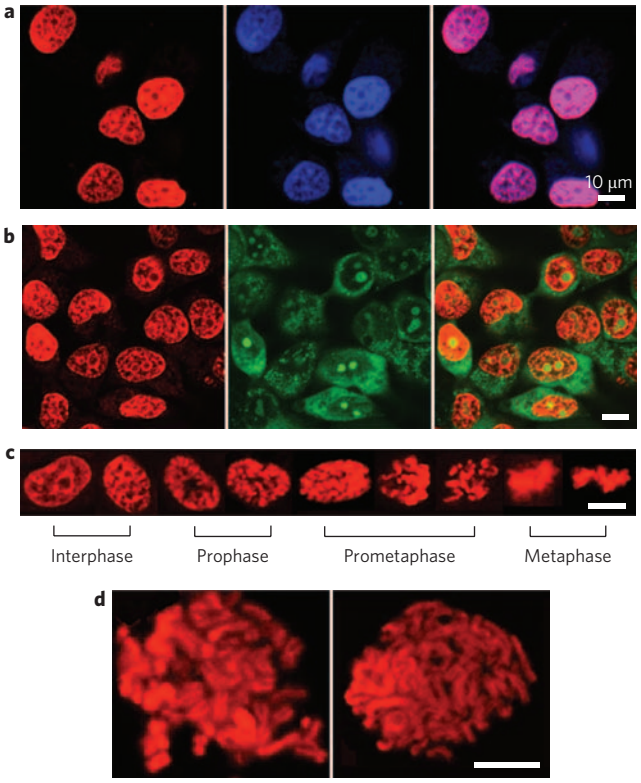

Figure 4 | A DNA-specific luminescent cellular imaging agent. a, Co-staining of **1** (red, left) with DNA-specific dye DAPI (DAPI = 4′,6-diamidino-2-phenylindole; blue, centre) and the overlay image (right). **b**, Co-staining of **1** (red, left) with general nucleic acid dye SYTO 9 (green, centre) and overlay image (right). Note the low co-localization of **1** with the green SYTO 9 emission from the nucleoli of cells. **c**, Asynchronous cell imaging shows mitotic cells stained by **1** visualizing chromosome aggregation through progression of mitosis. **d**, High magnification images of mitotic cells showing individual chromosomes. All scale bars represent 10 μM.

4 °C. Figure 2b shows that no luminescence is observed when the cells are incubated with the complex at this temperature, indicating that **1** enters cells and targets the nucleus by a temperature-dependent pathway and confirming that **1** is not a membrane-permeable molecule. As the most common energy-dependent method by which eukaryotic cells take up material is endocytosis, cells were co-incubated with **1** and several well-documented inhibitors of this process. Cellular uptake was then assessed by the extent of resultant nuclear staining by luminescence microscopy (Fig. 2).

As can be seen by the relative intensities of *in cellulo* luminescence after treatment with these inhibitors (Fig. 2a), co-incubation with **1** and the general endocytosis inhibitors chloroquine and ammonium chloride (two lysosomotropic agents)[21] or the specific endocytosis inhibitors chlorpromazine (clathrin-mediated)[22] and filipin (cavaeloe-mediated)[23] had no effect on the ability of **1** to function as a nuclear stain (Fig. 2a,c–f), showing that these two well-studied endocytotic pathways are not responsible for the uptake of **1**. Furthermore, neither colchicine or nocodazole, which disrupt the polymerization of microtubules and prevent membrane and endosomal trafficking[24], showed any inhibition of uptake (Fig. 2a,g,h). This data is therefore consistent with a non-endocytotic mechanism of uptake. This is not a surprising result when we consider the fact that the complex would still have to escape the endosome to target the nucleus. Our measurements of the lipophilicity of **1** show that the molecule remains hydrophilic in the acidic conditions similar to that found in endosomes ($\log P = -0.77$ at pH 5) and so the effects of acidification are unlikely to be responsible for release of **1** into the cytosol.

In addition to these luminescence microscopy studies, which rely on the DNA binding and subsequent activation of the 'light switch' effect to observe the *in cellulo* location of **1**, we are also able to show the cellular distribution of **1** in live cells using transition electron microscopy (TEM). As they incorporate a second row transition metal with high electron density, ruthenium complexes are able to scatter the electron beam used for imaging in TEM. This enhances contrast and is the phenomenon exploited in the use of reagents such as immunogold labels, ruthenium red and osmium tetroxide; hence the localization of **1** within live cells with high spatial resolution can be determined through TEM.

We therefore incubated MCF-7 cells with solutions of **1**, as for luminescence microscopy, before fixation and sectioning for TEM imaging. Figure 3a shows that although **1** is located throughout the cell cytosol, it is found in much higher concentration within the nucleus of the MCF-7 cells, and it localizes within heterochromatin. Notably, as highlighted in Fig. 3b, TEM micrographs show the absence of **1** from endosomal and lysosomal compartments, confirming that **1** is not transported into cells via an endocytotic pathway (Fig. 3a,b). Both nuclear localization and non-endocytotic uptake are further confirmed by co-staining with the phospholipid contrast reagent osmium tetroxide. As shown in Fig. 3c, cells incubated with **1** then co-stained with osmium tetroxide display highly contrasted nuclear heterochromatin, and again the endosomal compartments show no presence of compound **1**. As expected, the negative control micrograph of a cell stained only with osmium tetroxide shows a much less contrasted nuclear area (Fig. 3d).

As previously outlined, cellular uptake of hydrophilic, charged and polar molecules is generally very poor and recently strategies using either lipophilic ancillary ligands based on DIP (DIP = 4,7-diphenyl-1,l0-phenanthroline)[11–13,25] or conjugation to

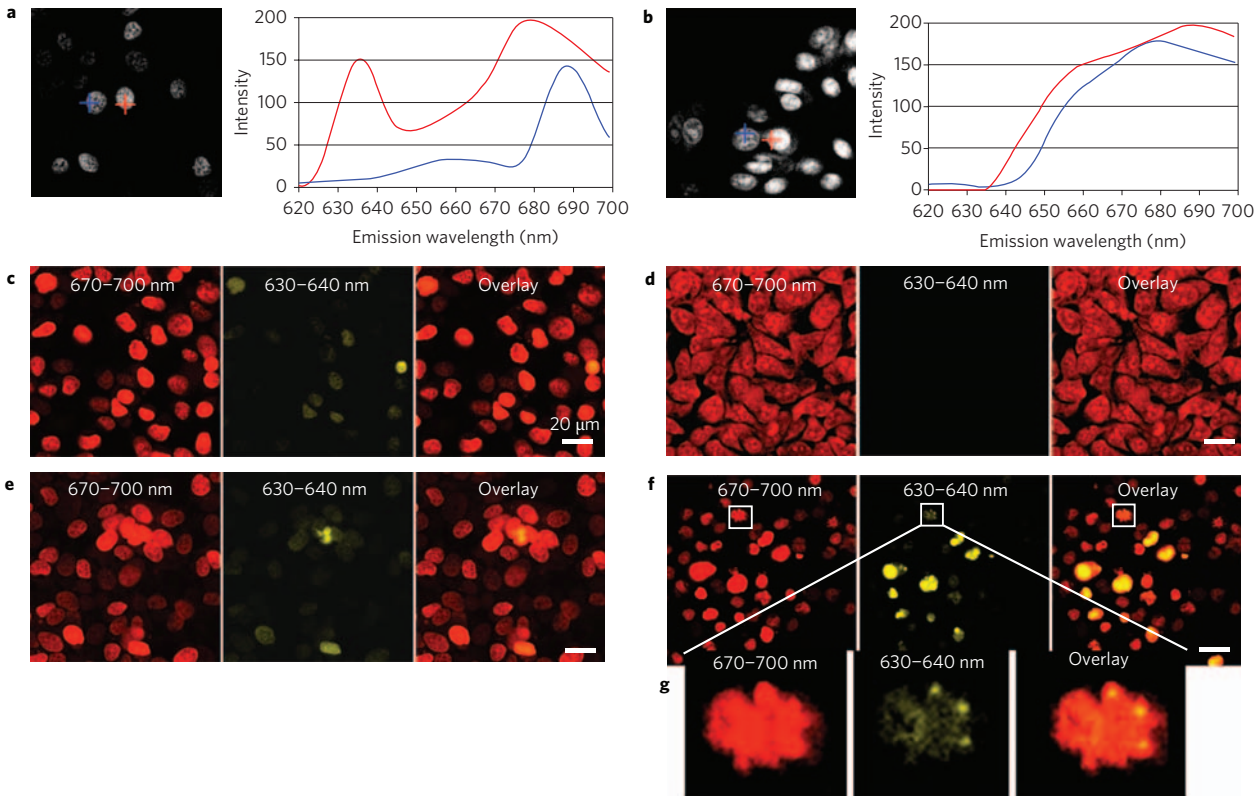

Figure 5 | Multiple-emission profile as a luminescent probe of DNA structure. a, Lambda stacking experiments show the emission profile of **1** in live MCF-7 cells to be composed of multiple emission peaks. The emission profile of two separate cellular regions (red and blue) show these peaks to have maxima of approximately 630 and 680 nm. The 680 nm peak is uniformly emitted from the nucleus (observed in both the red and blue region) but the 630 nm emission is found to be located in specific regions (red region only). **b**, Equivalent lambda stacking experiment of **1** in fixed MCF-7 cells displays only the 680 nm emission peak. **c**, Confocal microscopy images using two separate detection channels 670–700 nm (red) and 630–640 nm (yellow) show the multiple-emission profile of the nuclear luminescence of **1** bound to DNA and the specific localization of the 630–640 nm emission. **d**, Equivalent imaging experiment for fixed cells show that only the 670–700 nm red emission is present. **e**, MCF-7 cells fixed after incubation with **1** show that the distinctive multiple-emission properties seen in live cell imaging is retained, potentially due to **1** imaging a non-duplex DNA structure. **f**, L5178Y-R cells (which have extended G-rich telomeric DNA) stained with **1** (200 μM, 30 min) display a large increase in 630–640 nm emission. **g**, L5178Y-R metaphase chromosomes showing specific localization of the 630–640 nm emission peaks. All scale bars represent 20 μm.

protein/steroids[14,15,26] have been employed to increase membrane-permeability of DNA-binding metal coordination complexes. Although this has led to successful cellular uptake of both Ru(II) and Re(I)-based MLCT luminescent systems[11–15] the *in cellulo* DNA binding of such systems has not been successfully demonstrated. The work outlined herein shows that such an approach is not always required and represents a significant step in the development of these DNA binding systems towards *in vivo* applications. Further work into the exact mechanism of uptake is ongoing.

$[(phen)_2Ru(tpphz)Ru(phen)_2]^{4+}$: a probe of DNA structure

Higher-resolution imaging and co-staining with other commercially available fluorescent nuclear stains reveals that **1** is clearly targeting nuclear DNA. Incubation of MCF-7 cells with **1** and co-staining with the membrane-permeable DAPI ($\log P = 0.581$), a DNA minor-groove binder, shows strong co-localization of the two emission signals (Fig. 4a). Conversely, co-staining with the cyanine dye SYTO 9, a general nucleic acid stain, shows a clear difference in localization (Fig. 4b). Notably SYTO 9 preferentially binds RNA over DNA and as a consequence nucleoli, the site of rRNA synthesis and tRNA processing, are distinctly imaged through the dye's intense green emission. It is clear that **1** is a DNA-specific stain as, in contrast to SYTO 9, no emission from the complex is observed from nucleolar regions. Furthermore, **1** visualizes characteristic structural changes in nuclear DNA as cells progress through the cell cycle (Fig. 4c). When asynchronous cells are imaged, the majority of labelled cells are interphase but cells undergoing mitotic phases are also clearly observed. To image chromosomes in more detail, cells were halted in metaphase using colchicine as a mitotic spindle poison, stained and then mounted onto slides before imaging, allowing clear visualization of the aggregated chromosomes (Fig. 4d).

A structure-sensitive DNA imaging agent

One advantage in using such systems as cellular DNA probes is their ability to display a high degree of sensitivity in their DNA binding. For example, there is currently a great deal of interest in four-stranded DNA structures. The induction/stabilization of quadruplex DNA in G-rich sequences of DNA located at the ends of chromosomes (telomeres) is seen as an anti-cancer strategy[27] but nevertheless, to date, the actual detection of quadruplex formation in living cells has remained elusive. Previous *in vitro* studies have demonstrated that **1** binds to both duplex and quadruplex DNA with a high affinity; a distinctive blue-shifted 'light-switch' emission is displayed on binding to quadruplex DNA compared with the analogous duplex effect (maxima of ~630 nm and >650 nm respectively)[17]. This indicates that **1** has the ability to discriminate between different DNA structures and, therefore, the potential of **1** as a quadruplex DNA imaging tool has been explored.

It was found that 'light switch' emission due to the DNA bound complex within cells comprises two separate emission peaks.

Lambda stacking experiments, which measure the emission intensity across a range of wavelengths for a single excitation energy, revealed maxima at approximately 680 and 630 nm respectively. A representative Lambda stack displaying the emission profile of two separate regions in cells reveals the non-uniform specificity of the 630 peak in comparison with the prevalent 680 peak (Fig. 5a), suggesting that the 630 emission is from a different source. In order to observe the cellular localization of each of the signals, the image acquisition process was calibrated by defining a separate red (670–700 nm) and yellow (630–640 nm) channel. In Figure 5c, it is clear that the red emission shows the expected nuclear chromatin staining, but the yellow emission is localized in specific areas within nuclei and is not co-localized with the red emission. To determine if this effect is due to a non-duplex structure of DNA being imaged we explored the ability of **1** to induce/stabilize alternative forms of DNA by using formaldehyde fixation. This produces DNA–protein crosslinks and has the effect of 'freezing' DNA structure[28]. Using the novel imaging properties of the complex as a marker stain, fixed cell experiments were conducted, with MCF-7 cells being exposed to **1** before and after fixation. The incubation of fixed, permeabilized cells with **1** resulted in only the 680 nm emission being visible, with no detectable 630 nm peak (Fig. 5b,d). The observation of this single emission, which arises from **1** binding to native duplex DNA, indicates that **1** is incapable of inducing DNA structural changes after fixation. In contrast, when cells were fixed in an identical manner after incubation with **1**, the distinctive multiple emission profile is maintained (Fig. 5e). These results suggest that **1** induces/stabilizes multiple structures of DNA and that the 630 emission is due to an alternative non-duplex DNA structure.

In an attempt to further define the nature of the 630 nm emission, we selected the L5178Y-R mouse lymphoma cell line for further imaging experiments. This cell line has a large average length of G-rich telomeric DNA (80 kb compared to 2 kb in MCF-7 cells)[29] and therefore exhibits a greater potential for quadruplex formation. As shown in Fig. 5f, the staining of these cells by **1** results in a large increase in the yellow 630–640 nm emission compared with the MCF-7 cell line. Interestingly, this image also includes a mitotic cell showing three intense yellow points, apparently located at specific regions on the chromosomes (Fig. 5 g). These data would be in agreement with **1** functioning as a luminescent marker for quadruplex DNA; further work into ascribing the source of this *in cellulo* 630 nm peak is currently being undertaken.

In conclusion, we report the successful application of a dinuclear Ru(II) polypyridyl 'light switch' complex as an *in cellulo* nuclear DNA stain, well tolerated by eukaryotic and prokaryotic cells, and for use with both luminescence and transition electron microscopy. Highly unusually, despite the hydrophilicity of the molecule, it is taken up by live cells via a structure-specific and temperature-dependent non-endocytotic mechanism. Perhaps the most fascinating attribute of **1** as a new imaging tool is the existence on DNA binding of multiple emission peaks suggesting that this complex may find future application as an *in cellulo* DNA structural probe, specifically for quadruplex DNA.

Methods

Chemicals. All chemicals used were purchased from Sigma unless stated. The Ru(II) complexes were synthesized as previously described[16,17] and converted to their chloride salts.

Partition coefficients. Calculated octanol/water partition coefficients were obtained by using the Molinspiration software (www.molinspiration.com). Octanol/water partition coefficients for **1** and **2** were obtained using the 'shake-flask' method, with the concentration in each phase determined by UV–vis absorbance (Jasco V-630 Spectrophotometer). The partition coefficient, *P*, was calculated using $P = c_{oct}/c_{H2O}$ (where c = concentration). The experiment was repeated three times.

Cell culture. *Staphylococcus aureus* strain SH1000 spa- were grown in brain-heart infusion medium (Oxoid) at 37 °C. Colonies were incubated with **1** (200 μM) in a rotary shaker for 15 min at 4 °C or 37 °C, washed, and resuspended in GTE solution (50 mM Glucose, 10 mM EDTA, and 20 mM Tris. Cl at pH 7.5). A 5 μl aliquot was spread over a polylysine-coated glass slide and allowed to dry at room temperature. The preparation was mounted in H_2O and sealed with DPX mountant (BDH) before imaging. MCF-7 and L5178Y-R cells were cultured in RMPI 1640 medium (Invitrogen) supplemented with 2 mM L-glutamine, 100 IU ml^{-1} penicillin, 100 mg ml^{-1} streptomycin and 10% fetal calf serum, at 37 °C under a 5% CO_2 atmosphere. Cell cultures were treated with solutions of **1** and **2** (0.1 μM to 200 μM, 10% phosphate buffered saline solution (PBS): 90% cell media) for 24 hours before incubation with 0.5 mg ml^{-1} MTT (MTT = 3-(4,5-Dimethylthiazol-2-yl)-2,5-diphenyltetrazolium bromide) for 40 minutes. The formazan product was eluted using acidified isopropanol, and absorbance at 540 nm was quantified by spectrophotometer and cell viability determined (% untreated negative control). For imaging, MCF-7 cells were incubated with 500 μM **1** or **2** (10% PBS: 90% serum-free media) for 1 hour, and L5178Y-R cells were cultured in suspension and incubated with 200 μM of **1** for 30 minutes. All cells were washed with PBS before imaging. Co-staining was performed using 2 μM SYTO 9, 10 μM PI for 10 min or 500 nM DAPI for 2 min (in PBS). M-phase synchronization required incubation with colchicine (500 nM) for 48 hours before cells were detached and slide-mounted for imaging. For fixed-cell experiments, monolayers were treated with 10% formaldehyde (10 min). For staining after fixation, cells were additionally permeabilized with Triton (10 min) before exposure to 100 μM **1** or **2** (in PBS) for 15 minutes. Temperature dependence studies used cells that had been cooled at 4 °C for 30 minutes then incubated with 500 μM **1** (10% PBS: 90% serum-free media) at 4 °C for 1 hour. Inhibitor treatment required serum-free conditions throughout. Cells were treated with chloroquine, NH_4Cl, chlorpromazine, filipin, nocodazole and colchicine at the stated concentrations for 30 minutes, then with **1** (500 μM) plus the inhibitor for 1 hour before imaging.

Microscopy. MCF-7 and L5178Y-R cells were luminescently imaged on a Zeiss LSM 510 META upright confocal laser scanning microscope using 40× and 100× magnification long-range water-dipping lenses for monolayer cultures or a 63× oil-immersion lens for slide imaging. **1** and **2** were excited with an Ar-ion laser at 458 nm and emission monitored using META detection at 630–640 nm (yellow) and 670–700 nm (red) wavelengths as stated. SYTO 9 and PI were excited using 488 nm (Ar-ion) and 543 nm (He–Ne), respectively, and emission was collected using 500–530 nm (SYTO 9) and 565–615 nm (PI) bandfilters. For DAPI excitation, a Coherent Chameleon pulsed infrared multiphoton laser was used (800 nm) and the emission detected using a 420 nm long pass bandfilter. Image data acquisition and processing were performed using a Zeiss LSM image browser. *S. Aureus* stained cells were imaged using an Olympus IX70 inverted microscope with a 100× 1.3 NA oil immersion lens and digital camera. Excitation was provided by a mercury arc lamp with an excitation band pass filter of 420–490 nm, and a longpass 560 nm filter was used to visualize the luminescence. For quantitative uptake analysis in inhibition studies, luminescence intensity (% of 37 °C control, $n = 3$) was determined using data acquisition hardware and software ImageXpress 5000A (Axon Instruments), with an excitation wavelength of 465 nm and an emission band pass filter of 600–680 nm. For TEM, MCF-7 cells were incubated with **1** (500 μM, 1 h) then fixed using 3% glutaraldehyde and dehydrated using ethanol. TEM samples were sectioned in Araldite resin by microtome and examined on a FEI Tecnai instrument operating at 80 kV equipped with a Gatan 1 k CCD Camera.

Received 9 March 2009; accepted 10 September 2009; published online 18 October 2009

References

1. Tsien, R. Y., Ernst, L. & Waggoner, A. in *Handbook of Biological Confocal Microscopy* 3rd edn (ed. J. B. Pawley) 338–352 (Springer, 2006).
2. Martin, R. M., Leonhardt, H. & Cardoso, M. C. DNA labeling in living cells. *Cytometry Part A* **67,** 45–52 (2005).
3. Pfeifer, G. P., You, Y.-H. & Besaratinia, A. Mutations induced by ultraviolet light. *Mutat. Res.* **571,** 19–31 (2005).
4. Pandya, S., Yu, J. & Parker, D. Engineering emissive europium and terbium complexes for molecular imaging and sensing. *Dalton Trans.* 2757–2766 (2006).
5. Botchway, S. W. *et al.* Time-resolved and two-photon emission imaging microscopy of live cells with inert platinum complexes. *Proc. Natl Acad. Sci. USA* **105,** 16071–16076 (2008).
6. Friedman, A. E., Chambron, J. C., Sauvage, J. P., Turro, N. J. & Barton, J. K. A molecular light switch for DNA: $Ru(bpy)_2(dppz)^{2+}$. *J. Am. Chem. Soc.* **112,** 4960–4962 (1990).
7. Zeglis, B. M., Pierre, V. C. & Barton, J. K. Metallo-intercalators and metallo-insertors. *Chem. Commun.* 4565–4579 (2007).
8. Metcalfe, C. & Thomas, J. A. Kinetically inert transition metal complexes that reversibly bind to DNA. *Chem. Soc. Rev.* **32,** 215–224 (2003).
9. Jiménez-Hernández, M. E., Orellana, G., Montero, F. & Portolés, M. T. A ruthenium probe for cell viability measurement using flow cytometry, confocal microscopy and time-resolved luminescence. *Photochem. Photobiol.* **72,** 28–34 (2000).

10. Onfelt, B., Gostring, L., Lincoln, P., Norden, B. & Onfelt, A. Cell studies of the bisintercalator [u-C4(cpdppz)2-(phen)4Ru2]4+ : toxic effects and properties as a light emitting DNA probe in V79 Chinese hampster cells. *Mutagenesis* **17,** 317–320 (2002).
11. Amoroso, A. J. *et al*. Rhenium fac tricarbonyl bisimine complexes: biologically useful fluorochromes for cell imaging applications. *Chem. Commun.* 3066–3068 (2007).
12. Puckett, C. A. & Barton, J. K. Methods to explore cellular uptake of ruthenium complexes. *J. Am. Chem. Soc.* **129,** 46–47 (2007).
13. Puckett, C. A. & Barton, J. K. Mechanism of cellular uptake of a ruthenium polypyridyl complex. *Biochemistry* **47,** 11711–11716 (2008).
14. Lo, K. K. W., Lee, T. K. M., Lau, J. S. Y., Poon, W. L. & Cheng, S. H. Luminescent biological probes derived from ruthenium(II) estradiol polypyridine complexes. *Inorg. Chem.* **47,** 200–208 (2008).
15. Neugebauer, U. *et al*. Ruthenium polypyridyl peptide conjugates: membrane permeable probes for cellular imaging. *Chem. Commun.* 5307–5309 (2008).
16. Bolger, J., Gourdon, A., Ishow, E. & Launay, J.-P. Mononuclear and binuclear tetrapyrido [3.2-a: 2′, 3′-c: 3″, 2″-h: 2‴, 3‴-j] phenazine (tpphz) ruthenium and osmium complexes. *Inorg. Chem.* **35,** 2937–2944 (1996).
17. Rajput, C., Rutkaite, R., Swanson, L., Haq, I. & Thomas, J. A. Dinuclear monointercalating Ru(II) complexes that display high affinity binding to duplex and quadruplex DNA. *Chem. Eur. J.* **12,** 4611–4619 (2006).
18. Lutterman, D. A. *et al*. Intercalation is not required for DNA light-switch behavior. *J. Am. Chem. Soc.* **130,** 1163–1170 (2008).
19. Campagna, S., Serroni, S., Bodige, S. & MacDonnell, F. M. Absorption spectra, photophysical properties, and redox behavior of stereochemically pure dendritic ruthenium(II) tetramers and related dinuclear and mononuclear complexes. *Inorg. Chem.* **38,** 692–701 (1999).
20. Mailaender, C. *et al*. The MspA porin promotes growth and increases antibiotic susceptibility of both Mycobacterium bovis BCG and Mycobacterium tuberculosis. *Microbiology* **150,** 853–864 (2004).
21. Ziegler, H. K. & Unanue, E. R. Decrease in macrophage antigen catabolism caused by ammonia and chloroquine is associated with inhibition of antigen presentation to T cells. *Proc. Natl Acad. Sci. USA* **79,** 175–178 (1982).
22. Wang, L. H., Rothberg, K. G. & Anderson, R. G. Mis-assembly of clathrin lattices on endosomes reveals a regulatory switch for coated pit formation. *J. Cell Biol.* **123,** 1107–1117 (1993).
23. Schnitzer, J. E., Oh, P., Pinney, E. & Allard, J. Filipin-sensitive caveolae-mediated transport in endothelium: reduced transcytosis, scavenger endocytosis, and capillary permeability of select macromolecules. *J. Cell Biol.* **127,** 1217–1232 (1994).
24. Elkjaer, M. L., Birn, H., Agre, P., Christensen, E. I. & Nielsen, S. Effects of microtubule disruption on endocytosis, membrane recycling and polarized distribution of Aquaporin-1 and gp330 in proximal tubule cells. *Eur. J. Cell Biol.* **67,** 57–72 (1995).
25. Musatkina, E., Amouri, H., Lamoureux, M., Chepurnykh, T. & Cordier, C. Mono- and dicarboxylic polypyridyl-Ru complexes as potential cell DNA dyes and transfection agents. *J. Inorg. Biochem.* **101,** 1086–1089 (2007).
26. Brunner, J. & Barton, J. K. Targeting DNA Mismatches with rhodium intercalators functionalized with a cell-penetrating peptide. *Biochemistry* **45,** 12295–12302 (2006).
27. Hurley, L. H. DNA and its associated processes as targets for cancer therapy. *Nat. Rev. Cancer* **2,** 188–200 (2002).
28. Douglas, M. P. & Rogers, S. O. DNA damage caused by common cytological fixatives. *Mutat. Res.* **401,** 77–88 (1998).
29. Canela, A., Vera, E., Klatt, P. & Blasco, M. A. High-throughput telomere length quantification by FISH and its application to human population studies. *Proc. Natl Acad. Sci. USA* **104,** 5300–5305 (2007).

Acknowledgements

The author thanks C. Hill for TEM assistance and E. Smythe for helpful discussions. This work was supported by the EPSRC (UK) and the White Rose LSI-DTC.

Author contributions

M.R.G., G.B. and J.A.T. conceived and designed the experiments, M.R.G. and J.G.-L. performed the experiments, all the authors analysed the data, G.B., S.F., C.S. and J.A.T. contributed materials and analysis tools, M.R.G., G.B. and J.A.T. co-wrote the paper.

Additional information

Supplementary information accompanies this paper at www.nature.com/naturechemistry. The authors declare no competing financial interests. Reprints and permission information is available online at http://npg.nature.com/reprintsandpermissions/. Correspondence and requests for materials should be addressed to G.B. and J.A.T.